Dipl.-Inf. Patrick P. Neumann

Gas Source Localization and Gas Distribution Mapping with a Micro-Drone

BAM-Dissertationsreihe • Band 109
Berlin 2013

Die vorliegende Arbeit entstand an der BAM Bundesanstalt für Materialforschung und -prüfung.

Impressum

Gas Source Localization and
Gas Distribution Mapping
with a Micro-Drone

2013

Herausgeber:
BAM Bundesanstalt für Materialforschung und -prüfung
Unter den Eichen 87
12205 Berlin
Telefon: +49 30 8104-0
Telefax: +49 30 8112029
E-Mail: info@bam.de
Internet: www.bam.de

Copyright © 2013 by
BAM Bundesanstalt für Materialforschung und -prüfung

Layout: BAM-Referat Z.8

ISSN 1613-4249
ISBN 978-3-9815944-1-6

Gas Source Localization and Gas Distribution Mapping with a Micro-Drone

Dissertation

des Fachbereichs Mathematik und Informatik
der Freien Universität Berlin
zur Erlangung des Grades eines
Doktors der Naturwissenschaften
(Dr. rer. nat.)

vorgelegt von

Dipl.-Inf. Patrick P. Neumann

Promotionsausschuss:

Vorsitzender:	Prof. Dr.-Ing. habil.	Jochen H. Schiller
Gutachter:	Prof. Dr.	Achim J. Lilienthal
Gutachter:	Prof. Dr.	Helmut Alt
Gutachter:	Dr.-Ing.	Achim Liers
Gutachter:	Dr.-Ing.	Matthias Bartholmai

Tag der wissenschaftlichen Aussprache: 06.06.2013

Berlin 2013

Abstract

The objective of this Ph.D. thesis is the development and validation of a VTOL-based (Vertical Take Off and Landing) micro-drone for the measurement of gas concentrations, to locate gas emission sources, and to build gas distribution maps. Gas distribution mapping and localization of a static gas source are complex tasks due to the turbulent nature of gas transport under natural conditions [1] and becomes even more challenging when airborne. This is especially so, when using a VTOL-based micro-drone that induces disturbances through its rotors, which heavily affects gas distribution. Besides the adaptation of a micro-drone for gas concentration measurements, a novel method for the determination of the wind vector in real-time is presented. The on-board sensors for the flight control of the micro-drone provide a basis for the wind vector calculation. Furthermore, robot operating software for controlling the micro-drone autonomously is developed and used to validate the algorithms developed within this Ph.D. thesis in simulations and real-world experiments.

Three biologically inspired algorithms for locating gas sources are adapted and developed for use with the micro-drone: the surge-cast algorithm (a variant of the silkworm moth algorithm) [2], the zigzag / dung beetle algorithm [3], and a newly developed algorithm called “pseudo gradient algorithm”. The latter extracts from two spatially separated measuring positions the information necessary (concentration gradient and mean wind direction) to follow a gas plume to its emission source. The performance of the algorithms is evaluated in simulations and real-world experiments. The distance overhead and the gas source localization success rate are used as main performance criteria for comparing the algorithms.

Next, a new method for gas source localization (GSL) based on a particle filter (PF) is presented. Each particle represents a weighted hypothesis of the gas source position. As a first step, the PF-based GSL algorithm uses gas and wind measurements to reason about the trajectory of a gas patch since it was released by the gas source until it reaches the measurement position of the micro-drone. Because of the chaotic nature of wind, an uncertainty about the wind direction has to be considered in the reconstruction process, which extends this trajectory to a patch path envelope (PPE). In general, the PPE describes the envelope of an area which the gas patch has passed with high probability. Then, the weights of the particles are updated based on the PPE. Given a uniform wind field over the search space and a single gas source, the reconstruction of multiple trajectories at different measurement locations using sufficient gas and wind measurements can lead to an accurate estimate of the gas source location, whose distance to the true source location is used as the main performance criterion. Simulations and real-world experiments are used to validate the proposed method.

The aspect of environmental monitoring with a micro-drone is also discussed. Two different sampling approaches are suggested in order to address this problem. One method is the use of a predefined sweeping trajectory to explore the target area with the micro-drone in real-world gas distribution mapping experiments. As an alternative sampling approach an adaptive strategy is presented, which suggests next sampling points based on an artificial potential field to direct the micro-drone towards areas of high predictive mean and high predictive variance, while maximizing the coverage area. The purpose of the sensor planning component is to reduce the time that is necessary to converge to the final gas distribution model or to reliably identify important parameters of the distribution such as areas of high concentration. It is demonstrated that gas distribution models can provide an accurate estimate of the location of stationary gas sources. These strategies have been successfully tested in a variety of real-world experiments in different scenarios of gas release using different gas sensors to verify the reproducibility of the experiments. The adaptive strategy was also successfully validated in simulations using predefined sweeping trajectories as reference criteria.

The results of this Ph.D. thesis reflect the applicability of gas-sensitive micro-drones in a variety of scenarios of gas release. Effective counteractive measures can be set in motion after accidents involving gas emissions with the aid of spatially resolved gas concentration and wind data collected with micro-drones. Monitoring of geochemically active regions, landfills, CO_2 storage facilities, and the localization of gas leaks are further areas of application.

Zusammenfassung

Die Zielsetzung der Dissertation ist die Entwicklung und Validierung einer VTOL-fähigen (Vertical Take Off and Landing) Mikrodrohne zur Messung von Gaskonzentrationen, zur Lokalisierung von Gasemissionsquellen und zur Erstellung von Gasverteilungskarten. Neben der Adaption einer Mikrodrohne zur Gaskonzentrationsmessung wird ein neuartiges Verfahren zur Bestimmung des Windvektors in Echtzeit realisiert. Die Basis für die Windvektorberechnung bildet die Onboard-Sensorik zur Flugregelung der Mikrodrohne. Weiterhin wird eine neuartige Software zur autonomen Steuerung der Mikrodrohne vorgestellt, mit der eine ausführliche Validierung der im Rahmen dieser Dissertation entwickelten Algorithmen in Simulationen und Realexperimenten durchgeführt wird.

Zwei biologisch inspirierte Algorithmen zur Lokalisierung von Gasquellen wurden für den Einsatz mit der Mikrodrohne angepasst – die Entwicklung eines dritten Algorithmus wird ebenfalls beschrieben. Dieser Algorithmus extrahiert aus zwei räumlich getrennten Messpunkten die notwendigen Informationen (Konzentrationsgradient und mittlere Windrichtungen) um einer Gasfahne bis hin zur Emissionsquelle zu folgen. Die Leistungsfähigkeit der Algorithmen wurde in Simulationen und Realexperimenten bestimmt, wobei als Vergleichskriterium dabei die Abweichung der von der Mikrodrohne erstellten Trajektorie im Vergleich zur Ideallinie und die Erfolgsquote beim Lokalisieren der Gasquelle herangezogen wurden.

Im Anschluss wird eine neue Methode zur Quelllokalisierung beruhend auf einem Partikelfilter präsentiert. Dabei steht jedes Partikel für eine gewichtete Hypothese der Quellposition. Im ersten Schritt rekonstruiert der Partikelfilter anhand der Messdaten der Mikrodrohne den Weg, den das Gas von der Quelle bis zur Messposition genommen haben könnte, und aktualisiert auf Basis dieser Berechnung die Gewichtung der Partikel. Unsicherheiten bezüglich der gemessenen Windrichtung werden dabei in Form eines sich öffnenden Wind-Kegels in Flächenprojektion

(2D) berücksichtigt. Ausgehend von mehreren Messpositionen kann schließlich eine gute Schätzung der Quellposition erfolgen, deren Abweichung dabei ein Kriterium der Leistungsfähigkeit des Algorithmus darstellt. Simulationen und Realexperimente dienen hierbei zur Validierung des Verfahrens.

Auch auf den Aspekt der Umweltbeobachtung von Gasverteilungen mit einer Mikrodrohne wird eingegangen. Hierzu werden zwei Messstrategien zur Modellierung der Gasverteilung verglichen. Eine Strategie sieht die Messung entlang vordefinierter Sweeping-Trajektorien vor, wohingegen ein weiterer Ansatz adaptiv neue Messpositionen auf Basis eines kontinuierlich aktualisierten Gasverteilungsmodells vorschlägt. Diese adaptive Messstrategie verwendet künstliche Potentialfelder um die Mikrodrohne in Regionen mit hoher Gaskonzentration oder hoher Varianz der Gaskonzentration zu steuern, während generell eine möglichst umfassende Abdeckung der Überwachungsfläche angestrebt wird. Ziel ist die Minimierung der Zeit, die notwendig ist, um ein repräsentatives Gasverteilungsmodell zu erhalten. Es wird gezeigt, dass Gasverteilungsmodelle dazu beitragen können Positionen von Gasquellen zu bestimmen. Die Strategien wurden erfolgreich in einer Vielzahl von Realexperimenten in verschiedenen Szenarien der Gasfreisetzung erprobt und unter Verwendung unterschiedlicher Gassensortechnologien auf Reproduzierbarkeit der Experimente getestet. Die adaptive Messstrategie wurde darüber hinaus erfolgreich in Simulationen validiert.

Die Resultate dieser Dissertation spiegeln die Anwendbarkeit gassensitiver Mikrodrohnen unter verschiedenen Bedingungen der Gasfreisetzung wider. Effektive Gegenmaßnahmen bei Gefahrenszenarien nach Chemie- oder Gefahrgutunfällen können mit Hilfe ortsaufgelöster Gaskonzentrations- und Winddaten eingeleitet werden. Die Überwachung von geochemisch aktiven Regionen, Mülldeponien, CO_2-Speicherungsanlagen und die Lokalisierung von Leckagen bilden weitere Anwendungsfelder.

Acknowledgments

This Ph.D. thesis was conducted at Division 8.1 Sensors, Measurement and Testing Methods of the Federal Institute for Materials Research and Testing (BAM). I am grateful to all those who have supported and encouraged me throughout my Ph.D. thesis. In particular, I would like to acknowledge and thank my supervisors Prof. Dr. Jochen H. Schiller (FU Berlin), Prof. Dr. Achim J. Lilienthal (Örebro University), and Dr. Matthias Bartholmai (BAM) for their valuable thoughts, fruitful discussions, and revision of my publications.

I would like to express my special gratitude to my co-supervisor Prof. Dr. Achim J. Lilienthal, who invited me for two months to his lab "Mobile Robotics and Olfaction" at Örebro University and provided me with accommodation. There, I had the opportunity to work closely with other Ph.D. students. In this context, I want to thank (in alphabetical order) Sahar Asadi, Victor Hernandez Bennets, Javier G. Monroy (University of Málaga), Sepideh Pashami, Matteo Reggente, Dr. Marco Trincavelli, and the other members of the lab for their collaboration, their support, the good teamwork, and for being not only colleagues but also good friends.

I would like to thank Prof. Dr. Manfred Hennecke, Dr. Heinrich Heidt, and Dr. Werner Daum for the organizational supervision at BAM. My gratitude also goes to my colleagues from Division 8.1, in particular to (in alphabetical order) Jessica Erdmann, Stefan Hohendorf, Michael Kammermeier, Harald Kohlhoff, Manol Manolov, and the other members of our division who were involved in the development of the hardware and construction of prototypes for this Ph.D. thesis, shared their ideas with me, spent hours in front of an intensely smoking barbecue, and/or created a delightful working environment. Furthermore, I would like to thank my colleagues from Divisions 2.1 (Jörg Bethge and Dr. Abdel Karim Habib), 4.2 (Reinhard Noske), 6.4 (Dr. Ulrich Banach), 7.3 (Dr. Simone Krüger and Tina Raspe), and Airrobot, as well as associates and friends from the FU Berlin including the Botanical Garden of

Berlin (Michael Schnürmacher, Karsten Schomaker, and Daniel Werner), TU Berlin (Dr. Timm Janetzke and Prof. Dr. Wolfgang Nitsche), and TU Dresden for providing experiment facilities, their excellent cooperation, and their expert support. In this context, I would also like to thank Prof. Dr. Tamás Meggyes for checking my English in several publications and this Ph.D. thesis.

I would like to express my gratitude also to Prof. Dr. Ricardo Vieira Díaz and Dr. Emilio J. Vélez Herranz (Universidad Complutense de Madrid) and to Joaquin Naveran Eiriz (Casa de los Volcanes) for inviting us to fascinating Lanzarote, where we were able to gain our first experiences with the gas-sensitive micro-drone in preliminary field tests performed in the Parque Nacional de Timanfaya. The private guides, the presentations of your measurement equipment, the culinary delicacies of Lanzarote, and of course your hospitality are unforgotten.

Furthermore, I would like to thank Prof. Dr. Orlando Vaselli and Luciano Giannini (Università degli Studi di Firenze) for inviting us to the geochemically active Tuscany Region (Italy), where we performed the majority of the gas distribution mapping experiments. I want to thank both for their hospitality and for accompanying us during our stay. Moreover, I want to thank Orlando for helping me in a reckless rescue mission to retrieve the micro-drone and its payload from a gas-filled sink, and Luciano for the first (and hopefully not the last) flying lesson in a Tecnam P-92 Echo ultralight aircraft.

Finally, I want to thank my family and friends for supporting me throughout my Ph.D. thesis, especially my parents and my wife Dana who provided me with support and understanding for my 7-days working weeks (and for surprising me with the incredible and addictive raspberry tartlets from “KaDeWe”).

This research was supported by a Ph.D. program (BAM) as well as by funding (“MNPQ Transfer”; file number 28/07) from the Federal Ministry of Economics and Technology (BMWi). The funding is gratefully acknowledged.

Contents

Chapter 1

Introduction

At present, the release of hazardous and greenhouse gases is an acute threat to the environment/climate and mainly responsible for extensive ecological damage, both global (ozone layer depletion and global warming) and local (pollution and poisoning hazards caused by accidents). Gases may be released in many different ways and for various reasons: as exhaust gases from traffic or industry, as flue gases from fires, or as a consequence of incidents with chemicals. Other sources of gas emission are, e.g., geodynamically active regions, waste disposals, Carbon Capture & Storage (CCS) areas, industrial sites, landfill sites, and contaminated areas. Thus, an early localization of gas leaks and monitoring of potential areas of gas emission are essential.

> August 23, 2011 – Earthquake Could Cause Gas Leaks: *"The* 5.9 *earthquake centered near Richmond, Va., which struck the east coast this afternoon, could have damaged natural gas lines. Both the city of Philadelphia, and the state of Pennsylvania have issued warnings to residents to call* 911 *if they smell natural gas." [4]*

The fundamental requirement for gas emission control as well as effective counteractive measures in case of incidents or disasters such as the above mentioned earthquake is the availability of measurements of relevant gas concentrations in the area of interest with high spatial and temporal resolution, e.g., to provide incident planning staff with information to prevent citizens and rescue workers from being harmed or killed [5]. In order to obtain a truthful representation of the gas distribution and be able to locate gas sources, it is essential to collect spatially distributed concentration and wind measurements. The response of many gas sensors, however, is caused by direct interaction with the chemical compounds and thus represents only a small area around the sensor surface. For economical and deployment-related reasons, a stationary sensor network is in many cases not a viable solution. The measuring vehicles used up to now [6–8] which are equipped with appropriate gas analysis technology can carry out highly selective gas measurements, but are typically ground-based and cannot reach the emission source in certain cases due to, e.g., obstacles, rough terrain, and large gaps. Smaller handheld measurement devices are flexible and inexpensive, but the danger of hazardous gases to people can prevent their use very close to the emission source. Therefore, only remote sensing can often be carried out. Accordingly, a quickly deployable, flying mobile measurement device, which is able to measure gas concentrations and wind vectors in many different scenarios of gas release, is needed to perform the above mentioned gas source localization and monitoring tasks.

Micro Unmanned Aerial Vehicles (MUAVs) can be equipped with a variety of sensors and precisely navigated to a certain region of interest for remote sensing without endangering persons in critical areas. MUAVs are interesting because they are cost-efficient, easy to transport, and can be deployed in a short time. Micro Vertical Take-Off and Landing (VTOL) UAVs, such as quadrocopters (in the following referred to as micro-drones), have the ability to hover over a certain point of interest for a prolonged time. Their compact design and excellent maneuverability makes precise navigation which gives access even to small passages in urban terrain and on industrial sites possible.

In the past two decades a number of algorithms for gas source localization (GSL) and gas distribution mapping (GDM) have been presented. To the author's knowledge, implementations of these algorithms have been tested and evaluated so far on ground-based mobile robot platforms, Autonomous Underwater Vehicles (AUVs), and blimps. Gas distribution mapping and localization of a static gas source are complex tasks due to the turbulent nature of gas transport under natural conditions [1] (Fig. 1.1). Gas molecules emitted in natural environments are carried by the wind, forming a plume. Two physical processes that influence the transport of gas molecules and cause the dilution and dispersion downwind of the source are molecular diffusion and turbulence. Molecular diffusion is a very slow process and therefore negligible [10]. Turbulence causes the formation of eddies of different

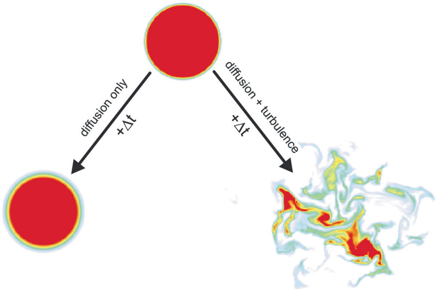

Figure 1.1: *Effect of turbulence compared to pure molecular diffusion (figure and caption are taken from Smyth and Moum [9]): At the top, the initial state is assumed to be a circular region of nearly homogeneous concentration, whereas two numerical solutions of the equations of motion obtained in the case of a motionless fluid (left) and in the case of fully developed, two-dimensional turbulence (right) are shown at the bottom. The mixed region (yellow/green) in the distribution on the right expands much more rapidly in the turbulent case (i.e., no smooth concentration gradients are formed pointing at the gas source).*

size [11]. This leads to a patchy and intermittent structure of plumes where high and low gas concentrations are spatially and temporally close [12]. Often, the actual gas source is located at the point of highest gas concentration, although it may occur that the highest concentration is measured far away from the gas source.

Ground-based mobile robots could be operated at very low speeds in the magnitude of approximately $\leq 0.1ms^{-1}$, which affects gas distribution only marginally in comparison to a micro-drone. The rotors of the micro-drone induce disturbance, which heavily affects the gas distribution. Thus, the task of gas source localization and gas distribution mapping becomes even more challenging when airborne. This Ph.D. thesis deals with the problem of gas source localization and gas distribution mapping in natural environments with a micro-drone. To the author's knowledge, it is the first time that these tasks are addressed with an airborne micro-drone in real-world scenarios.

The first part of this Ph.D. thesis discusses the development and in-depth validation of a gas-sensitive micro-drone that provides the basis for the real-world experiments performed throughout this work. A novel approach to estimate the wind vector based on the existing measurement data of the micro-drone's on-board sensors is implemented to avoid the need to use anemometric sensors. A detailed evaluation in wind tunnel and field tests is included. The robot operating software to autonomously control the micro-drone from the ground station and a simulation environment are presented as well.

The second part of this Ph.D. thesis deals with the problem of gas source localization with a micro-drone. The task of localizing a gas source can be broken down into three subtasks [13]:

1. Plume finding: attempting to get into contact with the gas.
2. Plume traversal: following the gas plume to its source.
3. Source declaration: determining the gas source location.

However, the source declaration phase is performed in parallel to the other two subtasks rather than merely at the end. Some algorithms may even not need to differentiate between plume finding and traversal, e.g., probabilistic algorithms (Sec. 2.2.2.1). This work deals with all three phases with the main focus on the latter two. Three reactive, biologically-inspired (bio-inspired) plume tracking strategies are implemented and a new measuring strategy especially designed for, but not limited to, a micro-drone is presented. This includes a statistical investigation of their performance and robustness. The task of declaring the source is still an open issue rarely addressed in the past. This work provides a possible solution for the whole gas source localization task, including gas source declaration for a gas-sensitive micro-drone, by incorporating a particle filter-based localization approach.

The third part of this work addresses the problem of gas distribution mapping with a micro-drone. Modeling the gas distribution is the task of deriving a truthful representation of the observed gas distribution from a set of spatially and temporally distributed measurements [14]. Two different sampling approaches are suggested in order to address this problem. First, predefined trajectories are used to explore the target area with the micro-drone in several real-world gas distribution mapping experiments. A detailed investigation concerning the suitability of micro-drones for gas distribution mapping is given in this context. However, building detailed gas distribution maps over large areas is time-consuming. To arrive at a truthful gas distribution model more quickly, a second approach is presented that allows for faster inference of a reasonably accurate estimate of the gas source location. The adaptive sensor planning algorithm suggests next sampling points based on an Artificial Potential Field (APF). The selection process considers three objectives to direct the sensor towards areas of high predictive mean and high predictive variance of the gas distribution while maximizing the coverage area. By introducing locality constraints, the results of the sensor planning component can be used to plan suitable paths for a micro-drone.

Nevertheless, all suggested solutions can be transferred to other robotic platforms regardless of the element for which the robot is specialized (land, water, and air).

1.1 Contributions

The main contributions of this Ph.D. thesis are:

1. Development and adaptation of two gas sensor modules, respectively, intended for use as payload for quadrocopter-based micro-drones, including their experiment evaluation with the Airrobot AR100-B micro-drone.

2. Development and experiment evaluation of three different methods to reduce disturbance of gas transport by the rotors of the micro-drone.

3. Introduction and experiment evaluation of a new approach to estimate the wind vector in real-time based on the existing measurement data of the micro-drone's on-board sensors which makes additional anemometric sensors superfluous. To the best of the author's knowledge, this approach is unique.

4. Demonstration of airborne measuring and monitoring of hazardous scenarios with quadrocopter-based micro-drones and realization of 22 real-world experiments in different outdoor environments (Tuscany Region, BAM Test Site 'Technical Safety', and Botanical Garden of Berlin) under varying wind and weather conditions. Furthermore, the suitability of the micro-drone for gas distribution mapping is evaluated (in general: environmental monitoring tasks), including a detailed evaluation of the experiment runs. It should be highlighted that the real-world experiments were performed with the gas-sensitive micro-drone in outdoor environments without simplifying the experiment setups.

5. Setup of a simulation environment for systematic gas source localization and gas distribution mapping experiments with a simulated micro-drone. This includes the development and integration of a filament-based gas dispersion

model by Pashami et al. [15], a GPS model, a gas sensor model, a simple disturbance model of the micro-drone, and a wind direction sensor model.

6. Tackle the problem of gas source localization and gas distribution mapping of static gas sources in natural environments with a gas-sensitive micro-drone.

7. Implementation of three reactive bio-inspired plume tracking strategies adapted for the micro-drone: the surge-cast algorithm (a variant of the silkworm moth algorithm) [2], the zigzag / dung beetle algorithm [3], and a newly developed algorithm called “pseudo gradient algorithm”. The latter incorporates a new measuring strategy especially designed for (but not limited to) a micro-drone. An experiment evaluation of the plume tracking strategies was performed in simulation and real-world experiments, including a detailed statistical analysis of their performance and robustness.

8. Introduction of an algorithm based on a particle filter to perform gas source localization. The main contribution is the proposed measurement model that uses gas and wind measurements to build a patch path envelope (PPE) and update the particles depending on their relative position to the PPE and the actual gas measurements. The PPE describes the envelope of an area the gas patch has passed with high probability. An experiment evaluation of this algorithm was performed in simulation and real-world experiments. Furthermore, an experiment observation demonstrates that the assumption of a uniform wind field does not hold in turbulence-dominated environments.

9. Introduction of a sensor and path planning strategy [16] that incorporates locality constraints to plan the path for a micro-drone. The algorithm uses information about the target area, previous sampling locations, and the current statistical gas distribution model to direct the sensor towards areas of high predictive mean, high predictive variance, while maximizing the coverage area using an artificial potential field. An experiment evaluation of this algorithm was performed in simulation and real-world experiments.

10. Confirmation of the observation that the gas distribution maps (and particularly the variance prediction) can provide good estimates of the gas source location.

1.2 Structure of the Thesis

The structure of this thesis is as follows:

Chapter 2 gives an overview of gas sensing technologies, which are relevant or interesting for mobile robotic applications, including a short discussion concerning the gas sensor selection for the micro-drone. Furthermore, a survey of related work on gas sensing with mobile robots and (micro) unmanned aerial vehicles is provided. Finally, a brief review of state-of-the-art wind vector estimation techniques for (micro) unmanned aerial vehicles is given.

Chapter 3 details the development and in-depth validation of a gas-sensitive micro-drone that is used in the real-world experiments of the present Ph.D. thesis. Furthermore, it presents a novel approach to estimate the wind vector based on the existing measurement data of the micro-drone's on-board sensors without a dedicated anemometer. The proposed approach is evaluated in wind tunnel and field tests. The second part of this chapter presents two different robot operating software to predefine measurement campaigns and to autonomously control the micro-drone from the ground station.

Chapter 4 discusses the need for simulation experiments and presents the setup of the simulation environment that was used for the investigations of this Ph.D. thesis.

Chapter 5 describes three bio-inspired plume tracking algorithms and their implementation for a gas-sensitive micro-drone including a new measuring strategy especially designed for, but not limited to, a micro-drone. An experiment comparison of these strategies in simulation and real-world experiments is also given, including a detailed statistical analysis of their performance and robustness.

Chapter 6 introduces a new algorithm based on a particle filter to perform gas source localization. A unique measurement model is proposed that uses gas and wind measurements to infer the location of the gas source. The algorithm was evaluated in simulation and real-world experiments.

Chapter 7 exemplifies how to address environmental monitoring tasks with a gas-sensitive micro-drone and presents the realization of 22 real-world experiments in a number of uncontrolled outdoor environments with varying wind and weather conditions to evaluate and discuss the suitability of the micro-drone for gas distribution mapping.

Chapter 8 introduces a sensor and path planning strategy that incorporates locality constraints in order to plan the path for a micro-drone and presents an experiment evaluation of this algorithm in simulation and real-world experiments.

Chapter 9 concludes the Ph.D. thesis and gives an outlook on future work.

Chapter 2

State of the Art and Related Work

2.1 Gas Sensor Technology

Coal miners used to bring canary birds to the mine shafts as an early detection system of life-threatening gases such as carbon dioxide (CO_2), carbon monoxide (CO), and methane (CH_4). The canary bird, normally a very songful bird, would stop singing and eventually die in the presence of these gases, signaling the miners to exit the mine quickly [17]. However, this out-of-time "detection system" was neither able to identify the threatening gas, nor its concentration.

Gas sensors are small devices that generate an electrical signal in the presence of a target gas. They are usually part of a safety system, which can be mobile or stationary, to identify and to quantify gaseous chemical volatiles. Gas sensors can be classified according to their operational principles. The most common sensors are thermal, mass, electrochemical, potentiometric, amperometric, conductometric, and optical sensors [18]. The general principle behind gas sensors is the fact that "changes in the gaseous atmosphere alter the sensor properties in a characteristic way" [5]. The requirements on gas sensors in robotics (and in other fields of application as well) are high sensitivity, selectivity, reliability, and robustness as well as a *rapid response time*, low power consumption, and compact size [19]. Additionally, the sensors should be inexpensive and commercially available.

Analytical equipment, such as infrared (IR) spectroscopy, gas chromatography (GC), and mass spectrometry (MS) constitute an alternative to the use of gas sensors [20]. However, these instruments are still too heavy, large, and expensive, making them unattractive for mobile robot applications, especially for micro-drones.

In the following subsections a brief overview of gas sensing technologies is provided, which are relevant or interesting for mobile robotic applications. Furthermore, their advantages and disadvantages are presented and the most promising sensors for the use on a micro-drone are identified. A complete survey of the different sensor technologies is beyond the scope of this Ph.D. thesis and can be found in [18].

2.1.1 Catalytic (Cat)

A catalytic (Cat) gas sensor is a thermal sensor. Cat gas sensors are composed of a so-called pellistor: a platinum (Pt) coil which is embedded in a pellet of sintered ceramic material coated with a porous catalytic metal. The porosity of the catalyst leads to an increased response time of the sensor. The Pt coil acts both as the heater and as the resistance thermometer [18]. Typical operating temperatures for the Pt coil are between $300°C$ and $500°C$. The presence of flammable gases (or vapors) causes a combustion at the catalytic surface of the sensor. The evolved heat from this reaction increases the temperature of the pellistor (heat of reaction), which also results in an increase of its resistance. This change in resistance is proportional to the concentration of the explosive gases or vapors. In addition to the catalytically-active element, the sensor also contains a heated, inactive compensator element [21]. Both elements are part of a Wheatstone bridge. The advantage is that environmental influences such as temperature and humidity are compensated. However, the fundamental problem of Cat gas sensors is the catalyst poisoning [18]: another chemical compound that bonds on the catalytic surface of the sensor reducing the effectiveness of the catalyst (a poisoned catalytic surface can no longer accelerate the desired chemical reaction). A more detailed description of Cat gas sensors can be found in [18].

Advantages of Cat gas sensors are their commercial availability, robustness, linearity, and the simple calibration routine. On the other hand, the heat-of-reaction principle requires relatively high gas concentrations resulting in a low sensitivity (in the magnitude of % by volume). Further disadvantages are the low selectivity – each flammable gas or vapor, which is burned catalytically, results in a change in resistance of the pellistor – and a comparatively high power consumption due to the high operating temperatures. However, the warm-up time of Cat gas sensors is much shorter than that of metal oxide (MOX) gas sensors (Sec. 2.1.4 – approx. $5min$).

2.1.2 Acoustic Wave (AW)

Acoustic Wave (AW) gas sensors, also known as Quartz Crystal Microbalance (QCM) gas sensors, are devices that use an oscillating piezoelectric substrate, usually a quartz crystal, as a highly sensitive balance to weigh gas molecules [19]. QMC sensors belong to the family of mass sensors and are also referred to as Surface Acoustic Wave (SAW) or Bulk Acoustic Wave (BAW) devices depending on whether the effect of surface waves or bulk waves is used [5]. By using different chemical coatings on the crystal with specific affinities, the QMC gas sensor can be made responsive to different gases. When gas molecules become temporarily attached to the coating, the effective crystal mass increases and lowers its resonant frequency. This relationship between effective crystal mass and resonant frequency is known as the Sauerbrey equation, which is the basic transduction relationship of QCM gas sensors [18]. The Sauerbrey equation is defined as:

$$\Delta f = -\frac{2 \cdot f^2 \cdot \Delta m}{\rho \cdot v}, \tag{2.1}$$

where Δf is the change in the resonant frequency of the crystal (the frequency shift), f is the resonant frequency of the crystal, Δm is the increase in mass of the crystal per unit area, ρ is the density of the crystal material, and v is the speed of sound waves in the crystal material. The frequency shift is proportional to the mass of the target gas.

The advantages of QCM sensors are the rapid response time, low power consumption, low weight, the possibility to control the selectivity over a wide range, long-term stability, and long lifetime. Disadvantages include comparatively low sensitivity to the target gas, limited robustness to variations in humidity, and relatively high temperature sensitivity.

2.1.3 Electrochemical (EC)

Electrochemical (EC) gas sensors are the largest and the oldest group of chemical sensors [18]. Nowadays, they consist of an electrolyte (solid or liquid) containing three electrodes: a sensing electrode, a counter electrode, and a reference electrode. An electronic potentiostat-circuit ensures a constant electrical voltage between sensing electrode and reference electrode [21]. Both the material of the electrodes and the electrolyte as well as the voltage are selected accordingly to guarantee that the target gas is electrochemically transformed (through oxidation or reduction) on the sensing electrode. At the same time, oxygen from the ambient air reacts at the counter electrode electrochemically. The flow of electrons between the sensing electrode and the counter electrode generated by this reaction is proportional to the gas concentration [21]. A more detailed description of EC gas sensors can be found in [18].

The advantages of EC gas sensors are their commercial availability, the low power consumption (the lowest among all types of sensors available for gas monitoring [22]), low weight, linearity, long-term stability, and an effective life span of one to three years. EC gas sensors are generally fairly selective to the target gas they are designed for [22]. The degree of selectivity, however, depends on the target gas and the concentration range for which the sensor is designed. The majority of toxic gases can be measured. The low cross-sensitivity to temperature, humidity, and other gases (due to selective filters) is also an advantage. On the other hand, the response time of EC gas sensors ranges from 30 to $60s$. The low sensitivity depending on the target gas is another disadvantage.

2.1.4 Metal Oxide (MOX)

Metal Oxide (MOX) gas sensors have been the most widely used gas sensors in mobile robot olfaction as well as in electronic nose applications [23] due to their commercial availability, their high sensitivity, the effective life span of three to five years, and their acceptable response and recovery times. MOX gas sensors are conductometric sensors. The basic MOX gas sensor consists of a heating element inside a ceramic tube coated with a semiconductor. The semiconductor is typically sintered tin dioxide (SnO_2) or zinc oxide (ZnO). Typical operating temperatures for MOX gas sensors lie between $300°C$ and $550°C$. The selectivity of these sensors is obtained to a certain extent either by doping the surface of the semiconductor with different additives or by setting different operating temperatures [23]. In general, the combustion process is not strongly selective to the precise structural details of molecules of the target gas [5]. The presence of reductive gases causes a drop in the resistance of the semiconductor. The resistance increases as the concentration of the target gas is reduced. This relationship between the sensor resistance and the concentration of the detected gas is nonlinear and can be approximated by [24]:

$$R_S \cong KC^{-\alpha}, \tag{2.2}$$

where R_S is the resistance of the sensor when exposed to the target gas, K is a scaling constant, C is the gas concentration, and α is the sensitivity of the sensor. A more detailed description of MOX gas sensors is given in [18, 24].

The disadvantages of MOX gas sensors are their comparatively high power consumption due to the high operating temperatures, the nonlinearity, the cross sensitivity to humidity, and the variance of the response characteristics between individual sensors [25]. The nonlinearity of the sensor also makes it difficult to calibrate. Additionally, MOX gas sensors typically have to be heated for 30 to $60min$ before proper usage. Poor selectivity is another disadvantage.

2.1.5 Conductive Polymer (CP)

A Conductive Polymer (CP) gas sensor is a conductometric sensor. The measurand of CP gas sensors is the resistance of the surface layer. In comparison to MOX gas sensors they use a thin polymer film instead of a semiconductor. A convenient method to deposit the polymer film across the gap between two electrodes is the electrochemical deposition [26] as the thickness of the film can be controlled accurately. Polypyrrole (PPy), polyaniline ($PAni$), polythiophene (PTh), and their derivatives typically have been used as the active layers of gas sensors. CP gas sensors respond to a wide range of organic vapors depending on their doping. However, the exact altering mechanism of the conductivity has not been understood clearly [26]. A more detailed description of CP gas sensors can be found in [26].

The advantages of CP gas sensors are that they have high sensitivities and short response and decay times. In addition, the power consumption of CP gas sensors is low as they can be operated at room temperature [27]. On the other hand, the actual level of sensitivity is approximately one order of magnitude lower than that of MOX gas sensors [5]. Further disadvantages are the sensitivity to humidity and the long-term drifts.

2.1.6 Infrared (IR)

Infrared (IR) gas sensors belong to the family of optical gas sensors. The principles of optical gas sensors are related to classical spectroscopy [18]. IR gas sensors typically consist of an IR source, a bandpass filter, and a detector element. A second bandpass filter and detector element in combination with an optional mirror can be used as reference to compensate for changes that occur in the sensor (e.g., the intensity of the light source and corrosion of the reflecting surfaces). The radiation from the IR source contains a wide spectral content. When this radiation interacts with gas molecules, one part of the energy has the same frequency as the gas molecule's natural frequency [22]. This energy is absorbed by the gas molecules while the rest of the radiation is transmitted. This absorbed radiation causes the gas molecules to gain energy, i.e., the gas molecules start to oscillate more strongly resulting in a temperature rise of the gas molecules. The increase in temperature is proportional to the concentration of the target gas. The absorbed radiation also causes a decrease in the strength of the original source at a particular wavelength (of the target gas). Both the temperature and the absorbed energy can be detected in dependence of the detector element. A more detailed description of IR gas sensors can be found in [22], whereas a more general description of optical gas sensors can be found in [18].

The advantages of IR gas sensors are their commercial availability, the high selectivity, the wide range of sensitivities, the long-term stability, and an effective life span of three to five years (in special cases up to 10 years). Very low cross-sensitivity to temperature and humidity is also an advantage. Furthermore, IR gas sensors are not sensitive to the airflow like the other presented gas sensors. They do not have the problem of poisoning and the maintenance effort is minimal due to larger calibration intervals. On the other hand, the power consumption of IR gas sensors is relatively high as they are typically heated to avoid condensation on the reflective surfaces. Another disadvantage is that the price of IR gas sensors can vary depending on the light source used.

2.1.7 Gas Sensor Selection

The objective of this work was to develop and validate a gas-sensing payload for a micro-drone for real application scenarios (Ch. 3). Targeted fields of operation are gas measurements in, e.g., accident scenarios, emission control, and monitoring of critical areas as well as gas leak detection and localization. Therefore, the following question has to be addressed:

"Which gas sensors are best suitable for use with a micro-drone with respect to the wide range of intended real application scenarios?"

In general, the suitability of certain gas sensors depends directly on their application scenario [22]. In the case of the given micro-drone, where constraints regarding the payload capacity (approx. $200g$) and the flight time (approx. $20min$ depending on the payload configuration) are given, gas sensors with high weight and high power consumption can theoretically be excluded from this decision process as they further reduce the flight time. However, if combustible gases (or vapors) have to be monitored and locations of possible gas leaks, e.g., on landfill sites (methane – CH_4) [Paper II] have to be inferred, one of the following relatively power-intensive gas sensors has to be chosen: Cat, MOX, or IR. This is especially relevant when operating the micro-drone in areas where gas compounds may become explosive. To avoid ignition, the micro-drone has to be shut down in time. Here, Cat and IR gas sensors are considered for the regular payload and MOX gas sensors are tried as part of an electronic nose developed by Örebro University (Sec. 3.2.2). MOX gas sensors are interesting for gas source localization and gas distribution mapping tasks due to their reasonably fast response and recovery times. Generally, MOX gas sensors cannot be recommended in application scenarios where calibrated gas sensors are needed due to, e.g., the sensor drift and the variance of the response characteristics between individual sensors [25]. To monitor toxic gases (and oxygen), EC gas sensors should be used in mobile applications. EC gas sensors are characterized by their very low power consumption, response times of 30 to $60s$, and their low cross-sensitivity to temperature, humidity, and other gases. On the other hand, QMB and CP gas sensors are not suitable for real-world applications. QMB gas sensors suffer from their generally low sensitivity to the target gas and the high cross-sensitivity to environmental influences such as temperature and humidity. However, the rapid response times may be beneficial for gas source localization and gas distribution mapping tasks. The sensitivity to humidity and the as yet incomplete scientific understanding of CP gas sensors constitute the criterion for exclusion of this kind of sensor.

In a market survey, a commercial available portable gas detector was identified which is applicable for the use with a micro-drone: the Dräger X-am 5600 (Sec.3.2.1).

It combines the most suitable gas sensor technology for real-world applications in one device and, in addition, features low mass, robustness, and compact design. The sensors can easily be exchanged and calibrated to meet the requirements of different application scenarios. The gas detector can measure many combustible gases and vapors with the Cat gas sensor as well as different (toxic) gases, e.g., oxygen (O_2), ozone (O_3), carbon monoxide (CO), hydrogen sulfide (H_2S), ammonia (NH_3), carbon dioxide (CO_2), sulfur dioxide (SO_2), phosphine (PH_3), hydrogen cyanide (HCN), nitric oxide (NO), nitrogen dioxide (NO_2), chlorine (Cl_2), hydrogen (H_2), phosgene ($COCl_2$), amine, odorants, and organic vapors (OV) with EC and IR gas sensors.

2.2 Gas Source Localization (GSL) with Mobile Robots

In the past two decades a number of algorithms for gas source localization (referred to as odor source localization in the literature) have been presented. Kowadlo and Russell [28] and Lochmatter [12] published two excellent surveys of the work in this field of research. Kowadlo and Russell have classified more than 25 algorithms in a Venn diagram (see Fig. 2.1). Lochmatter, on the other hand, has classified the gas source localization algorithms in ten categories, which are sketched in Fig. 2.2. Within this Ph.D. thesis, a brief overview is given of the existing algorithms according to the survey published by Lochmatter. In contrast to Lochmatter, the gradient-based algorithms are considered to be in the class of the bio-inspired plume tracking algorithms. This Ph.D. thesis does not elaborate on multi-robot collaboration schemes (swarms) for gas source localization since it is aimed to accomplish this task with a single micro-drone first. However, interesting approaches with multiple robots were suggested in [13, 29] (bio-inspired algorithm based on spiraling and upwind surge extended for multiple robots – Fig. 2.2 (e)), in [30–33] (algorithms based on Particle Swarm Optimization (PSO) – Fig. 2.2 (c)), and in [34] (a probabilistic approach called “infotaxis”, which was extended in this work for multiple robots – Fig. 2.2 (g)).

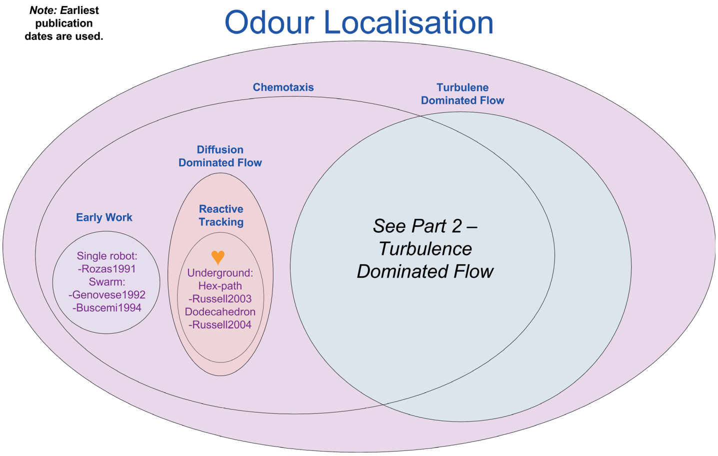

(a) Part 1

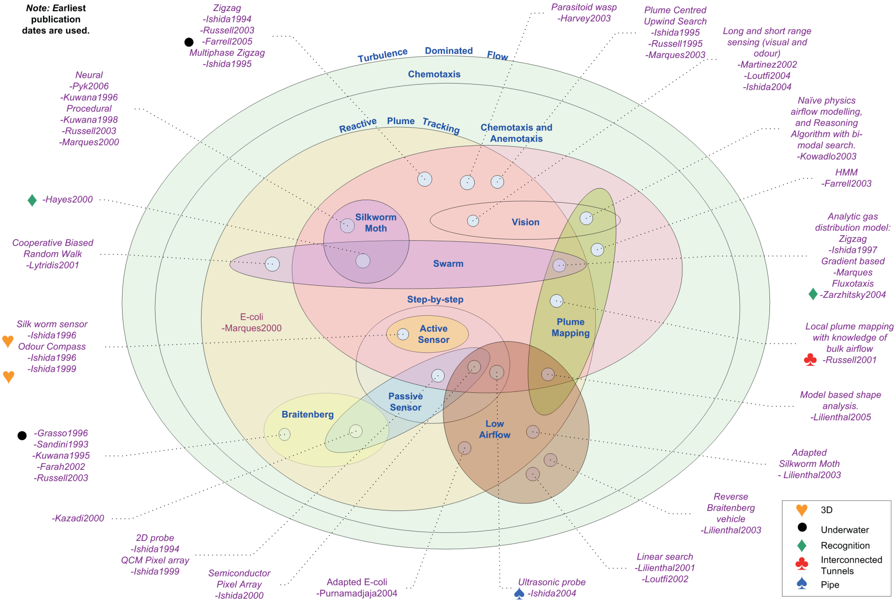

(b) Part 2

Figure 2.1: *Venn diagram of reported odor localization approaches (a) part 1 and (b) part 2 (from Kowadlo and Russell [28]).*

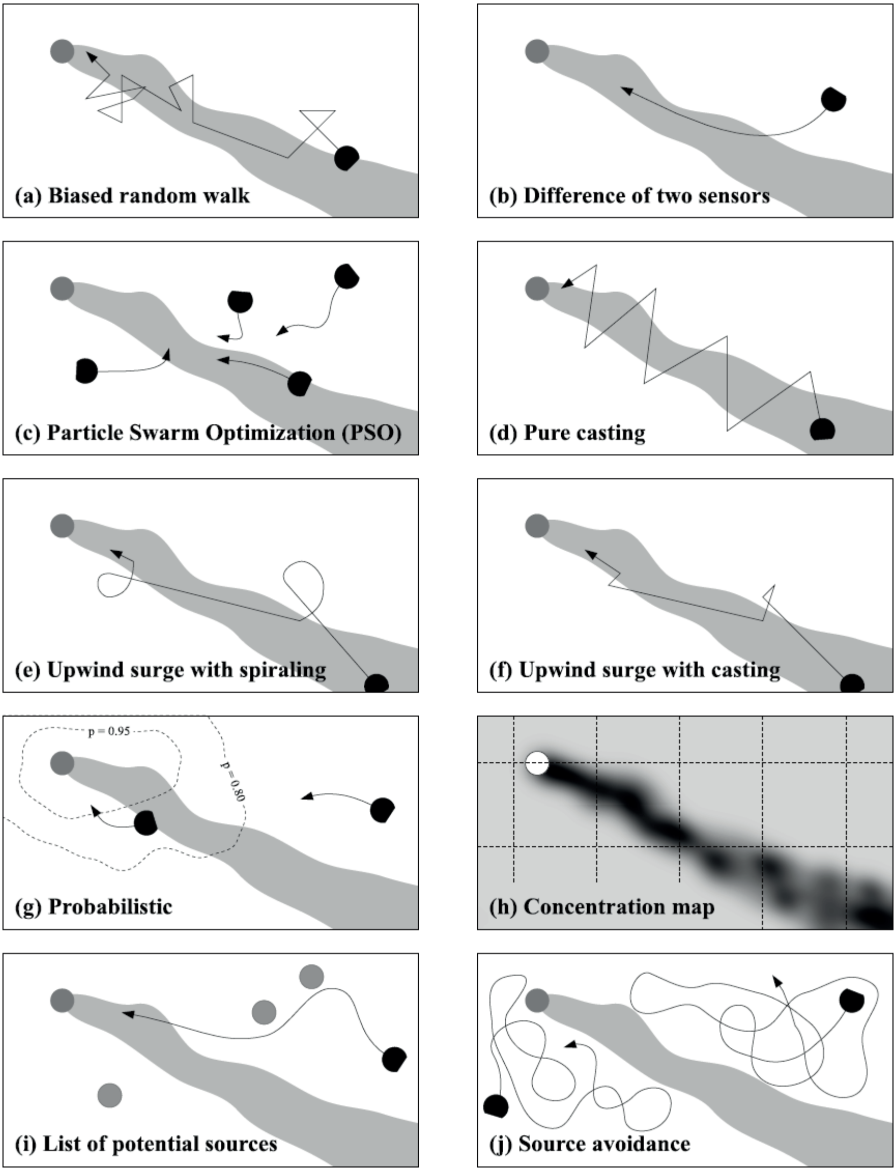

Figure 2.2: *Gas source localization approaches (from Lochmatter [12]).*

2.2.1 Bio-inspired Algorithms

The vast majority of approaches that have been proposed for gas source localization take inspiration from insects and other simple life forms. Insects have an outstanding ability to find distant sources of odors by tracking wind-borne odor plumes to their emission source [35]. In an analogous way, robots try to mimic the insects' plume tracking behavior to reach the source where they declare the end of their task [25,28]. Insects and other animals that have inspired robotics research for gas plume tracking include [Paper II]:

- Moths, which use odor localization to find mates [36–41].
- Lobsters, which use odor localization to locate food [42, 43].
- *Escherichia coli* bacteria, which use odor localization to locate nutrients [44].
- Dung beetles, which use odor localization to find hatching niches, habitation, and food [3, 44].

Most bio-inspired plume tracking algorithms are based on the well-studied behavior of moths [45–56]. The search pattern of the (silkworm) moth mainly contains the following three behaviors [44]:

1. Upwind surge: Moving upwind when exposed to pheromones.
2. Casting: After having lost the plume, swinging from side to side with increasing amplitude for a few seconds to reacquire the plume.
3. Spiraling: Adopting a circular motion pattern if the plume cannot be found.

A variety of state machine-based algorithms have been developed based on one or more of these three rules or variants thereof [3, 12, 13, 28, 29, 41, 55, 57–61] (Fig. 2.2 (d) to (f)). These algorithms generally require a wind direction sensor and a binary gas concentration sensor (typically a normal gas sensor which is thresholded). Some other algorithms use gradient information determined from spatially separated gas concentration measurements to move towards the gas source [12, 28, 43, 44, 62–70] (Fig. 2.2 (a) and (b)). These algorithms are typically equipped with one or two gas sensors only and do not need a wind direction sensor. In general, most of the state-of-the-art plume tracking algorithms are based on two principles: *chemotaxis* and *anemotaxis* [Paper II]. *Chemotaxis* refers to a mechanism in which the movement of an organism (or robot) is determined by the gas distribution, most often by the concentration gradient. *Anemotaxis* instead refers to a mechanism in which the movement of an organism (or robot) is determined by the perceived airflow (or fluid flow).

To the author's knowledge, implementations of these bio-inspired plume tracking algorithms have been tested and evaluated so far on ground-based robot platforms, Autonomous Underwater Vehicles (AUVs), and blimps. Almost all algorithms consider a 2D environment. Experiments in 3D environments are still rare [69–72]. Furthermore, most experiments have been performed under simplified conditions, such as a steady constant airflow and the presence of a single gas source emitting a known chemical compound at a constant release rate. However, the airflow in an open outdoor environment is turbulence-dominated [73], creating complex structures of gas patches with different concentration levels.

Ch. 5 discusses three bio-inspired plume tracking algorithms for a gas-sensitive micro-drone in more detail. The algorithms are based on the same basic principles as presented here (chemotaxis and anemotaxis). However, the selection concentrates on algorithms that move goal-oriented to the source. On the other hand, algorithms are refused that involve moving the robot on spirals, e.g., the spiral-surge algorithm from Hayes et al. [13], which seems not to be feasible to use with a micro-drone. The strong disturbances induced by the rotors destroy the plume structure permanently, making it more difficult or even impossible to track the plume to its source. The surge-cast algorithm (a variant of the silkworm moth algorithm) [2], the zigzag / dung beetle algorithm [3], and a newly developed algorithm called "pseudo gradient algorithm" are implemented as they appear to be the most promising algorithms to use with a micro-drone. The latter includes a new measuring strategy to deal with the strong disturbances induced by the rotors of the micro-drone – measuring a local concentration gradient with spatially separated sensors is not feasible in this case. The pseudo gradient algorithm also considers wind information to overcome the limitations of older gradient ascent methods that do not know whether they follow a plume towards or away from its source. The algorithms are evaluated in simulations *and* real-world experiments with a gas-sensitive micro-drone in a setup where no artificial conditions were introduced to simplify the experiments.

2.2.2 Probabilistic Algorithms

2.2.2.1 Information Theory

Vergassola et al. [74, 75] proposed a search strategy called “infotaxis” (Fig. 2.2 (g)). Infotaxis is based on probability and information theory and was especially designed to work in turbulence-dominated environments. The location of the source is modeled as a probability distribution which is derived from previously collected concentration measurements made in the environment. The robot tries to reduce the entropy of this distribution either by moving to neighboring locations for which a high information gain is expected or by standing still.

So far, there are only two works which have evaluated the concepts presented by infotaxis in real experiments with ground-based robots. Moraud and Martinez [76] assess the robustness and reliability of infotaxis for localizing a heat source. They argue that heat has similar dispersion properties as chemical compounds. However, the response and decay of temperature sensors are much faster than gas sensors. Additionally, a fan introduced an artificial airflow in the experiment area, which further simplifies the localization problem. Lochmatter [12] evaluated a statistical approach that follows the same principles as infotaxis. The experiments were performed inside a $18 \times 4m^2$ wind tunnel under laminar flow conditions with an ethanol gas source and a robot equipped with a commercial gas sensor.

As this Ph.D. thesis shows the feasibility of using a micro-drone for plume tracking by means of three representative algorithms and in order to keep the development effort within a certain limit, this work focuses on algorithms that are easy to implement. Future work should address the study of the usage of probabilistic algorithms with a micro-drone for plume tracking and gas source localization.

2.2.2.2 Bayesian Inference

Particle filter algorithms are commonly used in the field of robotics, e.g., in Simultaneous Localization And Mapping (SLAM). More recently Li et al. proposed in [77, 78] a gas source localization algorithm based on a particle filter. It estimates the location of the gas source in real-time while the robot performs an exploratory behavior in an outdoor environment with time-variant airflows [78]. The exploratory behavior was composed of the plume finding strategy specified by Li et al. [79] and the spiral-surge plume tracking strategy described by Hayes et al. [29] in order to collect gas concentration and wind measurements more effectively [78]. Li et al. use a likelihood function based on the probability density function introduced by Pang and Farrell [80] in combination with a gas patch path reconstruction approach to calculate a so-called observation window. Thus, the observation window defines the area in which the origin of the gas patch is assumed with high likelihood. In case of a detection event, particles are added and spread out in the observation window. Finally, the collected information is exploited by the particle filter algorithm, which terminates if all particles converged in a small area. They evaluated their algorithm in 33 real experiments, which they performed over an area of $10 \times 10m^2$ with an ethanol gas source and a mobile robot equipped with, i.a., a MOX gas sensor and an ultrasonic anemometer. A comparison with the Bayesian-inference-based gas source localization method introduced by Pang and Farrell [80] was carried out offline using the recorded experiment data. Li et al. showed that their particle filter-based gas source localization algorithm works more robust than the Bayesian-inference-based method. However, their success rate lay only around 79%. A disadvantage of this algorithm is that it assumes a roughly uniform airflow over the search space. Furthermore, simulation experiments to support the evaluation of the algorithm are missing.

Ch. 6 presents a new gas source localization algorithm based on a particle filter. The trajectory of a gas patch is reconstructed similar to [77, 78] by dividing the taken wind measurements into time intervals. In contrast to Li et al., uniformity in the wind field is not assumed and experiment results are provided which prove that their assumption does not hold. Furthermore, an uncertainty about the wind direction is considered in the reconstruction process due to the turbulent nature of wind, which extends this trajectory to a patch path envelope (PPE) instead of a single patch trajectory. The PPE describes the envelope of an area the gas patch has passed with high probability. The opening angle of the PPE depends on the stability of the wind direction, which is expressed by the circular variance. Finally, a function is defined that updates the particles based on their relative position to the most recent calculated PPE and the most recent binary concentration measure introduced by Li et al. [77]. The algorithm is successfully validated in simulations and real-world experiments.

2.2.3 Algorithms based on Gas Distribution Maps

Several authors studied the use of gas distribution maps for gas source localization purposes [14, 81–83] (Fig. 2.2 (h)). Their results show that the true source location does not always correlate with the location where the highest average gas concentrations were measured [12]. However, a good indicator for the source location was found to be the variance of the measured samples at a given location, which was significantly higher close to the source [1].

Ch. 7 discusses the usability of a micro-drone for gas distribution mapping. Furthermore, real-world experiments try to verify whether in the case of a micro-drone the variance still provides a better indicator for the gas source location than the mean. To estimate the gas distribution model, the algorithms Kernel DM+V [84] and Kernel DM+V/W [85] are used exemplarily. Kernel DM+V estimates predictive variance in addition to predictive mean of the gas distribution model. Kernel DM+V/W algorithm also considers wind information to compute the gas distribution model. Both algorithms are described in more detail in Sec. 7.1.

In Ch. 8, an Artificial Potential Field (APF) is used in the path planning and adaptive sampling to direct measurements to locations of high predictive mean, and high predictive variance of the current statistical gas distribution model. As a consequence of the performed observations in Ch. 7 and the results presented in [1], six estimators are defined that use both created models to determine the gas source location.

2.2.4 Other Approaches

Lochmatter also points to two other interesting approaches related to gas source localization [12]. The first approach was proposed by Lilienthal and Duckett [86] (Fig. 2.2 (j)). They programmed their robot to evade each local concentration maximum (including the source itself). Thus, regions of low concentration were explored, whereas regions of high concentration were left out. This helps to infer the location of the gas source as “the robot covers the whole available area except near the actual location of the source” [86]. The second approach was proposed by Kowadlo et al. [87] (Fig. 2.2 (i)). They combined vision, olfaction, and airflow maps for gas source localization. Based on the airflow maps, the algorithm computes a list of locations to take gas concentration measurements. The robot processes the list and uses the resulting information to reason about the potential gas source location. Then, the robot uses vision to reject potential sources from the list. Finally, olfaction is again used for source declaration. The algorithm is similar to the probabilistic algorithms, although the utility function is not based on probability theory [12].

Another interesting approach was introduced in [88] by Cabrita et al. (Fig. 2.2 (h)). They developed two algorithms based on particles (but not related to particle filtering): a plume mapping algorithm and an odor-oriented exploration and plume tracking algorithm. The (particle) plume mapping algorithm converts gas concentration measurements into a point cloud around the sensor's location with number of particles proportional to the measured gas concentration in parts per million (*ppm*). This requires properly calibrated gas sensors. The newly created point cloud is merged with the particle plume. Older particles which are located in this new region are removed to assure that the number of points in a certain region reflects the last concentration measurement in that area and to produce a smooth representation of the plume [88]. The particle plume explorer algorithm is divided into four steps. It draws a circle with a radius r around the robot and separates it into n slices. Next, slices which overlap with obstacles or contain a defined percentage of explored area are removed. When all slices have been removed, the robot enters a recovery behavior by searching for the closest viable spot to continue the exploration. A cost function, which incorporates the direction of growing gas concentrations, the direction of the current slice, and the orientation of the robot, is calculated for each remaining slice. Finally, the slice with minimum cost is chosen. Both algorithms were tested in simulations and in more "realistic scenarios" with mobile robots showing that both algorithms are reliable and robust. The disadvantage of these approaches is that properly calibrated sensors are needed and that the plume is not captured in a realistic manner.

2.3 Gas Distribution Mapping (GDM)

Modeling the gas distribution is the task of deriving a truthful representation of the observed gas distribution from a set of spatially and temporally distributed measurements of relevant variables, foremost gas concentration, but also wind, pressure, and temperature [14]. Asadi et al. [89] and Neumann et al. [PAPER III] published two surveys of the work in this field of research.

Probably the most straightforward statistical gas distribution modeling approach is to measure the response over a prolonged time with a grid of stationary gas sensors and discretize the model at the same resolution. This technique has been used, e.g., in [90], where each grid point is assigned the average concentration over the measurement period. A similar method is presented in [91], where maximum values of the measurement period are mapped instead of average concentrations. With an increasing area, however, building a dense grid of gas sensors involves an arbitrarily high number of fixed gas sensors [5]. This raises problems such as cost and lack of flexibility. Furthermore, an array of MOX gas sensors (used by Ishida et al. in [90]) would cause serious disturbances due to convective flows created by their built-in heaters [92].

An alternative to a network of stationary gas sensors is to use a single mobile sensor that consecutively collects samples at predefined locations. This avoids calibration issues of the sensor network and allows for adaptive sampling of the environment. Under the assumption of a stationary gas distribution, consecutive sampling is theoretically equivalent to simultaneous distributed measurements. Hayes et al. [13] use a group of mobile sensors to create a histogram representation of the gas distribution. The histogram bins collect the number of “odor hits” (these are measurements above a defined threshold) received by all sensors in the corresponding area while they followed a random walk pattern. This method requires even coverage of the environment and potentially discards some useful information by using only binary data. Additionally, it would also take a very long time to obtain statistically reliable results, and there is no extrapolation on the measurements apart from the quantization into the histogram bins. Therefore, it is doubtful whether this approach would scale well to larger environments. Pyk et al. [41] interpolate the sensor measurements at locations other than the measurement using bi-cubic or triangle-based cubic filtering, depending on whether or not the measurement locations formed an equidistant grid. A disadvantage of this method is that no spatial averaging is carried out and that fluctuations therefore appear directly in the map.

The Kernel extrapolation Distribution Mapping (Kernel DM) algorithm introduced by Lilienthal and Duckett discretizes the available space into grid cells and computes an estimate of the distribution mean for each cell by using a symmetric Gaussian kernel [84]. The Gaussian kernel weighs the importance of each sample to estimate gas distribution at each grid cell based on the cell’s distance from the respective measurement point. Kernel DM does not rely on even coverage of the environment. Lilienthal et al. [14] extended this approach to Kernel DM+V which estimates predictive variance in addition to predictive mean of the gas distribution model. Another approach to estimate the predictive variance in gas distribution modeling is the Gaussian Process Mixture model (GPM) proposed by Stachniss et al. [83]. It considers gas distribution modeling as a regression problem. Subsequent work is focused on extending the basic Kernel DM+V algorithm in a way that wind information [85], the third dimension [93, 94], and a time-dependent component [95] are also considered to compute the gas distribution model.

In this Ph.D. thesis, a micro-drone equipped with gas sensors is used to perform consecutive sampling. To estimate the gas distribution model, the Kernel DM+V/W algorithm [85] is used, which is an extension of Kernel DM+V that also considers wind information to compute the gas distribution model. The algorithm is described in more detail in Sec. 7.1 and used in Ch. 7 to model the gas distribution and in Ch. 8 as part of an adaptive sampling algorithm that directs measurements to locations of high predictive mean, and high predictive variance of the current statistical gas distribution model.

In the following subsections, an overview of existing approaches is given that deal with the problem of choosing the next sampling location based on the current knowledge of the gas distribution (or other spatial phenomena). A more detailed survey can be found in [16]. All of the presented approaches either try to minimize cost functions [96–99], are non-adaptive (offline) [97, 100, 101], or try to apply simple heuristics [102] in order to select next sampling locations. Only a few algorithms perform adaptive path planning [103, 104] to increase the information gain. However, these approaches are only capable of solving near-optimally small instances of the problem [104] and do not have any approximation guarantees [102] (NP-hard). Work based on artificial potential fields was so far only used to deploy mobile sensors in unknown environments [105, 106] and does not consider the measurements taken by the mobile sensors.

In Ch. 8, a modified Artificial Potential Field (APF) is used in the path planning and adaptive sampling algorithm to direct measurements to locations of high predictive mean, and high predictive variance of the current statistical gas distribution model. Additionally, information about previous sampling locations is considered to maximize the coverage area. This accomplishes a tradeoff between exploration and exploitation. By introducing locality constraints, suitable paths can be planned for a mobile gas sensor. The complexity of the algorithm is only $\mathcal{O}\left[(D/c)^2\right]$, where D is the dimension of the environment and c is the cell size.

2.3.1 Spatial Monitoring with Mobile Sensor Networks

Given a limited number of sensors, time, and power to monitor spatial phenomena, planning sampling locations that provide most informative samples to build an accurate model of the environment is critical. Several works have been published on spatial monitoring which address this problem. The selection process of sampling points in the state of the art is mostly based on different criteria such as accuracy of estimated measurements and resource constraints, e.g., mobility, time, power, and wireless communication.

Limited number of sensors to monitor spatial phenomena are often modeled as Gaussian Random Fields. Krause et al. [98] apply Gaussian Processes (GPs) to monitor spatial phenomena. Several criteria to choose the sampling locations have been extensively investigated and compared including Mutual Information (MI), entropy, and geometrical models. The results of this comparison on temperature and precipitation data sets indicated that the strategy with maximizing MI between explored and unseen locations outperformed other approaches significantly. A similar approach has been utilized to monitor the ecological condition of a river using single and multiple mobile sensors and to plan the path for mobile sensors [97].

To monitor the environment using a mobile sensor network, Muttreja et al. [96] present a data acquisition framework which uses sparse GPs to estimate spatio-temporal models and evaluates the observed data at each sensor location as a function of time. To minimize the energy consumption, the sensors are planned in a cluster structure and samples are collected whenever the confidence of the estimated model is below a desired threshold. To sample each sensor, an active learning based criterion is applied with the variance minimization as objective.

In [99], a discrete simulation optimization approach is proposed to select sensor placements in a multiple sensor system with a data fusion center. The objective is defined so as to increase the accuracy of the information about the spatial phenomena by minimizing the Mean Squared Error (MSE) and at the same time satisfy an energy consumption constraint insofar there is one. To achieve this goal a two-stage, random search-based simulation optimization algorithm is used. The selection of sampling points is based on an entropy criterion to minimize the resulting uncertainty and an MI criterion which selects places that are most informative about unseen locations.

2.3.2 Informative Path Planning

To explore the area with one mobile sensor where prior information about distribution and environment is not available, one straightforward solution is to sample in predefined locations. This sampling method is applied for gas distribution mapping in several experiments. The results are presented in Ch. 7.

To consider resource constraints, an alternative to predefined sampling strategies is to adaptively select sampling locations using information about samplings locations and measurement values. Most of the previous work on informative path planning has either dealt with non-adaptive approximation algorithms [97, 100, 101] that plan and commit the paths before any observations are made, or with adaptive (often myopic, i.e., limited look-ahead) heuristics that update and re-plan as new information is collected [102]. Partially Observable Markov Decision Processes (POMDPs) have been used to perform adaptive path planning in complex environments [103]. Singh et al. [104] present a novel non-myopic approach to adaptive informative path planning that represents a trade-off between exploration and exploitation. The approach was extensively evaluated on a search and rescue domain and on a scientific monitoring problem using a real robotic system.

2.3.3 Artificial Potential Fields in Mobile Robotics

Artificial Potential Field (APF) methods are used in a number of robotic applications including local navigation and obstacle avoidance. APF approaches have also been used for the spatial formation of a set of sensors, spatial monitoring, and coverage problems [105, 106].

In [105], an APF approach is used to deploy a decentralized mobile sensor network in an unknown environment. Each sensor is repelled from obstacles and other sensors and a viscous force is applied on the sensor to reach an equilibrium state. The spatial configuration of sensors is affected by changes in the environment (e.g., movement of obstacles) that can shift the equilibrium state.

Schwager et al. [106] treats multi-robot coverage problem as an optimization problem and unifies different existing strategies for deploying groups of robots in an environment. To solve the deployment problem, a cost function is proposed in which measurements from different sensors are combined in a *mixing function*. This *mixing function* enables relating different strategies including the geometric Voronoi-based coverage, the probabilistic variance minimization, and artificial potential field objectives by introducing a parameter. Using this approach and varying the objective by changing the parameter is then demonstrated on simulated data.

2.4 Environmental Monitoring using Gas-sensitive Unmanned Aerial Vehicles (UAVs)

Previous works on environmental monitoring using gas-sensitive Unmanned Aerial Vehicles (UAVs) elaborated methodologies to measure the spatial distribution of chemical plumes and to search for the emission sources.

Kovacina et al. [107] developed a rule-based, decentralized control algorithm that relies on constrained randomized behavior (symmetrical and asymmetrical search). The algorithm respects UAV restrictions on sensors, computation, and flight envelope and was validated in a simple simulation environment with a UAV swarm searching for and mapping a chemical cloud within a region.

Rutkowski et al. suggest in [69] bio-inspired control algorithms for winged UAVs to track a plume to its source in 3D by fusing gas, visual, and airspeed sensors. The motion of the tracking UAV is decomposed into two components – a component normal to and a component tangential to the wind direction. Each component is assigned its own algorithm to control the UAV based on wind and gas concentration measurements. The algorithms were tested in simple simulations only.

The use of a blimp-based gas-sensitive UAV for demining tasks including chemical mapping strategies based on a behavioral and a neuronal model of the moth is investigated by Bermúdez i Badia et al. [108]. The chemical mapping strategies were tested in simulations and real-world experiments. The authors conclude that their UAV "can produce fully autonomous chemical localizations based on two predefined sets of behaviors, random search and scanning". The chemical mapping strategies were tested in simulations and real-world experiments.

Bamberger et al. [109] developed a Stigmergic Potential Field (SPF) based approach to UAV swarming to coordinate movement, transient acts, and task allocation among cooperating vehicles. They performed real-world experiments with a single UAV which was deployed to a simulated plume (using simulated sensors). The UAV conducted an autonomous search of the designated area and characterized the spatial extent of the plume successfully.

An expert system for contaminant mapping based on a genetic algorithm with physical reasoning using the wind vector, online concentration measurements, and estimates of the source location to perform path planning for UAVs is presented by Kuroki et al. [110]. The method was tested in simulations using the Gaussian plume / puff model.

In the project AirShield (Airborne Remote Sensing for Hazard Inspection by Network Enabled Lightweight Drones) an autonomous swarm of Micro UAVs (MUAVs) was developed to support emergency units and improve the information basis of disasters [111]. The aim of the project is to detect leaking Chemical, Biological, Radiological, Nuclear, and Explosive (CBRNE) contaminants in their spatial extent to carry out hazard analysis. Within this project, two steering strategies of a swarm of UAVs to efficiently cover a region of interest in order to achieve a spatial 3D coverage for aerial plume detection were compared: the Self-repelling Random Walk (SRW) and the Cooperative-repelling Random Walk (CRW) [112]. These steering strategies were evaluated in simulations with respect to 3D coverage. The APF approach proposed within this Ph.D. thesis is also a self-repelling strategy. However, a two-dimensional (2D) version of the SRW presented in [112] is not considered within this Ph.D. thesis as it does not incorporate sensor data.

Real-world experiments with standard or micro UAVs in outdoor environments are rarely available in the literature, especially in the area of gas source localization and gas distribution mapping. Almost all of the related work is validated in simulated experiments only. This has the advantage that ground truth data is available. On the other hand, however, a gas dispersal simulation environment does not capture all relevant real-world effects and it is therefore unclear how the obtained results extend to realistic environments. A key contribution of this Ph.D. thesis is several real-world experiments performed in uncontrolled outdoor environments.

2.5 Wind Vector Estimation using Micro UAVs

Molnar and Stojcsics and Kroonenberg et al. present the adaption of a Pitot tube for winged small size UAVs in [113, 114]. A Pitot tube is the state-of-the-art flight speed determination method for aircraft and has its origin in pressure measurement. It consists of a tube which is aligned parallel to the fluid flow and a pressure measurement equipment in the rear part of the device. The wind vector is calculated as the difference between the flight vector and the ground vector which is obtained from GPS data. But for a quadrocopter, a Pitot tube is hardly applicable because of the inconsistent flight direction and low flight speeds ($\leq 12ms^{-1}$). Furthermore, additional hardware would be needed to compensate the micro-drone's inclination angle and turn the Pitot tube nearly in flight direction. This extra weight would reduce the available payload and the flight time of the micro-drone drastically.

There are other methods which consider wind information in the control of micro UAVs. In [115], a mathematical model is used to estimate the aerodynamic and speed stability of a micro-drone using real-time measurements. However, none of these approaches is able to estimate the wind vector based on the existing on-board sensors of the micro UAV.

Instead, Ch. 3 presents an approach which is able to estimate the wind vector based on the on-board sensors of the micro-drone and makes additional anemometric sensors superfluous. Thus, the valuable payload remains free for other sensors.

Chapter 3

Design of the Gas-Sensitive Micro-Drone

Recent developments in the field of Micro Unmanned Aerial Vehicles (MUAVs) and mobile gas measurement techniques have established new possibilities to search for and characterize hazardous airborne substances. The Federal Institute for Materials Research and Testing (BAM), in cooperation with Airrobot GmbH & Co. KG (Germany), has developed a mobile and flexible aerial-based measuring system as part of an R&D project funded by the Federal Ministry of Economics and Technology (BMWi) [Paper I, Paper III, Paper V–Paper VII, Paper XI]. Parts of this Ph.D. thesis were carried out within this R&D project. The concept of the project includes the development and validation of a gas-sensing payload (approx. $200g$) for the Airrobot AR100-B micro-drone (Fig. 3.1(a)), which is capable of operating in a variety of scenarios of gas emissions. For example, it detects exhaust gas from chimneys, flue gas in a fire, and gas emissions in the case of an accident involving chemicals or hazardous goods. Another field of application which is addressed is the spatially resolved emission control of geodynamically active regions, waste disposals, stockpiles, Carbon Capture & Storage (CCS) areas, industrial sites, landfill sites, and contaminated areas. Additionally, it should provide accurate gas concentration measurements and persons without extensive pilot experience should be able to control this measuring system. The validation and optimization of the measuring system was also part of this Ph.D. thesis.

MUAVs are interesting because they are cost-efficient, easy to transport, and can be deployed in short time. They are characterized by their compact design and

(a) (b)

Figure 3.1: *(a) Airrobot AR100-B micro-drone in flight. (b) Visualized disturbance induced by the rotors of the Airrobot AR100-B micro-drone using an AX-430 orange colored smoke bomb (photo taken at BAM TTS).*

excellent maneuverability, which makes precise navigation possible and gives access even to small passages, which is especially significant in urban terrain and industrial sites. Micro Vertical Take-Off and Landing (VTOL) UAVs, such as quadrocopters, additionally have the ability to hover over a certain point of interest for a prolonged time, which allow more informative gas concentration measurements in comparison to, e.g., a fixed-wing aircraft in view of the slow response times of popular chemical sensors. Blimps, on the other hand, have a more adverse size-to-payload proportion and are more affected by the wind.

However, the disadvantage of quadrocopters is given by the payload limitation to only a few hundred grams, the relatively short flight time, and the disturbances introduced by their rotors into the environment (Fig. 3.1(b)), which may destroy the original gas dispersion pattern. A blimp may ease some of these limitations, but the poor size-to-payload proportion, the high resistance to wind, and their inertial characteristics are not beneficial for gas concentration measurements in a turbulent outdoor environment, especially for gas source localization and gas distribution mapping.

The Airrobot AR100-B micro-drone (Fig. 3.1(a)) is such a quadrocopter. It presents an ideal platform for gas concentration measurements in the immediate vicinity of the object which causes the emission. A gas-sensing sensor module was developed and validated within the Ph.D. thesis for this micro-drone. The results show that this platform also provides an excellent robotic platform to validate the

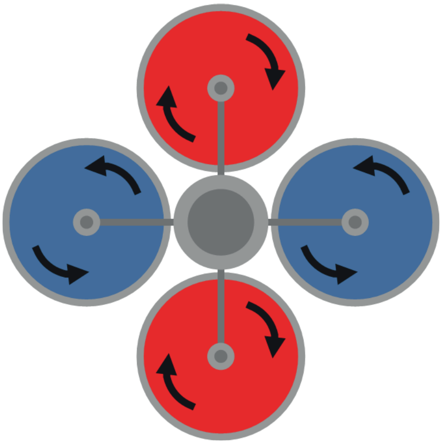

Figure 3.2: *Schematic diagram of the micro-drone (top view) with two clockwise (red) and two counterclockwise (blue) running rotors (figure reprinted from Büchi [116]).*

gas source localization and gas distribution mapping algorithms developed within this Ph.D. thesis (Ch. 5 to 8) in real-world experiments.

In the remainder of this chapter, first, the micro-drone is described, which is used as the robotic platform (Sec. 3.1). Next, the integration of gas-sensitive devices as payload is presented and the corresponding validation and calibration experiments are performed (Sec. 3.2). Sec. 3.3 identifies three different design approaches to improve the gas transport to the sensors and analyzes their functional performance. Then, a wind vector estimation approach that uses the existing on-board sensors of the micro-drone only is introduced and validated (Sec. 3.4). Finally, the developed robotic operating software to autonomously control the micro-drone is presented (Sec. 3.5) and conclusions are drawn (Sec. 3.7).

3.1 Airrobot AR100-B – Quadrocopter

The Airrobot AR100-B micro-drone has a diameter of $1m$ and is driven by four brushless electric motors ($\leq 2000rpm$). The micro-drone can be equipped with a variety of sensors and precisely navigated to a certain region of interest for remote sensing without endangering persons in critical areas. The basic structural parts of the micro-drone are made of carbon fiber. The maximum payload mass is $200g$ with a total flight mass of about $1.3kg$. The maximum flight time is about 20 to $30min$.

Table 3.1: *System parameters of the micro-drone.*

Property		Setting
Diameter		$1m$
Total Flight Mass		$1.3kg$
Payload Mass		$200g$
Operating Distance	$\leq$	$1km$
Flight Time	$\leq$	$30min$
Flight Speed	$\leq$	$12ms^{-1}$
Max. Wind Load	$\leq$	$8ms^{-1}$

The micro-drone can withstand a maximum wind speed of $8ms^{-1}$. Communication with the ground station is established by a wireless radio link. Data packets can include control instructions or data from the micro-drone's on-board sensors. The operating distance of the remote control and communication link is $1km$. A Global Positioning System (GPS) supports the micro-drone during operation. The micro-drone can be flown by line of sight, via on-board video camera and video goggles as well as by autonomous waypoint following. The latter allows for sending either single waypoints to the micro-drone which will be approached immediately or whole waypoint lists (waypoint mode). The waypoints contained in a waypoint list will be consecutively processed if the micro-drone is set to autonomous mode.

The Inertial Measurement Unit (IMU) is an important part of the micro-drone. It provides the basis for flight control and wind vector estimation [Paper III, Paper XI] and can be read out during operation. The IMU consists of three orthogonally arranged accelerometers, which detect linear accelerations along the x-, y-, and z-axis, and three orthogonally arranged rotation rate sensors, which measure angular accelerations along the x-, y-, and z-axis. Magnetic field sensors (compass) and GPS are used to improve the accuracy of the IMU and to compensate for sensor drift [117]. The IMU of the micro-drone also contains a barometric pressure sensor to control the micro-drone's altitude.

In comparison to a helicopter, the micro-drone is characterized by a less complicated and stronger mechanical system: the four brushless electric motors are connected directly to two clockwise and two counterclockwise running rotors. Fig. 3.2 illustrates the functional principle of the micro-drone. An inclination and therefore a drift of the micro-drone is achieved by changing the *revolutions per minute* (*rpm*) of the blue and red rotors, respectively. The right blue rotor has to turn with lower *rpm* and the left has to turn with higher *rpm* in order to fly the micro-drone to the right, for example. The pair-wise change of the *rpm* of the blue and red rotors cause a rotation around the yaw axis of the micro-drone (z-axis). The *rpm* of all rotors have to be uniformly changed in order to perform a climb or descent flight of the micro-drone.

3.1.1 Validation of the GPS-based Positioning System

The GPS receiver of the micro-drone is needed in the real world to easily perform self-localization, to hold the position via GPS, and to fly the micro-drone autonomously from one position to another. Therefore, the accuracy of the GPS receiver and the flight control of the micro-drone play an extremely important role, also in order to accurately perform gas source localization and gas distribution mapping. To measure the accuracy of the GPS holding system and the flight control, the following experiment was performed:

3.1.1.1 Experiment Setup

The micro-drone was controlled autonomously inside a $12 \times 8m^2$ region that is part of a much bigger open area. A total of 31 waypoints were sent to the micro-drone. GPS coordinates were recorded for $20s$ for each waypoint. As the micro-drone does not confirm the arrival of a waypoint, a trigger was used. The gathering of GPS data was started by the trigger when the micro-drone reached a waypoint within a radius of $1.5m$ and was stopped $20s$ later. Then the next waypoint was uploaded to the micro-drone.

The wind speed and direction varied during the experiment and were measured with the micro-drone based on their on-board sensors, which is fairly accurate (Sec. 3.4.3). The experiment conditions were quite harsh as the mean wind speed lay around $2ms^{-1}$ with wind gusts of up to $6.5ms^{-1}$.

3.1.1.2 Experiment Results

The distances d_{WP} and directions θ_{WP} from the uploaded waypoints to their corresponding GPS coordinates recorded by the micro-drone were calculated and eval-

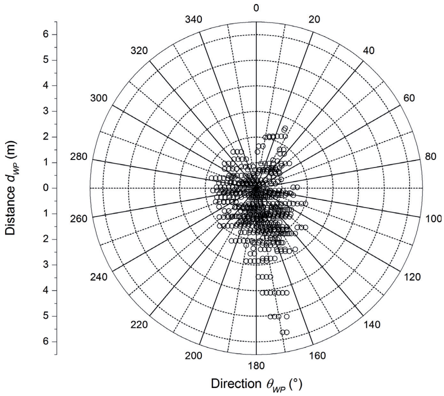

Figure 3.3: *Calculated distances d_{WP} and directions θ_{WP} from the uploaded waypoints to their corresponding GPS coordinates as recorded by the micro-drone.*

uated using Eq. B.1 and B.3 (Appendix B). A total of approximately 4,300 GPS coordinates were obtained during this experiment. The number of available satellites varied from 9 to 11. Fig. 3.3 shows the (distance, direction)-pairs of all obtained GPS coordinates in a circular diagram (similar to a windrose diagram). Here it is clearly visible that almost all these pairs are below a radius of $2m$ and that the directional component is almost uniformly distributed. The mean distance over all available GPS data to their corresponding waypoints is $1.17m$ with a standard deviation of $\pm 0.71m$. The respective confidence interval is $(1.15, 1.18)m$ at a confidence level of 95%.

The results show that the micro-drone is able to hover over a certain position regardless of changing wind conditions. However, the position is only accurate within approximately $\pm 1.17m$ and should be considered in the gas source localization and gas distribution mapping algorithms. In this Ph.D. thesis, this GPS positioning and flight control error is modeled (Sec. 4.2) and used in the simulation experiments. So far, this error is not considered in the presented gas source localization and gas distribution mapping algorithms.

3.2 Integration of Gas Sensors

Two different kinds of gas-sensing payload were developed for the micro-drone. The gas-sensing payload based on the gas detector X-am 5600 (Dräger Safety AG & Co.

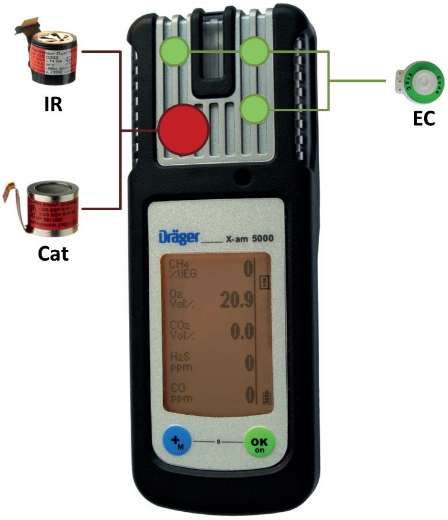

Figure 3.4: *Dräger X-am 5600 gas detector with electrochemical (EC), catalytic (Cat), and infrared (IR) sensors. The* IrDA*-transceiver is located in the upper part on the rear panel.*

KGaA, Germany) was developed and validated within the Ph.D. thesis. The electronic nose (e-nose) was developed by Örebro University within the project "Monitoring of Landfill Sites with a Gas-Sensitive Mobile Robot" (GasBot).

3.2.1 Dräger X-am 5600

A commercially available gas detector (Dräger X-am 5600), which is originally designed as a handheld device for personal safety, is the base unit of the gas-sensing payload for the micro-drone. It features low mass (approx. $233g$ incl. the rechargeable battery) and compact design ($47 \times 129 \times 31mm^3$ $[W \times H \times D]$). The modular concept allows the ad hoc exchange of the four sensors in the gas detector, which enables users to customize it for their specific application. Depending on the scenario, it can measure many combustible gases and vapors with the catalytic (Cat) sensor as well as different (toxic) gases, e.g., O_2, O_3, CO, H_2S, NH_3, CO_2, SO_2, PH_3, HCN, NO, NO_2, Cl_2, H_2, $COCl_2$, amine, odorants, and organic vapors (OV) with electrochemical (EC) and infrared (IR) sensors. Table 3.2 shows a survey of the existing sensors for this device (special low and high concentration sensors were not used within this survey). Their characteristics are high resolution, high measuring accuracy (relative measuring error), relatively fast response times (T_{50} / T_{90}[1]), and also the wide range of the sensors and the low current consumption of the gas detector (approx. $1.3mA$ (standby), $8.5mA$ (in measuring mode), and $120mA$ (in alarm mode; can be suppressed by software)). Additionally, the gas detector combines multiple sensor technologies (EC, IR, and Cat), which are relatively easy to calibrate in comparison to MOX gas sensors (Sec. 2.1.4). Therefore, the gas detector provides the base unit of the gas-sensing payload of the micro-drone.

A significant reduction in weight of the gas detector has been achieved by the removal of unnecessary components (e.g., the mounting clip) and the integrated rechargeable battery in order to meet the payload limitation of $200g$ (the gas detector weighs $121g$ incl. all sensors). The casing of the gas detector remained unmodified as it is designed for calibration and maintenance purposes and protected against water and dust according to IP 67 (see [119] for further information) and therefore capable of working outdoors.

A more lightweight lithium-based battery model AA ($20.5g$) serves as a power supply ($3.7V$ with $900mAh$) for the sensors until their next mission to achieve fast operational readiness and to avoid long warm-up times of the sensors (up to 20 hours – see Table 3.2). During missions, the power is supplied by the battery of the micro-drone. The mounting was specially designed for the gas detector. It is based on the payload adapter plate of Airrobot and can be easily mounted and dismounted.

An additional electronic board with the dimension of an AA battery controls the communication between the gas detector and the micro-drone via the integrated microcontroller (MSP430F2618, Texas Instruments Incorporated, USA) and appropriate device interfaces (*IrDA*, *RS232*, and I^2C). A temperature and humidity sensor (SHT15, Sensirion AG, Switzerland) was also integrated as both factors may affect the measurement data (however, no compensation for varying temperature or humidity was applied in the experiments presented in this Ph.D. thesis). The microcontroller queries the gas detector (*IrDA*) and samples the temperature and humidity sensor (proprietary protocol) permanently and introduces the data in the micro-drone's downlink (*RS232* and I^2C). At the same time, the microcontroller prevents the gas detector from entering in the relatively high power-consuming alarm

---

[1] The response time of the sensor is commonly specified by the T_{90} or T_{50} time. T_{90} is the time for the sensor's response current to reach 90% of its steady-state value. Similarly, the T_{50} metric is the time required for the sensor to reach 50% of its steady-state value [118].

Table 3.2: *Basic gas sensors for the Dräger X-am 5600 gas detector [21].*

Sensor	Sensor Technology	Unit	Measuring Range	Resolution	Response Time	Measuring Accuracy	Warming-up Time
Cl_2	EC	ppm	$[0, 20]$	0.05	$\leq 30s$ (T_{90})	$\leq \pm 2\%$	-
CO_2	EC	% by volume	$[0, 5]$	0.1	$\leq 30s$ (T_{50})	$\leq \pm 20\%$	$\leq 12hr$
CO	EC	ppm	$[0, 2{,}000]$	2	$\leq 15s$ (T_{90})	$\leq \pm 2\%$	$\leq 5min$
H_2S	EC	ppm	$[0, 200]$	1	$\leq 15s$ (T_{90})	$\leq \pm 2\%$	$\leq 5min$
NH_3	EC	ppm	$[0, 300]$	1	$\leq 10s$ (T_{50})	$\leq \pm 3\%$	$\leq 12hr$
NO_2	EC	ppm	$[0, 50]$	0.1	$\leq 15s$ (T_{90})	$\leq \pm 2\%$	$\leq 15min$
$OV - A$	EC	ppm	$[0, 200]$	0.5	$\leq 40s$ (T_{50})	$\leq \pm 20\%$	$\leq 18hr$
O_2	EC	% by volume	$[0, 25]$	0.1	$\leq 10s$ (T_{90})	$\leq \pm 1\%$	$\leq 15min$
O_3	EC	ppm	$[0, 10]$	0.01	$\leq 10s$ (T_{50})	$\leq \pm 3\%$	$\leq 2hr$
PH_3	EC	ppm	$[0, 20]$	0.01	$\leq 10s$ (T_{90})	$\leq \pm 2\%$	$\leq 15min$
SO_2	EC	ppm	$[0, 100]$	0.1	$\leq 15s$ (T_{90})	$\leq \pm 2\%$	$\leq 15min$
HCN	EC	ppm	$[0, 50]$	0.1	$\leq 10s$ (T_{50})	$\leq \pm 5\%$	$\leq 15min$
H_2	EC	ppm	$[0, 2{,}000]$	5	$\leq 10s$ (T_{90})	$\leq \pm 1\%$	$\leq 1hr$
NO	EC	ppm	$[0, 200]$	0.1	$\leq 10s$ (T_{90})	$\leq \pm 3\%$	$\leq 20hr$
$COCl_2$	EC	ppm	$[0, 10]$	0.01	$\leq 20s$ (T_{50})	$\leq \pm 5\%$	$\leq 1hr$
Amine	EC	ppm	$[0, 100]$	1	$\leq 30s$ (T_{90})	$\leq \pm 3\%$	$\leq 12hr$
Odorant	EC	ppm	$[0, 40]$	0.5	$\leq 90s$ (T_{90})	$\leq \pm 5\%$	$\leq 12hr$
CO_2	IR	% by volume	$[0, 5]$	0.01	$\leq 10s$[a] / $50s$[b] (T_{90})	$\leq \pm 5\%$	-
Ex[c] (e.g., CH_4)	IR	% by volume	$[0, 100]$	0.1	$\leq 20s$ (T_{90})	$\leq \pm 5\%$	-
Ex (e.g., CH_4)	Cat	% by volume	$[0, 100]$	0.1	$\leq 30s$ (T_{90})	$\leq \pm 2.5\%$	-

---

[a] pump operation

[b] diffusion operation

[c] Explosion-proof

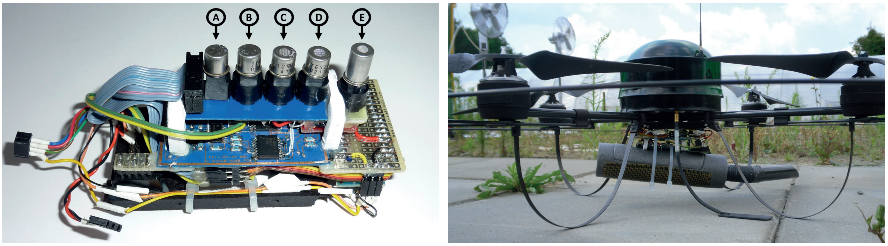

(a) (b)

Figure 3.5: *(a) The e-nose equipped with the following MOX (TGS26xx family) and EC (TGS4161) sensors: (A) TGS2602 (H_2S, NH_3), (B) TGS2600 (CO, CH_4), (C) TGS2610 (CH_4, LP gas), (D) TGS2611 (CH_4), and (E) TGS4161 (CO_2). (b) Micro-drone equipped with e-nose.*

mode. The *IrDA* communication and the gas detector itself allow a sampling rate of $1Hz$ for each sensor.

Dräger offers special battery cases for the gas detector, which allows to use the device with two commercially available batteries (AA). This battery case was used to integrate both the lithium-based battery and the electronic board. Only a small electronic board containing the temperature and humidity sensor and the *IrDA* transceiver to communicate with the gas detector was installed outside the casing.

The resulting overall weight of the gas-sensing payload including the above mentioned modifications amounts to $197g$. Further potential for reducing the weight of the payload is given by the casing of the gas detector, which weighs approximately $63g$.

3.2.2 Electronic Nose (e-nose)

An electronic nose (Fig. 3.5(a)) was specially adapted to the micro-drone by Örebro University. The e-nose has a size of $132 \times 52mm^2$ and weighs $100g$. The input voltage lies between 12 to $16V$ and the current consumption is around $300mA$. The e-nose has five sensor sockets, four of which can be equipped with the Figaro (Figaro Engineering Inc., Japan) TGS26xx family (MOX gas sensors) and one with the Figaro TGS4161 (CO_2; EC gas sensor). The basic measuring circuit used for the TGS26xx family is based on a voltage divider circuit (the voltage at the load resistor is measured), whereas the basic measuring circuit used for the TGS4161 is

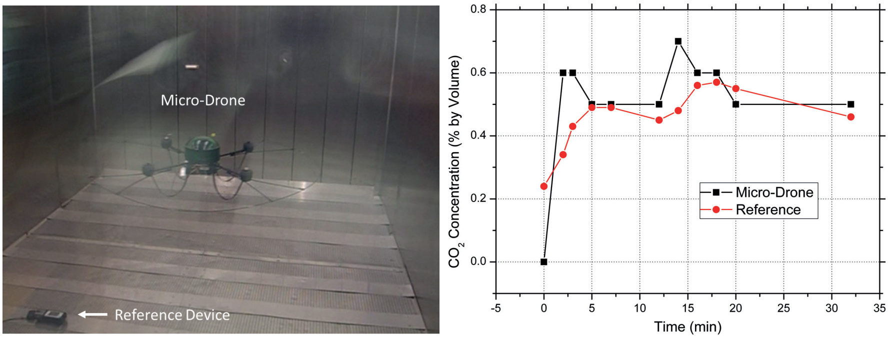

(a) (b)

Figure 3.6: *(a) Micro-drone flying in the $20m^3$ test chamber. (b) Comparison of the measured CO_2 concentration at the micro-drone and a reference device vs. time (the micro-drone had been airborne before the experiment started).*

based on an operational amplifier. Both circuits allow the measurement of voltages, which is directly correlated with a certain gas concentration. However, the sensors have to be calibrated in order to draw conclusions about the gas concentration to which the sensor is exposed. The heaters of the sensors are adjustable by software in the range of 0 to $7V$. Since the response of MOX gas sensors is highly dependent on their surface temperature (Sec. 2.1.4), a temperature modulation is supported by varying the heater voltage (not used during the experiments with the micro-drone).

However, only the TGS2611 (CH_4) and TGS4161 (CO_2) were used during the real-world experiments. The sensors were chosen because of their fast sensor response and decay (TGS2611 – CH_4), high sensitivity (TGS2611 – CH_4), and high selectivity (TGS4161 – CO_2) to their target gases. Sensor response experiments in an open environment with the TGS2611 (heater voltage: $5V$) and a methane source (1,000ppm) located around $0.3m$ away show response times of $T_{50} = 9.61s \pm 2.45s$ and $T_{90} = 22.64s \pm 4.21s$. The TGS4161 is characterized by a slow sensor response ($T_{90} = 1.5min$) and an accuracy of $\pm 20\%$ (at 1,000ppm). Both sensors allow a sampling rate of $8Hz$ for each sensor.

3.2.3 Validation Experiments – Dräger X-am 5600

3.2.3.1 Experiment Setup

Experiments in laboratory scale were carried out in a $20m^3$ test chamber (Fig. 3.6(a)) to measure different CO_2 concentrations for the validation of the system with respect to the measurement of gas concentrations in a medium-sized volume consisting of the same gas compound. Two commercially available gas detectors which were placed at different positions in the chamber were used as reference systems to provide ground truth measurements. One detector was identical to that used in the micro-drone's payload. The gas detectors were equipped with electrochemical CO_2 sensors. A circulating pump and a fan were operated to achieve homogeneous intermixing of the entire volume. The chamber was flushed at the beginning of each trial, i.e., the contained gas / air mixture was replaced with "clean" air to assure a CO_2-free[2] test chamber. The induction of CO_2 was carried out in series and intermittently for about $30s$ to regulate the CO_2 concentration. The micro-drone was started before CO_2 was induced.

3.2.3.2 Experiment Results

Taking into account the accuracy of the used CO_2 sensors (EC) in the different measurement devices used and the position-dependent delay (the time needed to achieve a homogeneous concentration in the test chamber), all values measured by the device of the micro-drone coincide with those measured by the reference devices (Fig. 3.6(b)). Therefore, the ability of the entire system to measure gas concentrations in a medium-sized volume has been satisfactorily verified. As a further step, the enhancement of the design and optimization of the system in order to implement a more point-wise gas concentration measurement is shown in Sec. 3.3.

3.2.4 Calibration Experiments – E-Nose

The calibration of MOX gas sensors is challenging as a sensitivity to other substances as well as temperature and humidity is usually given (Sec. 2.1.4). However, the TGS2611 (CH_4) and TGS4161 (CO_2) of the e-nose are calibrated in order to get a rough correlation between the sensor readings (V) and the present concentration

---

[2] Air contains $380ppm$ of the trace gas CO_2, which was neglected during the experiment.


(a) (b)

Figure 3.7: *The setup of the calibration experiments: (a) the e-nose mounted inside a calibration adapter connected via a small tube to (b) a multi gas controller (MKS Instruments, USA).*

(ppm). As a result, the results of the real-world experiments obtained with the Dräger X-am 5600 gas detector and the e-nose can be compared.

3.2.4.1 Experiment Setup

The e-nose was mounted to a calibration adapter (Fig. 3.7(a)), which was connected via a tube to a multi gas controller (MKS Instruments, USA, Fig. 3.7(b)). The multi-gas controller was used to expose the sensors of the e-nose with a defined concentration of CH_4 and CO_2, respectively. The cross-sensitivity to temperature and humidity was not considered during the calibration routine as "dry" calibration gas (i.e., traces of humidity are removed to a level that lies under the determination limit) at a temperature of approximately $25°C$ was used. The calibration curves were obtained successively by recording the stabilized responses of the sensors exposed to constant concentration levels over their measuring range (TGS2611 (CH_4) and TGS4161 (CO_2): $[0, 10{,}000]ppm$) consecutively. The TGS2611 (CH_4) was calibrated for the heater voltages of 4.5, 5.0, and $5.5V$, whereas the TGS4161 (CO_2) was only calibrated for the heater voltage of $5.0V$.

It should be noted that in a highly dynamic and turbulent environment the gas concentration will not reach a steady state [23].

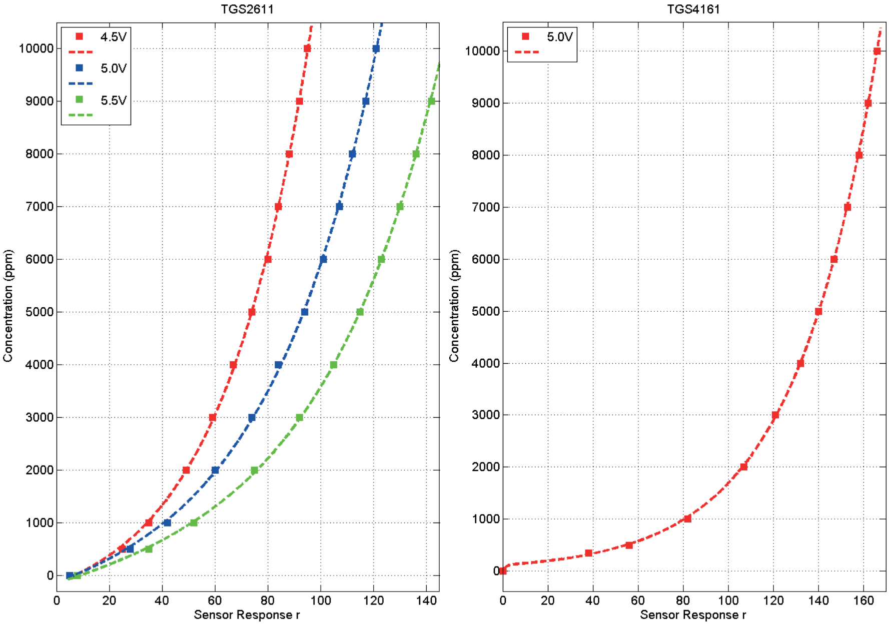

(a) (b)

Figure 3.8: *Calibration curves of the (a) TGS2611 (CH_4) at different heater voltages (4.5, 5.0, and 5.5V) and (b) the TGS4161 (CO_2) sensor.*

Table 3.3: *Approximation of the curve fitting parameters of the calibration curves (with 95% confidence intervals).*

	TGS2611			TGS4161
	$4.5V$	$5.0V$	$5.5V$	$5.0V$
a	698.9	598	447.6	113.6
	$(53.69, 1344)$	$(366.1, 830)$	$(357.6, 537.6)$	$(107.6, 119.5)$
b	0.0289	0.0235	0.0213	0.0270
	$(0.0221, 0.0358)$	$(0.0208, 0.0262)$	$(0.0200, 0.0226)$	$(0.0266, 0.0273)$
c	-842.5	-730.9	-601.8	-113.6
	$(-1383, -301.8)$	$(-927, -534.8)$	$(-738.9, -464.6)$	$(-197.1, -30.03)$
d	0.0015	-0.0067	-0.0114	-0.74
	$(-0.0259, 0.0288)$	$(-0.0248, 0.0114)$	$(-0.0259, 0.0032)$	$(-3.74, 3.74) \cdot e^{10}$

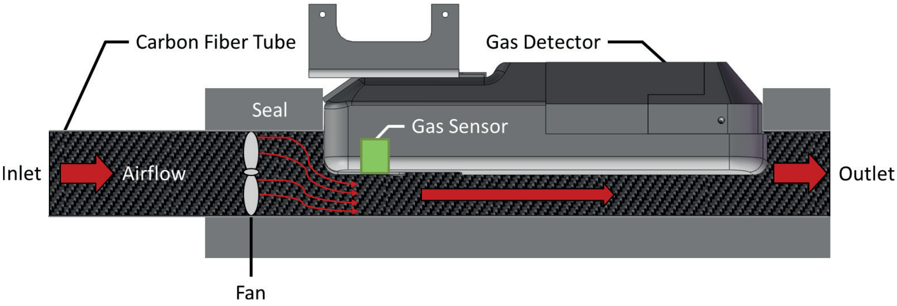

Figure 3.9: *Schematic diagram of the gas detector equipped with the constructional solution of the base unit of the semi-active and active gas transport approach (cross-section). The* $12V$ *axial fan (*$\varnothing 24mm \times 30mm$*) with an airflow of* $5.4m^3 \cdot h^{-1}$*, however, is only used for the constructional solution of the active gas transport approach.*

3.2.4.2 Experiment Results

The results can be seen in Fig. 3.8(a) and 3.8(b). Table 3.3 shows the approximation of the curve fitting parameters of the calibration curves. The curve fitting was done by calling the Matlab curve fitting toolbox “cftool”. A first-order exponential function for the curve fitting was used of the form: $f(x) = a \cdot \exp(b \cdot x) + c \cdot \exp(d \cdot x)$, where $f(x)$ is the fitted sensor response in V, x is the concentration value in ppm, and a, b, and c are the coefficients of the fitting.

3.3 Gas Transport to the Sensors

In Sec. 3.2.3 it was shown that measurements of gas concentrations in a large volume are feasible for the micro-drone equipped with the Dräger X-am 5600 gas detector. However, gas transport to the gas sensors is a critical process due to the induced disturbance by the rotors of the micro-drone, which basically dilute and disperse the surrounding gas-air mixture. This could be problematic for scenarios where point gas sources are present or the gas sensors work at the lower limit of detection.

3.3.1 Design Approaches of Gas Transportation

To improve the measurement capabilities of the micro-drone for small plumes, three different design approaches that lead to a less diluted gas-air mixture at the gas

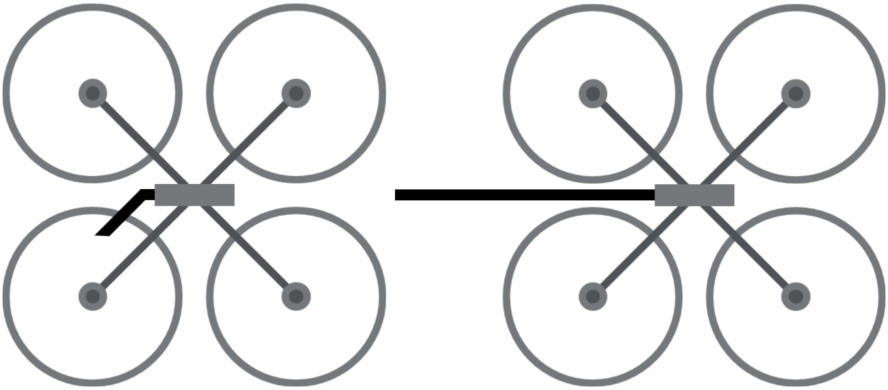

(a) Semi-active (b) Active

Figure 3.10: *Schematic diagram of the micro-drone (bottom view) equipped with the constructional solution of the (a) semi-active and (b) active gas transport approach. The tube of the active gas transport approach protrudes from the radius of the micro-drone by nearly* $0.3m$.

sensors were implemented and analyzed with respect to their functional performance:

- Passive gas transport: integration of the Dräger X-am 5600 gas detector below the micro-drone without any auxiliary device regarding the airflow.
- Semi-active gas transport: using the airflow generated by the rotors (see Figs. 3.9, 3.10(a), and 3.11(a)).
- Active gas transport: using additional fans and tubes (see Figs. 3.9, 3.10(b), and 3.11(b)).

When applying the passive approach, no artificial airflow is used to bring the gas to the sensors (the gas detector is mounted directly under the micro-drone without modification). When applying the semi-active gas transport approach, the gas-air mixture is conveyed through a carbon fiber tube using the suction effect of one rotor. The tube of the active gas transport approach protrudes from the radius of the micro-drone by nearly $0.3m$. Here, a $12V$ axial fan ($\varnothing 24mm \times 30mm$) with an airflow of $5.4m^3 \cdot h^{-1}$ was mounted inside the tube to draw in the gas-air mixture. Fig. 3.11 shows the design of the semi-active and active gas transport approach.

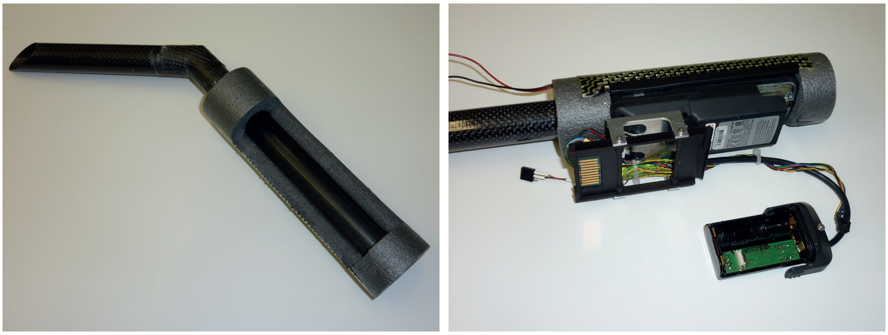

(a) Semi-active (b) Active

Figure 3.11: *(a) Design of the semi-active gas transport approach. (b) Integration of the Dräger X-am 5600 gas detector using the design of the active gas transport approach.*

The effective sensor response and decay can be sped up to some degree by an artificially generated airflow (compare Table 3.2 CO_2 – IR gas sensor) to achieve faster and more accurate gas concentration measurements with shorter residence time of the micro-drone at a certain position. The semi-active and active gas transport approaches are required and were developed within the Ph.D. thesis.

3.3.2 Validation Experiments

3.3.2.1 Experiment Setup

Reproducible environmental conditions are needed in order to be able to compare the different gas transport methods: a gas source with a constant release rate and stable airflow conditions. An experiment setup to create such a controlled environment was built up in the huge fire test hall of BAM (Fig. 3.12(a)). A CO_2 gas bottle connected to a pressure-reducing valve was used as the emission source. A fan generated stable airflow conditions and dispersed the gas as well. A defined measuring position was chosen for all experiments approximately $1m$ downwind from the fan in the height of the gas flow. A second Dräger X-am 5600 gas detector was used as reference system to provide reference measurements. The CO_2 infrared sensors were used in these experiments because of their faster response and higher accuracy (Sec. 3.2.1: Table 3.2).

One experiment for each gas transport mechanism was performed. At the begin-

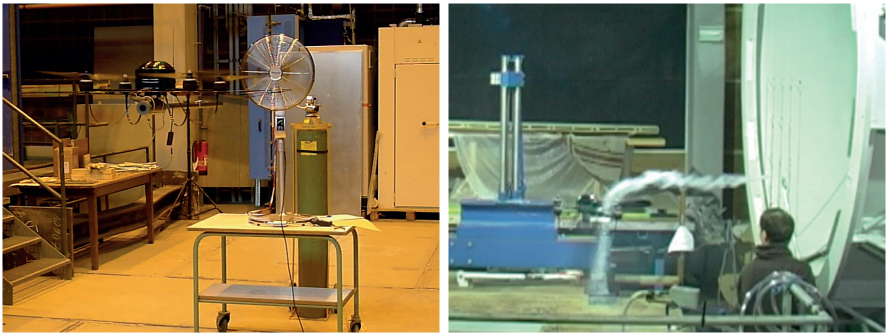

(a) (b)

Figure 3.12: *(a) Micro-drone in flight in front of the artificial emission source. (b) Micro-drone flying below a visualized plume in a wind tunnel.*

ning of each trial, the gas concentration was adjusted so that the reference sensor measured a stable value of 0.5% by volume. Afterwards, the micro-drone equipped with the Dräger X-am 5600 gas detector and one of the three gas transport mechanisms was flown to the measuring point to perform CO_2 measurements in flight for approximately $100s$.

3.3.2.2 Experiment Results

The results of the experiments are shown in Fig. 3.13. Significant differences can be seen between the different gas transport solutions. In contrast to measurements in a large volume of the same gas concentration (Sec. 3.2.3), none of the approaches is capable of measuring the reference gas concentration of 0.5% by volume. The highest measured concentrations (peaks) lay around 0.32 (passive), 0.30 (semi-active), and 0.39 (active) % by volume, which is 64, 60, and 78% of the reference measurements. The averaged measurement results, after the sensor responded, are more significant. The averaged concentrations were 0.18 ± 0.02 (passive), 0.26 ± 0.01 (semi-active), and 0.33 ± 0.02 (active) % by volume, which is 36, 52, and 66%, respectively, of the reference measurements.

The reason for the generally lower measurements compared to the reference sensor is the rotor movement of the micro-drone (Sec. 3.3). The active gas transport approach can avoid this dilution effect best with the long carbon fiber tube. The disadvantages of this method, however, are the additional weight (approx. $76g$), the

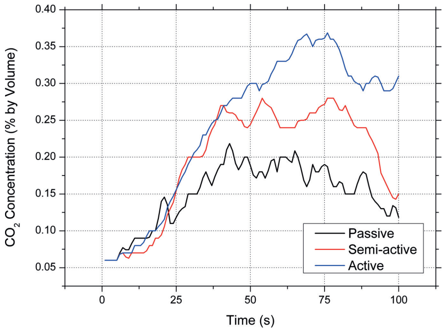

Figure 3.13: *Comparison of the design of gas transport: Measured CO_2 concentration at "stable" environmental conditions with micro-drone in flight. The active gas transport approach can avoid the dilution effect of the rotors of the micro-drone best with the long carbon fiber tube. However, a tradeoff between applicability and sensitivity is given by the semi-active payload.*

position of the tube inlet which strongly dictates the measurement results as well as the enlarged drone size that is exposed to wind. A tradeoff between applicability and sensitivity is given by the semi-active payload (approx. $26g$). Using the semi-active gas transport, it turns out that flying rather below the plume is advantageous. Fig. 3.12(b) demonstrates that the plume in front of the micro-drone is still intact, while the rotors redirect the plume completely downwards.

Each gas transport solution has its own advantages and disadvantages depending on the measurement scenario. The gas transport solutions can easily be changed since the standard design has been used. However, the semi-active gas transport approach was mainly used in the real-world experiments as it offers high applicability and reasonable sensitivity.

3.4 Estimation of the Wind Vector

The wind vector is important for many existing gas dispersion models [120, 121] to better characterize the dispersion properties of the plume, as well as for gas source localization (Sec. 2.2) and in some cases of gas distribution modeling (Sec. 2.3). Wind measurements are furthermore important since high wind speeds and strong wind gusts in the target area may also limit the use of the micro-drone presented in Sec. 3.1, which can only resist wind speeds of up to $8ms^{-1}$. Additionally, meteorological services like the German Weather Service (DWD) specify the averaged wind speed and direction only in a height of $10m$ above ground. However, wind speed and direction can vary locally and below a height of $10m$ above ground due to naturally occurring conditions (condition of the soil, strong temperature gradients, and type of the ecological system) or building density (countryside or city). Therefore, the on-board measurement of the wind vector in real-time is fundamental.

The response of many gas sensors is caused by direct interaction with the chemical compound and thus represents only a small area around the sensor surface ($\approx 0.01m^2$) [Paper III]. Additionally, a single gas sensor does not provide directional information. In order to mitigate these limitations, directional information in form of the wind vector (wind speed and direction) should be acquired. Consequently, the on-board measurement of the wind vector in real-time is crucial.

In the following section a new approach by Neumann et al. [Paper III, Paper XI] is described and validated to estimate the wind vector based on the existing measurement data of the micro-drone's on-board sensors (IMU) which makes additional anemometric sensors superfluous. This approach in combination with wind tunnel experiments to determine the relationship between inclination angles and wind speed is, to the best of the author's knowledge, unique.

3.4.1 Theory

The wind vector estimation presented in this section is based on the wind triangle (Fig. 3.14(b)). The wind triangle is commonly used in navigation and describes the relationships between the flight vector $\vec{v} = (r_v, \theta_v)$, the ground vector $\vec{w} = (r_w, \theta_w)$, and the wind vector $\vec{u} = (r_u, \theta_u)$, where r denotes the length and θ the directional component of the vectors. Here, the 2D case can be considered since the knowledge of the gravity vector is available. Two of the three vectors or four of the six parameters of the wind triangle (flight speed r_v, ground speed r_w, wind speed r_u, drift angle α, and the angles β and γ of the wind triangle) are needed in order to derive the remaining parameters. However, only the ground vector is directly given by the GPS receiver of the micro-drone.

In the following approach, the flight vector $\vec{v}$ is estimated based on the micro-drone's roll and pitch angle as well as on the system's orientation to the magnetic north pole, the latter determined by a compass. The micro-drone's IMU provides the corresponding angles ϕ (roll) and θ (pitch). Fig. 3.15 shows the local coordinate

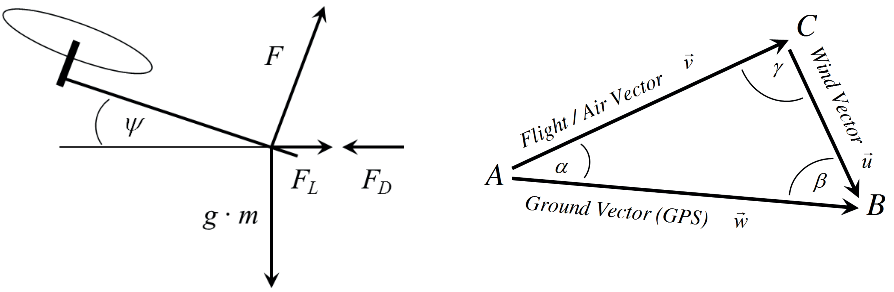

(a) (b)

Figure 3.14: *(a) Force diagram of the micro-drone, where ψ is the inclination angle of the micro-drone, g is the acceleration due to gravity, m is the total mass of the micro-drone (including the payload), F is the shear force, F_L is the drift force, and F_D is the drag force. (b) The wind triangle defined by the flight vector $\vec{v}$, the ground vector $\vec{w}$, and the wind vector $\vec{u}$.*

system of the micro-drone.

$$\vec{e}_{roll} = \begin{pmatrix} 0 \\ \cos\phi \\ \sin\phi \end{pmatrix}, \vec{e}_{pitch} = \begin{pmatrix} \cos\theta \\ 0 \\ -\sin\theta \end{pmatrix} \tag{3.1}$$

The inclination angle of the micro-drone ψ is calculated as the inverse scalar product from the cross product of the (rotated) unit vectors (Eq. 3.1) and $\vec{n}_{XY}$. $\vec{n}_{XY} = (0, 0, 1)$ is the normal unit vector to the XY-plane which is parallel to the ground (Fig. 3.15). Finally, the angle ψ can be used to calculate the drag force F_D. Fig. 3.14(a) shows the relationship between the forces.

$$\psi = \cos^{-1}\left(\frac{\vec{n}_{XY} \cdot (\vec{e}_{pitch} \times \vec{e}_{roll})}{|\vec{n}_{XY}| \cdot |\vec{e}_{pitch} \times \vec{e}_{roll}|}\right), \tag{3.2}$$

$$F_D = g \cdot m \cdot \tan\psi, \tag{3.3}$$

where g is the acceleration due to gravity and m is the total mass of the system. The flight speed can be calculated theoretically by using the definition of the drag coefficient c_d.

$$r_v = \sqrt{\frac{2 \cdot F_D}{\rho \cdot A_{proj} \cdot c_d}}, \tag{3.4}$$

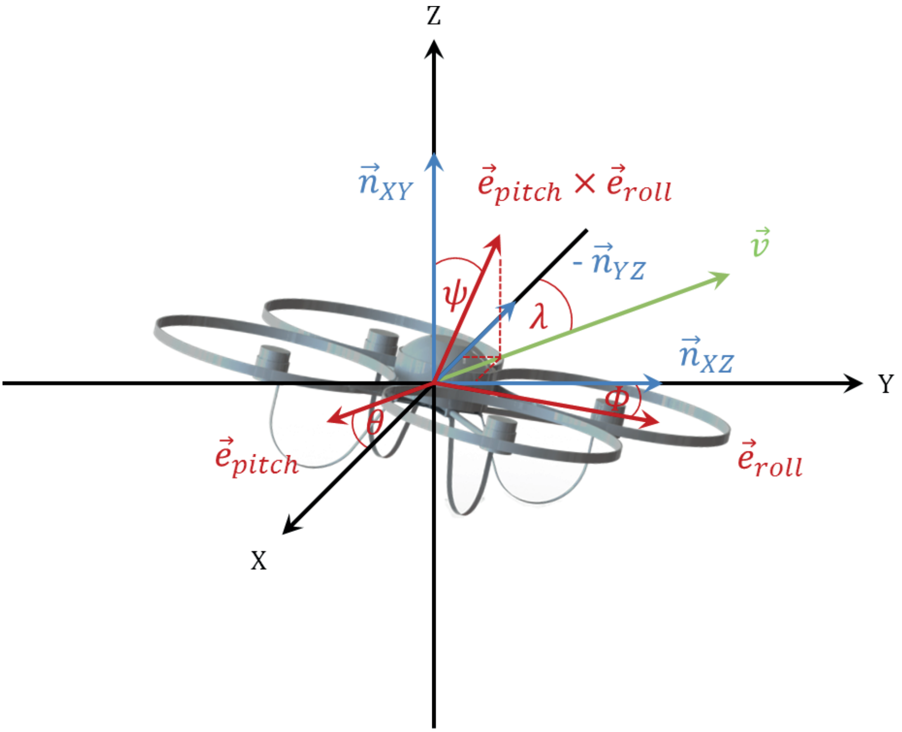

Figure 3.15: *Micro-drone with local coordinate system. The viewing direction of the micro-drone is considered as the inverse normal vector* $-\vec{n}_{YZ} = (-1, 0, 0)$.

where A_{proj} is the projected surface area and ρ is the density of the fluid (in this case air). The density of air depends on the temperature and humidity. However, A_{proj} and c_d are generally not known and have to be determined. The projected surface area A_{proj} can be generated for each inclination angle (increment step could be 1°) in 3D-CAD software using a 3D model of the micro-drone and a reference body with known projected surface area A_{ref} (e.g., a sphere; Eq. 3.5).

$$A_{proj} = \frac{\#P_{A_{proj}}}{\#P_{A_{ref}}} \cdot A_{ref}, \tag{3.5}$$

where $\#P_{A_{proj}}$ is the number of pixels in the projected surface area of the micro-drone and $\#P_{A_{ref}}$ is the number of pixels in the reference area. The drag coefficient c_d has to be investigated in wind tunnel experiments for different wind speeds. Both are described in Sec. 3.4.2.

To calculate the flight direction θ_v, first the angle λ between the viewing direction of the micro-drone, considered as the negative normal vector $-\vec{n}_{YZ} = (-1, 0, 0)$, and the projection of the vector $\vec{e}_{pitch} \times \vec{e}_{roll}$ onto the XY-plane is to be calculated using Eq. 3.6. In order to decide whether the vector $\vec{e}_{pitch} \times \vec{e}_{roll}$ is located on the left or right of the micro-drone with respect to the viewing direction, Eq. 3.7 must be solved. This distinction is required as the result of Eq. 3.6 will be within the interval $[0, 180]^\circ$. The flight direction θ_v is calculated by using the angle λ and the compass angle of the viewing direction of the micro-drone $\delta_{compass}$.

$$\lambda = \cos^{-1}\left(\frac{-\vec{n}_{YZ} \cdot (\vec{e}_{pitch} \times \vec{e}_{roll})_{XY}}{|-\vec{n}_{YZ}| \cdot |(\vec{e}_{pitch} \times \vec{e}_{roll})_{XY}|}\right) \tag{3.6}$$

$$\vec{n}_{XZ} \cdot (\vec{e}_{pitch} \times \vec{e}_{roll})_{XY} = \begin{cases} < 0 & \text{, if } \vec{e}_{pitch} \times \vec{e}_{roll} \text{ is left} \\ > 0 & \text{, if } \vec{e}_{pitch} \times \vec{e}_{roll} \text{ is right} \\ = 0 & \text{, otherwise} \end{cases} \tag{3.7}$$

$$\theta_v = \begin{cases} (360^\circ - \lambda + \delta_{compass}) \bmod 360^\circ & \text{, if Eq. 3.7} < 0 \\ (\lambda + \delta_{compass}) \bmod 360^\circ & \text{, otherwise} \end{cases} \tag{3.8}$$

Finally, the wind vector is calculated using the estimated flight vector $\vec{v}$ and the measured ground vector $\vec{w}$ using the wind triangle (Fig. 3.14(b)) and the law of cosines. The drift angle α equals the difference of θ_w and θ_v.

$$r_u = \sqrt{r_v^2 + r_w^2 - 2r_v \cdot r_w \cdot \cos\alpha} \tag{3.9}$$

$$\beta = \cos^{-1}\left(\frac{r_v^2 - r_w^2 - r_u^2}{-2r_w \cdot r_u}\right) \tag{3.10}$$

$$\theta_u = (\theta_w + 180^\circ \pm \beta) \bmod 360^\circ \tag{3.11}$$

Eqs. 3.9, 3.10 and 3.11 are used to get the wind speed r_u and direction θ_u for $0 < \alpha < 180^\circ$. The cases $\alpha = 0^\circ$ and 180° have to be considered separately. The sense of rotation of β in Eq. 3.11 depends on the flight direction θ_v, i.e., if the flight direction is within the interval $[\theta_w + 180^\circ, \theta_w] \bmod 360^\circ$, then rotation is clockwise $(+\beta)$, otherwise counterclockwise $(-\beta)$.

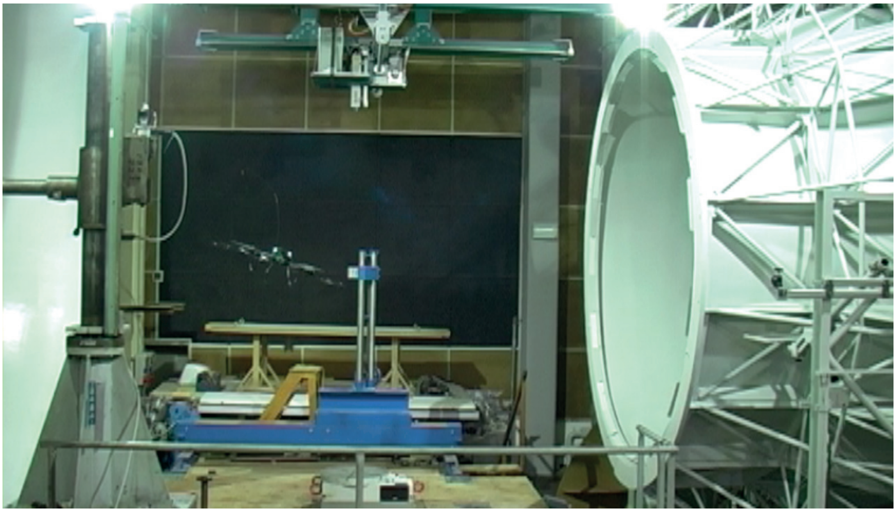

Figure 3.16: *Micro-drone in the wind tunnel at* $7.5ms^{-1}$.

3.4.2 Experiment Study

A wind tunnel is usually used to determine the drag coefficient c_d of an object. The object is mounted on a plate equipped with force sensors in order to measure drag force F_D. The drag coefficient c_d is then calculated using Eq. 3.4. However, the typically used force balance is not adequate for those experiments as the influence of the rotors of the mounted micro-drone at different wind speeds is not considered. Therefore, the flight vector $\vec{v}$ was calculated based on experimentally determined functions.

3.4.2.1 Experiment Setup

The experiments took place in a Göttingen-type wind tunnel [122] (Fig. 3.16; TU Dresden, Germany). The tunnel has a flow diameter of about $3m$ and an almost $4.5m$ long test section, which provided sufficient space for the experiments using the micro-drone. The speed of the airflow in the wind tunnel can be set precisely with a relative error $< 1\%$. The reference was measured using pressure sensors in the prechamber and in the free jet of the wind tunnel. The pressure sensor (Setra Systems, Inc., USA) in the prechamber of the wind tunnel was used to measure the

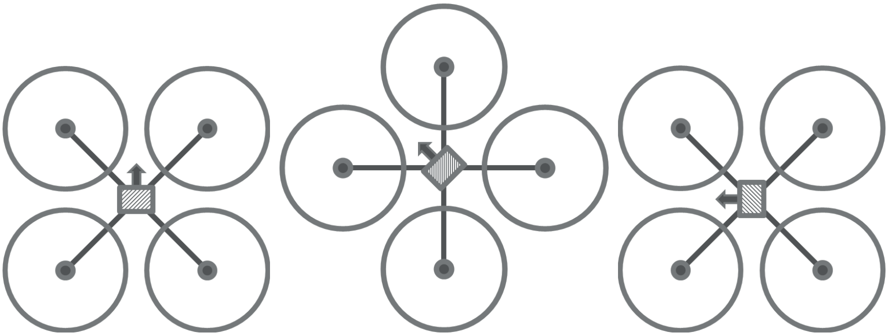
(a) (b) (c)

Figure 3.17: *Schematic diagram of the micro-drone (top view) with standard payload container represented as shaded box in different radial orientations: (a) 0°, (b) 45°, and (c) 90°. The arrows indicate the viewing direction of the micro-drone.*

total pressure P_t. The relative error of this sensor was less than $< \pm 1 Pa$. The static pressure was measured in the free jet using a barometric column with a measurement error of $\pm 0.5 mmHg$. Finally, Eq. 3.12 is used to calculate the flow speed v in the wind tunnel.

$$v = \sqrt{\frac{2(P_t - P_s)}{\rho}} \tag{3.12}$$

with

$$P_t = P_s + q, \tag{3.13}$$

where P_t is the total pressure, P_s is the static pressure, q is the dynamic pressure, and ρ is the air density ($1.2041 kg \cdot m^{-3}$ at $20°C$).

Different series of measurements were performed in the wind tunnel in different radial orientations of the micro-drone (without payload: 0° and 45°; with payload: 0°, 45°, and 90°) and with different payload configurations (different sizes and weights). The first experiments were performed with the AR100, whereas the second experiments were performed with its successor model AR100-B. In comparison to its predecessor, the AR100-B is slightly larger and the rotor heads are additionally equipped with flapping hinges which results in a larger projected surface area size A_{proj}. Fig. 3.17 shows the different radial orientations of the micro-drone investigated in the wind tunnel. The wind tunnel provided speeds from 0.0 up to $8.0ms^{-1}$ with an increment step of $0.5ms^{-1}$. Data was collected from the micro-drone's IMU for about $60s$ and was considered valid if the micro-drone held its position (controlled via camera) and wind speed in the wind tunnel was steady.

3.4.2.2 Experiment Results

Fig. 3.18 shows the results from the wind tunnel experiments. A relationship between the inclination angle of the micro-drone ψ and the flight speed r_v based on different series of measurements has been obtained. Two functions were derived for both micro-drones by interpolation using the method of least squares which can be used to directly calculate the flight speed r_v:

$$(r_v)_{\text{AR100}} = 0.004 \cdot \psi^2 + 0.396 \cdot \psi - 0.188 \tag{3.14}$$

$$(r_v)_{\text{AR100-B}} = \begin{cases} 0.019 \cdot \psi^3 - 0.258 \cdot \psi^2 + 1.447\psi - 1.119 & \text{, if } \psi \in [0, 7)^\circ \\ -0.002 \cdot \psi^2 + 0.556\psi - 1.153 & \text{, if } \psi \in [7, 18]^\circ \end{cases} \tag{3.15}$$

Eq. 3.14 applies for the micro-drone without flapping hinges (AR100) and is based on a quadratic function, whereas Eq. 3.15 is for the successor model with flapping hinges (AR100-B) and consists of two sub-functions: a cubic and a quadratic part. Fig. 3.19 shows the reference curves for the micro-drone (a) without and (b) with flapping hinges. Each function was created based on all experiments from the corresponding micro-drone. It can be observed that the behavior of the micro-drone in the wind tunnel in (a) is quadratic whereas the behavior in (b) seems to be nearly linear in the interval of approximately $[7, 18]^\circ$.

Further results show that different radial orientations (Fig. 3.18(a)) and payload configurations (Figs. 3.18(a) and 3.18(b)) of the micro-drones seem to be irrelevant and can be neglected. This can be seen in Table 3.4 which compares the different radial orientations of the micro-drone (AR100) with standard payload container ($\approx 200g$) and without payload. In all cases RMSE is $\leq \pm 0.74^\circ$ resulting in an average RMSE of $0.56^\circ \pm 0.23^\circ$.

The comparison of the different payload configuration (AR100-B) shows similar results: RMSE is $\leq \pm 0.67^\circ$ resulting in an average RMSE of $0.50^\circ \pm 0.19^\circ$. Here, the orientation angle was kept at 0°. The semi-active gas transport unit consists of two

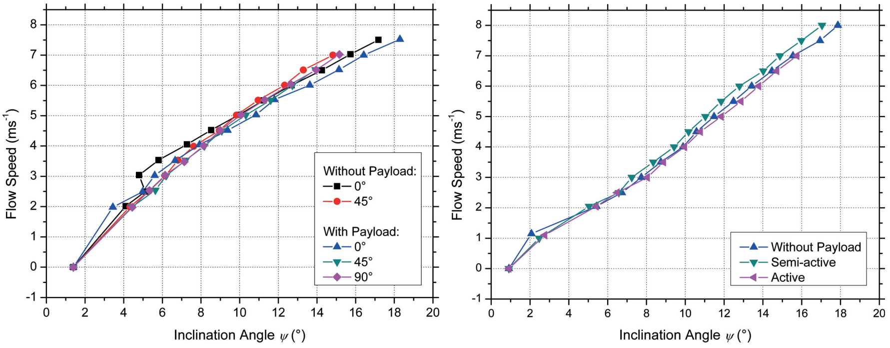

(a) (b)

Figure 3.18: *Inclination angle of the micro-drone* ψ *at different flow speeds* v*: (a) comparison of different radial orientations of the micro-drone with standard payload container (*$\approx 200g$*) and without payload (AR100) and (b) comparison of different payload configurations between approximately* 0 *to* 300g *(AR100-B).*

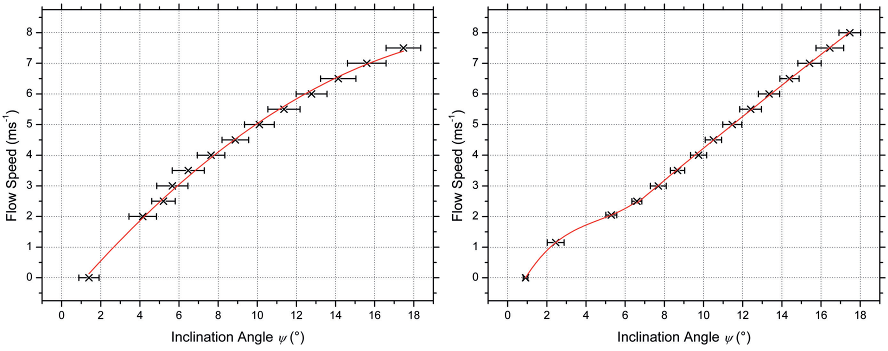

(a) (b)

Figure 3.19: *Flow speed* v *as a function of inclination angle* ψ *(micro-drone (a) without and (b) with flapping hinges in each case averaged over the available measurement data). The error bars indicate the standard deviation* $\pm\sigma$*.*

Table 3.4: *Top: Comparison of different radial orientations of the micro-drone with standard payload container (≈ 200g) and without payload. Bottom: Comparison of different payload configurations between approximately* 0 *to* 300*g (W = Without, SA = Semi-active, and A = Active).*

Micro-Drone	Orientation	Payload	MSE	RMSE
AR100	0° and 45°	No	0.43	0.66°
	0° and 0°	Yes / No	0.52	0.72°
	45° and 45°	Yes / No	0.16	0.41°
	0° and 45°	Yes	0.44	0.66°
	0° and 90°	Yes	0.55	0.74°
	45° and 90°	Yes	0.03	0.16°
AR100-B	0°	*W* and *SA*	0.29	0.54°
	0°	*W* and *A*	0.09	0.30°
	0°	*SA* and *A*	0.44	0.67°

tubes assembled in an angle at 45°, whereas the active gas transport unit consists only of one tube pointing in viewing direction (Sec. 3.3). Therefore, the projected surface area of the active gas transport unit will stay more or less constant over all possible inclination angles ψ, whereas the projected surface area size of the semi-active gas transport unit will change (at an orientation angle of 0°). This can be seen in Fig. 3.18(b) comparing the curve progressions of the active and semi-active payloads.

The flapping hinges of the rotors allow them to move within $7.0° \pm 1.0°$ at lower *rpm* of the motors. There, the centrifugal forces create greater inertia for the flapping hinges of the rotor heads. Thus the rotors can move to achieve a more stable hover. The centrifugal forces at higher *rpm* of the motors reduce the flapping hinge effect on the rotor heads and therefore increase directional control of the micro-drone. Fig. 3.20 shows the micro-drone (a) without and (b) with flapping hinges. The rotors of the micro-drone without flapping hinges are aligned almost parallel to the micro-drone, whereas the rotors with flapping hinges are aligned either more parallel to the ground or more parallel to the micro-drone depending on the *rpm* of the motors. This may explain the outlier at $1.15ms^{-1}$ (Fig. 3.19(b)) at lower *rpm*.

The analysis of the experiment results shows that different radial orientations and payload configuration have an influence on the inclination angle ψ. However, it was

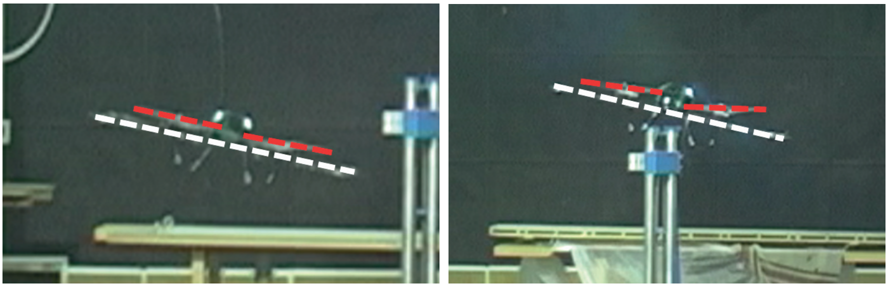

(a) (b)

Figure 3.20: *Comparison of the inclination angle of the micro-drone ψ and the alignment of the rotors equipped (a) without and (b) with flapping hinges.*

shown that the influence is negligible. Furthermore, the flapping hinges change the size of the projected surface area A_{proj} and the micro-drone's behavior at higher flow speeds v and inclination angles ψ (quadratic vs. linear), respectively. This effect has to be considered separately. Comparing the derived functions for both micro-drones with their averaged data points obtained from the wind tunnel experiments gives an RMSE of (a) $0.10ms^{-1}$ and (b) $0.05ms^{-1}$. Therefore, the reference functions can be used independently from the radial orientation and payload configuration of the micro-drones.

3.4.3 Validation Experiments

3.4.3.1 Experiment Setup

The validation experiments of the wind vector estimation took place on a wide open field at Örebro University (Sweden). An ultrasonic anemometer (Young 81000, R. M. Young Company, USA) was positioned at a height of approximately $2m$ and was used to perform the reference measurements (Fig. 3.21). The ultrasonic anemometer has an operating range between 0 and $40ms^{-1}$ with a resolution of $0.01ms^{-1}$ and an accuracy of $\pm1\%$ (in the range of 0 to $30ms^{-1}$). The resolution of the wind direction is 0.1° with an accuracy of $\pm2^\circ$ (in the range of 0 to $30ms^{-1}$). Therefore, the anemometer provides a highly precise reference for the wind vector estimation by the micro-drone.

The first experiment was to validate the wind vector estimation during hover-

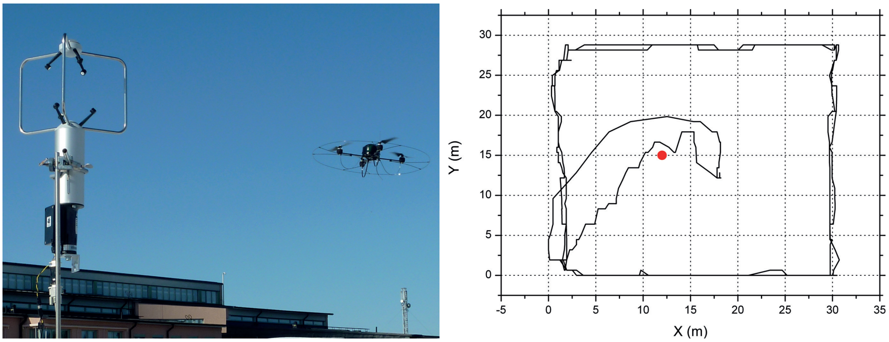

(a) (b)

Figure 3.21: *(a) Micro-drone with 3D ultrasonic anemometer (Young 81000, R. M. Young Company, USA). (b) The path taken by the micro-drone. The red dot indicates the position of the anemometer.*

ing flight of the micro-drone. Here, the micro-drone was manually positioned at a distance of 2 to $5m$ from the anemometer and at a height of $2m$. The position was chosen based on the actual wind data in a way that the generated airflow of the micro-drone's rotors did not influence the anemometer. Measurements with the IMU, GPS, and anemometer were recorded at the frequencies of $24Hz$, $4Hz$, and $1Hz$, respectively, for about $20min$. The position was controlled automatically using only the on-board GPS of the micro-drone. The second experiment was to validate the wind vector estimation during flight of the micro-drone. Therefore, four waypoints were placed around the anemometer in a square of size $30 \times 30m^2$, thus positioning the anemometer almost in the center (Fig. 3.21(b)) of the area of the experiments. The micro-drone autonomously visited each waypoint twice, before the experiment was completed.

For the evaluation of these results, the assumption has to be made that the wind vector measured at the anemometer and the micro-drone are comparable, i.e., that the wind field does not change drastically over the distance between the reference measurement with the anemometer and the position of the micro-drone.

3.4.3.2 Experiment Results

In general, a good match between the wind speed and direction measured with the micro-drone and the wind speed and direction measured with the Young anemometer was found, see Figs. 3.22 to 3.25, respectively. Exceptions in form of small variations can be seen in Figs. 3.22 and 3.23, e.g., between 150 and 200s, and 1100 and 1150s. However, greater variations in the measured wind directions can be observed in Fig. 3.23 around 650s and 900s: deviations of the measurements taken with the micro-drone compared to the reference may be as high as 60°. The reason for these variations could be traced to inaccuracies of the GPS receiver or a problem with the GPS-based positioning system of the micro-drone (e.g., oversteering). Further reasons include the different measuring positions and varying distance of the micro-drone to the anemometer. The calculated RMSE for the wind speed is $\pm 0.71 ms^{-1}$ (moving average of 10s) and $\pm 0.60 ms^{-1}$ (moving average of 20s) with the micro-drone hovering close to the anemometer and $\pm 0.53 ms^{-1}$ (moving average of 10s) and $\pm 0.36 ms^{-1}$ (moving average of 20s) with the micro-drone flying around the anemometer.

A systematic offset of approximately 15° was discovered comparing the wind direction data, which can be traced to a poor north alignment of the anemometer and the inferior compass used. Here, the uncertainties are most likely introduced by the assumption of a uniform wind field (see Sec. 6.1.1.3), the imprecise synchronization of measured GPS and IMU data, and a given packet loss of the data transmission in the downlink of the micro-drone. If the measurement data of the anemometer is corrected with the above mentioned offset, an RMSE value of ±17.76° (moving average of 10s) and ±14.02° (moving average of 20s) with the micro-drone hovering close to the anemometer can be calculated using directional statistics (Appendix A, Eq. A.1). The RMSE in flight is ±18.79° (moving average of 10s) and ±14.77° (moving average of 20s).

The results of the wind vector validation are promising (Table 3.5). In this form, the wind vector estimation is of great importance to the field of application and represents a major improvement over the existing systems (e.g., Pitot tube) for a quadrocopter. No additional Pitot tube or anemometric sensor has to be mounted in order to obtain the wind vector and valuable payload capacity is saved for other sensors. Because on the fact that the micro-drone already runs a Kalman filter to obtain less noisy data from the IMU, averaging the calculated wind vector over the last 20s is sufficient in order to obtain a good estimation of the wind vector.

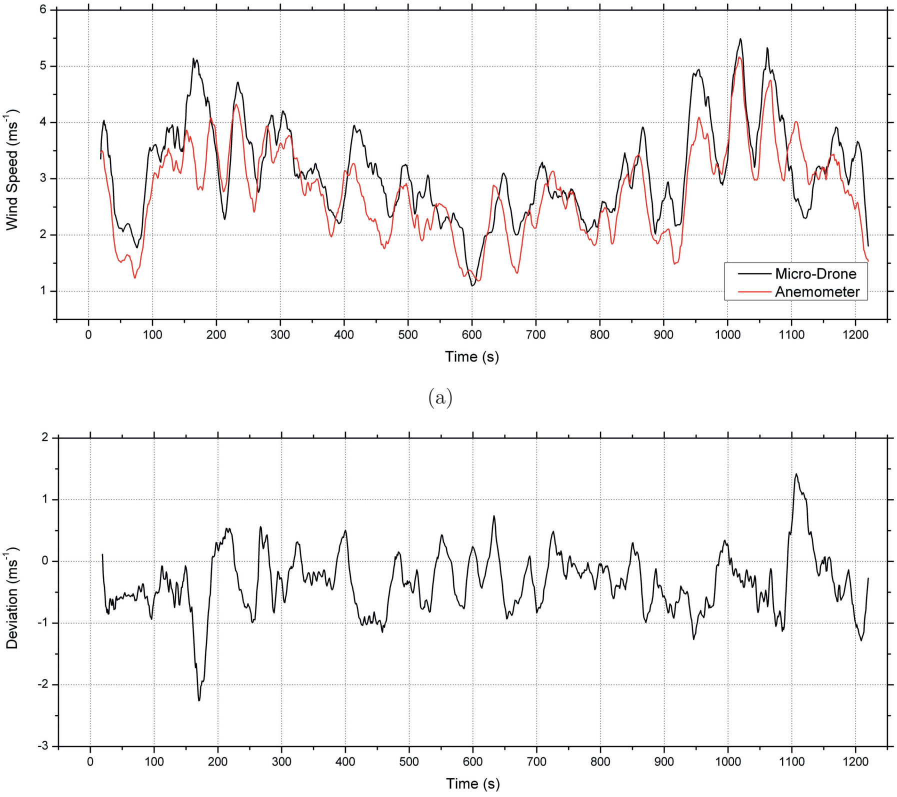

(a)

(b)

Figure 3.22: *Experiment 1: (a) Validation of the wind speed estimation and (b) the deviation of the reference to the measurement. The data was averaged over the last* 20*s using a sliding window.*

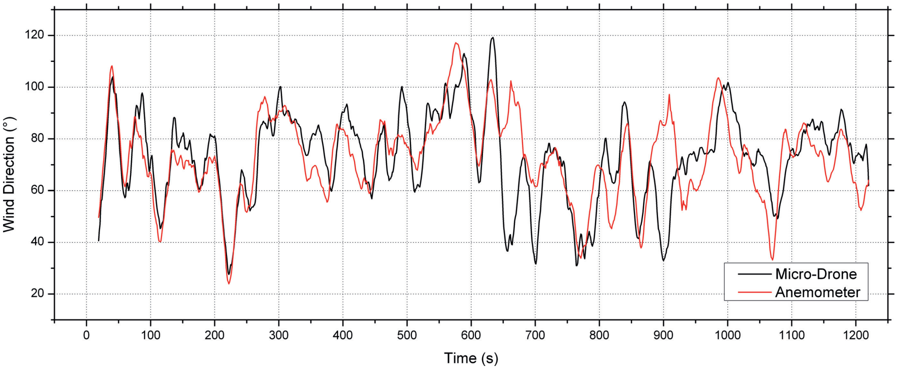

(a)

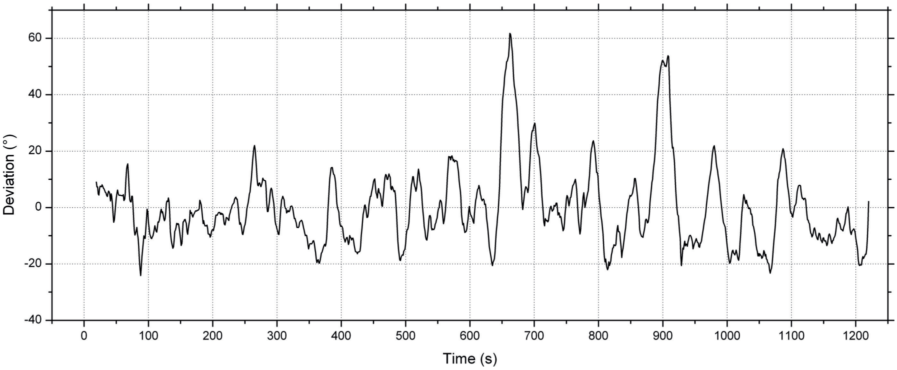

(b)

Figure 3.23: *Experiment 1: (a) Validation of the wind direction estimation (corrected with an offset due to a systematic error in the experiment setup) and (b) the deviation of the reference to the measurement. The data was averaged over the last* 20*s using a sliding window.*

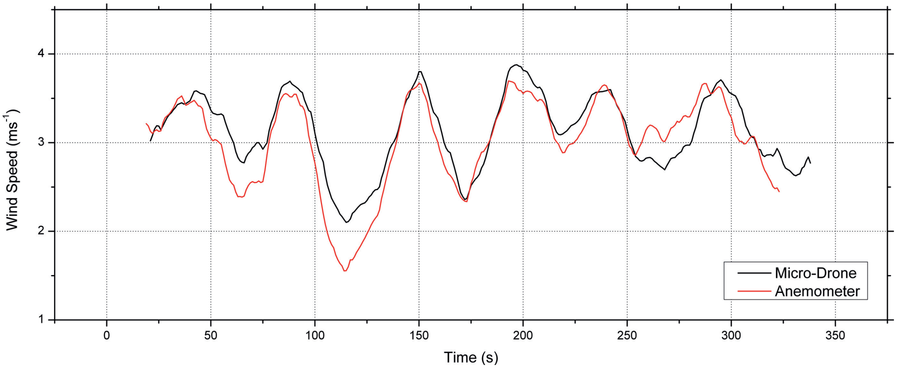

(a)

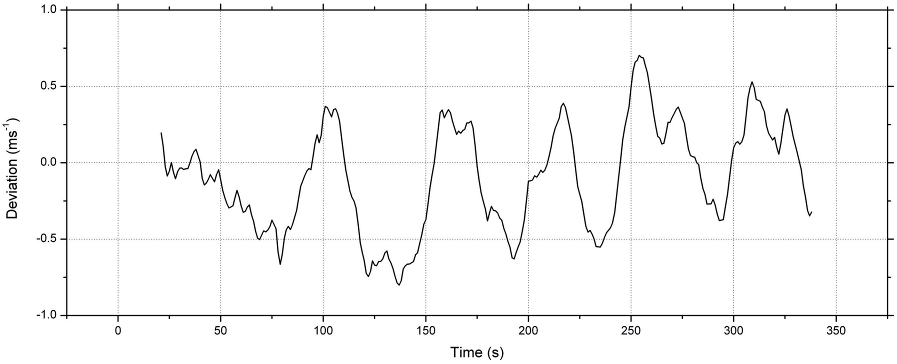

(b)

Figure 3.24: *Experiment 2: (a) Validation of the wind speed estimation and (b) the deviation of the reference to the measurement. The data was averaged over the last* 20s *using a sliding window.*

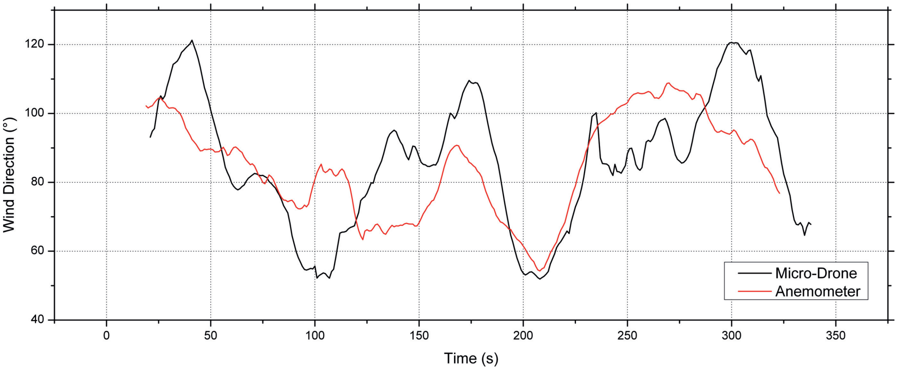

(a)

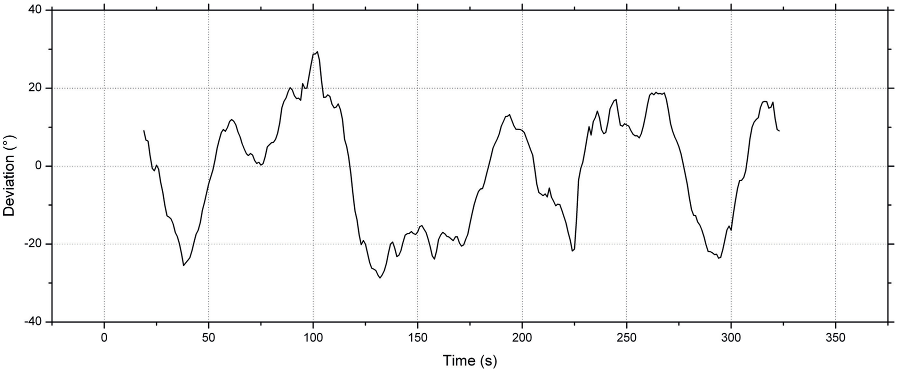

(b)

Figure 3.25: *Experiment 2: (a) Validation of the wind direction estimation and (b) the deviation of the reference to the measurement ((a) corrected with an offset due to a systematic error in the experiment setup). The data was averaged over the past 20s using a sliding window.*

Table 3.5: *MSE and RMSE of the wind vector estimation.*

Moving Average	Wind Speed				Wind Direction			
	Hovering		Flying		Hovering		Flying	
	MSE	RMSE	MSE	RMSE	MSE	RMSE	MSE	RMSE
	-	(ms^{-1})	-	(ms^{-1})	-	$(^\circ)$	-	$(^\circ)$
-	1.19	1.09	0.75	0.87	847.94	29.12	1002.47	31.66
$5s$	0.72	0.85	0.46	0.68	495.60	22.26	623.36	24.97
$10s$	0.50	0.71	0.29	0.53	315.26	17.76	353.06	18.79
$20s$	0.36	0.60	0.13	0.36	196.63	14.02	218.22	14.77

3.5 Development of the Robot Operating Software

The micro-drone does not provide the computational performance to autonomously control itself and to execute the gas source localization and gas distribution mapping algorithms presented in Ch. 5 to 8. Additional hardware on board connected to the control unit of the micro-drone would be needed to perform these tasks and to transmit the corresponding control sequences (e.g., *rpm* of the motors or waypoints). Another way would be to connect a computer via USB cable to the ground station and to introduce the corresponding control sequences in the uplink of the micro-drone. However, the limited flight time of the micro-drone and the already heavy gas-sensing payload (approx. $200g$ without gas transport solutions) do not allow to add further powerful hardware. Therefore, the second alternative was chosen.

Two different robot operating software with Graphical User Interface (GUI) were developed for the ground station within this Ph.D. thesis. The first software can be used to predefine a certain measurement campaign, whereas the second can be used to autonomously control the micro-drone. Both software use the method presented in Sec.3.5.1 to calculate new waypoints (GPS coordinates which can be uploaded to the micro-drone) based on the current position of the micro-drone and a given azimuth direction angle and distance (step size).

3.5.1 Waypoint Calculation

The following method is a part of the great circle navigation formulae and shows how to calculate a new waypoint $wp_2 = (\theta_2, \phi_2)$ based on the current position $wp_1 = (\theta_1, \phi_1)$, an azimuth direction angle δ, and a distance d from wp_1 to wp_2 (all values are given in radians):

$$\phi_2 = \sin^{-1}\left(\sin(\phi_1) \cdot \cos(d') + \cos(\phi_1) \cdot \sin(d') \cdot \cos(\delta)\right), \tag{3.16}$$

$$\begin{aligned}\theta_2 = (\theta_1 + \operatorname{atan2}(&\sin(\delta) \cdot \sin(d') \cdot \cos(\phi_1), \\ &\cos(d') - \sin(\phi_1) \cdot \sin(\phi_2)) + \pi) \bmod (2\pi) - \pi,\end{aligned} \tag{3.17}$$

where θ is the longitude of waypoint wp, ϕ is the latitude of waypoint wp, and $d' = d/6378137$ (the constant 6378137 is related to the World Geodetic System 1984 (WGS 84)). Eqs. 3.16 and 3.17 were taken from [123].

3.5.2 Measurement Campaign Software

The measurement campaign software makes it possible to define different measurement campaigns in the form of waypoint lists. Such a list can be uploaded to the micro-drone using the Airrobot software for the ground station. The start position, altitude, flight speed, orientation, residence time, and the step size in x- and y-direction of the micro-drone, as well as the search area size can be defined here. Additionally, an area coverage mode (sweeping, zigzagging, and spiraling) can be chosen. A dynamic change of the waypoint list cannot be applied since the list has to be downloaded, changed, and uploaded again. Furthermore, the time needed to upload a waypoint list – depending on the number of elements – is relatively high. However, it is possible to transmit a single waypoint with fewer parameters to the micro-drone. This approach is used in the following section.

3.5.3 Autonomous Control Software

Fig. 3.26 shows a screenshot of the robot operating software for the autonomous control of the micro-drone. It features the visualization of current measurement

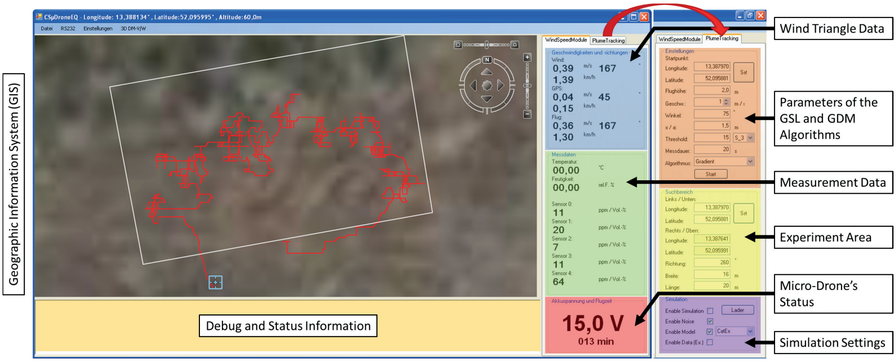

CSμDroneEQ - Longitude: 13,388134°, Latitude:52,095995°, Altitude:60,0m

Geschwindigkeiten und -richtungen
Wind:
0,39 m/s 167 °
1,39 km/h
GPS:
0,04 m/s 45 °
0,15 km/h
Flug:
0,36 m/s 167 °
1,30 km/h

Messdaten
Temperatur:
00,00 °C
Feutigkeit:
00,00 rel.F. %
Sensor 0:
11 ppm / Vol.-%
Sensor 1:
20 ppm / Vol.-%
Sensor 2:
7 ppm / Vol.-%
Sensor 3:
11 ppm / Vol.-%
Sensor 4:
64 ppm / Vol.-%

Akkuspannung und Flugzeit
15,0 V
013 min

Einstellungen
Startpunkt:
Longitude: 13,387970
Latitude: 52,095881
Flughöhe: 2,0 m
Geschw.: 1 m / s
Winkel: 75 °
x / a: 1,5 m
Threshold: 15 S_3
Messdauer: 20 s
Algorithmus: Gradient

Suchbereich
Links / Unten:
Longitude: 13,387970
Latitude: 52,095881
Rechts / Oben:
Longitude: 13,387641
Latitude: 52,095991
Richtung: 260 °
Breite: 16 m
Länge: 20 m

Simulation
Enable Simulation ☐
Enable Noise ☑
Enable Model ☑ CatEx
Enable Data (Ex.) ☐

Figure 3.26: *Screenshot of the robot operating software for the autonomous control of the micro-drone and the Google Earth Geographic Information System (GIS).*

data (wind-, ground-, and flight vector, temperature, humidity, concentration values, battery voltage, and flight time of the micro-drone), the visualization of the trajectory taken by the micro-drone and its current position, different control possibilities in form of the gas source localization (GSL) and gas distribution mapping (GDM) algorithms (Ch. 5 to 8), and the generation of new waypoints. Additionally, the start position, altitude, flight speed, orientation, residence time, the step size of the micro-drone, and the search area size can be defined here.

Fig. 3.27 shows the developed underlying system architecture of the autonomous control software. It was developed based on the sense-plan-act architecture [124] commonly used in robotics. A computer is connected via USB cable to the ground station. The ground station receives and routes correct received downlink data to the computer. Here, the software logs the received data and passes them to the Data Fusion Unit (DFU). The DFU stores the data in a large look-up table for the algorithms (Ch. 5 to 8) and fuses the data to estimate the wind vector (Sec. 3.4). The DFU also provides the GPS coordinates for the Geographic Information System (GIS). The GIS is based on Google Earth and shows the geographical data, the trajectory taken by the micro-drone, and its current position. Here, the area borders for the real-world experiments can be chosen by simple mouse click. The GIS and the DFU provide the necessary data for the algorithms. The decision where to perform a new measurement is made in the algorithm part and is based on past and current measurement data (gas concentration, wind vector, etc.) and the area the

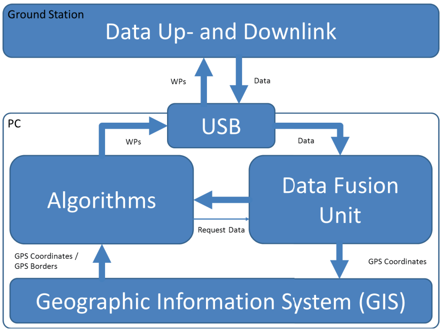

Figure 3.27: *System architecture of the autonomous control software.*

micro-drone already covered. The waypoints (WPs) are calculated and transmitted via USB to the uplink of the micro-drone. After correct reception, the micro-drone flies directly to this new waypoint.

3.6 Field Test: Gas Measurements in a Volcanic Crater

To validate and optimize the system for real-world application scenarios, a field test was carried out in the harsh conditions of a volcanic crater (Fig. 3.28) [Paper VII]. Area of operation was one of the craters in Timanfaya National Park on the Canary Island Lanzarote. Despite being inactive, gas emission was assumed at the bottom of the volcano. Lichen growing there showed different color in some areas, which might be an indicator of a gas impact. Wind and rocky terrain as well as the distance between micro-drone and pilot contributed to challenging operation conditions. The experiments' objective was to fly down to the bottom of the crater, land at the area of discolored lichen, perform regular gas measurements during the whole mission, and return to the starting point. All operation was to be carried out via remote control and the sensing data was to be transmitted and displayed in real time.

The experiment was performed successfully. During two consecutive flights the navigation and data transmission worked well and proved the capability of the system to operate in real-world conditions. The received remote sensing data showed low concentrations of SO_2, a typical volcanic gas, which likely explains the presence of the discolored lichen. SO_2 was detected also in other areas of the Timanfaya

Figure 3.28: *Field test in Timanfaya National Park (Lanzarote, Canary Islands).*

region. Besides the gas measurement data, GPS and altitude information were also transmitted as well as a video stream during the flight.

3.7 Summary and Conclusions

The combination of a micro-drone with chemical sensors to devise a mobile and flexible gas measurement device creates new possibilities in estimating the risk potential in a variety of scenarios without endangering people. Targeted fields of operation are gas measurements in accident scenarios, emission control, and monitoring of critical areas (including environmental monitoring tasks). This chapter describes a prototype of a gas-sensitive micro-drone and demonstrates its performance in a number of validation experiments. An important enhancement for gas source localization and gas distribution mapping is the possibility to estimate wind vectors without a dedicated anemometer (which would consume valuable payload) using only the micro-drone's on-board sensors. The proposed wind vector estimation approach was evaluated in a wind tunnel and field tests and constitutes a major improvement over existing systems (e.g., Pitot tube and any kind of anemometer) for a quadrocopter. Furthermore, robot operating software were developed for the ground station to autonomously control the micro-drone during the real-world experiments using one of the algorithms presented in the following chapters. The first software can be used to predefine measurement campaigns (e.g., to collect data for gas distribution mapping), whereas the second can be used to autonomously control the micro-drone based on the sense-plan-act scheme. The latter is mainly used for the gas source localization and gas distribution mapping algorithms.

Future work should include the improvement of data synchronization between IMU and GPS to minimize the error in the wind vector estimate. One way to achieve this could be to perform the involved calculations directly on-board the micro-drone to avoid any delay due to wireless communication and packet loss of the downlink of the micro-drone. In general, an extension of the wind vector estimation approach to 3D would provide valuable information for any 3D gas source localization and gas distribution mapping algorithm. This could be done by incorporating data of other sensors, such as the *rpm* of the rotors and the altitude data of the barometric pressure sensor. A modification of the gas transport design approaches to further improve the sensing capabilities of the micro-drone would be beneficial as well. This could be combined with an airflow model of the micro-drone to estimate a local concentration gradient when using more than one gas sensor.

It should be noted that it is the first time that a gas-sensitive micro-drone based on a quadrocopter has been developed. Therefore, it was necessary to gain experience in this new and challenging field of research, thus making the development effort to a significant part of this Ph.D. thesis.

Chapter 4

Setup of the Simulation Environment

The evaluation of algorithms for gas source localization and gas distribution mapping requires reliable ground truth information. Simulated data offers ground truth information and the possibility to repeat experiments under identical conditions [15]. Thus, large test sets can be run and simple debugging of the algorithms can be performed.

Gas distribution models developed for atmospheric dispersion such as CALPUFF, RIMPUFF, and PUFF-PLUME [120, 121] cannot capture all the relevant aspects of gas propagation with a sufficient level of detail [14] which make them unsuitable for simulation experiments with gas-sensitive mobile robots (and micro-drones). Instead, the filament-based gas dispersion model developed by Pashami et al. [15] is used. It combines flow simulation using standard Computational Fluid Dynamics (CFD) methods with the filament-based gas propagation model introduced by Farrell et al. [125]. The latter produces a challenging and physically plausible simulation model while achieving significant computational simplifications [125].

The simulation environment was developed and integrated in the autonomous control software (see Sec. 3.5.3) to benefit from the already existing GIS. The algorithms still carry out their computations based on real-world coordinates. Simply, the real-world coordinates must be transformed into the local coordinate system of the simulation data. The advantage of this approach is that it allows use of the same software implementation of the algorithms as on the real micro-drone.

The simulation setup includes a filament-based gas dispersion model (Sec. 4.1),

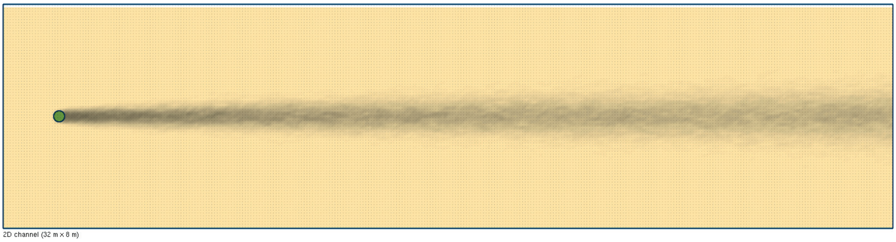

Figure 4.1: *Plume propagation in the simulated wind tunnel after* 99s.

a GPS model of the micro-drone (Sec. 4.2), a gas sensor model (Sec. 4.3), a simple disturbance model of the micro-drone (Sec. 4.4), a wind direction sensor model (Sec. 4.5), and functions to perform transformations between the global and local coordinate system (Appendix B).

4.1 Filament-Based Gas Dispersion Model

The complex interaction of gas with its surroundings is typically characterized by three physical effects: molecular diffusion, turbulence, and advection [15]. The filament-based gas dispersion model developed by Pashami et al. [15] takes all these effects into account. It simulates gas dispersion for compressible flows with a realistic turbulence model. The implementation of this model is divided into two parts: the flow simulation with OpenFOAM (see Sec. 4.1.1) and the filament-based gas dispersion approach introduced by Farrell et al. [125]. The results in [15] show that the plume generated in simulations is comparable to a real plume in a wind tunnel. Fig. 4.1 shows the plume propagation of one simulation experiment in a $32 \times 8m^2$ wind tunnel under predominantly laminar airflow.

4.1.1 OpenFOAM Flow Model

The OpenFOAM (Open Field Operation and Manipulation) CFD Toolbox is used to numerically solve the equations of fluid flow. The “rhoPisoFoam” solver for compressible, laminar, or turbulent flows was used within the simulation experiments.

4.1.2 Filament-based Gas Dispersion

The gas propagation model by Farrell et al. [125] simulates gas as a set of filaments ($i = 0, \ldots, N$), each containing a constant amount of molecules or particles $Q = 8.3 \times 10^9$. Filaments are defined by their position, $p_{i,t}$ and width, $R_{i,t}$.

In each time step t, the position of every filament is updated according to the wind flow $v_{i,t}$ and a stochastic process:

$$p_{i,\Delta t} = p_{i,t} + v_{p_{i,t}} \Delta t + \varepsilon_p, \tag{4.1}$$

where $v_{p_{i,t}}$ is the wind vector at position $p_{i,t}$. The stochastic component ε_p is a vector of three independent Gaussian random variables, $\mathcal{N}\left(0, \sigma_p^2\right)$, with standard deviation $\sigma_p = 0.1m$.

To model molecular diffusion, filaments become wider with time while their peak concentration decreases. The width of a filament evolves as

$$R_{i,t+\Delta t} = R_{i,t} + \frac{\gamma}{2R_{i,t}} \text{ with } \gamma = 4 \times 10^{-7}. \tag{4.2}$$

Here, the gas source releases 500 such filaments per second with an initial width of $R_{i,t} = 0.20m$. The filaments are uniformly distributed over the circular area of the source.

4.2 GPS Model

Based on the results of Sec. 3.1.1, the error of the GPS is simply modeled as a vector with samples of a non-zero-mean normal distribution with σ^2 set to 1.17:

$$\begin{pmatrix} x_m \\ y_m \end{pmatrix}_{\text{noise}} = \begin{pmatrix} \mathcal{N}\left(x_m, 1.17\right) \\ \mathcal{N}\left(y_m, 1.17\right) \end{pmatrix}, \tag{4.3}$$

where (x_m, y_m) is the position of the micro-drone.

4.3 Gas Sensor Model

The model of a perfect gas sensor is not suitable for realistic simulation experiments. Therefore, the simulation environment developed within this Ph.D. thesis was extended with a more realistic sensor model.

4.3.1 Sensor Response Experiment

In order to determine the responses of the different sensors used in the gas detector (IR – CO_2, Cat – CH_4, and EC – CO), the following experiment was performed: the gas detector was inserted in a calibration adapter which was connected to a trigger valve ($0.5l \cdot min^{-1}$) using a short flexible tube. A gas cylinder containing the corresponding calibration gas was attached to this trigger valve. During the experiments the gas detector was connected to a computer using a USB to IR converter. Measurements were recorded on the computer at a frequency of $1Hz$.

The following procedure was repeated for each sensor type: The trigger valve was opened until the sensor output reached a steady value. The gas detector was then removed from the calibration adapter and inserted into the active gas transport method in order to expose the sensor to “clean air”. The integrated small fan was used to speed up the sensor decay. The sensor readings were normalized to the interval $[0, 1]$ using Eq. 4.4 [14] in order to get the sensor response values r_i:

$$r_i = \frac{R_i - \min(R_i)}{\max(R_i) - \min(R_i)}, \tag{4.4}$$

where i is the sample index and R_i are the calibrated gas concentration measurements taken by the gas sensor used.

4.3.2 Sensor Model

The sensor model was developed in analogy to the one presented by Lilienthal and Duckett [126]. Here, the recorded sensor response values of each sensor were fitted to a first-order sensor model to model the sensor response as an exponential rise and decay. Fig.4.2 shows exemplarily the real gas sensor readings of the Cat gas sensor together with the fitted sensor model of the sensor response. As a comparison, Fig. 4.3(a) shows the fitted sensor model of the response of the IR gas sensor. Based on the experiment results (Fig. 4.3(b)), a sensor model (Eqs. 4.5 to 4.9) was developed which separates into four parts according to the four regions shown in Fig.4.2:

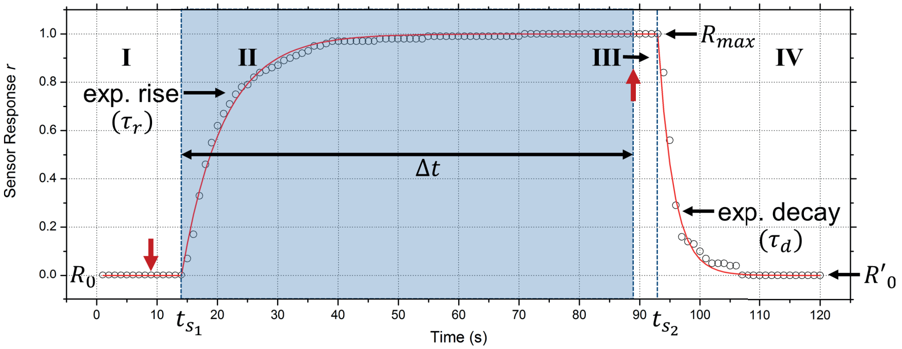

Figure 4.2: *Real gas sensor readings of the Cat gas sensor (circles) together with the fitted (first-order) sensor model of the sensor response (red line). The four regions of the applied model (Eqs. 4.5 to 4.9) are labeled with Roman numerals. The red arrows indicate the moments, where the trigger valve was opened and closed. The measurement values were normalized to the interval* $[0,1]$.

$$r(t) = \begin{cases} r_I(t) & \text{, if } t < t_{s1} \\ r_{II}(t) & \text{, if } t_{s1} < t < t_{s1} + \Delta t \\ r_{III}(t) & \text{, if } t_{s1} + \Delta t < t < t_{s1} + \Delta t + t_{s2} \\ r_{IV}(t) & \text{, if } t_{s1} + \Delta t + t_{s2} < t \end{cases} \tag{4.5}$$

$$r_I(t) = R_0 \tag{4.6}$$

$$r_{II}(t) = R_0 + (R_{max} - R_0) \cdot \begin{cases} (1 - e^{\frac{t - t_{s_1}}{\tau_r}}) & \text{(Cat and EC)} \\ \eta \cdot (1 - e^{-\frac{t - t_{s_1}}{\tau_{IR_1}}}) + (1 - \eta) \cdot (1 - e^{-\frac{t - t_{s_1}}{\tau_{IR_2}}}) & \text{(IR)} \end{cases} \tag{4.7}$$

$$r_{III}(t) = R_{max} \tag{4.8}$$

$$r_{IV}(t) = R'_0 + (R_{max} - R'_0) \cdot e^{-\frac{t - t_{s_1} - \Delta t - t_{s_2}}{\tau_d}}, \tag{4.9}$$

where

$$R_0 \leq R'_0 < R_{max}. \tag{4.10}$$

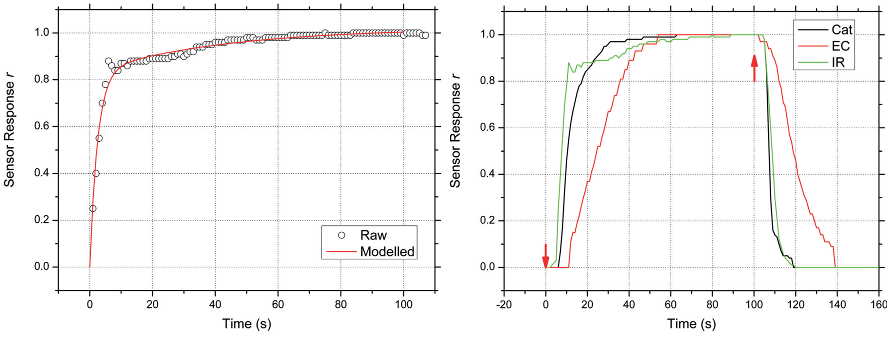

(a)

(b)

Figure 4.3: *(a) Sensor response of the IR gas sensor. The circles are the real gas sensor readings and the red line is the fitted sensor model of the sensor response. (b) Result of the sensor response experiment using the three different gas sensors (Cat, EC, and IR): the red arrows indicate the moments, where the trigger valve was opened and closed, respectively. The measurement values were normalized to the interval* $[0, 1]$.

The sensor model contains 8 and 10 adjustable parameters, respectively, for the different gas sensors (the parameters which are used only for the IR gas sensor model are marked with an asterisk): R_0 is the sensor response level before the sensor is exposed to the target gas, R_{max} is the response level after the sensor responded, and R'_0 is the response level after the sensor decayed. τ_r, $\tau_{IR_1}{}^*$, and $\tau_{IR_2}{}^*$ are the time constants of the sensor response, whereas τ_d is the time constant of the sensor decay. The constant η^* is used to modify the amplitude of both terms in Eq. 4.7. t_{s_1} is the time before the sensor started to respond, t_{s_2} is the time before the sensor started to decay, and Δt is the duration of the rising period. However, t_{s_1} and t_{s_2} were only considered at the beginning of each measurement period as they describe the time needed for the gas / air mixture to reach the gas-sensitive element of the sensor. Small fluctuations within one measurement period due to, e.g., varying measurement positions of the micro-drone (Sec. 4.2), were not delayed additionally.

The Levenberg-Marquardt algorithm [127] was used to fit the sensor model to the recorded response values in order to obtain the following parameters: τ_r, τ_{IR_1}, τ_{IR_2}, τ_d, and η. The parameters t_{s_1} and t_{s_2} were determined by subtracting the timestamps of the first sensor response and decay with the timestamp when the trigger valve was opened and closed, respectively. Table 4.1 contains the results of

Table 4.1: Gas sensor model parameters.

		Cat		EC		IR	
		Response	Decay	Response	Decay	Response	Decay
τ_r in (s)	Value	7.0126	-	16.1812	-	-	-
	σ	0.0199	-	0.0014	-	-	-
τ_{IR_1} in (s)	Value	-	-	-	-	2.4958	-
	σ	-	-	-	-	0.1001	-
τ_{IR_2} in (s)	Value	-	-	-	-	42.5273	-
	σ	-	-	-	-	7.4442	-
τ_d in (s)	Value	-	2.8862	-	14.2792	-	4.1862
	σ	-	0.0663	-	0.3292	-	0.0940
η	Value	-	-	-	-	0.8312	-
	σ	-	-	-	-	0.0128	-
$1-\eta$	Value	-	-	-	-	0.1911	-
	σ	-	-	-	-	0.0090	-
t_{s_1} in (s)		5	-	10	-	4	-
t_{s_2} in (s)		-	4	-	7	-	4
MSE		0.0266	0.0377	0.1528	0.1878	0.0318	0.0523

the parameter estimation.

4.4 Simple Disturbance Model

To model the disturbances of the rotors on both the measurements and the involved dilution of the gas / air mixture (i.e., the stirring of the surrounding air by the rotors), the gas concentration values are simply averaged at the measurement position given by the filament-based gas dispersion model (Sec. 4.1) within a radius of $0.5m$ before applying the gas sensor model (Sec. 4.3). The radius of $0.5m$ corresponds to the radius of the micro-drone. Therefore, the result of a measurement at the plume boundary is reduced significantly as the rotors dilute the gas with the surrounding "clean air" (many low and zero concentration values can be found close to the plume boundary). Accordingly, results of measurements directly inside the plume are not influenced so much as many high concentration values can be found in the close vicinity of that measurement position.

4.5 Wind Direction Sensor Model

The wind sensor is modeled as a perfect sensor with the option to add noise to the directional component. The noise is added using samples of a zero-mean normal distribution ($\mathcal{N}\left(0, \sigma_\theta^2\right)$):

$$(\theta_u)_{\text{noise}} = \left(\theta_u + \mathcal{N}\left(0, \sigma_\theta^2\right)\right) \bmod 360^\circ, \tag{4.11}$$

where θ_u is the available wind direction in the simulation data. The noisy wind direction $(\theta_u)_{\text{noise}}$ is rotated into the local coordinate system of the simulation environment. The wind speed r_u is not distorted additionally with noise.

To model the circular variance S_0 (Appendix A), i samples of a zero-mean normal distribution are drawn ($\mathcal{N}\left(0, \sigma_{S_0}^2\right)$) with a frequency of $1Hz$ over the measuring time ΔT. $\sigma_{S_0}^2$ is set to 23.08, which corresponds to the average variance of single wind measurements taken with the micro-drone in real-world experiments. Finally, S_0 is calculated using Eq. A.3, which is relevant for the algorithm presented in Ch. 6.

4.6 Summary and Conclusions

This chapter described the simulation environment which was set up to run experiments on simulated data. Simulated data provides ground truth information and the possibility to repeat experiments under identical conditions [15]. Thus, large test sets can be run and simple and fast debugging of the algorithms is supported. However, despite all the effort spent on the simulation environment, it still constitutes a significant simplification of real conditions and makes real-world experiments an essential part of the validation process of new algorithms. Future work should address the influence of the micro-drones' rotor movement on gas dispersion and an extension to the 3rd dimension.

Chapter 5

Plume Tracking Implemented on a Micro-Drone

This chapter presents the development of three bio-inspired plume tracking algorithms for the gas-sensitive micro-drone: the surge-cast algorithm (a variant of the silkworm moth algorithm) [2], the zigzag / dung beetle algorithm [3], and a newly developed algorithm called “pseudo gradient algorithm” [Paper IV, Paper IX]. The algorithms were developed under the assumption that an arbitrary rectangular search area defined by four GPS coordinates and a main search direction are given. They were successfully tested in simulations and real-world experiments with the micro-drone equipped with the e-nose. At this point, it should be highlighted again that it is the first time that real-world plume tracking experiments with a gas-sensitive micro-drone were completed successfully in a setup where no artificial conditions were introduced to simplify the experiments.

Note that next measuring positions are calculated by the method introduced in Sec. 3.5.1, which requires the current position of the micro-drone, an azimuth direction angle, and a defined step size. The minimum step size and the minimum flight speed of the micro-drone are limited to $1m$ and $1ms^{-1}$, respectively, which also had to be considered in the development process. Because of the constraints given by the micro-drone operated in waypoint mode and to take the slow response times of the used gas sensors into consideration, the micro-drone is stopped at each calculated position to collect gas and wind measurements for a specified measurement time and reject samples taken in between the stops.

The remainder of this chapter firstly describes three bio-inspired plume tracking algorithms (Sec. 5.1) and their modifications to be used in combination with the micro-drone. Next, the performance of the three plume tracking algorithms are compared with each other in simulations under controlled environmental conditions and to the work by Lochmatter [2, 12] (Sec. 5.2). Finally, real-world experiments are performed. The results are compared with each other and again to the work by Lochmatter (Sec. 5.3) and conclusions are drawn (Sec. 5.4).

5.1 Gas Source Localization

As stated in [28], reactive gas source localization algorithms can be separated into three phases: 1. plume acquisition (finding the plume), 2. plume tracking (moving the robot guided by the gas plume), and 3. source declaration (predicting the most likely location of the emitting source and deciding that a source has been found). The focus of this chapter lies on the first two phases: plume acquisition and plume tracking. Sec. 5.1.3 offers a suggestion how to solve the source declaration phase.

The first two algorithms presented in this section use only binary gas information from the sensor, i.e., they detect either the presence or absence of the target gas. Different gas concentration levels are ignored. To obtain this binary value, the average measured gas concentration is thresholded. Using binary gas information helps to mitigate calibration issues with the gas sensors. However, more sophisticated algorithms could be used to detect the presence or absence of the target gas. Since gas molecules emitted in natural environments are carried by the wind to form a plume, measuring the wind direction gives valuable information about the gas source location. The wind speed, on the other hand, is ignored.

5.1.1 Plume Acquisition

Possible plume acquisition strategies to make contact with the plume are passive monitoring of the environment and active exploration strategies. The passive strategy is to wait until the sensors of the mobile robot detect a concentration level of the target gas above a certain threshold. This indeed can minimize the energy consumption of, e.g., ground-based mobile robots. However, in the case of a micro-drone, where the energy consumption for the hovering of the micro-drone is high, the passive strategy is not feasible. Instead, an active exploration strategy has to be used, for example, a randomized (e.g., random walk) or systematic search (e.g., move the mobile robot orthogonally to the wind direction). Here, the following systematic search algorithm, called *sweeping*, was implemented and used for the three plume tracking algorithms:

- collect gas sensor and wind measurements while keeping the micro-drone at a fixed position for a prolonged time (here: $20s$);
- average the gas concentration and wind measurements over the measurement time;
- if the averaged gas concentration $\bar{c}$ is below a given threshold th_c ($\bar{c} \leq th_c$), make a step orthogonal to the wind direction[1]: if this new position is outside the search space, calculate an alternative position in upwind direction (make one step in upwind direction[2]) and change the sweeping direction;
- if the averaged gas concentration $\bar{c}$ is above a given threshold th_c ($\bar{c} > th_c$), change to the plume tracking phase;
- repeat using the first step.

5.1.2 Plume Tracking

All three presented plume tracking algorithms are based on two principles: chemotaxis and anemotaxis (Sec. 2.2). Fig. 5.1 shows a good comparison of typical trajectories created by the three reactive plume tracking algorithms discussed here.

5.1.2.1 Surge-Cast Algorithm

Lochmatter and Martinoli presented the *surge-cast* algorithm in [2]. It is a combination of plume tracking strategies used by the silkworm moth:

- **Upwind surge**: straight upwind movement as long as the moth is in the plume.
- **Casting**: side-to-side searching (zigzagging) to reacquire the plume after losing contact.

---

[1] Alternatively the search direction could be used if the wind is very variable (unstable).

[2] If the new point still remains outside the search space, calculate an alternative position using the search direction instead. This ensures that the micro-drone stays within the search space.

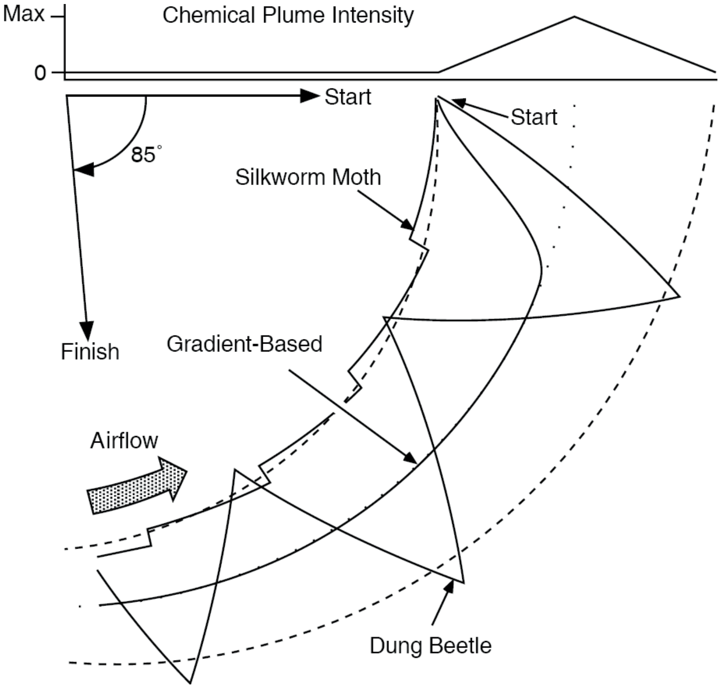

Figure 5.1: *Comparison of the trajectories of three reactive plume tracking algorithms obtained from simulation: the start and finish positions of the robot are shown with arrows, and the plume, including centerline, is traced by dotted lines (from Russell et al. [44]).*

- **Spiraling**: an irregular, spiral-like movement if casting failed to reacquire the plume.

The basic algorithm works as follows: The robot moves straight upwind until it loses contact with the plume for a certain distance d_{lost}. Then it tries to reacquire the plume by searching crosswind for a defined distance d_{cast} on both sides. The chance of reacquiring the plume in the first crosswind movement is maximized by measuring the wind direction to estimate on which side the robot has left the plume. Every time the robot switches its behavior from upwind surge to casting and vice versa, the wind direction is re-measured.

The *surge-cast* algorithm for the micro-drone works as follows:

- collect gas sensor and wind measurements while keeping the micro-drone at a fixed position for a prolonged time (here: $20s$);

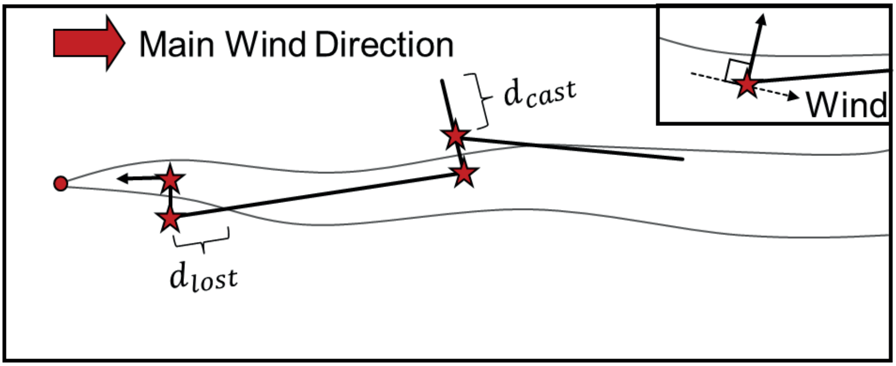

Figure 5.2: *Illustration of the surge-cast algorithm. The stars indicate the positions where the wind direction is measured, whereas the gas concentration is measured continuously. The plume is traced by the gray solid lines and the source is indicated by the red dot. The red arrow illustrates the main wind direction. The figure was adapted from Lochmatter and Martinoli [2].*

- average the gas concentration and wind measurements over the measurement time;
- if the averaged gas concentration $\bar{c}$ is above the threshold th_c ($\bar{c} > th_c$), perform an upwind surge (move the micro-drone one step straight forward in wind direction);
- if the averaged gas concentration $\bar{c}$ is below the threshold th_c ($\bar{c} \leq th_c$), carry out casting in crosswind direction with increasing step size: *# no detection events* × *step size* (return to sweeping, if no concentration was detected after a defined number of steps)
- repeat using the first step.

Instead of considering the distance d_{lost} in the algorithm, the plume is declared lost in the surge-cast algorithm used here when the micro-drone measures an average gas concentration below the threshold th_c at a certain position (after one step). The distance d_{cast} is defined as a multiple of the step size to take account of the minimum step size of the micro-drone of $1m$. Furthermore, the wind is remeasured in every iteration of the algorithm to adapt faster to changing wind conditions.

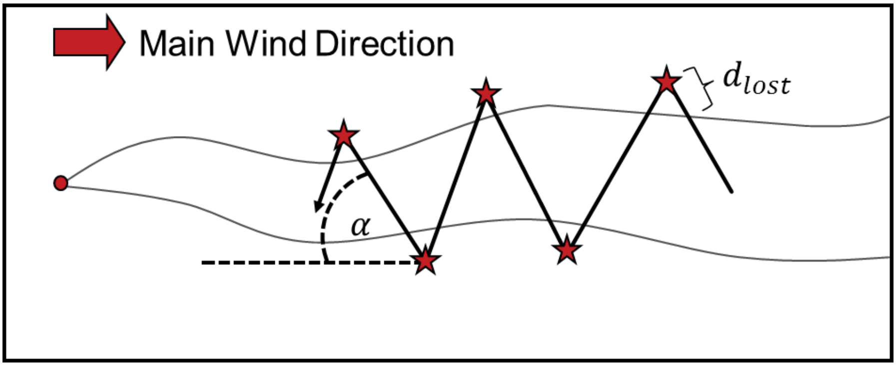

Figure 5.3: *Illustration of the zigzag algorithm introduced by Ishida et al. [3]. The plume is traced by the gray solid lines and the source is indicated by the red dot. The red arrow illustrates the main wind direction. The stars indicate the positions where the wind direction is measured, whereas the gas concentration is measured continuously.*

5.1.2.2 Zigzag/Dung Beetle Algorithm

The zigzag or dung beetle algorithm was first reported by Ishida et al. [3]. The basic algorithm works as follows: The robot moves upwind at an angle α (e.g., $\alpha = 60°$) across the plume. If the gas sensor measures a concentration below a given threshold th_c, the robot is assumed to have reached the edge of the plume. It remeasures the wind direction and continues moving upwind at an angle $-\alpha$ with respect to the upwind direction. This procedure is repeated causing the robot to move in a zigzag fashion within the plume. The robot is stopped when it has reached the source. A sample trajectory can be seen in Fig. 5.3.

During the experiments in [3] the delay of the gas sensor response was considered indirectly by slowing down the movement of the robot to $0.002ms^{-1}$. However, the slowest flight speed of the micro-drone can be set to $1ms^{-1}$. In order to consider the delay of the gas sensor response and the inaccuracies given by the indirect measuring principle of the wind presented in Ch. 3, the following *zigzagging* algorithm was developed in analogy to the one presented in [3]. The algorithm changes its behavior from sweeping into zigzagging once the averaged gas concentration $\bar{c}$ is above the threshold th_c.

- collect gas sensor and wind measurements while keeping the micro-drone at a

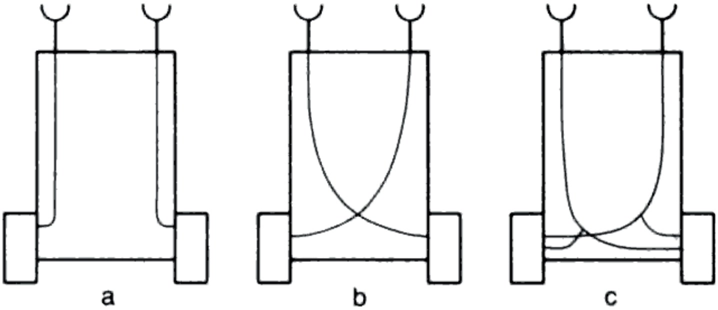

Figure 5.4: *Illustration of the Braitenberg vehicle type 2 with two motors and two sensors. Each sensor connected to (a) the motor on the same side, (b) the motor on the opposite side (cross coupling), and (c) both motors. The figure was extracted from Braitenberg [128].*

fixed position for a prolonged time (here: $20s$);

- average the gas concentration and wind measurements over the measurement time;
- if the averaged gas concentration $\bar{c}$ is above the threshold th_c ($\bar{c} > th_c$) or the new position after the movement of the micro-drone is outside the search space, set α to $-\alpha$;
- if the averaged gas concentration $\bar{c}$ is below the threshold th_c ($\bar{c} \leq th_c$) for a predefined number of steps, return to sweeping;
- turn the micro-drone $\alpha°$ from upwind direction and move a step forward;
- repeat using the first step.

The upwind angle α has a major influence on the performance of the zigzag algorithm [2, 12]. The performance decreases with increasing α resulting in a high distance overhead as the robot has to turn more often at the plume boundaries to stay within the plume. On the other hand it becomes more robust. Small angles result in a low distance overhead but cause the algorithm to decrease its robustness as it might lose the plume easily.

5.1.2.3 Pseudo Gradient Algorithm

The idea for the first gradient-based algorithms for plume tracking goes back to Braitenberg [128]. The chemical gradient is measured by a pair of bilateral gas sensors mounted on each side of a robot, each directly controlling the speed of a wheel. Each sensor is connected to (a) the motor on the same side, (b) the motor on the opposite side (cross coupling), or (c) both motors. Although it was a purely chemotactic approach, a Braitenberg-style robot is able to track a plume towards a gas source by following the concentration gradient [65]. Fig. 5.1 shows a sample trajectory. A representative algorithm is as follows [28]:

- Turn clockwise in proportion to the concentration difference. A negative value indicates a counterclockwise turn. The magnitude of the turn is limited to ±16°);
- Move forward $0.02m$;
- Repeat using step one.

As no wind information is considered in this algorithm, the robot does not know whether it is following a plume towards or away from its source. Turning the robot in proportion to the concentration gradient in dependence of the upwind direction solves this problem [44]. As the rotors of the micro-drone introduce strong disturbance, measuring a local concentration gradient with spatially separated sensors is not feasible. Instead a new measuring strategy was developed, which basically splits up one measuring position into two spatially separated ones. In order to respect the minimum step size of the micro-drone of $1m$ and to progress faster to the source, the step size in upwind direction d_{up} was set to $d_{cross} + d_{cross}/2$. After the gas sensor has detected a concentration above a threshold th_c, the following procedure is repeated [Paper IV, Paper IX]:

- collect gas sensor and wind measurements while keeping the micro-drone at position p_1 for a prolonged time (here: $20s$);
- calculate the averaged gas concentration $\bar{c}_{p_1}$ and wind direction $(\bar{\theta}_u)_{p_1}$ over the measurement time;
- make a step orthogonal to the wind direction (the direction of the first cross-wind step is given by the current sweeping direction);

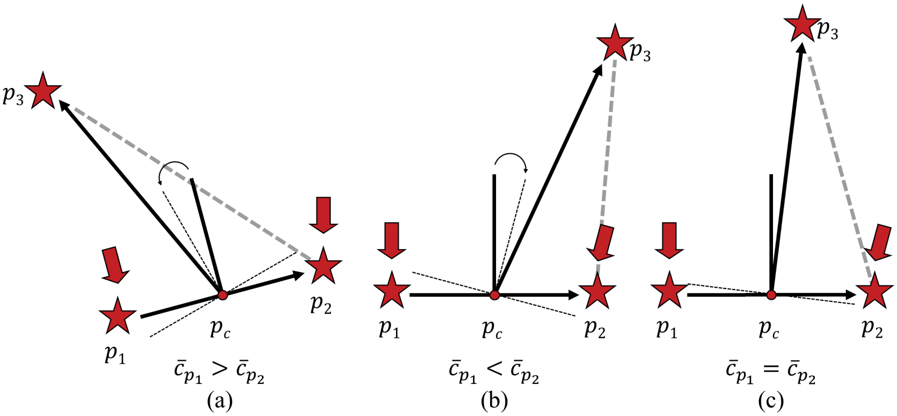

Figure 5.5: *Three different cases of the pseudo gradient algorithm: (a)* $\bar{c}_{p_1} > \bar{c}_{p_2}$*, (b)* $\bar{c}_{p_1} < \bar{c}_{p_2}$*, and (c)* $\bar{c}_{p_1} = \bar{c}_{p_2}$*. The case* $\bar{c}_{p_1} = \bar{c}_{p_2} = 0$ *restarts the plume acquisition phase. The red stars indicate the measuring positions, the red arrows illustrate the averaged wind directions, and the gray dotted line is the flight path of the micro-drone.*

- collect gas sensor and wind measurements while keeping the micro-drone at position p_2 for a prolonged time;
- calculate the averaged gas concentration $\bar{c}_{p_2}$ and wind direction $(\bar{\theta}_u)_{p_2}$ over the measurement time;
- calculate the *pseudo* concentration gradient (a concentration below the threshold $\bar{c} < th_c$ will be set to 0; if $\bar{c}_{p_1} = \bar{c}_{p_2} = 0$, the direction of the crosswind movement is inverted and sweeping is restarted):

$$grad(\bar{c}_{p_1}, \bar{c}_{p_2}) = \frac{\bar{c}_{p1}}{\bar{c}_{p_1} + \bar{c}_{p_2}},\ grad(\bar{c}_{p_1}, \bar{c}_{p_2}) \in [0, 1]$$

- if $grad(\bar{c}_{p_1}, \bar{c}_{p_2}) > 0.5$, set β to $-\beta$, invert the direction of the crosswind movement, and calculate the new measuring position p_3 based on the averaged wind direction determined at position p_1 and the center position p_c using the equations in Sec. 3.5.1 (see Fig. 5.5(a)):

$$\delta = (\bar{\theta}_u)_{p_1} + \beta \cdot 2 \cdot (grad(\bar{c}_{p_1}, \bar{c}_{p_2}) - 0.5),$$

  where β denotes the maximum upwind angle the micro-drone can take.

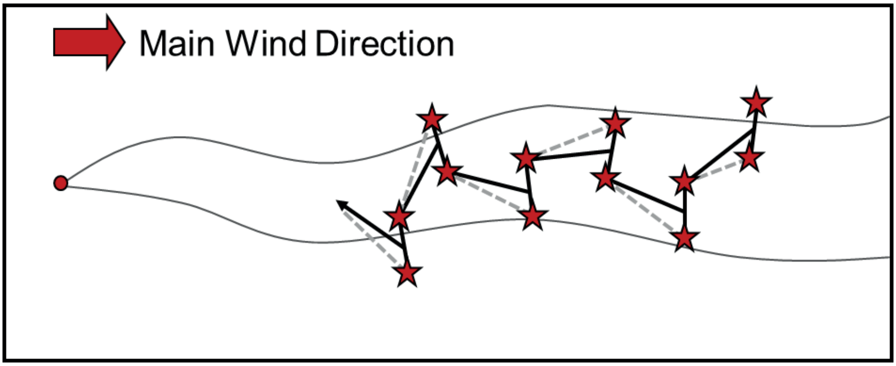

Figure 5.6: *Idealized sample trajectory of the pseudo gradient algorithm. The red stars indicate the measuring positions, whereas the source is indicated by the red dot. The plume is traced by the gray solid lines and the gray dotted line is the flight path of the micro-drone. The red arrow illustrates the main wind direction.*

- if $grad(\bar{c}_{p_1}, \bar{c}_{p_2}) < 0.5$, calculate the new measuring position p_3 based on the averaged wind direction determined at position p_2 and the center position p_c (see Fig. 5.5(b)):

$$\delta = (\bar{\theta}_u)_{p_2} + \beta \cdot 2 \cdot (1 - grad(\bar{c}_{p_1}, \bar{c}_{p_2}) - 0.5)$$

- if $grad(\bar{c}_{p_1}, \bar{c}_{p_2}) = 0.5$, calculate the new measuring position p_3 based on the averaged wind direction of both measuring points p_1 and p_2 and the center position p_c (see Fig. 5.5(c)):

$$\delta = (\bar{\theta}_u)_{p_1, p_2}$$

- fly the micro-drone autonomously directly from position p_2 to position p_3 and repeat using the first step.

Fig. 5.6 shows a sample trajectory of the pseudo gradient algorithm.

5.1.3 Source Declaration

In recent work, the problem of gas source declaration has often been ignored and replaced in experiment trials by establishing that the mobile robot reached a predefined proximity to the known location of the gas source. This was performed visually by a human observer [28]. First approaches without human interaction were suggested, e.g., in [13, 77, 78, 86, 129–132]. For example, Li sent his REMUS AUV on cloverleaf trajectories to estimate the source location [132]. His source declaration module uses the six most recent detection points to calculate a bounding box using three of the six most upstream locations. When the diameter of the box become small enough, the source is assumed to be found and the center of the box was used to estimate its location. Due to the navigation system's relative inaccuracy of the REMUS AUV, the location estimate was only accurate a few dozen meters. The source declaration phase is not considered within this chapter, but can be done using the particle filter-based gas source localization algorithm presented in Sec. 6.

5.2 Simulation Experiments

Simulations were performed in order to determine the performance ($\hat{=}$ distance overhead) and robustness ($\hat{=}$ success rate) of each plume tracking algorithm under repeatable conditions using the simulation environment presented in Ch. 4.

5.2.1 Experiment Environment and Setup

The experiment area is a simulated wind tunnel with a size of $32 \times 8m^2$. The flow speed in the wind tunnel was set to $0.5ms^{-1}$. A circular gas source with a radius of $0.2m$ was placed in the experiment area at position $(2, 4)m$. In each run the micro-drone was started inside the plume approximately at position $(31, 4)m$ about $29m$ downwind from the source. The step size was set to $1m$ to model the system characteristics of the micro-drone. The IR gas sensor model was used to simulate the sensor response (Sec. 4.3). The simple disturbance model (Sec. 4.4) and the GPS model (Sec. 4.2) of the micro-drone were used as well. The measuring time at each sampling location was set to $20s$ with a sampling frequency of $1Hz$, and the threshold th_c was set to 0.05 (the concentration data was normalized before usage). The parameter α of the zigzag algorithm and the parameter β of the pseudo gradient algorithm were successively set to 15°, 30°, 60°, and 75° (zigzag) and 30°, 60°, and 90° (pseudo gradient). The wind sensor noise σ_θ^2 (Sec. 4.5) was variable during all sets of experiments, and a total of 100 runs were performed for each value of $\sigma_\theta^2 \in \{0.00, 14.02, 17.76, 22.26, 29.12, 60.00, 90.00\}$, where 14.02°, 17.76°, 22.26°, and 29.12° correspond to the RMSE of the wind vector estimation of the hovering

Table 5.1: *Configurations of the different sets of the plume tracking simulation experiments.*

Set	Algorithm	Parameter	Wind Sensor Noise σ_θ^2	Runs
1	Surge-Cast	-	variable	700
2	Zigzag	$\alpha = 15°$	variable	2,800
3		$\alpha = 30°$		
4		$\alpha = 60°$		
5		$\alpha = 75°$		
6	Pseudo Gradient	$\beta = 30°$	variable	2,100
7		$\beta = 60°$		
8		$\beta = 90°$		

micro-drone using different averaging times (Sec. 3.4.3). Thus, a total of 700 runs were performed for each set of experiments (Table 5.1).

A run was considered successful if the micro-drone reached a $1.5 \times 2m^2$ large area centered in front of the source, and unsuccessful if the robot touched an arena wall or passed the target area. This stop criterion was chosen in a way that the micro-drone stopped almost in front of the gas source. Furthermore, the step size constraint of $\geq 1m$ does not allow the micro-drone to track a small scale plume. The plume width at the source location has approximately the same width as the source itself (here: $\varnothing = 0.4m$). Therefore, it is most likely that the micro-drone jumps over the plume without detecting a concentration level above the threshold. This is also the reason why larger step sizes of the micro-drone were not investigated.

5.2.2 Experiment Results

A total of 5,600 runs were performed for the three plume tracking algorithms. A sample trajectory of a successful run for each algorithm can be seen in Fig. 5.7.

The results of the surge-cast algorithm are shown in Fig. 5.8. The performance of this algorithm is fairly good. The distance overhead of the algorithm is ≤ 1.5 for $\sigma_\theta^2 \leq 29.12$ and it seems that the wind sensor noise has only a marginal influence on the performance of the algorithm as long as the error does not exceed $\sigma_\theta^2 > 29.12$. However, the wind sensor noise greatly affects the success rate. Reasonable success rates above 90% were only obtained up to a wind sensor error of $\sigma_\theta^2 = 22.26$. A success rate of 100% was only achieved with a wind sensor error of $\sigma_\theta^2 = 0.00$.

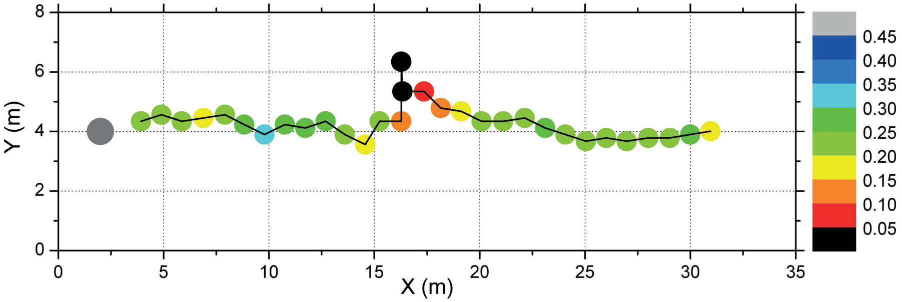

(a) Surge-cast

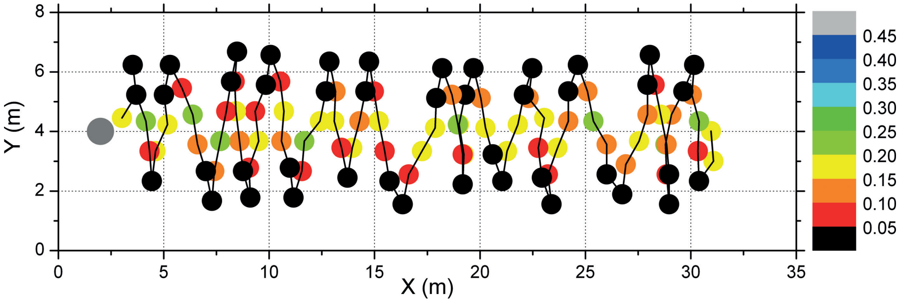

(b) Zigzag; $\alpha = 75°$

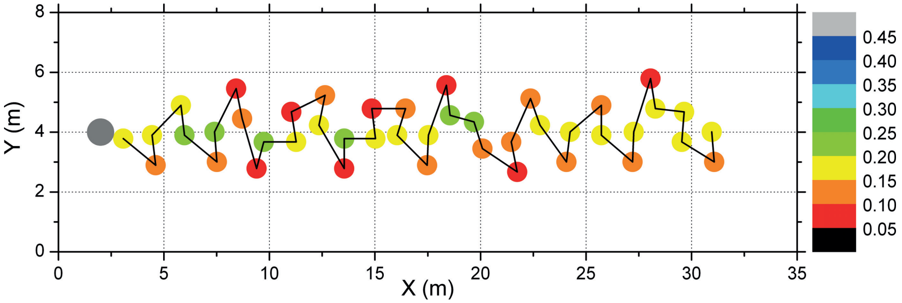

(c) Pseudo Gradient; $\beta = 90°$

Figure 5.7: *Trajectories of successful simulation runs of all three plume tracking algorithms with* $\sigma_\theta^2 = 14.02$. *The source is indicated by the large gray circle at position* $(2, 4)m$. *The smaller colored circles show the measured concentration at the sampling locations.*

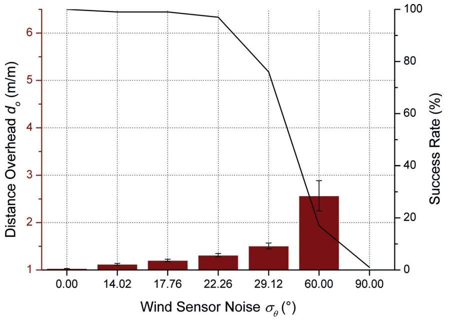

Figure 5.8: *Simulation results obtained using the surge-cast algorithm. The error bars indicate the confidence interval with 95% confidence level for the mean (assuming normally distributed data). The last bar is omitted because no run was successful here.*

Fig. 5.9 presents the results of the zigzag algorithm. The performance of this algorithm depends heavily on its parameter α (upwind angle): small upwind angles result in a small distance overhead but also in a low success rate, whereas a large angle significantly increases the success rate and the distance overhead at the same time as the micro-drone has to turn more often at the plume boundaries to stay within the plume. Thus, the upwind angle α presents a tradeoff between robustness and performance of this algorithm and has to be chosen carefully. Again it seems that the wind sensor noise has only a small influence on the performance of the algorithm. Reasonable results with high success rates ($> 90\%$) up to a wind sensor error of $\sigma_\theta^2 = 29.12$ were only obtained with $\alpha = 60°$ and $75°$. Success rates of 100% were achieved with $\alpha = 60°$ and $75°$ up to a wind sensor error of $\sigma_\theta^2 = 22.26$.

The results of the pseudo gradient algorithm are presented in Fig. 5.10. The parameter β has only a minor influence on the performance and the success rate of the algorithm. The value of β should not be too small as a small angle probably prevents the micro-drone from reacquiring the plume if lost. The wind sensor noise seems to affect mainly the success rate of the algorithm. Reasonable results with high success rates ($> 90\%$) up to $\sigma_\theta^2 = 29.12$ were obtained with β set to 60° and 90°. Success rates of 100% were achieved with $\beta = 90°$ up to a wind sensor error of $\sigma_\theta^2 = 17.76$.

Fig. 5.11 shows a summary of the obtained simulation results of all three algorithms with $\sigma_\theta^2 = 14.02$. It can be seen that the zigzag algorithm with $\alpha = 15°$ and the surge-cast algorithm have the best distance overhead (1.07±0.05 and 1.12±0.10),

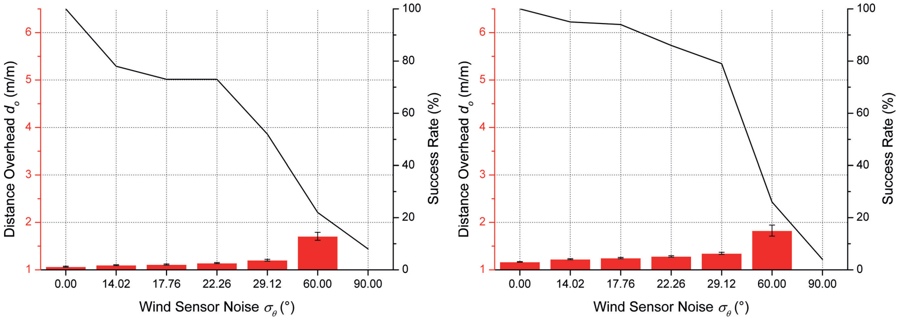

(a) $\alpha = 15°$ (b) $\alpha = 30°$

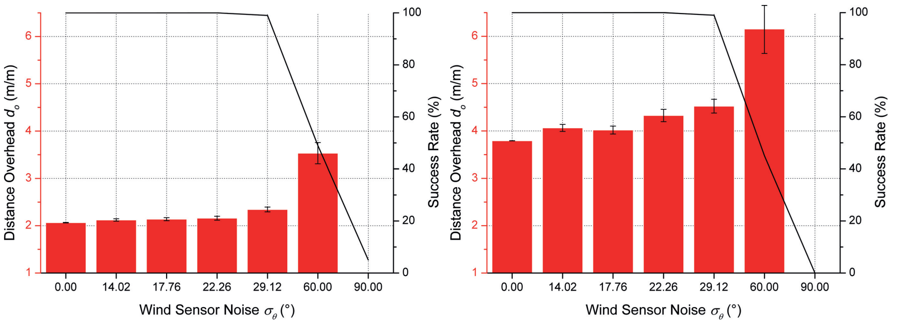

(c) $\alpha = 60°$ (d) $\alpha = 75°$

Figure 5.9: *Simulation results obtained using the zigzag (casting) algorithm with α (upwind angle) set to (a) 15°, (b) 30°, (c) 60°, and (d) 75°. The error bars indicate the confidence interval with 95% confidence level for the mean (assuming normally distributed data). The last bar is omitted in each bar plot because of the small number of successful runs.*

followed by the zigzag algorithm with $\alpha = 30°$ (1.23 ± 0.06). The pseudo gradient algorithm has a distance overhead of 1.81 ± 0.05 ($\beta = 30°$), 1.91 ± 0.08 ($\beta = 60°$), and 2.04 ± 0.15 ($\beta = 90°$) and lies in the medium range, followed by the zigzag algorithm with $\alpha = 60°$ (2.12 ± 0.13) and $\alpha = 75°$ (4.06 ± 0.38). Therefore, the zigzag algorithm with $\alpha = 15°$ and 30° and the surge-cast algorithm are the most efficient algorithms within this comparison, but also the least robust ones. Even with a small wind sensor error of only $\sigma_\theta^2 = 14.02$, they are not able to reach success rates of 100%. High robustness and reasonable distance overheads are given by the pseudo gradient algorithm and the zigzag algorithm with $\alpha = 60°$. The zigzag algorithm with $\alpha = 75°$ offers the highest robustness but produces the worst distance

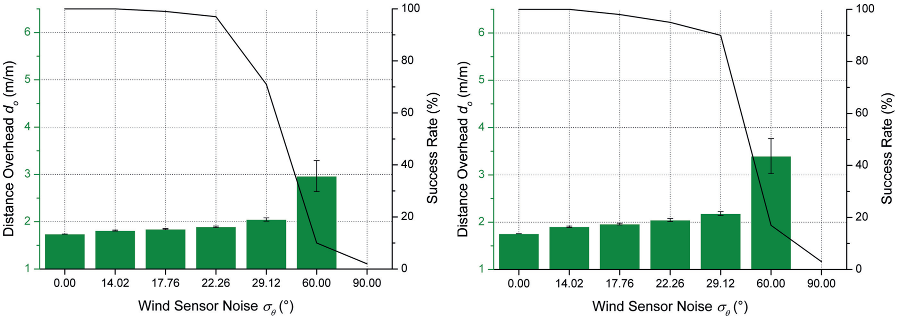

(a) $\beta = 30°$ (b) $\beta = 60°$

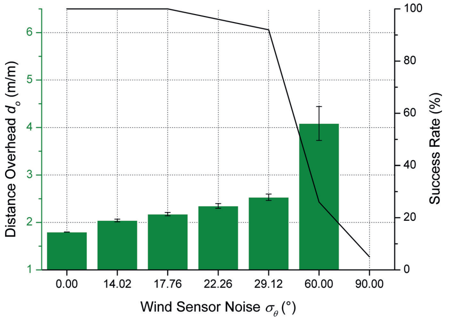

(c) $\beta = 90°$

Figure 5.10: *Simulation results obtained using the pseudo gradient algorithm with β set to (a) 30°, (b) 60°, and (c) 90°. The error bars indicate the confidence interval with 95% confidence level for the mean (assuming normally distributed data). The last bar is omitted in each bar plot because of the small number of successful runs.*

overhead in this comparison.

Lochmatter [2, 12] also performed 1,350 simulated runs for pure casting (zigzag), surge-spiraling, and surge-casting using a realistic Webots[3] simulation environment extended with a simple advection model and the filament-based gas dispersion model by Farrell et al. [125] (the same model as presented in Ch. 4). The experiments were performed over an area of $16 \times 4m^2$. In each run, the robot was released in the plume at a position about $14.5m$ downwind from the source. A run was considered successful if the robot reached the source, and unsuccessful if the robot touched an arena wall.

---

[3] Webots is a commercial realistic robotic simulator.

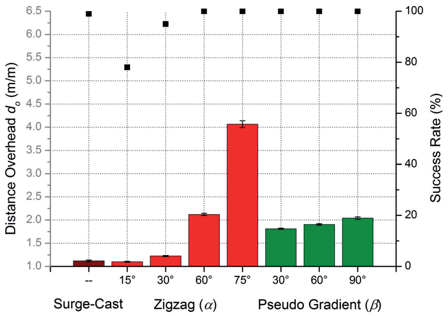

Figure 5.11: *Comparison of the obtained simulation results of all three algorithms with* $\sigma_\theta^2 = 14.02$*. The error bars indicate the confidence interval with* 95% *confidence level for the mean (assuming normally distributed data).*

For the surge-cast algorithm Lochmatter showed that choosing the cast distance d_{cast} too small, lets the algorithm fail as the robot could not reacquire the plume. The results presented here are comparable with the results he obtained at cast distances of approximately $0.61m$ (Fig. 5.12(a)). The behavior of the distance overhead and success rate of the surge-cast algorithm with increasing wind sensor noise are also comparable with the results from Lochmatter (Fig. 5.12(b)). However, Lochmatter demonstrated that casting for plume reacquisition is faster than spiraling if reliable wind direction information is available, but less robust. Therefore, additional robustness was added to the current implementation of the algorithm presented here by increasing the cast distance until the plume is found or the number of *no detection events* exceeds a predefined number.

For the casting algorithm, Lochmatter demonstrated that the upwind angle α has a major influence on the performance and that choosing this parameter is a tradeoff between performance and robustness, which confirms the results presented here. Acceptable success rates were only achieved with $\alpha \geq 20°$. The results presented here are comparable with the results he obtained at upwind angles of 15°, 30°, and 45° (correlates with the results presented here with $\alpha = 60°$; Fig. 5.12(c)). The behavior of the distance overhead and success rate of the zigzag algorithm with increasing wind sensor noise is also comparable with the results from Lochmatter (Fig. 5.12(d)). Additionally, he showed that "the accuracy of the wind sensor only has a marginal impact on the performance, and no visible influence on the robustness as long as the accuracy is below a certain threshold". However, pure casting would

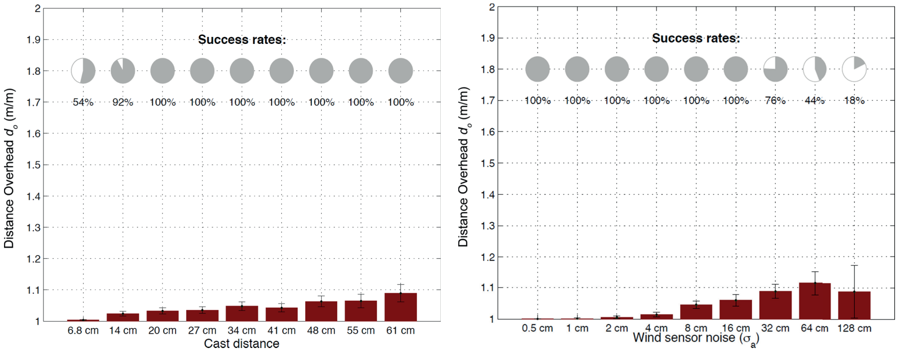

(a) Surge-cast with varying cast distance (b) Surge-cast with varying wind sensor noise σ_a

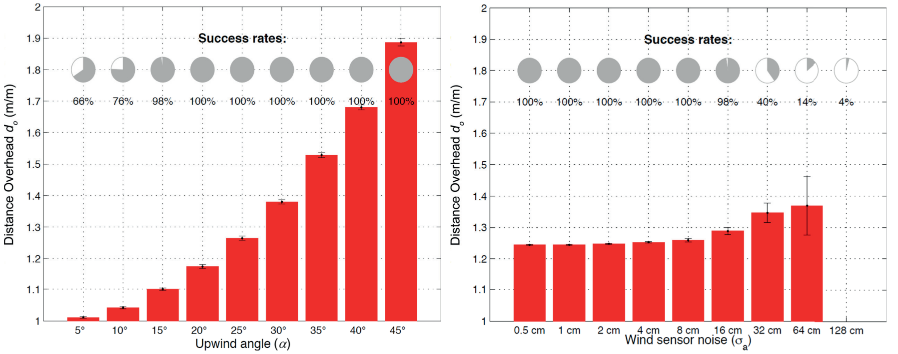

(c) Casting with varying upwind angle α (d) Casting with varying wind sensor noise

Figure 5.12: *Simulation results of Lochmatter [12] obtained using the casting and the surge-cast algorithm with a wind sensor noise set to* $\sigma_a = 0.1m$*: surge-cast with (a) varying cast distance* (d_{cast}) *and (b) varying wind sensor noise* σ_a *and casting (zigzag) with (c) varying upwind angle* (α) *and (d) varying wind sensor noise. The error bars indicate the confidence interval with* 95% *confidence level for the mean (assuming normally distributed data). The figure and caption were adopted from [12].*

not work in environments without a main wind flow.

Among the three algorithms tested in [2, 12], the surge-spiral algorithm is the preferred strategy as it is the most robust and has the performance over a wide parameter range followed by the surge-cast algorithm. Pure casting is the least performant algorithm. Unfortunately, a gradient-based algorithm was not considered in Lochmatter's comparison.

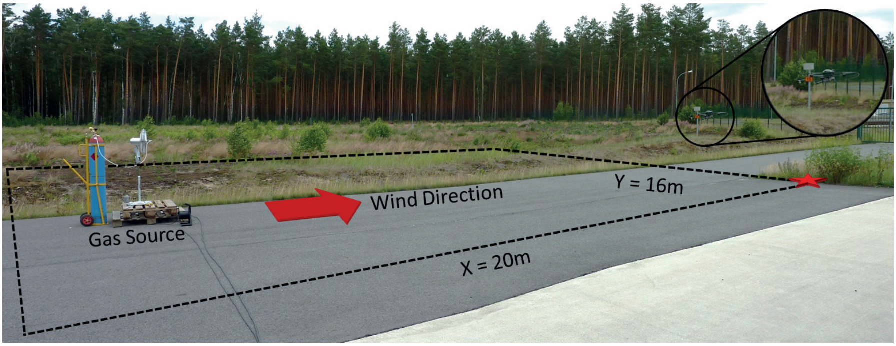

Figure 5.13: *Setup of the real-world plume tracking experiments: The experiment area was set to* $20 \times 16m^2$ *with the gas source positioned approximately at position* $(3.2, 5.7)m$ *from the bottom left corner. The red arrow illustrates the main wind direction during the experiments. The start position of the micro-drone is indicated by the red star. The micro-drone can be seen in the image enlargement in the top right corner of the figure.*

5.3 Real-world Experiments

It is very difficult to set up a controlled airflow environment to perform *initial* plume tracking experiments, especially when GPS is needed to control the micro-drone. The first idea was to carry out these experiments in a vacant 100-year-old greenhouse (approx. $10 \times 15m^2$). However, the structure of the greenhouse acts as a Faraday cage which produces an extremely inaccurate GPS signal. A new greenhouse built of aluminum and plastic foil gave far better results, but it provided only an experiment area of approximately $5 \times 15m^2$. The relatively small area size, the system characteristics of the micro-drone (minimum step size, accuracy of the GPS-based positioning system, slow sensor recovery), and especially the fact that controlled environmental setups are not desirable when targeting to real-world applications [Paper II], led to the conclusion that the realization of the plume tracking experiments have to be realized outdoors. Expensive indoor localization systems like an indoor GPS system or a camera system were not considered within this Ph.D. thesis.

5.3.1 Experiment Environment and Setup

All plume tracking experiments were carried out in a $20 \times 16m^2$ wide open outdoor area surrounded by trees and buildings, which introduced a certain level of turbulence (Fig. 5.13). The micro-drone was equipped with the e-nose with a sampling rate of $8Hz$ for each sensor. The step size of the micro-drone was set to $1.5m$ for the surge-cast and the pseudo gradient algorithm, and to $2.0m$ for the zigzag algorithm. The parameter α of the zigzag algorithm was set to $60°$ in the first and $75°$ in the second run. The parameter β of the pseudo gradient algorithm was set to $60°$. The flight speed of the micro-drone between the measurement positions was set to $1ms^{-1}$. Because of the low altitude of the micro-drone of about $1.5m$ and the inaccuracies given by the altitude control of the micro-drone below $< 5m$, the altitude was kept constant manually during the experiments. A CH_4 (99.5%-pure methane) gas cylinder connected to a pressure-reducing valve was used as the gas source. The outlet of the gas source was extended with a small tube, which was attached to a fan in order to spread the analyte away from the cylinder and to improve the gas dispersion. The air current introduced by the fan also prevented the CH_4 from immediately rising up to the atmosphere when released. The gas source was placed approximately at position $(3.2, 5.7)m$ from the bottom left corner. The starting point of the trajectory is illustrated by the red star. The corresponding algorithm was activated directly after take-off, which started the experiment.

Here, an experiment setup is built where no artificial conditions were introduced to simplify the experiments. In comparison to a wind tunnel, the fan did not produce a laminar wind flow over the experiment area. Instead, additional turbulences were introduced by the gas cylinder and the running fan. Note that the results of the experiments were published in [Paper IV, Paper IX].

5.3.2 Experiment Results

The wind conditions during the experiments were quite stable and permitted performing a total of 6 successful runs: each algorithm was conducted twice. The circular variance S_0 (Appendix A) is used here to describe the degree of turbulence (stability of the wind) during the different experiment runs.

Figs. 5.14(a) to 5.14(c) show the trajectories produced by the micro-drone. The plume acquisition phase was excluded from the evaluation to make the results rudi-

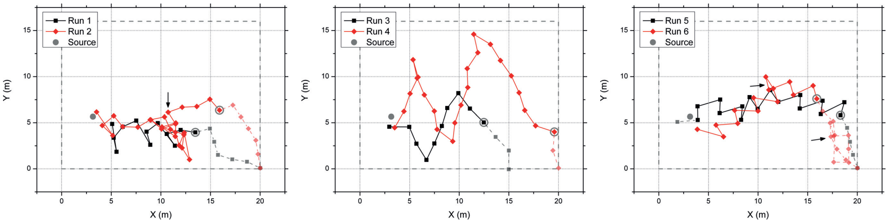

(a) Surge-Cast (b) Zigzag (c) Pseudo Gradient

Figure 5.14: *Trajectories of the micro-drone in real-world experiments including the plume acquisition phase using (a) the surge-cast, (b) the zigzag ($\alpha = 60°$ [black] and $75°$ [red]), and (c) the pseudo gradient algorithm ($\beta = 60°$). The experiment area is illustrated by the gray dotted line. The source position is indicated by the gray point. The gray circles mark the position of the first gas concentration measurements above the threshold. The position where the wind direction started turning up to $180°$ is indicated with black arrows (in run #2 and #6).*

mentarily comparable with each other and to the wind tunnel experiments performed by Lochmatter [12]. Runs #2 (surge-cast) and #6 (pseudo gradient) are particularly noteworthy. Here the wind direction varied significantly during the runs which precluded the micro-drone making further progress for some time (Table 5.2 – circular variance). This is indicated in Fig. 5.14 with black arrows. Table 5.2 shows a compilation of the experiment results. However, the overlapping confidence intervals, the small number of experiments, the different chosen step sizes and upwind angles for the zigzag algorithm, and the constantly changing structure of the plume (due to changing wind conditions) do not permit obtaining strong statistical significance of the performance of the algorithm.

Lochmatter's Ph.D. thesis [12] compared three bio-inspired algorithms in experiments with real robots in an $18 \times 4m^2$ large wind tunnel: pure casting (zigzagging), surge-spiraling, and surge-casting. A total of 7×20 runs were performed with the following configurations: $d_{lost} = 0.40m$, $d_{cast} = \{0.14, 0.43, 0.72\}\,m$, $\alpha = \{10, 20, 30\}^{\circ}$, and $d_{gap} = 0.58m$ (the parameter for the surge-spiraling algorithm). In each run the robot was released in the plume at a position approximately $14.5m$ downwind from the source. The results of the experiments suggest that the surge-cast algorithm ($d_o = \{1.12, 1.10, 1.05\}$) slightly outperforms the surge-spiraling algorithm ($d_o = 1.14$) as the algorithm moves the robot only backward and forward instead of moving it in complete circles to reacquire the plume. The pure casting algorithm,

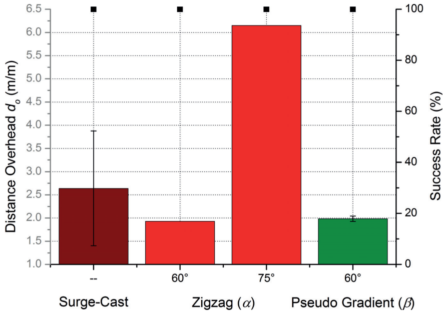

Figure 5.15: *Comparison of the distance overhead d_o (mean with 95% confidence interval) and success rate of the surge-cast, the zigzag ($\alpha = 60°$ and 75°), and the pseudo gradient algorithm ($\beta = 60°$). The traveled distance needed to acquire the plume was not considered here.*

however, decreases its performance with increasing α as the robot has to turn more often at the plume boundaries to stay within the plume ($d_o = \{1.16, 1.43, 1.63\}$). Unfortunately, a gradient-based algorithm was not considered in his comparison.

The implementation of the bio-inspired algorithms used in this Ph.D. thesis are slightly different to their initial implementation (e.g., d_{lost} and d_{cast} were removed) to be conform with the system characteristics of the micro-drone (minimum step size of $1m$). The results of these algorithms are shown in Fig. 5.15. Nevertheless the results can be used to draw further conclusions since the class of algorithms is the same. Here the magnitude of the distance overhead is about twice as large as in the results from Lochmatter. Reproducible conditions in the wind tunnel using a laminar airflow allow for generation of approximately the same plume structure (width, intermittency, and concentrations) within the experiment setup. This cannot be achieved in the real world, especially since the wind direction constantly changes by a few degrees. Even the experiment setup introduced additional turbulence. Another problem is the different chosen α parameters used with the zigzag algorithm.

The results demonstrate that plume tracking can be performed in a real-world outdoor environment with a reasonable degree of turbulence. The micro-drone was able to reacquire the plume even during varying wind conditions and successfully reached the gas source in 6 of 6 trials. Comparing the results of Lochmatter with the results presented here indicates that the surge-cast algorithm has a higher per-

Table 5.2: *Results of the real-world plume tracking experiments (excluding the plume acquisition phase).*

	Surge-Cast		Zigzag		Pseudo Gradient	
Run	1	2	3	4	5	6
Traveled Distance d_t (m)	21.01	41.78	18.06	44.18	29.65	26.02
Distance Overhead d_o (m/m)	2.01	3.27	1.93	2.67	1.96	2.02
Mean	2.64		-		1.99	
95% Confidence Interval	$(1.40, 3.88)$		-		$(1.93, 2.04)$	
Mean Wind Speed (ms^{-1})	3.10	3.18	2.22	3.23	3.48	3.26
σ (ms^{-1})	±1.59	±1.72	±1.03	±1.52	±1.71	±1.61
Mean Wind Direction (°)	235.93	234,58	246.60	249.25	243.21	242.17
Circular Variance	0.19	0.20	0.17	0.14	0.16	0.16

formance than pure casting (zigzagging; $\alpha = 75°$), even though pure casting is more robust. Further, it can be seen that the pseudo gradient algorithm is at least as efficient in the real world as the surge-cast algorithm due to the frequently performed reacquire (casting) steps of the surge-cast algorithm.

5.4 Summary and Conclusions

In this chapter, three bio-inspired plume tracking algorithms and their implementation for a gas-sensitive micro-drone were described as well as a new measuring strategy especially designed for, but not limited to, a micro-drone. Their performance was evaluated in simulation and real-world experiments. The simulation results suggest that the surge-cast algorithm is the most performant algorithm, followed by the zigzag algorithm with $\alpha = 15°$. However, Lochmatter's and the results presented here show that the robustness of both algorithms decreases faster with increasing wind sensor noise than the pseudo gradient algorithm and the zigzag algorithm with $\alpha = 60°$ and $75°$. Thus, the current implementation of the surge-cast algorithm does not seem to be recommendable to use with the micro-drone. The pseudo gradient algorithm presents a high-performance and robust alternative to the zigzag algorithm. Furthermore, the results of the real-world experiments demonstrate that plume tracking using a gas-sensitive micro-drone can be done when particular environmental conditions are given. The micro-drone was able to reacquire the plume even during periods of strongly changing wind. The initial results from the real-world experiments indicate that the pseudo gradient algorithm is at least as efficient as the surge-cast algorithm. A strong correlation between the results from simulation and real-world experiments can be found for the pseudo gradient algorithm and the zigzag algorithm. Thus, as concerns the current implementation of the surge-cast algorithm, the pseudo gradient algorithm and the zigzag algorithm are the most promising algorithms to use with the micro-drone. However, [Paper II] demonstrates the weakness of state-of-the-art bio-inspired plume tracking algorithms that directly mimic insect behavior. It is argued that the gas sensing mechanisms available to robotic systems are completely different from biological receptors and that the chaotic properties of natural environments do not allow the formation of a steady gas plume that would lead a robot to the gas source using a form of bio-inspired anemotaxis. These claims were supported by data collected in four different experiment areas (indoor and outdoor) with three different platforms (ground-based and flying). It was shown that although the explored experiment areas are not of considerable size and the measurement points are spatially dense, there is hardly any regularity in the wind direction measured with the anemometer carried by the mobile robots and the micro-drone. It was also shown that large directional fluctuations were observed between measurements taken at a single waypoint. This clearly indicates that the assumption of laminar airflow does not hold in any of the four environments.

The relatively small number of real-world experiments does not allow for obtaining strong statistical significance regarding the performance of the plume tracking algorithms. Therefore, future work should include running large test sets with different wind and weather conditions on, e.g., wide open landfill sites to obtain the performance and robustness of these algorithms in natural environments. At the same time, implementations of probabilistic gas source localization algorithms should be adapted to work with gas-sensitive micro-drones and tested in real-world experiments as well. In general, the domain of probabilistic gas source localization algorithms gives ample room for developing new algorithms.

Although it was shown that plume tracking is possible under certain circumstances in the real world, there is no guarantee that state-of-the-art bio-inspired plume tracking algorithms lead a robot reliably to the gas source (especially if wind direction is constantly turning). One possible application could be to locate the source of a pollution caused by, e.g., industrial chimneys in a higher atmospheric layer, where the airflow is more stable, or on wide open landfill sites.

Chapter 6

Gas Source Localization using a Particle Filter (PF)

This chapter presents the development of a gas source localization (GSL) algorithm based on a particle filter (PF). It uses gas and wind measurements to reason about the trajectory of a gas patch from where it was released by the gas source until it reaches the measurement position of the micro-drone (Fig. 6.1). The trajectory is backtracked (and approximated) by dividing the taken wind measurements into time intervals. The averaged wind vectors of each interval are then used to reconstruct the trajectory in reverse. Given a uniform wind field over the search space and a single gas source, the reconstruction of multiple trajectories at different measurement locations using sufficient gas and wind measurements can lead to an accurate estimate of the gas source location. Non-uniform wind fields, which are typical for realistic environments, are accounted for by considering a patch path envelope (PPE) instead of a single patch trajectory. The PPE describes the envelope of an area through which the gas patch has likely moved. The source is considered to be found (declared), if the location estimate, represented by the particles of the PF, remains within a small region for a defined number of iterations. As exploratory behavior, sweeping along a predefined path and plume tracking are considered. In this Ph.D. thesis, the pseudo gradient plume tracking algorithm presented in Sec. 5.1.2.3 is mainly used. The algorithm is successfully validated in simulation and real-world experiments.

Note that the algorithm is only used for estimating the gas source location and not for controlling the micro-drone. Additionally, it is assumed that the underlying

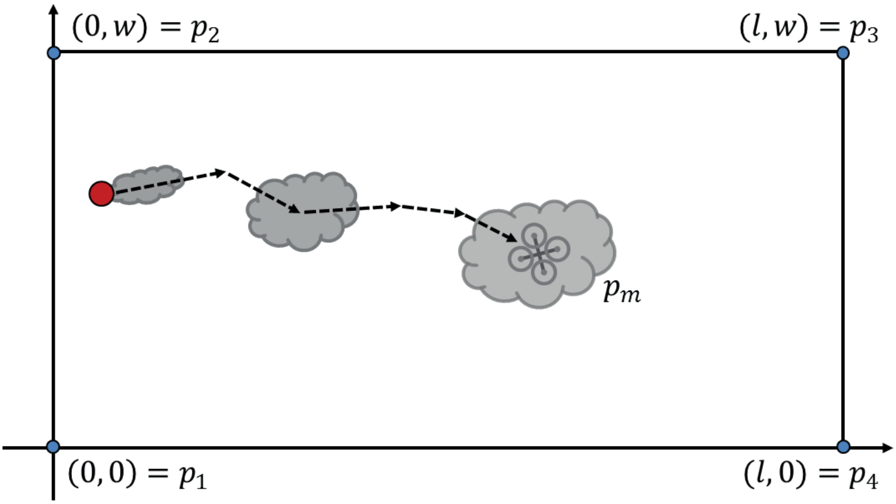

Figure 6.1: *Trajectory of the gas path since release at the source. The source location is denoted by the large red dot and the position of the micro-drone is denoted by* p_m*.* p_i *with* $i \in [1, 4]$ *are the corner points of the rectangular search area,* l *is the length, and* w *is the width of the search area. The length of the arrow represents the average wind speed and its orientation is represented by the circular mean direction.*

control algorithm used allows the micro-drone to collect gas and wind measurements at fixed measuring positions during a fixed time interval and that an arbitrary rectangular search area defined by four GPS coordinates is given (Fig. 6.1). As the wind vector estimation with the micro-drone can only determine the x- and y-component of the wind, this Ph.D. thesis focuses on the 2D case only.

In the remainder of this chapter, first, the basic particle filter and the applied modifications are described (Sec. 6.1). Next, Sec. 6.1.1 describes the measurement model of the particle filter that consists of the processing of the sensor data and the construction of the PPE. Secs. 6.1.2 and 6.1.3 describe the phases of the particle filter and Sec. 6.1.4 presents the modality to estimate the gas source location based on the particle set. Then, simulation and real-world experiments are performed (Sec. 6.2 and 6.3) and conclusions are drawn (Sec. 6.5).

6.1 Particle Filter-based Gas Source Localization Algorithm

The Particle Filter (PF), also known as Sequential Monte Carlo Method (SMC), is an alternative nonparametric implementation of the Bayes filter [133] and a generalization of the Kalman filter for nonlinear and/or non-Gaussian problems. It is commonly used in the field of robotics, e.g., in robot localization, SLAM, and robot fault diagnosis to track a variable of interest as it evolves over time [134]. Here, the PF is used to estimate gas source location.

The basic concept of PFs is that any probability density function (*pdf*) can be represented by a set of N random state samples (particles) drawn from this *pdf* to approximate the target's true world state (here: the location of the gas source): $\mathcal{X}_t := x_t^{[1]}, x_t^{[2]}, \dots, x_t^{[N]}$. Each particle $x_t^{[i]}$ is a copy of the variable of interest associated with an importance weight $\omega_t^{[i]} \in \Omega_t$ and a set of relevant state parameters. The importance weight indicates the quality of that specific particle and defines its contribution to the overall estimate of the variable of interest. The denser a subregion of the state space is populated by particles with high importance weights, the more likely it is that the true world state falls into this region.

The basic PF consists of three phases in order to construct the particle set $\mathcal{X}_t$ recursively from the set $\mathcal{X}_{t-1}$: *prediction*, *update*, and *resampling*. Each particle $x_{t-1}^{[i]} \in \mathcal{X}_{t-1}$ is processed within the *prediction* phase based on the *pdf* to generate a hypothetical state $\bar{x}_t^{[i]} \in \bar{\mathcal{X}}_t$. The *prediction* phase uses a motion model in order to simulate the effect that an action has on the particle set (with appropriate noise added) [134]. The *update* phase calculates for each particle $x_t^{[i]}$ the new importance weight $\omega_t^{[i]} \in \Omega_t$ based on the importance weight $\omega_{t-1}^{[i]} \in \Omega_{t-1}$, the latest sensor information available, and the measurement model to accurately describe the *pdf*. The measurement model describes how measurements are generated from the hidden true world state [135]. Finally, in the *resampling* phase, the algorithm draws N particles with replacement from the temporary set $\bar{\mathcal{X}}_t$ to generate a new particle set $\mathcal{X}_t$. The probability of drawing each particle is given by its importance weight, i.e., particles with importance weights close to zero tend to be removed. In the beginning, the particles are equally distributed over the state space if no prior information about the *pdf* is given.

Algorithm 6.1 provides a formal description of the core function of the suggested

Algorithm 6.1 Core function of the PF-based GSL algorithm.

```
Require: $\mathcal{X}_{t-1}$, $\Omega_{t-1}$, $C_t$, and $z_t$.
 1: $\bar{\mathcal{X}}_t = \mathcal{X}_{t-1}$
 2: $\bar{\Omega}_t = f(\bar{\mathcal{X}}_t, \Omega_{t-1}, C_t, z_t)$
 3: Normalize($\bar{\Omega}_t$)
 4: if $\hat{N}_{eff} \geq \gamma \cdot N$ then
 5:     $\mathcal{X}_t = \bar{\mathcal{X}}_t$
 6:     $\Omega_t = \bar{\Omega}_t$
 7: else
 8:     $\mathcal{X}_t = \Omega_t = \emptyset$
 9:     for $i = 1$ to $N$ do
10:         $j = rand(1, 100)$
11:         if $j \leq \delta \cdot 100$ then
12:             if $z_t = 1$ then
13:                 $\mathcal{X}_t = \mathcal{X}_t \cup \left\{\bar{x}_t^{[k]} \text{ drawn uniformly from } F_{l,w} \cap S_t\right\}$
14:             else
15:                 $\mathcal{X}_t = \mathcal{X}_t \cup \left\{\bar{x}_t^{[k]} \text{ drawn uniformly from } F_{l,w} \setminus C_t\right\}$
16:             end if
17:         else
18:             $\mathcal{X}_t = \mathcal{X}_t \cup \left\{\bar{x}_t^{[k]} \text{ drawn from } \bar{\mathcal{X}}_t \text{ with probability } \propto \bar{\omega}_t^{[k]}\right\}$
19:         end if
20:         $\Omega_t = \Omega_t \cup \left\{\omega_t^{[i]} = 1/N\right\}$
21:     end for
22: end if
```

PF-based GSL algorithm. The input is the particle set $\mathcal{X}_{t-1}$ with weights Ω_{t-1}, along with the most recently calculated PPE C_t (Sec. 6.1.1.2) and the most recent binary concentration measurement z_t (Sec. 6.1.1.1).

Line 1 implements the PF *prediction* step. As the location of a static gas source is of interest only, the particle sets $\bar{\mathcal{X}}_t$ and $\mathcal{X}_{t-1}$ are identical.

Line 2 implements the measurement *update*. The new importance weights $\bar{\Omega}_t$ are computed based on the function $f(\bar{\mathcal{X}}_t, \Omega_{t-1}, C_t, z_t)$ that considers the relative position of a particle with respect to the PPE C_t and the binary concentration measurement z_t. Actually, this function is intended to update only a single importance weight $\omega_{t-1}^{[i]}$ given the corresponding particle $\bar{x}_t^{[i]}$, but was generalized here for the purpose of simplification. The measurement model is described in Sec. 6.1.1. The full measurement update is described in Sec. 6.1.2.

Line 3 normalizes the importance weights $\bar{\Omega}_t$ (Sec. 6.1.3).

Line 4 checks whether the effective sample size $\hat{N}_{eff}$ has dropped under a predefined threshold $\gamma \cdot N$ ($\gamma \in [0, 1]$) and whether *resampling* has to be performed or not (explained in detail in Sec. 6.1.3). If *resampling* is not necessary, the temporary sets $\bar{\mathcal{X}}_t$ and $\bar{\Omega}_t$ are the result sets (lines 5 and 6).

Lines 3 to 21 implement the *resampling* step of the PF. In lines 9 to 21, the new particle set $\mathcal{X}_t$ is built. A particle $\bar{x}_t^{[k]}$ is drawn with probability δ uniformly from the area $F_{l,w} \cap S_t$, if $z_t = 1$ (gas detection event), and from the search area $F_{l,w} \setminus C_t$, if $z_t = 0$ (non-detection event; see lines 11 to 16), where S_t defines the area in upwind direction of the micro-drone and $F_{l,w}$ is the search area. A particle $\bar{x}_t^{[k]}$ is drawn with probability $1 - \delta$ from $\bar{\mathcal{X}}_t$ according to its importance weight $\bar{\omega}_t^{[k]}$ (line 18). This resampling procedure is explained in detail in Sec. 6.1.3. S_t and $F_{l,w}$ are defined as

$$S_t = \Big\{(x, y) \mid \Big\langle((x, y) - m_0), (\cos \bar{\theta}_t, \sin \bar{\theta}_t)\Big\rangle \geq 0\Big\} \tag{6.1}$$

and

$$F_{l,w} = \{(x, y) \mid 0 \leq x \leq l \wedge 0 \leq y \leq w\}\,, \tag{6.2}$$

where m_0 is related to the position of the micro-drone and explained in more detail in Sec. 6.1.1, $\bar{\theta}_t$ is the averaged wind direction at iteration t, and l is the length and w is the width of the search area. Finally, the importance weights of all particles are set to $1/N$ (line 20).

In the beginning, each particle $x_0^{[i]}$ is initialized with the weight $\omega_0^{[i]} = 1/N$ and the position $(x_0^{[i]}, y_0^{[i]})$ drawn uniformly from the search area $F_{l,w}$, if no a priori knowledge about the gas source location is given. An estimate of the gas source location is obtained by, e.g., the weighted sum of all particles. A detailed description of an alternative gas source estimation strategy is given in Sec. 6.1.4.

6.1.1 Measurement Model

This section details the measurement model of the proposed PF-based GSL algorithm. The measurement model links the information from the used sensors to the hidden true world state [135]. It includes the sensor data processing (Secs. 6.1.1.1 and 6.1.1.2) and the path reconstruction of the gas patch (Sec. 6.1.1.4) in form of a PPE. For this purpose, the properties of the wind field are relevant. Therefore, Sec. 6.1.1.3 demonstrates that uniformity in the wind field does not exist.

6.1.1.1 Gas Concentration Measurements

At each iteration t, the micro-drone collects gas and wind measurements at a fixed measuring position during a fixed time interval ΔT. To decide whether the micro-drone was within the plume or not, a binary concentration measure z_t with an adaptive threshold $\bar{c}_t$ was used as proposed by Li et al. [77]. It is defined as:

$$z_t = \begin{cases} 1 & \text{, if } c_t > \bar{c}_{t-1} \\ 0 & \text{, otherwise} \end{cases} \tag{6.3}$$

with

$$\bar{c}_t = \begin{cases} \lambda \bar{c}_{t-1} + (1-\lambda) c_t & \text{, if } t \geq 1 \\ c_t & \text{, if } t = 0, \end{cases} \tag{6.4}$$

where c_t is the measured gas concentration averaged over the measurement interval ΔT at iteration t, c_0 is the initial gas concentration detected at the start of the algorithm, and $\lambda \in [0,1]$. The adaptive threshold $\bar{c}_t$ is also called exponential moving average (EMA). Values of λ close to 1 are less responsive to recent measurements, while values of λ closer to zero give greater weight to recent measurements. Thus, the weighting for each gas measurement in the past decreases exponentially over time, supporting, e.g., the adaptation to changes of the baseline of the gas sensor and the hysteresis of the sensor response. $z_t = 1$ indicates a gas-detection event at iteration t, whereas a non-detection event is represented as $z_t = 0$. As proposed in [77], λ is set to 0.5 during all experiments to respond correctly in time to all gas-detection events.

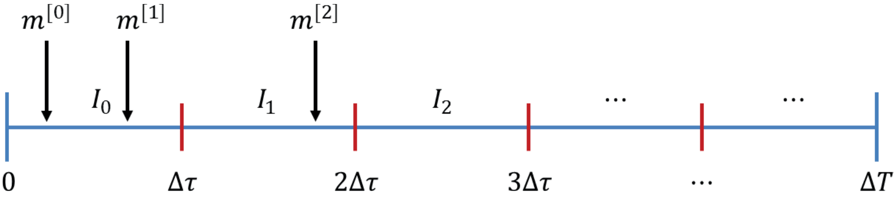

Figure 6.2: *Classification of the wind measurements in averaging intervals: The raw measurements in each interval I_j are averaged to form a new measurement value $\bar{m}^{[j]}$.*

6.1.1.2 Wind Measurements

At each iteration t, the micro-drone computes a PPE from a set of single wind measurements $M = \left\{m^{[i]}\right\}$ taken at a fixed position and during a fixed time interval ΔT. Each measurement consists of the measurement time τ relative to the measurement start time, the wind speed r_u, and the wind direction θ_u: $m^{[i]} = (\tau^{[i]}, r_u^{[i]}, \theta_u^{[i]})$.

The measurement interval ΔT is further split into $n \in \mathbb{N}^+$ intervals of equal size $\Delta\tau$ (Fig. 6.2) to calculate the average wind direction and its uncertainty (variance). The value of $\Delta\tau$ (or n) is chosen so that $\Delta\tau \cdot n = \Delta T$. The raw measurements in each interval are averaged to form a new measurement value $\bar{m}$, which consists of the averaged wind speed $\bar{r}_u$, the averaged wind direction $\bar{\theta}_u$, and the circular variance S_0: $\bar{m}^{[j]} = (\bar{r}_u^{[j]}, \bar{\theta}_u^{[j]}, S_0^{[j]})$. Let

$$I_j = \left\{i : j \cdot \Delta\tau \leq \tau^{[i]} \leq (j+1) \cdot \Delta\tau\right\} \tag{6.5}$$

be the indices of all measurements $m^{[i]}$ in subinterval j. Then

$$\bar{r}_u^{[j]} = \frac{1}{|I_j|} \sum_{i \in I_j} r_u^{[i]}, \tag{6.6}$$

$\bar{\theta}_u^{[j]}\left(\{(\theta_u)_i : i \in I_j\}\right)$ is computed according to Eq. A.1, and $S_0^{[j]}\left(\{(\theta_u)_i : i \in I_j\}\right)$ according to Eq. A.3 (see Appendix A). $\bar{M}$ is defined to be the chronologically (increasing) ordered list of the averaged measurements $\bar{m}^{[j]}$.

6.1.1.3 Non-Uniformity of the Wind Field

Li et al. [78] assume a wind field that is uniform over a certain area at each instant but subject to changes over time (i.e., the wind vector field is constant within this

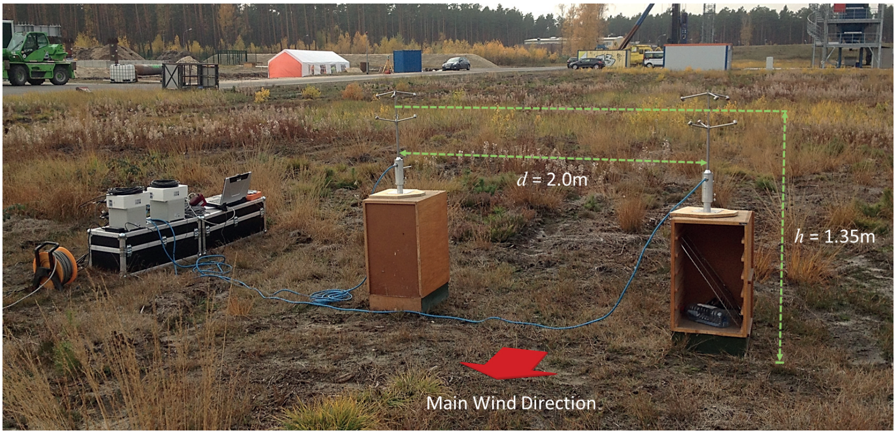

Figure 6.3: *Experiment setup to ascertain to which degree the assumption of a uniform wind field holds in a realistic scenario.*

area for a fixed time t but may change as a whole for different t). Under this assumption it is possible to reconstruct the path of gas patches from the available wind measurements taken at any position, which simplifies the GSL problem to a certain extent. Li et al. claim in [78] that a time-varying wind field can be regarded as roughly uniform within a circular domain around the robot, when the airflow is not *too weak* (above $0.2ms^{-1}$) and the radius of this domain is not too large (less than the distance traveled by the airflow in $10s$). Here, an experiment was performed similar to the one presented by Li et al. to ascertain to which degree the assumption of a uniform wind field holds in a realistic scenario.

Experiment Setup The test was carried out in an open outdoor environment at BAM TTS on a cloudy day. Trees and buildings around this area introduced a certain level of turbulence. Two ultrasonic anemometers (uSonic-3 Scientific (former: USA-1), Metek GmbH, Germany) were mounted at a height of approximately $1.35m$ at a distance of approximately $2m$ of one another (according to the requirement of Li et al. [78]), as illustrated in Fig. 6.3. The ultrasonic anemometers have an operating range of 0 up to $60ms^{-1}$ with a resolution of $0.01ms^{-1}$ and an accuracy of $\pm0.1ms^{-1}$. The resolution of the wind direction is $0.1°$ with an accuracy of $\pm2°$. The wind measurements were recorded at a frequency of $1Hz$ for about $83min$.

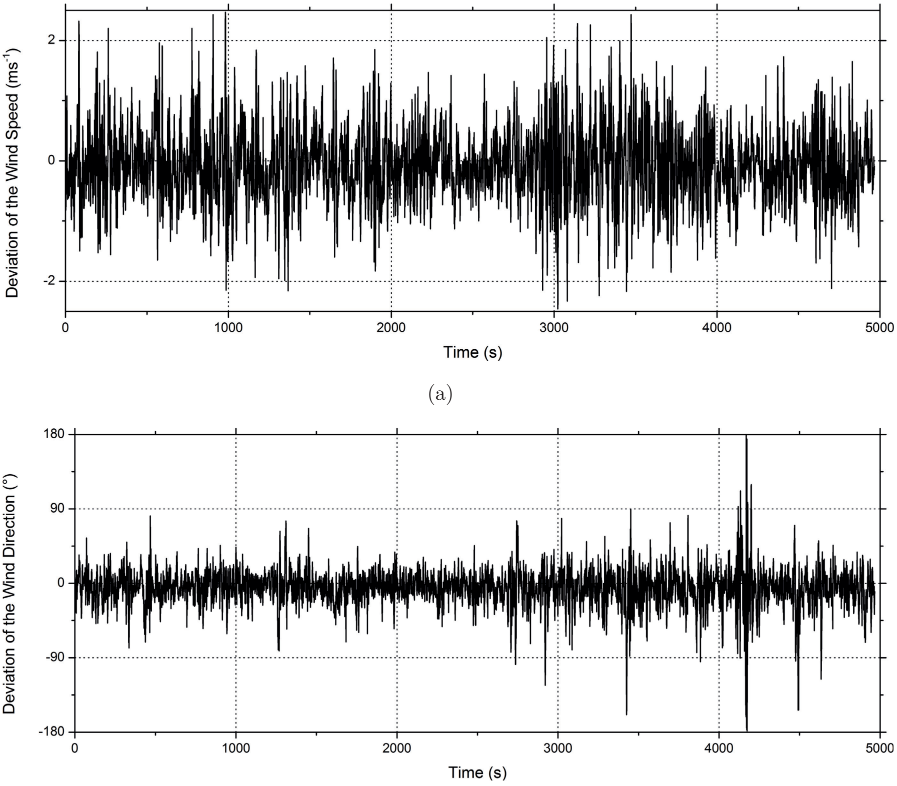

(a)

(b)

Figure 6.4: *Deviation of (a) wind speed and (b) wind direction between the measurements at both ultrasonic anemometers.*

Experiment Results When evaluating the wind data, it has to be kept in mind that the sensitivity of the anemometers allows detecting the effects of micro-scale eddies, which may disrupt the measurements to a certain extent. A total of 4,982 samples were collected with both anemometers, and only 15 of these measurements were *too weak* according to the requirement of Li et al. [78], i.e., below $0.2ms^{-1}$. The measurements that do not conform to Li's requirements were removed from the data set to perform the evaluation of this experiment. The measured wind speed in the remaining data set was in the range of approximately 0.2 to $5.3ms^{-1}$ (i.e., *not weak* according to the requirement of Li et al. [78]) and the measured wind direction was between 146° and 61°. Fig. 6.4 shows corresponding deviations between the two anemometers, both of (a) the wind speed and (b) the wind direction. Uniformity in the wind field would result in negligibly small deviations in the measured wind vectors. The results, however, show that uniformity in the wind field is not given (Fig. 6.4). Instead, differences in the measured values up to $\approx 2.5ms^{-1}$ (wind speed) and $\approx 179°$ (wind direction) occurred. For example, a deviation of the wind direction of $\approx 179°$ can be seen after approximately 4,170s in Fig. 6.4(b). At the same time, a wind speed of $0.47ms^{-1}$ (anemometer 1) and $0.74ms^{-1}$ (anemometer 2) was measured, which indicates that the wind speed was not *too weak* while the wind apparently blew from almost opposite directions. Thus, the claim of a roughly uniform wind field by Li et al. does not hold.

In general, the wind speed and direction can vary locally due to naturally occurring conditions (condition of the soil, strong temperature gradients, and type of the ecological system) or building density (countryside and city). Further observations confirm that the weather conditions (sunny vs. cloudy) have an impact on the wind field due to convective currents induced by solar radiation. The claim of a roughly uniform wind field by Li et al. may possibly hold for the particular conditions considered in [78] (cloudy, daytime and season the experiment was performed (November), the surface of the experiment area, and its surrounding area), but cannot be generalized for all possible real-world environments.

6.1.1.4 Construction of the Patch Path Envelope (PPE) in Uniform Wind Fields

At each iteration t, the path of the wind $\{m_j\}_{j=1:n}$ is calculated based on the mean wind directions $\bar{\theta}_u^{[j]}$ and the length of the path line segments s_j using the great circle navigation formulae presented in Sec. 3.5.1 (Eqs. 3.16 and 3.17) starting from the position of the micro-drone p_m.

$$s_j = \Delta\tau \cdot \bar{r}_u^{[j]}, \tag{6.7}$$

where $\bar{r}_u^{[j]}$ is the mean wind speed and $\Delta\tau$ the averaging period (Sec. 6.1.1.2).

Fig. 6.5 shows the reverse wind path starting from the position of the micro-drone moving in upwind direction to rebuild the wind field using the history of averaged wind measurements M. Using this approach with a perfect wind sensor could accurately indicate the direction of the gas source if a concentration above a certain threshold is detected. However, a perfect wind sensor does not exist and a

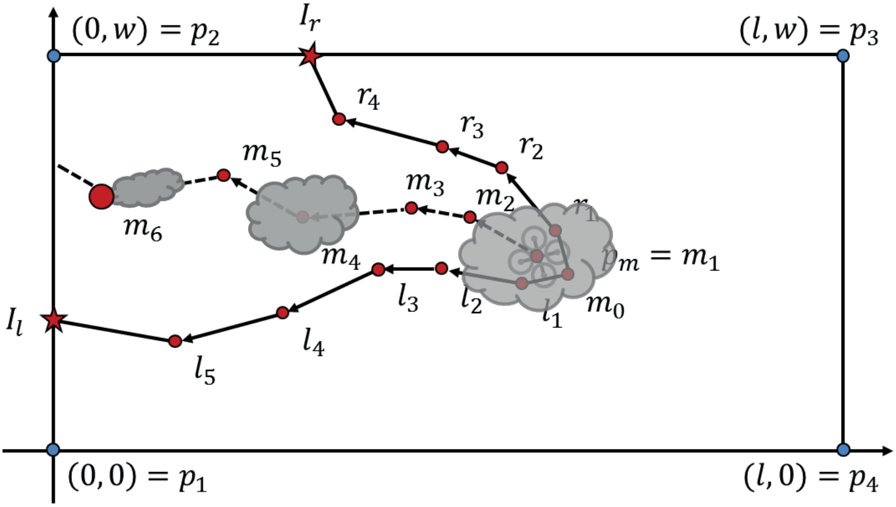

Figure 6.5: *Path reconstruction in uniform wind fields using the wind information measured with the micro-drone. The source location is denoted by the large red dot and the position of the micro-drone is denoted by* p_m*,* p_i *with* $i \in [1,4]$ *are the corner points of the rectangular search area, and* l *is the length and* w *is the width of the search area. The measurement radius of the micro-drone is approximated with a simple triangle given by the positions* m_0*,* l_1*, and* r_1*.*

wind field in the real world is not uniform (Sec. 6.1.1.3). Furthermore, the airflow in an open outdoor environment is affected by turbulent advection [73] which disperses and dilutes the gas plume, creating complex structures of gas patches [PAPER II].

Here, the circular variance is used to consider the non-regularity of the wind flow direction (see Appendix A). The idea is to split up the path into two paths that describe the extreme cases the gas patch may have traveled, resulting in a PPE: one left $\{l_j\}_{j=1:n}$ and one right $\{r_j\}_{j=1:n}$ (Fig. 6.5). The stability of the wind within each averaging interval is used to decide how the two paths will drift apart. Stable wind conditions ($S_0 = 0$) result in line segments in $\{l_j\}_{j=1:n}$ and $\{r_j\}_{j=1:n}$ parallel to the corresponding path segment in $\{m_j\}_{j=1:n}$, whereas absolutely unstable wind conditions ($S_0 = 1$) produce line segments orthogonal to it. The PPE can be interpreted as a probability area containing the gas source.

The paths are calculated using the great circle navigation formulae from Sec. 3.5.1 to extend the boundary of the envelope of the gas patch paths based on earlier wind measurements (under the assumption of a uniform wind field). The positions l_{j+1} and r_{j+1} are determined based on the positions l_j and r_j, the azimuth direction angles δ_{l_j} and δ_{r_j}, and length of the path line segments s_j. The azimuth direction angles δ_{l_j} and δ_{r_j} are shown in Fig. 6.5 by the direction of the direction vectors $\overrightarrow{l_j l_{j+1}}$ and $\overrightarrow{r_j r_{j+1}}$ and are calculated as follows:

$$\delta_{l_j} = \left(\bar{\theta}_u^{[j]} - 90° \cdot S_0^{[j]}\right) \bmod 360° \tag{6.8}$$

$$\delta_{r_j} = \left(\bar{\theta}_u^{[j]} + 90° \cdot S_0^{[j]}\right) \bmod 360° \tag{6.9}$$

The PPE's first segment is approximated with a simple triangle with its right angle rotated in downwind direction. The values are based on the averaged wind measurements in position m_1 (Fig. 6.5). By so doing the micro-drone's measurement radius determined by the rotor movement is taken into account and numerical stability is achieved under stable wind conditions. This includes the possibility that line segments may overlay at the beginning of the paths when the circular variance is zero. Here again, the great circle navigation formulae is used to calculate the corresponding positions m_0, l_1, and r_1 using the position of the micro-drone $p_m = m_1$, the azimuth direction angles δ_{m_0}, δ_{l_1}, and δ_{r_1}, and the micro-drone's radius of $0.5m$.

$$\delta_{m_0} = \left(\bar{\theta}_u^{[1]} + 180°\right) \bmod 360° \tag{6.10}$$

$$\delta_{l_1} = \left(\bar{\theta}_u^{[1]} - 90°\right) \bmod 360° \tag{6.11}$$

$$\delta_{r_1} = \left(\bar{\theta}_u^{[1]} + 90°\right) \bmod 360° \tag{6.12}$$

To complete the polygonal PPE C_t, the intersection points of the line segments with the area border have to be calculated. The intersection points of two lines are calculated using the method presented in [136]. Finally, the polygon delimiting the PPE C_t is constructed counterclockwise by adding the vertex m_0, the vertices $\{r_j\}_{j=1:k_r}$ (e.g., in Fig. 6.5 $k_r = 4$), the intersection point I_r, all corner points of the area border in between the intersection points (e.g., in Fig. 6.5 only p_2), the intersection point I_l, the vertices $\{r_j\}_{j=k_l:1}$ (e.g., in Fig. 6.5 $k_l = 5$), and m_0 to close the PPE. k_l and k_r correspond to the number of vertices of the left and right boundaries of the PPE, respectively, within the area border.

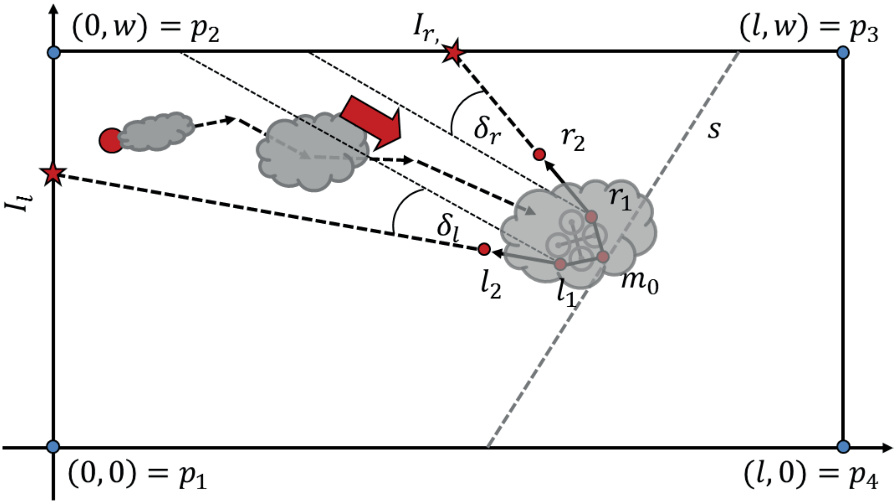

Figure 6.6: *Construction of the PPE for the micro-drone in real-world environments in non-uniform wind fields. The source location is denoted by the large red dot. The measurement radius of the micro-drone is approximated with a simple triangle given by the positions m_0, l_1, and r_1. The search area is defined by the four points p_1 to p_4.*

6.1.1.5 Construction of the Patch Path Envelope (PPE) in Non-Uniform Wind Fields

The method described above can be used for a ground-based mobile robot equipped with a highly precise ultrasonic anemometer under uniform airflow conditions. Since this Ph.D. thesis considers collecting the wind measurements with the micro-drone in turbulent real-world environments with non-uniform wind fields, this approach has to be adapted. Furthermore, the wind direction error (RMSE) in the wind vector estimation approach for the micro-drone is only reasonable when averaging the wind measurements over 20s (Sec. 3.4.3).

The left and right boundaries of the PPE are calculated based on the positions l_1 and r_1 and the azimuth direction angles δ_l and δ_r (Fig. 6.6), which are calculated as follows:

$$\delta_{l,r} = \left(\bar{\theta}_u \pm 90^\circ \cdot S_0\right) \bmod 360^\circ \tag{6.13}$$

In comparison to the original approach, the mean wind direction and the circular

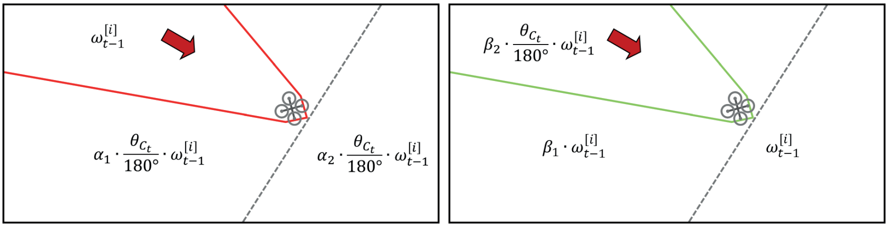

(a) $z_t = 1$

(b) $z_t = 0$

Figure 6.7: *Classification of the particles into three classes for (a) $z_t = 1$ (gas hit $\widehat{=}$ red PPE) and (b) $z_t = 0$ (no gas hit $\widehat{=}$ green PPE): particles located inside the PPE, particles located outside of the PPE in upwind direction with respect to line s, and particles located outside the PPE in downwind direction with respect to line s. The line s is denoted by the gray dotted line.*

variance calculated over the whole time interval ΔT is used to determine the PPE. This time, the polygon delimiting the PPE C_t is constructed counterclockwise by adding the vertex m_0, r_1, the intersection point I_r, all corner points of the area border in between the intersection points, the intersection point I_l, l_1, and m_0 to close the PPE. The output of this stage is the PPE C_t that has an opening angle of $\theta_{C_t} = \delta_l + \delta_r$. The simplified version of the PPE construction is shown in Fig. 6.6.

6.1.2 Update Step

The update phase calculates the new importance weight $\bar{\omega}_t^{[i]} \in \bar{\Omega}_t$ for each particle $\bar{x}_t^{[i]} \in \bar{\mathcal{X}}_t$ based on the previous importance weight $\bar{\omega}_{t-1}^{[i]} \in \bar{\Omega}_{t-1}$, the PPE C_t (Sec. 6.1.1.4), and the binary concentration value z_t (Sec. 6.1.1.1). Particles within the PPE are processed differently than particles that lie outside the PPE. A fast point-in-polygon test based on the Jordan curve theorem is used to decide whether a particle lies within the PPE or not [137]. Furthermore, a straight line s orthogonal to the averaged wind direction is defined that goes through vertex m_0 (in Fig. 6.7 denoted by the gray dotted line). Now, the particles are classified in one of the following three classes: particles located *inside* the PPE ($\bar{x}_t^{[i]} \in C_t$), particles located *outside* of the PPE in upwind direction with respect to line s ($\bar{x}_t^{[i]} \notin C_t \wedge \bar{x}_t^{[i]} \in F_{l,w} \cap S_t$ – see Eq. 6.1), and particles located *outside* the PPE in downwind direction with respect to line s ($\bar{x}_t^{[i]} \notin C_t \wedge \bar{x}_t^{[i]} \in F_{l,w} \setminus S_t$). Then, the following function is used to update the corresponding importance weights:

$$\underbrace{f(\bar{x}_t^{[i]}, \omega_{t-1}^{[i]}, C_t, z_t)}_{\bar{\omega}_t^{[i]}} = \begin{cases} \omega_{t-1}^{[i]} & \text{, if } z_t = 1 \wedge \bar{x}_t^{[i]} \in C_t & \text{(6.14a)} \\ \alpha_1 \cdot \dfrac{\theta_{C_t}}{180^\circ} \cdot \omega_{t-1}^{[i]}, & \text{if } z_t = 1 \wedge \bar{x}_t^{[i]} \notin C_t \wedge \bar{x}_t^{[i]} \in F_{l,w} \cap S_t & \text{(6.14b)} \\ \alpha_2 \cdot \dfrac{\theta_{C_t}}{180^\circ} \cdot \omega_{t-1}^{[i]}, & \text{if } z_t = 1 \wedge \bar{x}_t^{[i]} \in F_{l,w} \setminus S_t & \text{(6.14c)} \\ \beta_2 \cdot \dfrac{\theta_{C_t}}{180^\circ} \cdot \omega_{t-1}^{[i]}, & \text{if } z_t = 0 \wedge \bar{x}_t^{[i]} \in C_t & \text{(6.14d)} \\ \beta_1 \cdot \omega_{t-1}^{[i]} & \text{, if } z_t = 0 \wedge \bar{x}_t^{[i]} \notin C_t \wedge \bar{x}_t^{[i]} \in F_{l,w} \cap S_t & \text{(6.14e)} \\ \omega_{t-1}^{[i]} & \text{, if } z_t = 0 \wedge \bar{x}_t^{[i]} \in F_{l,w} \setminus S_t, & \text{(6.14f)} \end{cases}$$

where $\alpha_{1,2}$ and $\beta_{1,2}$ are meta-parameters which adjust the contribution of the old importance weight $\omega_{t-1}^{[i]}$ of particle $\bar{x}_t^{[i]}$ at iteration t to the new importance weight $\omega_t^{[i]}$ and $\theta_{C_t} \in (0, 180]^\circ$ is the opening angle of the first segment of the PPE (and not of the triangle).

In the case of a detection event (Fig. 6.7(a)), the gas source is assumed to be located *inside* the PPE. Thus, the new importance weight of a particle inside the PPE is set equal to its old weight (Eq. 6.14a). The weighting of particles outside the PPE depends on their relative position to line s: particles located in upwind direction of line s still have a higher probability to be located at the source (Eq. 6.14b) than particles located in downwind direction of line s (Eq. 6.14c). This classification of the particles is implemented by setting $\alpha_1 > \alpha_2$. For simplification, α_2 is set to α_1^2. In the case of a non-detection event, the gas source is assumed to be located *outside* the PPE. Thus, particles inside the PPE should be punished more (Eq. 6.14d) than particles which are located outside (Eqs. 6.14e and 6.14f). Again, particles outside the PPE are distinct due to their relative position to line s. This classification of the particles is implemented as well by setting $\beta_1 > \beta_2 = \beta_1^2$.

The term $\theta_{C_t}/180^\circ$ in Eq. 6.14 additionally punishes particles in dependency of the stability of the wind. The stability of the wind controls the opening angle of the PPE θ_{C_t}, which is calculated as $2 \cdot S_0 \cdot 90^\circ$ (since θ_{C_t} is by definition $\in (0, 180]^\circ$). Small opening angles reflect stable wind conditions. In a detection event, it is assumed that the gas source is located within the PPE as the measured gas was released by the source and transported by the wind and forming a plume. Thus, it is very unlikely that particles which are located outside the PPE reflect the gas source location. Therefore, an additional punishment of these particles is justified. In a non-detection event, it is assumed that the gas source is not located within the

PPE, which allows further punishment of these particles as well. On the other hand, large opening angles indicate unstable wind conditions. Here, it is not possible to limit the large number of possible source locations as the origin of the measured concentration is more uncertain. Therefore, the punishment of the particles should be much lower or should be even omitted, e.g., $S_0 = 1$ results by definition in the maximum possible opening angle of 180°.

6.1.3 Resampling Step

One problem which can occur using PF algorithms is the degeneration of particles, i.e., most of them have negligible importance weights. This impairs the effectiveness of the algorithm. In order to focus the computational resources of the PF algorithm to the relevant regions in the state space [133], *resampling* strategies are needed.

The *resampling* step is a "probabilistic implementation of the Darwinian idea of survival of the fittest" [133]. It draws N particles with replacement from the temporary set $\bar{\mathcal{X}}_t$ according to their importance weights [133], i.e., particles with small importance weights are (probabilistically) eliminated, whereas particles with higher importance weights are (probabilistically) duplicated. *Resampling* requires normalized importance weights:

$$\bar{\omega}_t^{[i]} = \frac{\bar{\omega}_t^{[i]}}{\sum_{i=1}^{N} \bar{\omega}_t^{[i]}}. \tag{6.15}$$

Thus, the resulting particle set $\mathcal{X}_t$ contains many duplicates of the particles with higher importance weights as they are drawn with replacement. Particles, which cannot be found in the set $\mathcal{X}_t$, tend to be those particles with lower importance weights [133]. Gaussian noise is added to the positions of the drawn particles $x_t^{[i]}$ (with $\sigma^2 = 0.1m^2$) to prevent multiple duplicates from being at the exactly same position. The distribution of particles changes during this process. The *resampling* algorithm of Carpenter et al. [138] is used as it is easy to implement, it runs in linear time in the number of particles, and other *resampling* strategies are generally found to provide comparable results [139]. See Appendix F for a formal description of the algorithm. A survey of common *resampling* strategies and variations thereof can be found in [134].

The basic PF algorithm resamples the particle set at each iteration. Liu shows in [140] that *resampling* decreases the efficiency of the sampled representation when the particle weights are approximately the same.

The effective sample size $\hat{N}_{eff}$ is a useful metric to decide whether *resampling* is necessary [141] or not and can be approximated as [142]:

$$\hat{N}_{eff} = \frac{1}{\sum_{i=1}^{N}(\bar{\omega}_t^{[i]})^2}, \tag{6.16}$$

where $\bar{\omega}_t^{[i]}$ is the normalized importance weight of particle $\bar{x}_t^{[i]}$.

If the effective sample size $\hat{N}_{eff}$ drops below a given threshold (e.g., $N/2$) *resampling* should take place, i.e., eliminating particles with small importance weights and duplicating the particles with larger importance weights. Thus, clusters of particles with larger importance weights are formed. This is problematic in a detection event ($z_t = 1$) when no particle is left within the PPE C_t. Therefore, particles are drawn uniformly from the search area $F_{l,w}$ with a probability of $\delta = 0.1$ and the importance weight of each drawn particle is set to $1/N$. To be more specific, the particles are drawn uniformly from the upwind part of the search area with respect to line s ($F_{l,w} \cap S_t$), if $z_t = 1$ (gas-detection event) or from the search area excluding the area of the PPE ($F_{l,w} \setminus C_t$), if $z_t = 0$ (non-detection event).

6.1.4 Estimation of the Gas Source Location

The particle set $\mathcal{X}_t$ can be used to estimate the location of the gas source $\bar{x}_s$. An obvious strategy may be to calculate the weighted mean over all particles as:

$$\bar{x}_s = \sum_{i=1}^{N} \omega_t^{[i]} x_t^{[i]}. \tag{6.17}$$

However, observations have shown that the weighted mean is often not a good estimator since it is strongly affected by outliers (which in addition occur frequently as a consequence of resampling). Furthermore, it is very unlikely that all particles will converge in one certain point considering the turbulent nature of the wind. Assuming the particles to be in a large cluster with the weighted mean located within the cluster or in its close vicinity and the micro-drone already has passed the source, as shown in Fig. 6.8(a), then, it is very unlikely that a concentration above the threshold will be detected if the wind direction has not changed much. That means that from now on all particles are punished except for those that are located in downwind direction of line s (see Sec. 6.1.2). These particular particles will keep their

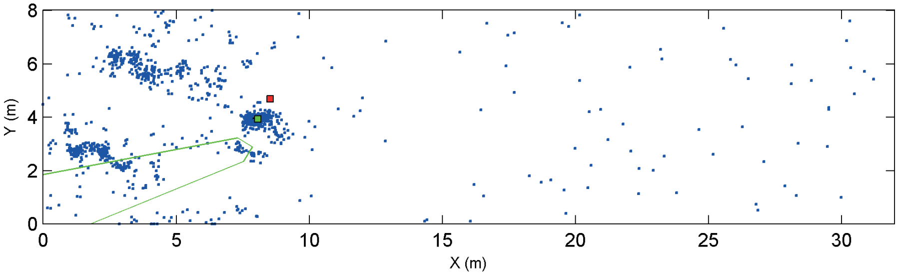

(a) Iteration = 220

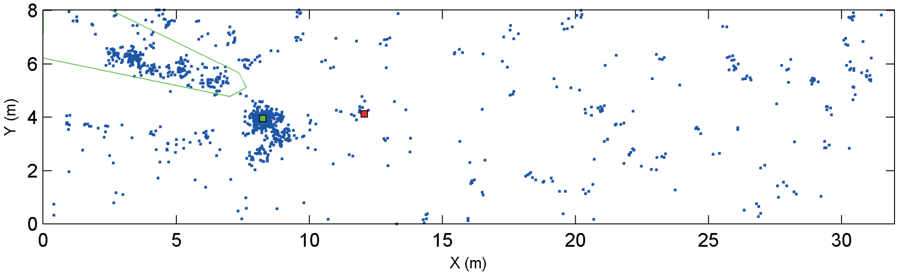

(b) Iteration = 222

Figure 6.8: *PF-based GSL algorithm using sweeping after (a) 220 and (b) 222 iterations. The blue points are the particles. The red point denotes the prediction of the weighted mean and the green point denotes the particle with the highest number of neighbors within a radius of* $\varepsilon = 0.5m$*, which in this case corresponds almost to the true source location.*

old importance weight, which will shift the prediction of the weighted mean away from the cluster further in downwind direction (Fig. 6.8(b)). The *resampling* step speeds up this shift as it introduces (with probability $\delta = 0.1$) uniformly distributed particles and sets the importance weight of each particle to $1/N$.

A more sophisticated strategy involves analyzing the particle clusters that have evolved over time. The proposed strategy searches the particle $x_t^{[k]}$ with the highest number of neighbors within a certain radius ε, i.e., the k for which

$$\left|\left\{x_t^{[j]} \mid \forall j \in [1, N] \wedge k \neq j : |x_t^{[k]} - x_t^{[j]}| \leq \varepsilon\right\}\right|$$

is maximized. In the current implementation, ε is set to $0.5m$. This particle $x_t^{[k]}$ is called the Maximum Neighbors Estimate (MNE) and used as the estimate of the gas source location ($\bar{x}_s = x_t^{[k]}$). The importance weights of the MNEs and increasing

ε are other criteria of meta-parameters to select the gas source location estimate, if more than one particle satisfies this expression. The relative number of neighbors of that particle and their total weight may be used to describe the confidence of the estimate. This approach may be extended by calculating the weighted average over the MNE vicinity. However, this Ph.D. thesis only elaborates on the MNE itself.

6.2 Simulation Experiments

In order to evaluate the performance of the PF-based GSL algorithm, the parameters $\alpha \in [0.1, 1.0]$ and $\beta \in [0.1, 1.0]$ are optimized with respect to the average localization error and the success rate for datasets collected with two different control algorithms: the pseudo gradient algorithm (Ch. 5) and sweeping. The localization error is defined as the distance between the true gas source location and the estimate described in Sec.6.1.4. The success rate is the ratio of successful localizations to the total number of performed experiments, in which the localization error l_{err} is less than or equal to $1.5m$.

6.2.1 Experiment Environment and Setup

The experiment area is a simulated wind tunnel with an area of $32 \times 8m^2$. The flow speed in the wind tunnel was set to $0.5ms^{-1}$. A circular gas source with a radius of $0.2m$ was placed in the experiment area approximately at position $(8, 4)m$ (in Fig. 6.9 illustrated with the red dot). To validate the determined meta-parameter sets, a total of six different source positions were tested. For each control algorithm, each experiment was repeated 100 times. In each run the simulated micro-drone started at position $(32, 0)m$ when using sweeping and at position $(31, y_{source})m$ when using the gradient-based algorithm, where y_{source} corresponds to the y-coordinate of the position of the current gas source. Here, the micro-drone was started directly inside the plume to force the micro-drone to immediately start the plume tracking behavior. The step size for both control algorithms was set to $1m$ to model the system characteristics of the micro-drone. The upwind angle of the gradient-based algorithm was set to 90°. The IR gas sensor model was used to simulate the sensor response (Sec. 4.3). The simple disturbance model (Sec. 4.4) and the GPS model (Sec. 4.2) of the micro-drone were used as well. The measuring time at each sampling location was set to $20s$ with a sampling frequency of $1Hz$. To model the lower limit

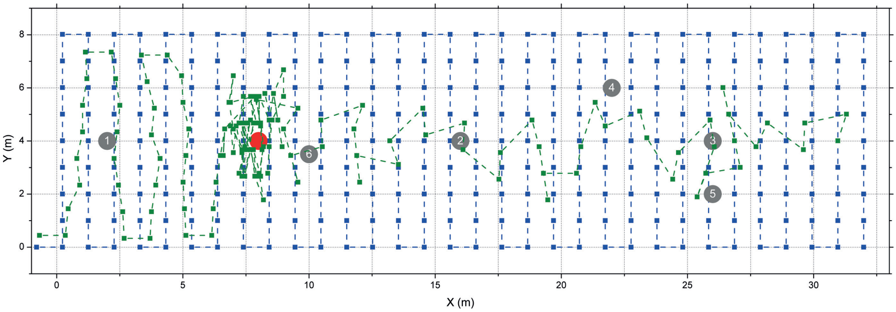

Figure 6.9: *Simulated PF-based GSL experiments. The gray and red dots are the different tested gas source locations (the red source was used for the parameter study). The blue and green squares denote the measurement positions where the micro-drone stopped to take samples. The dashed blue line illustrates the idealized trajectory of the micro-drone using sweeping and the dashed green line illustrates a sample trajectory of the micro-drone using the gradient-based algorithm tracking the plume emitted by the red source.*

of detection of the modeled gas sensor, a threshold th_c was defined and set to 0.05 (the concentration data was normalized before usage). The parameters γ and δ (both related to the PF-based GSL algorithm) were set heuristically to 0.5 and 0.1, respectively. The number of particles N was set to 1,000. The wind sensor noise σ_θ^2 (Sec. 4.5) was set to 14.02. The noise $\sigma_{S_0}^2$ to calculate the circular variance S_0 was set to 23.08 and corresponds to the characteristics of the micro-drone, i.e., the proposed algorithm is optimized especially for the used robotic platform and its measuring capabilities and characteristics.

6.2.2 Experiment Results

6.2.2.1 Parameter Optimization

Fig. 6.10 shows the dependency of the source localization accuracy on the meta-parameters for both control algorithms after the last measurement point for the gas source located approximately at position $(8, 4)m$. In general, it is evident that the average localization error decreases strongly with increasing β. On the other hand, the average localization error increases with increasing α. Thus, it seems to be beneficial to choose a small value for α and a large value for β. This means that,

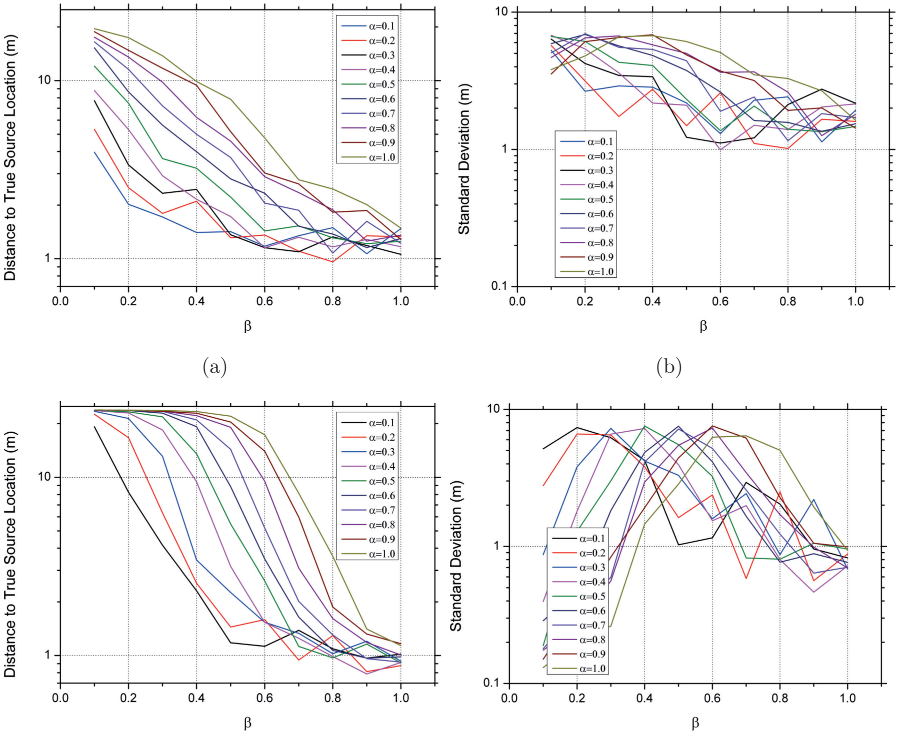

(a) (b)

(c) (d)

Figure 6.10: *Dependency of the source localization accuracy on the meta-parameters of the PF-based GSL algorithm for gradient-based control algorithm [(a) to (b)] and sweeping [(c) to (d)]. Note that the plots are created using a linear scale for the x-axis and a base* 10 *logarithmic scale for the y-axis for better data representation.*

in the case of a gas-detection event, particles located *outside* the PPE are punished much harder (with α or α^2, depending on their position to line s) than, in the case of a non-detection event, those particles located in upwind direction of line s (they are punished with β or β^2 depending on their relative position to the PPE). This position-dependent punishment of the particles allows them to accumulate at the location of the gas source and its close proximity.

A good parameter set for the gradient-based algorithm which minimizes the average localization error and maximizes the success rate is found to be $(\alpha, \beta) = (0.2, 0.8)$ (Figs. 6.10(a) and 6.10(b)). The average error in the simulations with this parame-

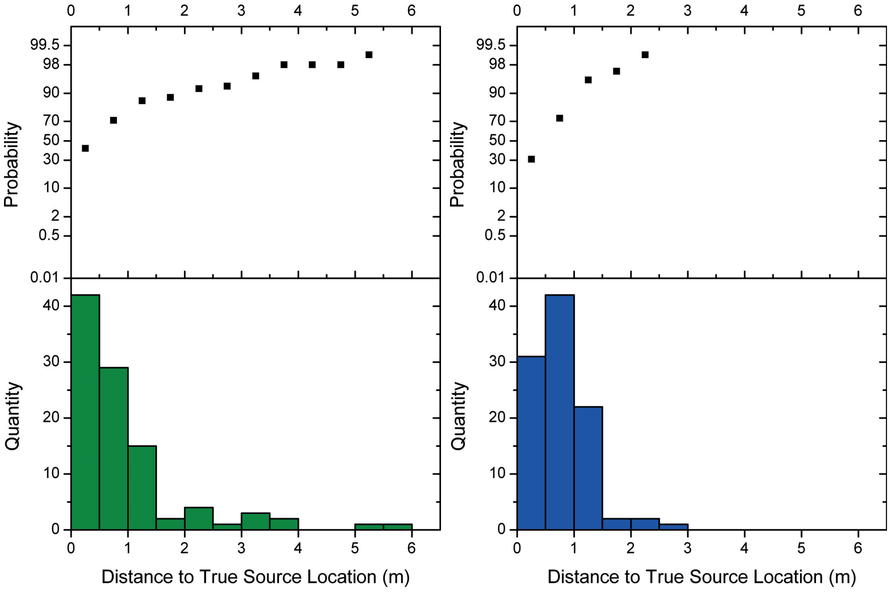

(a) Gradient-based: $\alpha = 0.2$ and $\beta = 0.8$ (b) Sweeping: $\alpha = 0.4$ and $\beta = 0.9$

Figure 6.11: *Classification of the localization error and cumulative success rate of the PF-based GSL algorithm using (a) the gradient-based algorithm and (b) sweeping.*

ter set was only $0.96m \pm 1.01m$ with a success rate of 86% (Appendix D Table D.1). Although the parameter sets $(\alpha, \beta) = (0.3, 0.9)$ and $(0.3, 1.0)$ achieve better success rates (89%), the average localization error is worse for both combinations due to outliers ($1.19m \pm 2.75m$ and $1.06m \pm 2.17m$). Fig. 6.11(a) shows the results for the parameter set $(\alpha, \beta) = (0.2, 0.8)$ in more detail (the parameter sets $(\alpha, \beta) = (0.3, 0.9)$ and $(0.3, 1.0)$ are given in the following as reference in parentheses): 42% of the results have a localization error of $l_{err} < 0.5m$ (34% and 36%), 29% of the results have a localization error of $0.5m \leq l_{err} < 1.0m$ (40% and 36%), and 15% of the results have a localization error of $1.0m \leq l_{err} < 1.5m$ (15% and 17%). For example, the best result for the *weighted mean* over all particles was obtained for the parameter set $(\alpha, \beta) = (0.3, 1.0)$. The average localization error for this parameter set was $2.14m \pm 1.95m$ (with a success rate of 53%).

A good parameter set for sweeping is $(\alpha, \beta) = (0.4, 0.9)$ (Figs. 6.10(c) and 6.10(d)). The average localization error in the simulations with this parameter set was $0.79m \pm 0.46m$ with a success rate of 95% (Appendix D Table D.2). The second best parameter set $(\alpha, \beta) = (0.2, 0.9)$, for example, has an average localization error of $0.81m \pm 0.56m$ with a success rate of 89%. Fig. 6.11(b) shows the results for the parameter set $(\alpha, \beta) = (0.4, 0.9)$ in more detail (the parameter set $(\alpha, \beta) = (0.2, 0.9)$ is given in the following as reference in parentheses): 31% of the results have a localization error of $l_{err} < 0.5m$ (32%), 42% of the results have a localization error of $0.5m \leq l_{err} < 1.0m$ (39%), and 22% of the results have a localization error of $1.0m \leq l_{err} < 1.5m$ (18%). For example, the best result for the *weighted mean* was obtained for the parameter set $(\alpha, \beta) = (0.7, 1.0)$. The average localization error for this parameter set was $1.87m \pm 1.51m$ (with a success rate of 50%).

Comparing the results of the MNE with those obtained with the weighted mean confirms the observations made in Sec. 6.1.4 that the weighted mean is often not a good estimator since it is strongly affected by outliers. The MNE, on the other hand, provides satisfying results (Sec. 6.5 presents directions for future work).

6.2.2.2 Results of the Validation Experiments

To validate the determined meta-parameter sets for each control algorithm, a total of six different source positions were tested. Fig. 6.12 and Table 6.1 show the corresponding results after the last measurement point for both control algorithms.

The average error of successful localizations is given in parentheses in Table 6.1. It can be seen that the success rates using the gradient-based algorithm are in the range of 76 to 89%. The average error of successful localizations is mostly reproducible for all source positions ($\leq 0.62m \pm 0.37m$) except for source #2 and #3, where this error is insignificantly higher ($0.97m \pm 0.31m$ and $1.11m \pm 0.37m$). The average number of erroneous gas source location estimates including outliers ($18.7\% \pm 4.8\%$) is also slightly higher than in the previous experiment (14%).

The success rates using sweeping are in the range of 81 to 92%. The average error of successful localizations can be reproduced for almost all source positions and is $\leq 0.80m \pm 0.37m$. An exception is source #2, where this error is slightly higher ($\leq 0.98m \pm 0.36m$).

A particular challenge for the algorithm using sweeping constitutes source #6 as it is located in the middle of two successive measuring positions centered between two successive sweeps (Fig. 6.9). Still, the algorithm is able to locate the gas source with a success rate of 81%. The error rate of successful localizations is only $0.36m \pm 0.38m$.

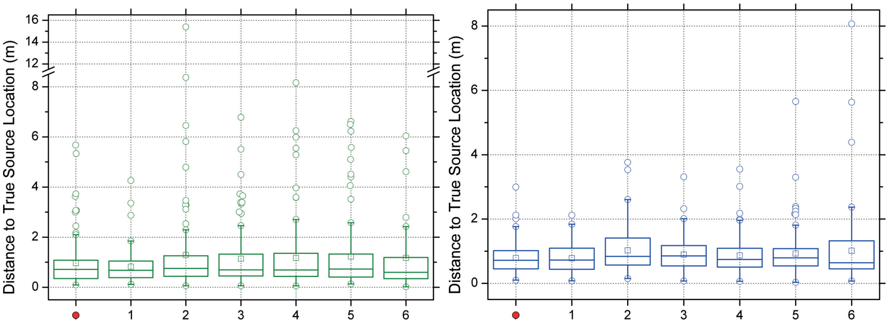

(a) Gradient-based: $\alpha = 0.2$ and $\beta = 0.8$ (b) Sweeping: $\alpha = 0.4$ and $\beta = 0.9$

Figure 6.12: *Box-plot of the gas source location estimate (distance to true source location) for the seven source locations using (a) the gradient-based algorithm and (b) sweeping. The red dot denotes the source used for the parameter study. The box shows the lower/upper quartile and the line denotes the median. The mean is denoted by the small □. The ○ stands for outliers.*

A more detailed evaluation shows that (the result of the parameter optimization is given as a reference in parentheses) 34% of the results have a localization error of $l_{err} < 0.5m$ (31%), 29% of the results have a localization error of $0.5m \leq l_{err} < 1.0m$ (42%), and 18% of the results have a localization error of $1.0m \leq l_{err} < 1.5m$ (22%).

In general, it is evident that the number of outliers of incorrect gas source location estimates is much higher when using the gradient-based control algorithm than using sweeping. The measuring positions of the sweeping trajectory are predefined by the start position and the step size of the micro-drone. The averaged measuring positions differ from the predefined measuring positions only due to the relatively high GPS positioning error of the micro-drone. However, each measuring point of the grid is visited only once. The gradient-based control algorithm shows a different behavior in the immediate vicinity of the source. There, the algorithm often switches its behavior from plume tracking to sweeping and vice versa (Fig.6.9). This precludes further progress of the micro-drone for some time, but might be used to indicate the proximity to the gas source. However, it seems that this behavior in combination with inaccurate wind measurements may disrupt the estimator. Fig. 6.13 shows exemplary the PF-based GSL algorithm using the gradient-based control algorithm after 133 and 134 iterations. After 133 iterations, the algorithms were able to obtain a good estimate of the gas source location (green dot), which was displaced further

Table 6.1: *Results of the validation experiments of the PF-based GSL algorithm. The average error of successful localizations is given in parentheses.*

		Gradient-based		Sweeping	
Source Number	Source Position (m)	Localization Error (m)	Success Rate (%)	Localization Error (m)	Success Rate (%)
●	$(8, 4)$	0.96 ± 1.01 (0.62 ± 0.37)	86	0.79 ± 0.46 (0.72 ± 0.34)	95
1	$(2, 4)$	0.82 ± 0.64 (0.44 ± 0.35)	89	0.78 ± 0.45 (0.80 ± 0.37)	92
2	$(16, 4)$	1.29 ± 1.94 (0.97 ± 0.31)	78	1.02 ± 0.67 (0.98 ± 0.36)	81
3	$(26, 4)$	1.14 ± 1.16 (1.11 ± 0.37)	82	0.90 ± 0.53 (0.78 ± 0.34)	87
4	$(22, 6)$	1.17 ± 1.40 (0.61 ± 0.36)	79	0.87 ± 0.58 (0.77 ± 0.33)	88
5	$(26, 2)$	1.22 ± 1.40 (0.58 ± 0.34)	76	0.93 ± 0.74 (0.77 ± 0.35)	89
6	$(10, 3.5)$	1.18 ± 1.79 (0.30 ± 0.37)	84	1.01 ± 1.08 (0.36 ± 0.38)	81

upwind in the next iteration due to an “erroneous” particle classification in the proximity to the gas source: the gas source is located *inside* the PPE, although no gas-detection event is indicated. In iteration 135, the position of the estimator jumps approximately to position $(4, 4)m$, which almost coincides with the red dot in Fig. 6.13(b).

However, the results are good considering the slow response of the modeled gas sensor and the relatively high GPS positioning error of the micro-drone ($\pm 1.17m$). In the current state of the algorithm, it seems that sweeping is a better strategy to use with the PF-based GSL algorithm than the gradient-based control algorithm for the above mentioned reasons.

6.3 Real-world Experiments

As the PF-based GSL algorithm is only used for estimating the gas source location and not for controlling the micro-drone, no additional real-world experiments are

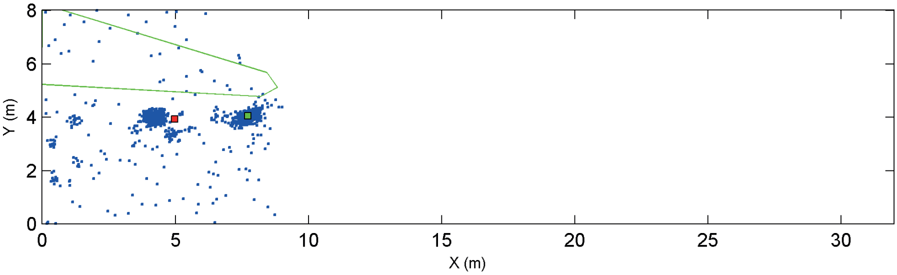

(a) Iteration = 133: $\hat{N}_{eff} = 508.79$

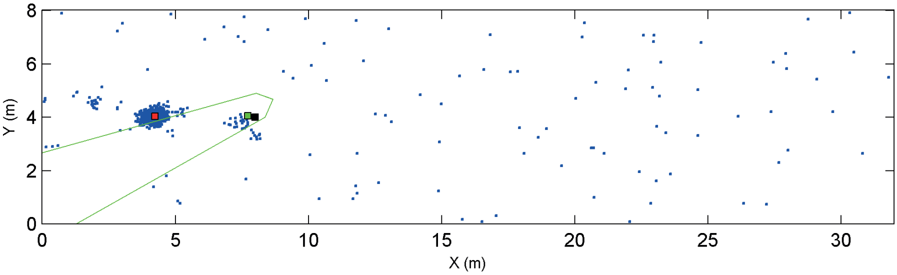

(b) Iteration = 134: $\hat{N}_{eff} = 328.47$

Figure 6.13: *Particles (blue points) of the PF-based GSL algorithm using the pseudo gradient plume tracking algorithm after (a) 133 and (b) 134 iterations (after resampling). The estimated gas source location is indicated by the green point that corresponds to the MNE with* $\varepsilon = 0.5m$*. The red point denotes the prediction of the weighted mean. The true gas source location is denoted by the black point (in (a) hidden by the green point). The PPE for a non-detection event is indicated by the green lines.*

performed. Instead, the obtained experiment data from Ch. 5 (plume tracking) and 7 (gas distribution mapping) is used to test the algorithm under real-world effects.

6.3.1 Experiment Environment and Setup

The experiment setup for the PF-based GSL experiments using plume tracking strategies is described in Sec. 5.3.1, whereas the experiment setup for the experiments using sweeping is described in Sec. 7.3.2 and 7.3.3. However, a short summary of the experiment setups is given below.

The e-nose was used for all experiments performed on the BAM TTS (MOX – CH_4) and for trial #1 and trial #6 to #8 of the experiments performed in the botanical garden (EC – CO_2). For the remaining trials, the Dräger X-am 5600 gas detector was used (IR – CO_2). The step size of the micro-drone varied from 1.0 to 2.0m depending on the individual experiment setup. The altitude of the micro-drone was roughly constant for each experiment and varied between 1.5 and 2.0m. The flight speed of the micro-drone between the measurement positions was set to $1ms^{-1}$. At each measuring position, the micro-drone stopped to take gas concentration and wind measurements for about 20s. A gas cylinder (BAM TTS – CH_4 and botanical garden – CO_2) connected to a pressure-reducing valve was used as the gas source during all selected experiments and placed within the experiment area. The outlet of the gas source was extended with a small tube, which was attached to a fan in order to spread the analyte away from the cylinder. The size of the experiment area varied from $5 \times 5m^2$ to $20 \times 16m^2$.

As in the simulation experiments, the parameters γ and δ were set to 0.5 and 0.1, respectively. The number of particles N was set to 1,000.

6.3.2 Experiment Results

Table 6.2 shows the results of the real-world PF-based GSL experiments. A total number of 6 trials were performed within the scope of the plume tracking experiments presented in Sec.5.3, where each of the following algorithms were conducted twice: surge-cast (trial # 1 and #2), zigzag (trial #3 and #4), and pseudo gradient (trial #5 and #6). The corresponding trajectories of the three plume tracking algorithms can be seen in Sec. 5.3.2, Fig. 5.14. Another 13 trials were performed within the scope of the GDM experiments using predefined sweeping trajectories. Information regarding the wind conditions during the experiments can be found in Secs. 5.3.2, 7.4.2, and 7.4.3.

Although the plume tracking experiments were stopped directly after the micro-drone passed the source, the algorithm was able to locate the gas source with a success rate of 83.3% (5 of 6 trials succeeded). Measurements behind the gas source would have been advantageous to obtain a more accurate and reliable gas source location estimate. However, an average error of successful localizations of $0.69m \pm 0.35m$ (the average localization error is $1.05m \pm 0.94m$) could be obtained. This result is very good considering, e.g., the GPS positioning system error of the micro-drone ($\pm 1.17m$) and is in line with the simulation results presented in Sec. 6.2.2, where the success rate varied from 76 to 89% and the average error of successful

Table 6.2: *Results of the real-world PF-based GSL experiments.*

Trial	#Iterations	Localization Error (m)	#Neighbors $\varepsilon = 0.5m$	Location	Area (m^2)	Strategy
1	25	0.73	242	BAM TTS	20×16	Plume Tracking
2	36	1.18	416			
3	17	0.77	224			
4	29	2.86	608			
5	24	0.56	307			
6	38	0.21	604			
1	28	1.32	308	BAM TTS	5×5	Sweeping
2	28	0.46	186			
3	28	1.09	664			
4	43	0.36	659		20×14	
5	41	0.85	177			
1	42	1.08	174	Botanical Garden	6×6	Sweeping
2	47	1.33	659			
3	21	2.68	454		12×6	
4	25	0.20	236			
5	17	0.45	206			
6	24	0.93	541			
7	25	0.52	145			
8	25	0.89	183			

localizations was between $0.30m \pm 0.37m$ and $1.11m \pm 0.37m$ (the average localization error was between $0.82m \pm 0.64m$ and $1.29m \pm 1.94m$).

The last sweep in the GDM experiments was also performed directly in front of the gas source, i.e., the experiments were stopped immediately after the micro-drone passed the source. Nevertheless, the success rate of 92.3% (12 of 13 trial succeeded) is relatively high. The average error of successful localizations is $0.79m \pm 0.38m$ (the average localization error is $0.94m \pm 0.64m$). Again, this result matches nicely with the simulation results. There, the success rate varied from 81 to 95%. The average error of successful localizations was between $0.36m \pm 0.38m$ and $0.98m \pm 0.36m$ (the average localization error was between $0.78m \pm 0.45m$ and $1.02m \pm 0.67m$).

Trial #2 to #5 of the botanical garden experiments should be highlighted as the TGS4161 gas sensor was used, which has a sensor response of $T_{90} = 1.5min$

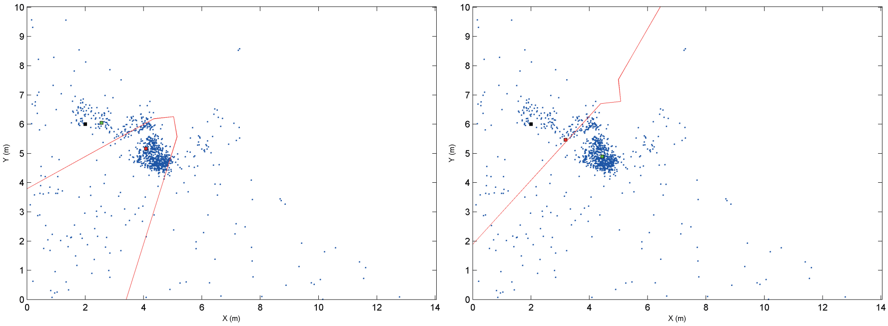

(a) Iteration = 19 (b) Iteration = 20

Figure 6.14: *GDM experiment (trial #3 performed in the botanical garden) after (a) 19 and (b) 20 iterations. The blue points represent the particles of the PF-based GSL algorithm. The estimated gas source location is indicated by the green point that corresponds to the MNE with $\varepsilon = 0.5m$. The red point denotes the prediction of the weighted mean. The true gas source location is denoted by the black point. The PPE for a detection event is indicated by the red lines.*

(the slowest gas sensor used within this Ph.D. thesis). Trial #3 of the botanical garden experiments (Fig. 6.14) is particularly noteworthy as the localization error after 21 iterations is $2.68m$. However, this high localization error was caused by an "erroneous" particle classification during iteration 19 (Fig. 6.14(a)): a gas detection event is indicated and the gas source is located *outside* the PPE. Before that event, the localization error was only $0.56m$. A chronological description of the occurrences offers valuable information about the reason for the incorrect gas source location estimate:

Iteration 18: A relative stable west wind (270° with $S_0 = 0.35$) prevailed during iteration 18, which carried the gas from the source most likely along the x-axis of the experiment area. During that time, the micro-drone was located approximately at position $(4.06, 3.92)m$. The particles are mainly concentrated in the immediate vicinity of the estimator located at position $(2.56, 6.05)m$.

Iteration 19: The micro-drone moved to position $(4.08, 5.95)m$ to take samples, which corresponds nearly to the y-coordinate of the gas source location. This location could have been part of the plume centerline in the previous iteration. At this location, the micro-drone measured a southwest wind (220°), i.e., the

> wind had turned in the meanwhile by almost 50°. The wind was relatively stable during the measuring period ($S_0 = 0.24$ and $r_u = 1.32ms^{-1}$). Although the wind had turned significantly, the micro-drone was able to detect traces of gas, leading to an *erroneous* detection event since the gas source was not located inside the PPE. Finally, *resampling* changed the distribution of the particles, resulting in a displacement of the estimator in iteration 20 (due to a significant drop in the effective sample size $\hat{N}_{eff} = 235.68$).

Another *resampling* after iteration 21 may have restored the previous gas source location estimate due to a correct detection event during iteration 20 (Fig. 6.14(b)). Fig. 6.14(b) shows furthermore what happens to the PPE when unstable wind conditions are present ($S_0 = 0.92$). Here, the opening angle of the PPE reaches almost 171.5° of the maximum possible 180°.

Unfortunately, the small number of experiments does not permit obtaining strong statistical significance of the algorithm's performance. However, the results indicate the potential of this approach for localizing gas emission sources and its suitability for a gas-sensitive micro-drone.

6.4 Related Work

Li et al. [78] performed an experiment with 33 trials over an area of $10 \times 10m^2$ to test the performance of their PF-based GSL algorithm. A humidifier containing liquid ethanol was used as the gas source. As an experiment platform they used a ground-based mobile robot equipped with an anemometer (Windsonic, Gill Instruments Ltd.) and a MOX gas sensor (MiCS-5135, e2v Technologies (UK) Ltd.). The speed of the robot was set to $0.2ms^{-1}$. The wind speed varied from 0.15 to $4.02ms^{-1}$ and the wind direction varied from -270 to 184°. Information concerning the stability of the wind is lacking completely. They considered a run to be successful if the last 20 estimated gas source locations (calculated with the weighted mean over all particles) are within a radius of $\leq 0.5m$. With their approach they were able to obtain a success rate of 79% with an average localization error of $0.29m \pm 0.04m$. It would be interesting to see the results for each individual run to evaluate the performance of the algorithm with respect to outliers. However, due to the different platforms used, the different experiment setups, and the different definition of the success rate it, is not possible to compare the experiment results from Li et al. with the presented results obtained from real-world experiments. A direct comparison of both algorithms using the gas-sensitive micro-drone would be of great interest. Such a comparison would be possible if the corresponding data sets or the source code from Li et al. were available. The data sets recorded within this Ph.D. thesis using the micro-drone will be published online.

In contrast to the PF-based GSL algorithm of Li et al. [78], we introduce a novel PF-based algorithm that uses both gas-detection and non-detection events to estimate the location of a gas source. Furthermore, the proposed approach does not rely on a roughly uniform wind field, which in the real world does not exist. Instead, measured wind data, mean and variance of the wind to be precise, were included in the proposed approach as indicator for the wind stability.

6.5 Summary and Conclusions

This chapter presents a novel PF-based GSL algorithm that is independent from the exploration strategy used. The algorithm uses gas and wind measurements to reason about the trajectory of a gas patch when estimating the gas source location.

In robotic simulations, the meta-parameters of the proposed PF-based GSL algorithm were optimized in order to find optimal parameter sets for the gas-sensitive micro-drone. As control algorithms, a gradient-based algorithm and sweeping were considered. These parameter sets were successfully validated for both control algorithms in additional simulation experiments with variable source positions. However, the simulation results suggest that each control algorithm has its own, different optimal parameter configuration. A possible explanation can be seen in the number of measurements taken inside the plume. A plume tracking strategy tries to stay within the plume and switches only to sweeping when the plume cannot be reacquired, whereas sweeping will not diverge from the predefined measuring grid.

Although the relatively small number of real-world experiments did not allow obtaining strong statistical significance regarding the performance of the proposed algorithm, the results indicate the potential of the proposed approach for accurately localizing a single gas emission source emitting a known chemical compound in turbulent outdoor environments with a micro-drone, also under highly unstable wind conditions (botanical garden experiments). Its suitability for a gas-sensitive micro-drone is shown as well. Furthermore, the results suggest that the different gas sensors used (MOX, EC, and IR) did not have a major impact on the success rate and the localization error. In general, a good correlation between the results from simulation and real-world experiments can be found for both control algorithms using the particular best-suited parameter set.

For purposes of simplification, several parameters of the PF-based GSL algorithm were heuristically set to decrease the complexity of the problem. Future work should investigate the influence of the following parameters in more detail (the parameters which were set heuristically are marked with an asterisk; the remaining parameters were adapted from [78]): $N = 1{,}000$ the number of particles*, $\gamma = 0.5$ the threshold for *resampling* the particle set (adapted from [78]), $\varepsilon = 0.5m$ the radius of the gas source location estimate*, $\lambda = 0.5$ the exponential moving average parameter of the binary concentration threshold (adapted from [78]), $\delta = 0.1$ the probability that a particle is drawn uniformly from the search area instead of the particle set*, and $\sigma^2 = 0.1$ the variance used to add Gaussian noise to the position of particles drawn from the particle set*.

The measurement model of the PF gives ample room for further improvements, e.g., the PPE may be divided into more regions. Particles far away from the measuring position should not be punished the same way as particles located in the immediate vicinity. More sophisticated clustering strategies could be developed to determine the gas source location estimate. Future work should also include extending the algorithm to the 3rd dimension and, of course, more real-world and simulation experiments have to be performed to test the algorithm extensively. Moreover, the micro-drone should also take more samples behind the gas source in the real-world experiments to verify the final estimate and to complete the declaration step independently.

Chapter 7

Gas Distribution Mapping using a Micro-Drone

Gas distribution mapping (GDM) can be used in a number of relevant application areas where a better understanding of the gas dispersion is needed, such as environmental monitoring and safety and security related fields [143]. To build a predictive gas distribution model, the Kernel DM+V/W algorithm introduced by Reggente and Lilienthal [85] is used in this Ph.D. thesis, which is an extension of Kernel DM+V [14] that also considers wind information to compute the gas distribution model. It provides the basis for data interpretation and evaluation of results of autonomous real-world outdoor experiments performed in the geochemically active Tuscany Region (Italy), on the BAM TTS, and in the Botanical Garden of Berlin and it is also part of the adaptive sensor planning algorithm presented in Ch. 8.

The input to this algorithm is a set $D = \{(x_1,r_1,\vec{u}_1),\ \ldots,\ (x_n,r_n,\vec{u}_n)\}$ with gas sensor measurements r_i and airflow measurements $\vec{u}_i$ collected at locations x_i. The output is a grid model that computes an estimate of distribution mean and variance for each cell. The 2D version of the Kernel DM+V/W algorithm [85] is used to avoid the higher computational complexity of the 3D Kernel DM+V/W algorithm [94] and because the limited battery capacity of the micro-drone does not permit a full 3D search. Furthermore, the field of main application is surface monitoring, which demands 2D results. In the experiments, the micro-drone was kept in a single 2D plane. The algorithm is described in more detail in Sec. 7.1.

In the remainder of this chapter, first, the applied GDM algorithm is summarized. Then, the four different experiment environments and setups of the real-world experiments are described (Sec. 7.3). Sec. 7.4 presents the results of the real-world experiments, analyzes differences between gas distribution maps created with the Kernel DM+V and the Kernel DM+V/W algorithm, and investigates the following aspects in detail: time to converge to a stable representation of the natural gas distribution (Sec. 7.4.1), gas sensor technology (Sec. 7.4.3), and reproducibility of the experiments (Secs. 7.4.1 to 7.4.3). Finally, it is concluded that the gas-sensitive micro-drone is suitable for GDM and the limitations given by the platform are presented (Sec. 7.5).

7.1 Kernel DM+V/W Algorithm

The Kernel DM+V/W algorithm [85] works as follows: In the first step, it computes weights $\omega_i^{(k)}$ that model the information content of measurement i at grid cell k. This is done by evaluating a two-dimensional, multivariate Gaussian kernel $\mathcal{N}$ at the distance between the location of the measurement i and the center $x^{(k)}$ of the cell k:

$$\omega_i^{(k)}(\sigma) = \mathcal{N}\left(\left|x^{(k)} - x_i\right|, \sigma\right). \tag{7.1}$$

The shape and orientation of the kernel depend on the local airflow vector $\vec{u}$ and on two meta-parameters that determine a spatial scale (σ) and a wind scale (γ). If no wind is measured (or if no wind information is available), the Gaussian kernel has a circular shape and corresponds to the Kernel DM+V algorithm (Eq. 7.1). In the case of a non-zero wind measurement the kernel is replaced by an elliptic, bivariate Gaussian, which takes the shape of an elongated ellipse with the semimajor axis rotated in wind direction and stretched according to the strength of the wind (Eqs. 7.2 to 7.8). This bivariate normal distribution is governed by a mean vector μ (the point of measurement) and a 2×2 covariance matrix Σ. The covariance matrix is computed according to the local airflow vector $\vec{u}$ at the sensor location as follows:

- To describe the length of the semimajor and semiminor axis of the ellipse (a, b) in terms of the kernel width σ of the symmetric Gaussian kernel, the constraint is set that the area of the ellipse remains constant (Eq. 7.2). The semimajor axis a is stretched according to the strength of the wind and calculated using Eq. 7.3. Eq. 7.4 determines the length of the semiminor axis by combining

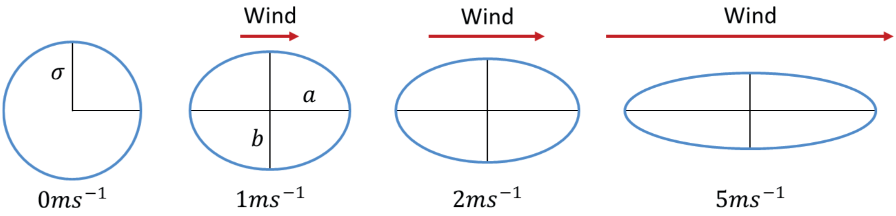

Figure 7.1: *Influence of different wind speeds on the kernel shape with $\gamma = 0.2s$ and $\sigma = 1.2m$. The arrow's length represents the wind speed in ms^{-1}.*

Eqs. 7.2 and 7.3:

$$\pi\sigma^2 = \pi ab \tag{7.2}$$

$$a = \sigma + \gamma \left|\vec{u}\right| \tag{7.3}$$

$$b = \frac{\sigma}{1 + \gamma \left|\vec{u}\right| / \sigma} \tag{7.4}$$

Eqs.7.3 and 7.4 are used to estimate the eigenvalues of the covariance matrix. The covariance matrix is diagonal and the elements of $\Sigma(\sigma_x, \sigma_y)$ are $\sigma_x = a$ and $\sigma_y = b$:

$$\Sigma(\sigma_x, \sigma_y) = \begin{pmatrix} \sigma_x & 0 \\ 0 & \sigma_y \end{pmatrix} = \begin{pmatrix} a & 0 \\ 0 & b \end{pmatrix}. \tag{7.5}$$

- The covariance matrix is rotated so that the semimajor axis is aligned with the wind direction θ:

$$\Sigma_{R(\theta)} = R(\theta)\Sigma R(\theta)^{-1}, \tag{7.6}$$

where

$$R(\theta) = \begin{pmatrix} \cos\theta & -\sin\theta \\ \sin\theta & \cos\theta \end{pmatrix} \tag{7.7}$$

is the rotation matrix.

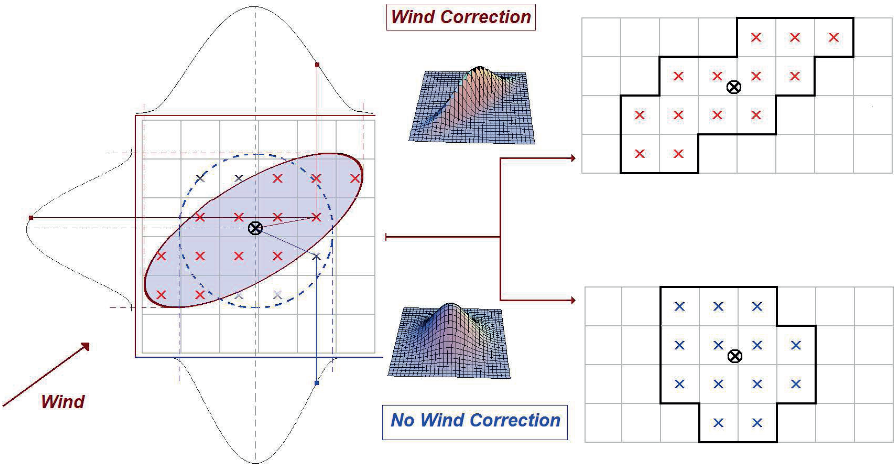

Figure 7.2: *Discretization of the Gaussian kernel onto a grid. Left side: Model of the information content of a gas sensor reading (the sampling location is depicted in the center by a black ⊗) in the case of a radially symmetric Gaussian kernel and bivariate Gaussian kernel, respectively. The blue dashed circle represents the contour of the kernel in absence of wind and the red solid line shows the elliptic contour of the kernel for the case of non-zero wind. Right side: strongly affected cells are surrounded by a strong border. The figure and caption were reproduced from Reggente and Lilienthal [85].*

- Finally, the Mahalanobis distance D between the location of the measurement i and the center $\mu = x^{(k)}$ of the cell k is used to calculate the corresponding weights:

$$\omega_i^{(k)}(\sigma) = D(x_i, x^{(k)}) = \sqrt{(x_i - x^{(k)})^T \Sigma_{R(\theta)}^{-1} (x_i - x^{(k)})} \tag{7.8}$$

  Fig. 7.2 illustrates how the wind correction is applied and Fig. 7.1 shows the influence of the different wind speeds on the kernel shape with $\gamma = 0.2s$ and $\sigma = 1.2m$.

Second, weights $\omega_i^{(k)}$, weighted sensor readings $\omega_i^{(k)}(\sigma) \cdot r_i$, and weighted variance contributions $\omega_i^{(k)}(\sigma) \cdot (r_i - r^{k(i)})^2$ are integrated and stored in temporary grid maps:

$$\Omega^{(k)}(\sigma) = \sum_{i=1}^{n} \omega_i^{(k)}(\sigma), \tag{7.9}$$

$$R^{(k)}(\sigma) = \sum_{i=1}^{n} \omega_i^{(k)}(\sigma) \cdot r_i, \tag{7.10}$$

$$V^{(k)}(\sigma) = \sum_{i=1}^{n} \omega_i^{(k)}(\sigma) \cdot (r_i - r^{k(i)})^2. \tag{7.11}$$

The variance contributions are computed using the difference between the actual measurements r_i and the corresponding prediction of the model $r^{(k(i))}$, i.e., the predictive mean for the grid cell $k(i)$ closest to the point at which r_i was measured.

Third, a confidence map $\alpha^{(k)}$ is computed from the integrated weights $\Omega^{(k)}$ using another scaling parameter σ_Ω as a soft threshold:

$$\alpha^{(k)}(\sigma) = 1 - e^{-\frac{\Omega^{(k)}(\sigma)}{\sigma_\Omega^2}}. \tag{7.12}$$

The confidence map expresses an increased confidence at locations for which a large number of sensor readings is available in the close vicinity (“close” is to be understood relative to the kernel width σ).

Finally, the map estimate of the mean $r^{(k)}$ and the corresponding variance estimate $v^{(k)}$ is calculated using Eqs. 7.13 and 7.14 as

$$r^{(k)}(\sigma) = \alpha^{(k)} \frac{R^{(k)}}{\Omega^{(k)}} + \left\{1 - \alpha^{(k)}\right\} \cdot \bar{r}, \tag{7.13}$$

$$v^{(k)}(\sigma) = \alpha^{(k)} \frac{V^{(k)}}{\Omega^{(k)}} + \left\{1 - \alpha^{(k)}\right\} \cdot \bar{v}. \tag{7.14}$$

The final estimate is obtained by linear interpolation between the map prediction and an *a priori* estimate for cells with low confidence. For the mean, the *a priori* estimate $\bar{r}$ is computed as the average concentration over all sensor readings. Similarly, the average over all variance contributions $\bar{v}$ is used to estimate the distribution variance in regions far away from measurement points.

Note that measurements in between two sampling locations are not used in this creation process to reduce the influence of a memory effect in the sensor response due to the slow sensor recovery. Furthermore, the wind vector was averaged over all the measurements collected at a measurement position due to the accuracy of the wind vector estimation presented in Sec. 3.4, i.e., the average wind vector was used for all individual gas sensor measurements acquired at the measurement position.

7.2 Data Acquisition Strategy

Lilienthal and Duckett suggest in [130] (for a precursor of the Kernel DM+V/W algorithm) that in order to build concentration grid maps, the sensor's trajectory must roughly cover the search space and measurements must be taken from multiple directions: 1. to update cells multiple times, 2. to increase spatial accuracy, and 3. to compensate the memory effect in the sensor response due to the slow sensor recovery. This can be achieved in a straightforward way by moving a mobile robot along predefined trajectories that comply with the above mentioned requirements. For example, Lilienthal programmed his mobile robot to move along two different predefined trajectories: a rectangular spiral and a sweeping movement [5]. The rectangular spiral consists of a sequence of inward and outward movements with randomly chosen starting corner and direction. The sweeping movement was implemented as a trajectory consisting of four segments scanning the area from each starting corner.

In the case of a micro-drone, which introduces sustainable disturbances to gas distribution and thus destroys important evidence, it is not desirable to visit measurement positions more than once in a certain time period. Moving the micro-drone along a spiral is also problematic as the disturbance in the upwind part of the spiral could destroy the plume structure in its downwind part. In order to obtain more truthful gas distribution models, the micro-drone is moved in each experiment along a predefined sweeping trajectory preferably in upwind direction. As a result, the effect that has the disturbances of the micro-drone on the resulting gas distribution model is expected to be minimized. Furthermore, building detailed gas distribution maps over large areas is time-consuming and the batteries of the micro-drone (equipped with payload) only provide power for approximately $20min$. Thus, performing just a single sweep is desirable for the above mentioned reasons. Ch. 8 will introduce a more sophisticated data acquisition strategy based on artificial potential fields and locality constraints.

7.3 Experiment Environments and Setup

In the following Secs. 7.3.1 to 7.3.3, the experiment environments and setups of the real-world GDM experiments are described in detail. Three sets of experiments with a total of 22 trials were performed in the Tuscany Region [Paper I, Paper III], on the BAM TTS [Paper II, Paper IX], and the Botanical Garden of Berlin [Paper X]. The first set of experiments was conducted in volcanic environments with several natural gas sources emitting high concentrations of, i.a., CO_2 and H_2S. The second and third sets of experiments were performed under more controlled conditions with an artificial gas source. The size of the exploration area and the distance between consecutive waypoints in x- and y-direction can be seen in Table 7.1, which provides a brief summary of the experiment environments and the corresponding experiment setups.

Note that the origin of the local coordinate system does not coincide with the starting positions of the micro-drone, which are indicated in Figs. 7.3 to 7.6 by the red stars.

7.3.1 Tuscany Region

A first set of ten real-world GDM experiments were performed in the geochemically active Tuscany Region close to Mount Amiata (Italy). The first four trials were performed in the riverbed of the Ambra river close to the city Arezzo, whereas the last five trials were performed in a region called “Inferno” close to the village Bagni San Filippo. Both locations had the advantage of containing several natural gas sources emitting high concentrations of, e.g., carbon dioxide (CO_2) and hydrogen sulfide (H_2S).

Table 7.1: *Experiment environments and setup of the GDM experiments.*

Location	Area m^2	Waypoint Distance $(x, y)m$	Gas Source	Source Type	Trials
Tuscany Region	5×20	$(2.5, 4.0)$	CO_2	natural, area	4
	20×24	$(4.0, 4.0)$	CO_2, H_2S		6
BAM TTS	5×5	$(1.0, 1.0)$	CH_4	artificial, point	3
	20×14	$(2.0, 2.0)$			2
Botanical Garden	6×6	$(1.0, 1.0)$	CO_2	artificial, point	2
	12×6	$(2.0, 2.0)$			6

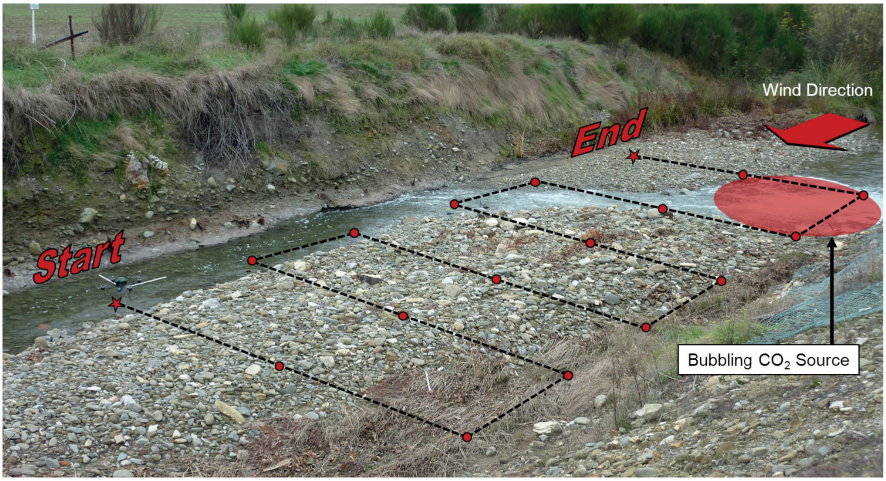

Figure 7.3: *Pre-programmed flight trajectory of the micro-drone within the "Ambra" experiments. The red area indicates the approximately* $3.0 \times 3.0m^2$ *large area source located in the upper one-third of the experiment area. The red dots indicate the sampling locations on the trajectory, whereas the starting and end points are indicated by red stars. The red arrow illustrates the main wind direction during the experiments.*

7.3.1.1 Ambra River Trials

The first four trials were performed in the Ambra river's riverbed over an area of $5 \times 20m^2$. The sweeping trajectory of the micro-drone was pre-programmed with the measurement campaign software (Sec. 3.5.2) and uploaded to the micro-drone before the experiments. In the experiments the step size was set to $2.5m$ in x direction and $4.0m$ in y direction. Starting and end points of the trajectory are labeled accordingly with a red star (Fig. 7.3). The Dräger X-am 5600 gas detector was equipped with CO_2, H_2S, CO, and CH_4 sensors. Measurements were recorded at a frequency of $1Hz$. The red dots show the positions where the micro-drone stopped to take gas concentration and wind measurements for about $20s$, which corresponds roughly to the response times of the used sensors. The position was controlled using only the on-board GPS of the micro-drone. The micro-drone was set to autonomous waypoint mode directly after take-off, which started the experiment. The flight speed of the micro-drone between the stops was set to $1ms^{-1}$. Because of the low altitude of the micro-drone of about 0.3 to $0.5m$, the altitude was kept constant manually during the

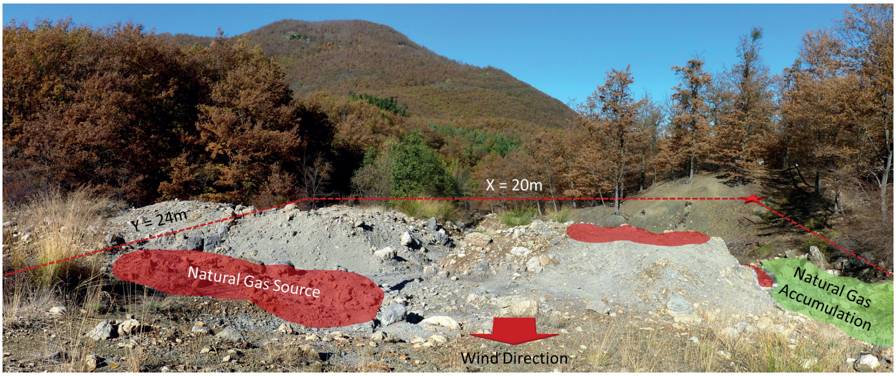

Figure 7.4: *Experiment environment and setup of the "Inferno" experiments. The geologic characteristics of this area are highlighted with transparent area markings: The red areas indicate three visible, naturally bubbling CO_2 and H_2S area sources of approximately $6.0 \times 3.0m^2$ (left), $3.0 \times 1.0m^2$ (middle), and $2.0 \times 2.0m^2$ (right). The green area shows a zone of natural gas accumulation forming a "river" to the right of the elevation in the middle. The information about this zone was given by a local expert and was confirmed by several control samples taken by hand. The red arrow shows the main wind direction. The starting point of the micro-drone is indicated by the red star in the rear right corner of the experiment area.*

experiments. Take-off and landing were also performed manually. Each trial took about 10 to $12min$ to complete. The time between the experiments was $5min$, i.e., relatively short as the disturbance of the gas distribution by the micro-drone is still visible in subsequent trials. A naturally bubbling CO_2 area source of approximately $3.0 \times 3.0m^2$ was within the upper one-third of the experiment area with the center located at position around $x = 5.5m$ and $y = 22.0m$ (Fig. 7.7).

7.3.1.2 Inferno Trials

Another five trials were conducted over an area of $20 \times 24m^2$ in a region called "Inferno" (Fig. 7.4). The experiment setup was comparable to the one described in Sec. 7.3.1.1 with the following exceptions: The step size in x and y direction was set to $4.0m$. Furthermore, three visible, naturally bubbling CO_2 and H_2S area sources of approximately $6.0 \times 3.0m^2$ (left), $3.0 \times 1.0m^2$ (middle), and $2.0 \times 2.0m^2$ (right) were located within the experiment area. Their centers were located approximately

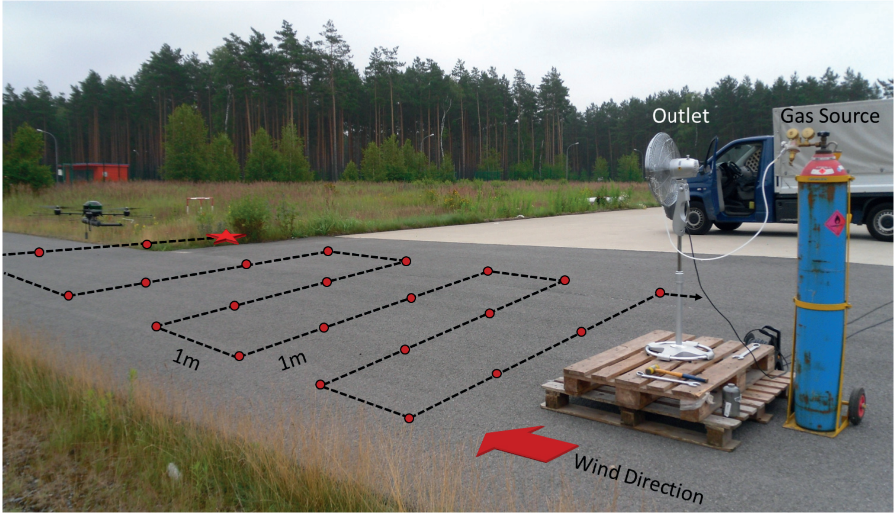

Figure 7.5: *Experiment environment and setup of the experiments performed on the BAM Test Site 'Technical Safety'. The pre-programmed flight trajectory of the micro-drone is shown with a dashed line. The red dots indicate the sampling positions on the trajectory, whereas the starting point is indicated by the red star. The red arrow illustrates the main wind direction during the experiments. The combination of a CH_4 gas cylinder and a fan was used as the emission source.*

at position $(11, 18)m$, $(15, 12)m$, and $(17, 5)m$ (Figs. 7.8 and 7.9). A zone of natural gas accumulation was also located inside the experiment area. Its center was located approximately at position $(10, 2.5)m$. The information about the zone of natural gas accumulation was given by a local expert and was confirmed by several control samples taken by hand.

Additionally, the experiments were performed on two different days with different weather conditions (foggy vs. sunny). This time, the time between the experiments was $30min$ on day 1 and approximately 10 to $15min$ on day 2.

7.3.2 BAM TTS Trials

Fig. 7.5 shows the experiment setup of the second set of five GDM experiments. The experiments were carried out in a natural environment on the BAM Test Site 'Technical Safety' (BAM TTS) over an area of $5 \times 5m^2$ and $20 \times 14m^2$ (Fig. 7.5).

The area is surrounded by trees and buildings, which introduced a certain level of turbulence. The micro-drone was equipped with the e-nose (Sec. 3.2.2), which supports a sampling rate of $8Hz$ for each sensor. The step size of the micro-drone in x and y direction was set to $1.0m$ for the smaller area and $2.0m$ for the larger area. The flight speed of the micro-drone between the measurement positions was set to $1ms^{-1}$. The micro-drone was programmed to explore the experiment areas following a sweeping trajectory using the autonomous control software presented in Sec. 3.5.3. The starting point is illustrated by the red star. Because of the low altitude requirement of the micro-drone, the altitude was kept constant manually at about 1.5 to $2.0m$ during the experiments. A CH_4 (99.5%-pure methane) gas cylinder connected to a pressure-reducing valve was used as the gas source. The outlet of the gas source was extended with a small tube which was attached to a fan in order to spread the analyte away from the cylinder. The air current introduced by the fan also prevented the CH_4 from immediately rising up to the atmosphere when released [PAPER II]. The micro-drone was set to autonomous waypoint mode directly after take-off, which started the experiment.

7.3.3 Botanical Garden Trials

The last set of experiments was performed in the Botanical Garden of Berlin over an area of $6 \times 6m^2$ and $12 \times 6m^2$ (Fig. 7.6). The experiment setup was similar to the one described in Sec. 7.3.2 with the following exceptions: A CO_2 gas cylinder was used as the gas source and four fans were placed in the experiment area instead of one. The gas outlet was connected to one of the two fans in the middle (see Fig. 7.6). Both the e-nose (Sec. 3.2.2) and the Dräger X-am 5600 gas detector (Sec. 3.2.1) were used successively, each equipped with CO_2 sensors. The CO_2 sensor of the e-nose is based on an EC cell, whereas the Dräger X-am 5600 gas detector was equipped with the corresponding IR sensor. In total, four trials were performed for each sensor configuration.

The e-nose uses the Figaro TGS4161 gas sensor (EC) for the CO_2 measurements. The measurement range is $[350, 10{,}000]ppm$ with a resolution of $1ppm$. The Figaro sensor offers a high selectivity to CO_2. However, this sensor is characterized by a slow sensor response ($T_{90} = 1.5min$) and an accuracy of only ±20% (at $1{,}000ppm$ steady state). On the contrary, the Dräger X-am 5600 gas detector uses the IR gas sensor to perform accurate CO_2 concentration measurements (±5%). The measurement

Figure 7.6: *Experiment environment and setup of the experiments performed in the Botanical Garden of Berlin. The starting point is indicated by the red star. The red arrow illustrates the main wind direction during the experiments. The rectangular area marked with the red dashed line shows the experiment area of* $6 \times 6m^2$*, whereas the rectangular area marked with the black dashed line shows the* $12 \times 6m^2$ *experiment area.*

range is $[0, 25]$ % by volume with a resolution of 0.01% by volume. The advantage of the IR gas sensor is the faster sensor response of only $T_{90} \leq 10s$ *(pump)* and $T_{90} \leq 50s$ (diffusion). The lower resolution of only 0.01% by volume can definitely be identified as a disadvantage of the IR sensor.

7.4 Results of the Real-world Experiments

The sets of gas distribution maps presented in this section were created using the Kernel DM+V/W algorithm [85] (Sec. 7.1) with γ heuristically set to $0.2s$ and a cell size of $0.15m$. The kernel width σ was also set heuristically and varied from 0.4 to $1.2m$ depending on the experiment setup. The smaller value of the kernel width was chosen when a dense set of measurements was available (i.e., the spacing along the exploration path was $1m$), whereas the larger value served to smooth the maps accordingly when only sparse measurements distributed over a large area

Table 7.2: *Wind conditions during the Ambra experiments.*

Trial	#Samples	Mean Wind Speed (ms^{-1})	σ (ms^{-1})	Mean Wind Direction (°)	Circular Variance
1	1,684	0.86	±0.58	57	0.94
2	2,649	1.04	±0.62	299	0.67
3	2,362	0.74	±0.62	330	0.73
4	2,113	0.71	±0.58	30	0.87

were available (i.e., the spacing along the exploration path was $\geq 2m$; see Table 7.1). Generally, it was required to obtain high confidence ($\alpha^{(k)}$) over the whole experiment area and not only along the trajectory of the micro-drone due to an undersized Gaussian kernel. The exact value of σ_Ω is not critical as long it is of the right scale [144], it was set in relation to the kernel width to $\mathcal{N}(0, \sigma)$.

For each trial, an airflow map was generated using the corresponding experiment data. At each waypoint where the micro-drone was stopped to take samples, a mean wind vector was computed. The arrow's length in the airflow maps in Figs. 7.7 to 7.12 represents the average wind speed and the circular mean direction is represented by the arrow's orientation. For the purpose of simplification the wind direction was rotated so that the top, right, bottom, and left of each airflow diagram correspond to the cardinal directions: north (0° and 360°), east (90°), south (180°), and west (270°). In Tables 7.2 to 7.5, the mean wind direction is reported by the direction from which it originates. Unless explicitly described, the blue squares denote the measurement positions where the micro-drone stopped to take samples and the dashed blue line illustrates the trajectory of the micro-drone in each airflow map.

7.4.1 Tuscany Region

7.4.1.1 Ambra River Trials

Wind conditions during all four trials were relatively unstable (Table 7.2). The average wind speed was in the range of approximately 0.7 to $1.0ms^{-1}$ and the average wind direction was between 299° and 30°. The degree of stability for each trial is given by the circular variance which was around 0.67 and 0.94.

Fig. 7.7(a) illustrates the predictive mean map and the predictive variance map

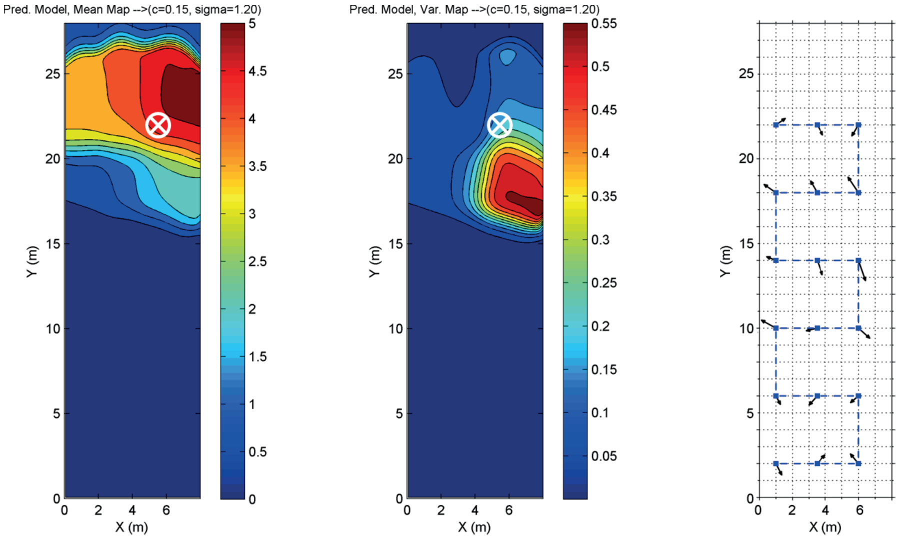

(a) Trial #1; CO_2

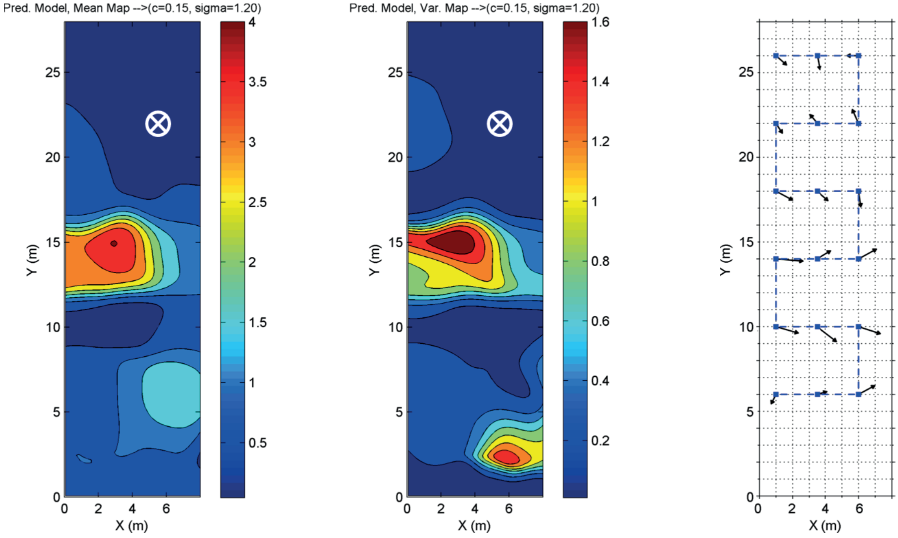

(b) Trial #2; CO_2

Figure 7.7: *Ambra experiments: Predictive mean (left) and variance map (middle) of the gas distribution (in % by volume) and the mean airflow map (right) of the (a) 1st to (d) 4th trial. The center of the area source is denoted by* $\otimes$. *The starting position of the micro-drone is (a)* $(1,2)m$ *and (b) to (d)* $(1,6)m$.

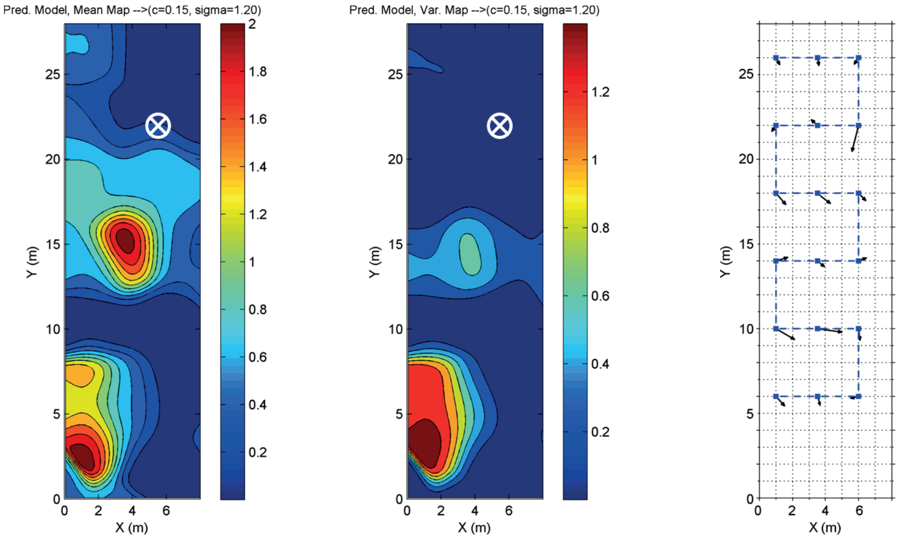

(c) Trial #3; CO_2

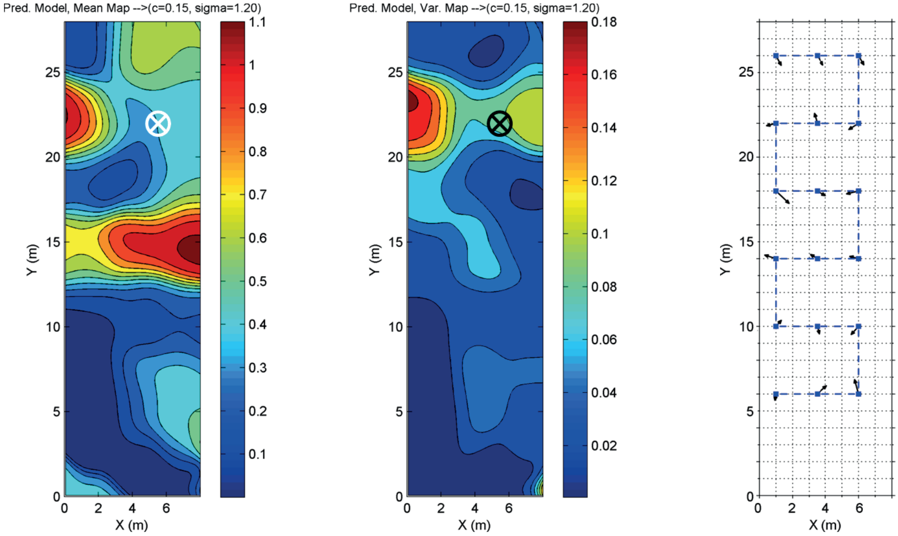

(d) Trial #4; CO_2

Figure 7.7: *Ambra experiments: Predictive mean (left) and variance map (middle) of the gas distribution (in % by volume) and the mean airflow map (right) of the (a) 1st to (d) 4th trial. The center of the area source is denoted by* $\otimes$. *The starting position of the micro-drone is (a)* $(1, 2)m$ *and (b) to (d)* $(1, 6)m$.

of the gas distribution and the computed airflow map in the first trial. Here, the position of the maximum measured concentration correlates approximately with the position of the gas source in the map (compare with Fig. 7.3) as the first trial likely had the advantage of an intact natural gas distribution. Figs. 7.7(b) to 7.7(d) show the results of the subsequent trials where the maximum of the predictive mean appears approximately in the middle of each map. Since the time between the experiments was only $5min$, a likely explanation is that the micro-drone's rotors, which act like a mixer that destroys the original gas dispersion pattern, have caused an alteration in the gas distribution by changing the magnitude and the position of the concentration maxima in the first trial. This finding is supported by the observation that the maximum concentration decreased steadily over the four trials. Since re-adjusting of the natural gas distribution needs time, the first trial is more relevant and provides best results to reflect the area's gas emitting characteristics. The change in the sweeping pattern (and the starting point) $4m$ to the north after the first trial was performed to obtain more relevant data close to the area source without changing the remaining measurement positions from the first trial. Only the sequence of visits was changed.

Higher reproducibility is given for trials #2 to #4 and the qualitative results remain more constant in all three created maps. The quantitative results differ more pronouncedly as the maximum concentrations decrease over time and with increasing disturbance/ventilation induced by rotor movement. However, the four trials can be seen as a chronological sequence as the maximum concentration decreases over time. Further experiments were performed in other parts of the Tuscany Region with similar results (Sec. 7.4.1.2).

The results (predictive mean and variance maps) of the Kernel DM+V/W algorithm are very similar to the results of the Kernel DM+V algorithm and are therefore not shown here. One reason for this is the small chosen parameter γ, which stretches the kernel according to the strength of the wind, and the low wind speeds during all trials (see Fig. 7.1).

7.4.1.2 Inferno Trials

The experiments in the Inferno region were performed on two different days under different weather conditions. The first day was foggy with an average temperature of approximately $12°C$ and an average relative humidity of 77%. The average wind

Table 7.3: *Wind conditions during the Inferno experiments.*

Day	Trial	#Samples	Mean Wind Speed (ms^{-1})	σ (ms^{-1})	Mean Wind Direction (°)	Circular Variance
1	1	3,999	0.42	±0.37	209	0.83
	2	4,418	0.41	±0.36	98	0.78
2	3	5,287	1.32	±0.78	92	0.54
	4	4,026	1.24	±0.64	75	0.56
	5	3,631	0.45	±0.41	105	0.97
	6	3,193	1.08	±0.76	49	0.86

speed during the experiments was $0.4ms^{-1}$. The directional component of the measured wind was most likely affected by the combination of the low wind speed and the inaccuracies given by the GPS receiver (Sec. 3.1.1). Thus, no reliable statement concerning the degree of stability of the wind conditions can be made as the micro-drone consistently measured very low wind speeds. Altogether the weather conditions on the first day permitted higher gas accumulations close to the ground as no strong wind flow was present. The second day was sunny with an average temperature of almost $18°C$ and an average relative humidity of 58%. The average wind speed was in the range of approximately 1.1 to $1.3ms^{-1}$ and the average wind direction was between 49° and 105°. The circular variance was around 0.54 and 0.86. An exception is trial #5 where the average wind speed lay around $0.5ms^{-1}$ again (compare with day 1). The stronger wind conditions of the second day likely enhanced dispersion and dilution of the volcanic gases. Additionally, a significantly higher solar radiation produced convective currents, which further dispersed and diluted the volcanic gases. Therefore, lower maximum concentration levels were measured over the experiment area. This can be observed in Fig. 7.8 comparing trial #1 and #3 and in Fig. 7.9 comparing trial #1 and #6.

The results from selected GDM experiments can be seen in Figs. 7.8 and 7.9. Figs. 7.8(a) to 7.8(c) and Figs. 7.9(a) to 7.9(c) show the predictive mean map (left) and the predictive variance map (middle) of the CO_2 and H_2S distribution, respectively. The corresponding airflow maps can be seen in the right part of each figure. It seems that especially the created gas distribution maps from day 1 reflect the area's gas emitting characteristics best as the positions of the concentration rich ar-

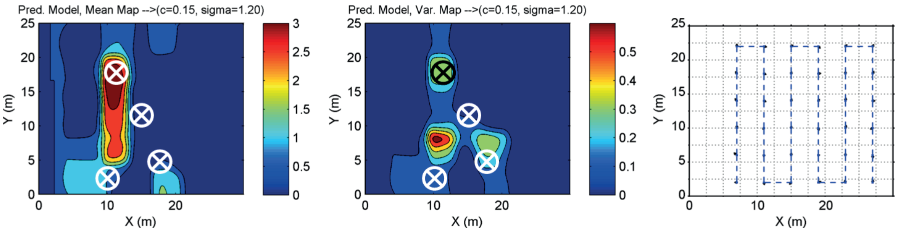

(a) Trial #1; day 1; CO_2

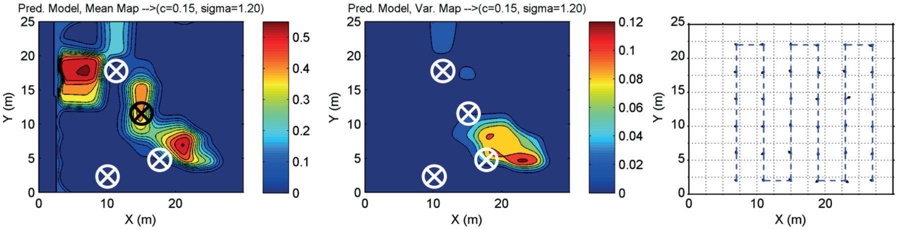

(b) Trial #2; day 1; CO_2

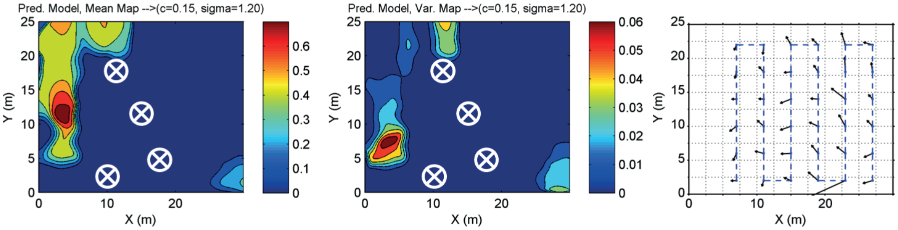

(c) Trial #3; day 2; CO_2

Figure 7.8: *Inferno experiments: Predictive mean (left) and variance map (middle) of the gas distribution of the (a) 1st, (b) 2nd, and (c) 3rd trial. The figures on the right show the corresponding mean airflow maps and the path of the micro-drone. The centers of the area sources are denoted by* $\otimes$. *The starting position of the micro-drone is located at position* $(27, 2)m$. *The* CO_2 *concentration value is given in % by volume.*

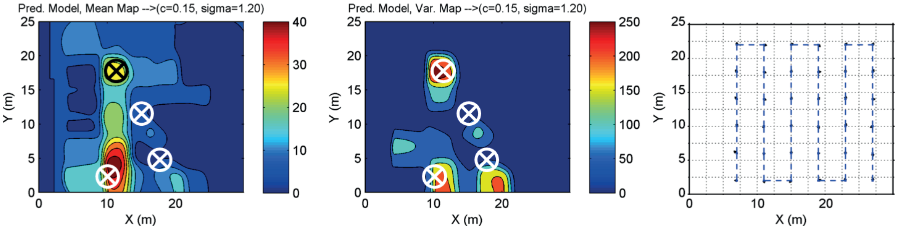

(a) Trial #1; day 1; H_2S

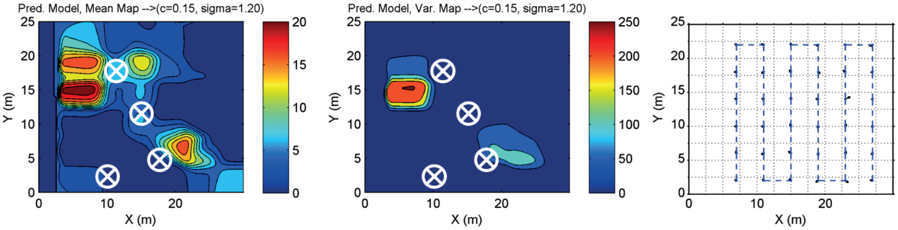

(b) Trial #2; day 1; H_2S

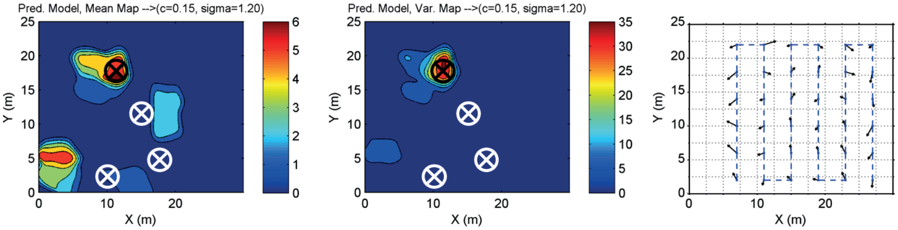

(c) Trial #6; day 2; H_2S

Figure 7.9: *Inferno experiments: Predictive mean (left) and variance map (middle) of the gas distribution of the (a) 1st, (b) 2nd, and (c) 6th trial. The figures on the right show the corresponding mean airflow maps and the path of the micro-drone. The centers of the area sources are denoted by* $\otimes$. *The starting position of the micro-drone is located at position* $(27, 2)m$. *The* H_2S *concentration value is given in ppm.*

eas correspond roughly to several naturally bubbling area sources. However, it can be observed that not every source can be found in the final map for various reasons (e.g., unknown release rate). The qualitative results remain more or less comparable. This can be seen when comparing Figs. 7.8(a) and 7.8(b) from day 1 with each other (CO_2) and Figs. 7.9(a) and 7.9(b) from day 1 with Fig. 7.9(c) from day 2 (H_2S). However, the gas distribution maps from day 2 (Fig. 7.8(c)) differ more strongly from those created on day 1 (Figs. 7.8(a) and 7.8(b)). A likely explanation is that the different weather and wind conditions (i.a., higher wind speeds on day 2) did not allow the gas to accumulate in the vicinity of their sources resulting in a poor correlation. The quantitative results differ more strongly. The maximum concentration on day 1 (and day 2) decreases over time and with increasing disturbances induced by rotor movement. Here, a drop in the maximum concentration from 3 to approximately 0.5 % by volume (CO_2) and from 40 to $20ppm$ (H_2S) was detected. The drop in concentration is another indication for the assumption that the influence of the micro-drone's rotors causes dispersion that changes the magnitude and the position of the concentration maxima and that re-adjusting of the natural gas distribution needs time (depending on the release rate of the gas source). Again, the first trial probably altered the gas distribution. Additionally, weather and wind conditions on the second day did not permit repetition of the high concentration measurements from the first day. This can be seen by comparing Figs. 7.8(a) and 7.8(c).

The predictive variance maps (H_2S) in Figs. 7.9(a) and 7.9(c) from the different days indicate accurately the position of the $6 \times 3m^2$ area source, whose center was located approximately at position $(11, 18)m$. Furthermore, the $3 \times 1m^2$ (with the center located approx. at position $(15, 12)m$) and $2 \times 2m^2$ (with the center located approx. at position $(17, 5)m$) area sources can also be identified partially in both the predictive mean maps and the predictive variance maps (compare Figs. 7.8(a), 7.8(b), and 7.9(a) to 7.9(c) with Fig. 7.4), even though the micro-drone flew over the experiment area several times (Fig. 7.9(c) – trial #6). The area of natural gas accumulation can also be discovered in both the predictive mean maps and the predictive variance maps of trail #1 and #6 in the lower left part of Figs. 7.8(a), 7.9(a), and 7.9(c). Additionally, the CO_2 and H_2S distribution maps indicate, that the same area sources emit both CO_2 and H_2S as Figs. 7.8(a), 7.8(b), and 7.9(a), 7.9(b) show comparable qualitative results.

Table 7.4: *Wind conditions on the BAM TTS.*

Trial	#Samples	Mean Wind Speed (ms^{-1})	σ (ms^{-1})	Mean Wind Direction (°)	Circular Variance
1	9,938	1.38	±0.71	247	0.32
2	7,871	1.65	±0.82	246	0.21
3	10,939	1.57	±0.82	259	0.26

All results of the Kernel DM+V/W algorithm are very similar to the results of the Kernel DM+V algorithm due to the low wind speeds during the trials and the mostly unmodified kernel shape (see Fig. 7.1). The results of the Kernel DM+V algorithm are therefore not shown here.

7.4.2 BAM TTS Trials

Fig. 7.10 shows the results of the experiments performed over the $5 \times 5m^2$ large area on the BAM TTS. Wind conditions during all three trials were very stable (Table 7.4): the average wind speed ranged from approximately 1.4 to $1.7ms^{-1}$ and the average wind direction was between 246° and 259°. The degree of stability for each trial is given by the circular variance which lay around 0.21 and 0.32. Here, the airflow produced by the fan can be neglected as the area of influence is only limited to the immediate proximity of the fan. Additionally, the airflow maps in Fig. 7.10 reflect the stability of the local wind conditions as almost all wind vectors point approximately in the same direction.

The gas emission of the artificial gas source used in the experiments was started at the beginning of each trial. The artificial gas source had a more or less constant release rate over the period of the experiment as the pressure-reducing valve was set to a constant pressure of approximately $5bar$. The artificial gas source and the stable wind conditions on the BAM TTS with the relatively high wind speeds permitted instant formation of a reproducible plume moving away from its source (Fig. 7.10).

Reproducibility is given for trial #1 to #3 as the qualitative and quantitative results remain more or less comparable in all created maps. Small variations in the plume propagation can be explained by changes in the wind field during each experiment run. The results from the last trial differ slightly as the airflow map shows stronger variations in the wind field. However, all gas distribution maps

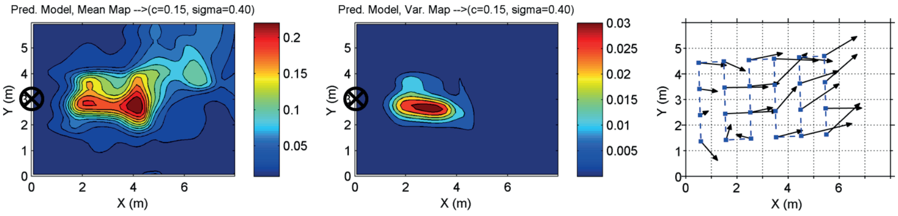

(a) Trial #1; CH_4

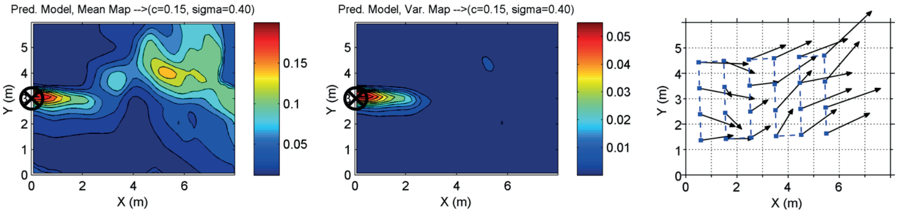

(b) Trial #2; CH_4

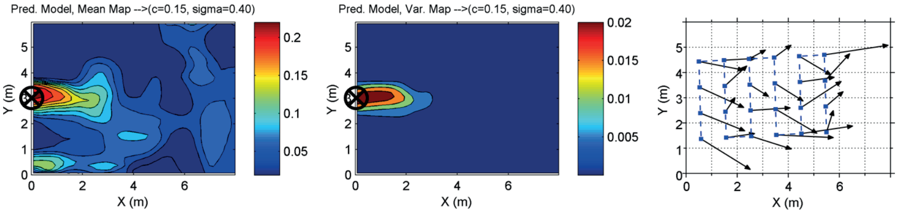

(c) Trial #3; CH_4

Figure 7.10: *BAM TTS: Predictive mean (left) and variance map (middle) of the gas distribution of the (a) 1st, (b) 2nd, and (c) 3rd trial created using* ***Kernel DM+V/W****. The figures on the right show the corresponding mean airflow maps and the path of the micro-drone. The gas source was located approximately at position* $(0, 3)m$ *and is denoted by* $\otimes$*. The starting position of the micro-drone is located approximately at position* $(5.5, 1.5)m$*. The* CH_4 *concentration value is given in % by volume.*

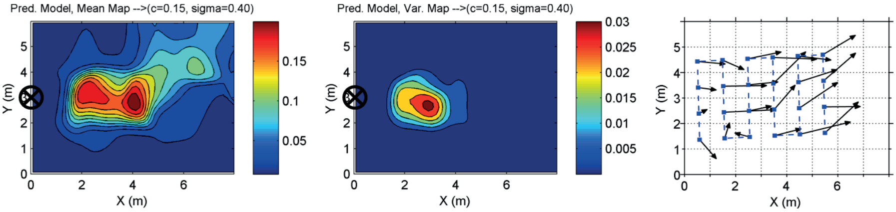

(a) Trial #1; CH_4

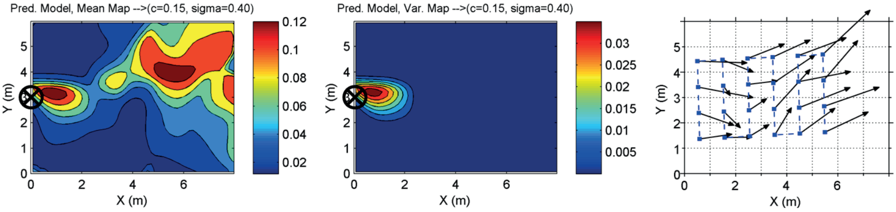

(b) Trial #2; CH_4

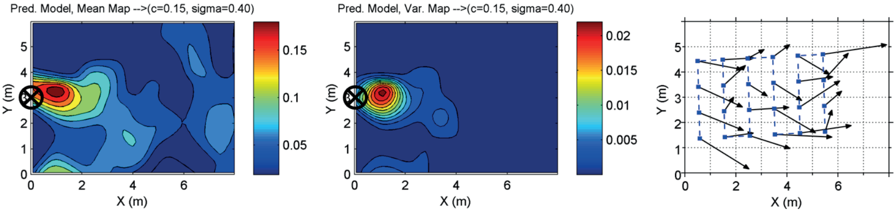

(c) Trial #3; CH_4

Figure 7.11: *BAM TTS: Predictive mean (left) and variance map (middle) of the gas distribution of the (a) 1st, (b) 2nd, and (c) 3rd trial using* ***Kernel DM+V****. The figures on the right show the corresponding mean airflow maps and the path of the micro-drone. The gas source was located approximately at position* $(0, 3)m$ *and is denoted by* $\otimes$*. The starting position of the micro-drone is located approximately at position* $(5.5, 1.5)m$*. The* CH_4 *concentration value is given in % by volume.*

created with the Kernel DM+V/W algorithm match the corresponding airflow maps. The areas of high predictive mean and high predictive variance in trial #2 and #3 accurately indicate the location of the gas source (at position $(0, 3)m$), which can be seen in Figs. 7.10(b) and 7.10(c). As the micro-drone had to pass the gas source very close in the last sweep, the altitude of the micro-drone had to be changed manually to avoid collision with the fan. This occurred in trial #1 due to the inaccuracies given by the GPS positioning system. Therefore, the last sweep in trial #1 was performed at an altitude of approximately $1m$ directly above the fan and the plume, respectively. This resulted in low concentration values near the source, which displaced the measured maximum concentrations approximately 2 to $4m$ further downwind.

The disturbances produced by the rotors of the micro-drone did not affect the plume propagation and gas dispersion sustainably as compared to the Tuscany experiments (Sec. 7.4.1). There, the maximum concentrations decreased over time and induced disturbance by rotor movement, which most likely caused a change in the magnitude and the position of the concentration maxima. This can be explained by the different prior conditions given for each scenario: The gas sources in the Tuscany region had the time to accumulate regions of higher gas concentrations, whereas the gas emission of the artificial gas source used in the remaining experiments was started at the beginning of each trial. The artificial gas source had a more or less constant release rate over the period of the experiment as the pressure-reducing valve was set to a constant pressure of approximately $5bar$, whereas the natural gas source has an unknown release rate. Therefore, it is hard to predict the point in time when the natural gas distribution was recovered. The combination of the smaller experiment area, the artificial gas source, and the artificially supported stable wind conditions on the BAM TTS with relatively high wind speeds permitted instant formation of a reproducible plume moving away from its source. The prevailing weather (foggy vs. sunny, e.g., convective currents) and wind conditions (e.g., stability of the wind and low vs. high wind speeds) are natural factors which additionally influenced the plume propagation and gas dispersion in the Tuscany region more pronouncedly than in the trials performed on the BAM TTS.

Comparing the results of the Kernel DM+V/W algorithm with the results of the Kernel DM+V algorithm demonstrates that the stronger wind speeds in all three trials have a significant influence on the shape of concentration areas in both

Table 7.5: *Wind conditions in the Botanical Garden of Berlin.*

Trial	#Samples	Mean Wind Speed (ms^{-1})	σ (ms^{-1})	Mean Wind Direction (°)	Circular Variance
3	7,161	1.07	±0.70	172	0.56
4	15,580	1.09	±0.66	140	0.67
6	8,020	1.43	±0.85	106	0.58
7	8,087	0.99	±0.77	91	0.55

predictive mean and variance maps. The Kernel DM+V/W algorithm basically models – depending on the wind and the chosen parameter γ (Fig. 7.1) – elliptic shaped areas due to its kernel modification (Fig. 7.10), whereas the Kernel DM+V algorithm models rather circular shaped areas (Fig. 7.11). The kernel shape changes the predicted plume structure slightly and is visible in all created maps. An elliptic kernel aligned in wind direction narrows the plume, whereas a circular kernel widens the plume. Additionally, the maximum concentrations in Fig. 7.11 (Kernel DM+V) differ noticeably from the maximum concentrations in Fig. 7.10 (Kernel DM+V/W). This difference is caused by the difference in the computation of the weights of both algorithms as different sensor readings (measurement positions) will be considered due to the kernel shape.

7.4.3 Botanical Garden Trials

Despite artificial ventilation, the wind conditions during all trials were very unstable in the botanical garden trials (Table 7.5). The average wind speed ranged between approximately 1.0 and 1.4ms^{-1} and the average wind direction changed between 91 and 172°. The circular variance lay around 0.55 and 0.78, which indicates that the wind vectors were highly spread. However, the produced gas distribution maps show that CO_2 may be dispersed in x direction using the four fans.

Fig. 7.12 shows exemplarily the results of trial #3, #4, #6, and #7 performed in the Botanical Garden of Berlin. Trial #3 and #4 were performed with the e-nose, whereas the Dräger X-am 5600 gas detector was used in trial #6 and #7. The quantitative results remain more or less comparable in all created maps, while the qualitative results differ more strongly. For instance, the produced predictive mean maps of trial #3 and #4 (Figs. 7.12(a) and 7.12(b)) do not allow identification

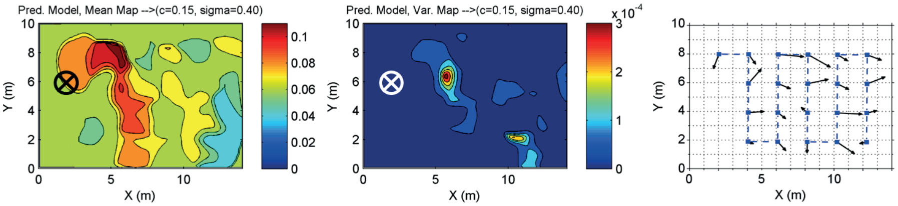

(a) Trial #3; CO_2; EC gas sensor

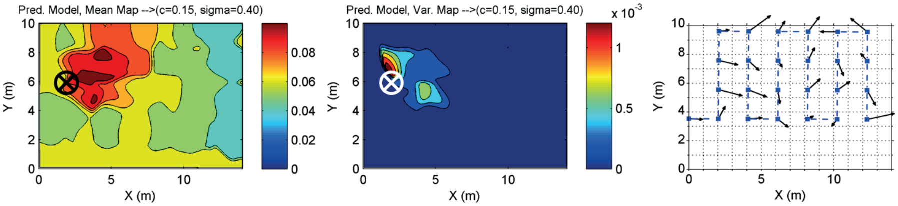

(b) Trial #4; CO_2; EC gas sensor

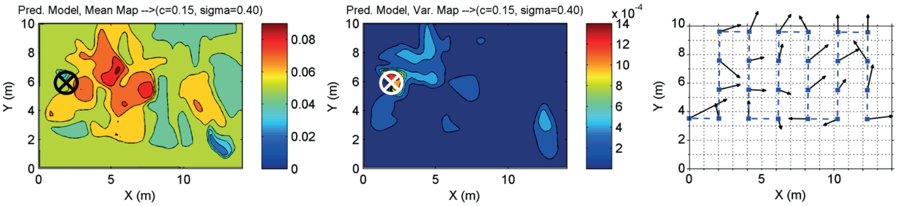

(c) Trial #6; CO_2; IR gas sensor

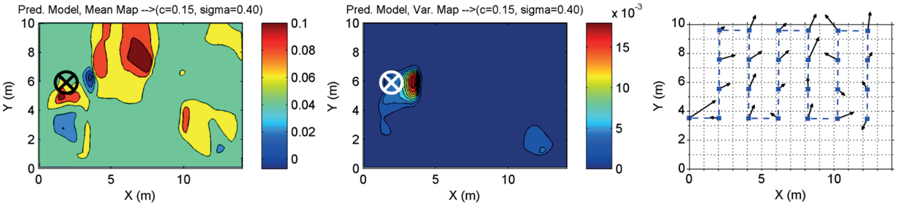

(d) Trial #7; CO_2; IR gas sensor

Figure 7.12: *Botanical garden: Predictive mean (left) and variance map (middle) of the gas distribution and the corresponding mean airflow map (right) of the (a) 3rd, (b) 4th, (c) 6th, and (d) 7th trial created using* ***Kernel DM+V/W****. The gas source was located approximately at position* $(2,6)m$ *and is denoted by* $\otimes$*. The starting position of the micro-drone is located at position approximately (a)* $(12,2)m$ *and (b) to (d)* $(12,3.5)m$*. The* CO_2 *concentration value is given in % by volume.*

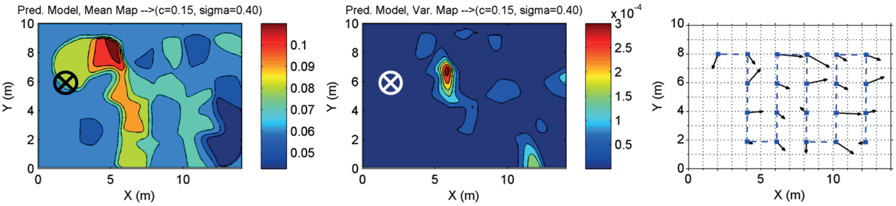

(a) Trial #3; CO_2; EC gas sensor

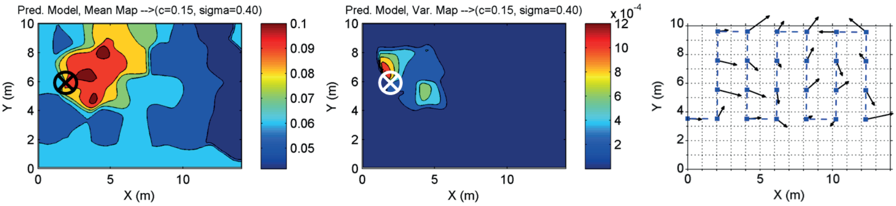

(b) Trial #4; CO_2; EC gas sensor

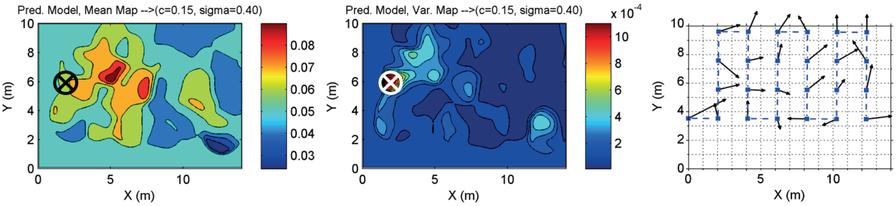

(c) Trial #6; CO_2; IR gas sensor

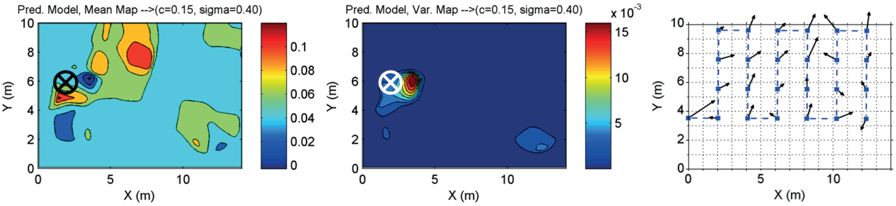

(d) Trial #7; CO_2; IR gas sensor

Figure 7.13: *Botanical garden: Created predictive mean (left) and variance map (middle) of the gas distribution using **Kernel DM+V** and the corresponding mean airflow map (right) of the (a) 3rd, (b) 4th, (c) 6th, and (d) 7th trial. The gas source was located approximately at position* $(2,6)m$ *and is denoted by* $\otimes$. *The starting position of the micro-drone is located approximately at position (a)* $(12,2)m$ *and (b) to (d)* $(12,3.5)m$. *The* CO_2 *concentration value is given in % by volume.*

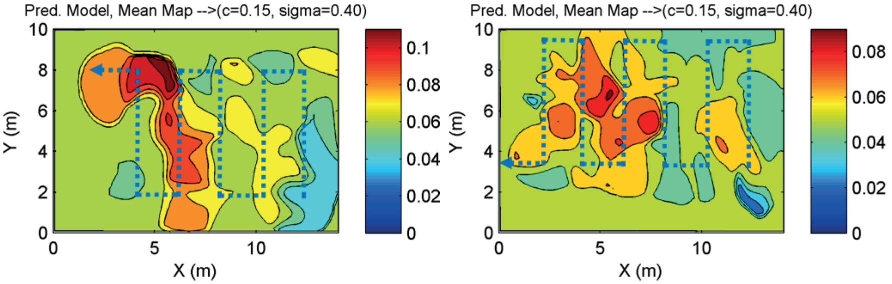

(a) Trial #3; CO_2; EC gas sensor (b) Trial #6; CO_2; IR gas sensor

Figure 7.14: *Comparison of the trajectory of the micro-drone and the predictive mean map of the gas distribution of the (a) 3rd and (b) 6th trial. The trajectory of the micro-drone is denoted by the dashed blue line.*

of a plume structure. Instead, it seems that the sensor of the e-nose retains high measured concentrations for quite a long time due to the slow sensor recovery, most likely expanding the local measurement to a much larger area with slowly decreasing concentration values following the sweeping movement of the micro-drone. In contrast to that, an intermittent plume propagating in x direction can be identified in the produced predictive mean maps of trial #6 and #7 (Figs. 7.12(c) and 7.12(d)).

All presented results of the Kernel DM+V/W algorithm (Fig. 7.12) are very similar to the results of the Kernel DM+V algorithm (Fig. 7.13). Small variations are visible between all maps due to the difference in the kernel shape of both algorithms (circular vs. elliptic). Additionally, the maximum concentrations in Fig. 7.12 differ from the maximum concentrations in Fig. 7.13 (see Sec. 7.4.2 for a more detailed description).

Fig. 7.14 shows a comparison of the produced predictive mean maps of the gas distribution and the trajectory taken by the micro-drone in trial #3 and #6. Here, it can be clearly seen that a memory effect in the sensor response due to the slow sensor may heavily affect the final gas distribution map (Fig. 7.14(a)). For instance, the e-nose measured a high CO_2 concentration at position $(6, 8)m$. The decay of the sensor most likely persisted until the micro-drone reached the position $(4, 2)m$. This effect is not visible in trial #6 (Fig. 7.14(b)) using the Dräger X-am 5600 gas detector. However, the source location is indicated roughly by the high concentration variance in five of the eight predictive variance maps (Figs. 7.12(b) to 7.12(d)). An exception is, e.g., trial #3, where the high concentration variance is displaced approximately $3m$ from the real source location. The reason for that could be the lacking last sweep (due to an exhausted battery). The IR gas sensor of the Dräger X-am 5600 gas detector, however, has a considerably better spatial resolution over the area as it supports shorter response and decay times (i.e., the memory effect of the IR sensor is much lower than the memory effect of the EC sensor used by the e-nose).

7.5 Summary and Conclusions

Gas Distribution Mapping (GDM) by an autonomous, flying gas-sensitive micro-drone in an uncontrolled environment is an extremely challenging field of research. The application of the Kernel DM+V/W algorithm in combination with the estimation of the wind vector using a micro-drone is very promising with respect to the results of the presented real-world GDM experiments even though the explored areas presented in this chapter are not of considerable size. The first set of experiments in the geochemically active Tuscany region in particular highlight that the micro-drone may not be suitable for *repeated* monitoring under low-wind conditions when quantitative reproducibility is needed since it substantially disturb gas distribution. The qualitative results still might be useful for identifying the gas source locations. However, the time between each mission has to be long enough to allow a recovery of the natural gas distribution. The other sets of experiments showed that qualitative and quantitative reproducibility depend on the stability of wind and weather conditions, and that gas sensors with faster response times are required in order to reduce the measurement time and be able to cover larger areas.

Furthermore, the true source location was indicated more often in the predictive variance maps than in the predictive mean maps. This is in line with previous observations that the concentration variance often provides a better indication of the gas source location [1] than the mean.

One general problem is the memory effect in the sensor response due to the slow sensor recovery, which can be observed especially in the two trials performed in the Botanical Garden of Berlin using the e-nose. Therefore, it is beneficial to use sensors with faster response and decay times (e.g., TGS2611 – CH_4) for generating truthful representations of gas dispersion (Sec. 7.4.3). However, sensors with fast response and decay times are not always available for the target gas. To reduce the memory effect in the response of sensors with slow response and decay times, Ishida et al. [90] proposed the integration of a sensor dynamics model to “reconstruct the actual gas distribution from the time-series response data considering the delay”. As a consequence of the slow sensor recovery, a gas source might also be hidden in the final gas distribution map if multiple gas sources that release different concentration levels of the same gas are present. Therefore, depending on the trajectory of the micro-drone, a gas source releasing a lower concentration may be masked by another, spatially close gas source releasing a higher concentration of the same gas (i.e., that the sensor decay of the higher concentration may hide the lower concentration), which makes the localization of these sources a challenging task. The approach of a Multi-Chamber Electronic Nose (MCE nose) proposed by Gonzalez et al. [145] could overcome this limitation as it “alternate[s] between sensing and recovery states [using redundant sensors], providing, as a whole, a device capable of sensing changes in chemical concentrations faster”. Future work should additionally include the GPS positioning error of the micro-drone for more accurate gas distribution maps.

Lilienthal and Duckett argue in [130] (for a precursor of the Kernel DM+V/W algorithm) that building concentration grid maps requires a robot trajectory that roughly covers the entire search space and passes particular measurement positions from multiple directions. However, in the case of a micro-drone, which introduces sustainable disturbances to the environment that modifies the current gas distribution and thus destroys important evidence, it is not desirable to visit measurement positions more than once. Instead, performing just one full sweep in each experiment seemed to be suitable regarding the experiment results, even though the Kernel DM+V/W algorithm had to be run outside its specification. Furthermore, using sweeping trajectories to build detailed gas distribution maps over large areas is time consuming. The batteries of the micro-drone (equipped with payload) only provide power for approximately $20min$. New battery technologies may overcome this limitation in the near future. However, adaptive sampling strategies have to be developed or a swarm of multiple gas-sensitive micro-drones has to be deployed. But even a single gas-sensitive micro-drone causes extensive disturbance in the exploration area and therefore a swarm may even faster interfere with data to be measured. One possible alternative to overcome this problem may be to partition a large area into smaller subregions (e.g., including wind information in the decision process such that a micro-drone does not disturb the subregions assigned to other micro-drones).

Afterwards, each micro-drone can explore its assigned subregion. The 3D version of the Kernel DM+V/W algorithm from Reggente and Lilienthal [94] may be used when additional constraints are respected (e.g., the produced downward directed airflow by the micro-drone's rotors heavily influences the gas distribution directly under the micro-drone up to a range of approx. $5 - 10m$). Therefore, intelligent exploration strategies for the 2D and 3D case have to be developed.

Chapter 8

Sensor and Path Planning Strategy for a Micro-Drone

Using sweeping trajectories to build detailed gas distribution maps over large areas is extremely time consuming. A more detailed discussion about alternative data acquisition strategies is given in Sec. 7.2. However, the batteries of the micro-drone (equipped with payload) only provide power for approximately $20min$. With the micro-drone taking samples for $20s$ at each measurement position, the battery restricts the micro-drone to a total of ≤ 60 measurement positions while a minimum of 100 measurement positions are needed to cover an area of $5 \times 20m^2$ with a resolution of $1m$, for example ("Ambra" experiments in the Tuscany Region). Gas-sensitive mobile robots therefore require a thoroughly designed sensor planning strategy that selects preferable sampling locations based on the current knowledge about the environment and, more specifically, about gas distribution. The purpose of the sensor planning component is to reduce the time that is necessary to converge to the final gas distribution model or to reliably identify important parameters of the distribution such as areas of high concentration. Sensor planning is especially important in the case of a flying gas-sensitive robot such as the one considered in this Ph.D. thesis due to its limited battery life time.

In this Ph.D. thesis, a newly developed sensor planning approach [16] is adapted by introducing locality constraints to plan the path for a micro-drone [Paper III, Paper XII]. The sensor planning algorithm uses information about the target area and previous sampling locations to maximize the coverage area. In addition, it considers the continuously updated statistical gas distribution model (Sec. 7.1) to direct sensor measurements towards locations of high mean concentration and high concentration variance. The different objectives are combined in an Artificial Potential Field (APF) in a way that allows to include additional objectives, e.g., from human operators, in an intuitive and straightforward way. In addition to the introduction of the modified APF-based sensor planning algorithm and the demonstration on a gas-sensitive micro-drone, this chapter demonstrates again that the peak in the predictive variance model can provide an accurate estimation for the location of a stationary gas source.

Note that this chapter has emerged from a cooperation with Sahar Asadi who is a Ph.D. student at Applied Autonomous Sensor Systems (AASS), Örebro University, Sweden. A declaration of collaboration with the corresponding contributions of Sahar Asadi and Patrick P. Neumann can be found in Sec. 8.1.

In the remainder of this chapter, first, the basic APF-based sensor planning algorithm is described (Sec. 8.2). Then, two different locality constraints are introduced to select the next measurement position (Sec. 8.2.1). Next, the complete sensor and path planning algorithm for the micro-drone is described (Sec. 8.3). Finally, simulation and real-world experiments are performed to evaluate the performance of the APF-based sensor planning algorithms (Secs. 8.4 and 8.5) and conclusions are drawn (Sec. 8.6).

8.1 Declaration of Collaboration

This chapter emerged from a collaborative work with Sahar Asadi who is a Ph.D. student at Applied Autonomous Sensor Systems (AASS), Örebro University (Sweden). The main focus of her Ph.D. research is gas distribution modeling and sensor planning. Within the context of this collaboration, we optimized an adaptive sensor planning approach based on an Artificial Potential Field (APF) for the purpose of gas distribution study and gas source localization using a gas-sensitive micro-drone. Furthermore, we selected together evaluation criteria and measures described in Sec. 8.4 and Appendix E. Some of the initial results of this collaboration are presented in [Paper III], [Paper X], and [Paper XII].

The initial adaptive APF-based sensor planning for gas sensors (see Sec. 8.5) was originally introduced by Sahar Asadi. In the proposed method, the APF was defined using only predictive mean and variance information of the estimated gas distribution maps (using the Kernel DM+V/W algorithm) and a repulsive potential of previous measurement locations to choose the next sampling position [Paper III, Paper XII].

Sahar Asadi's main contribution within this collaboration was (1) the theoretical part of the adaptive APF-based sensor planning algorithm, including theoretical studies using the defined distance measures, (2) performing simulation experiments, and (3) optimization of sensor planning parameters and gas distribution modeling parameters.

The main contribution of this Ph.D. thesis within this collaboration was (1) the design of the robotic platform (see Ch. 3), (2) design of the experiment setup of the real-world experiments including data collection with the micro-drone (see Sec. 8.5), (3) the optimization of the sensor planning algorithm for a single gas-sensitive micro-drone by adding locality constraints (see Secs. 8.2.1 and 8.3), and (4) enhancement of the sensor planning parameters in simulation (see Sec. 8.4).

After evaluation of first simulation and real-world experiments, we worked on potential improvements of the initial sensor planning method and tested suitable alternatives. Within this context and as part of Sahar Asadi's Ph.D. research, an improved version of the APF-based method was proposed. Within this Ph.D. thesis, this novel method was evaluated in simulation experiments. This improved version of the APF-based sensor planning has not been published yet and is in preparation; however, upon on our agreement this algorithm is presented in this Ph.D. thesis in Sec. 8.2. It includes confidence map in addition to predictive mean and variance to build the APF. Furthermore, the predictive maps are used instead of an integration over predictive mean values (cf. Eqs. 8.1 to 8.3 in Sec. 8.2 with Eqs. 8.10 to 8.12 in Sec. 8.5).

The real-world experiments took place in an early stage of the algorithm and thus were performed using the initial version of the APF-based sensor planning algorithm (Sec. 8.5). The simulations, on the other hand, were performed using the improved version of the sensor planning algorithm (Sec. 8.2).

8.2 Adaptive Sensor Planning

In each step, the adaptive sensor planning (SP) component (denoted by adaptive SP in the following) [Paper III, Paper XII] suggests a selectable number n_{sp} of locations to place sensors in the area of interest in the next iteration. The algorithm uses information about the target area, previous sampling locations, and the current statistical gas distribution model. The selection process considers three objectives to direct the sensor towards areas of (1) high predictive mean, (2) high predictive variance, while (3) maximizing the coverage area.

The first two objectives implement exploitation of the information in the gas distribution model ("using the current belief about the state of the environment most effectively [104]"). They are achieved by an attractive potential generated by pseudo electric charges placed in each grid cell center of the corresponding created gas distribution model. The strength of these charges is given by the corresponding predictive mean and variance. Accordingly, two APF contributions are determined for each cell k as

$$APF_M^{(k)} = r^{(k)}, \tag{8.1}$$

$$APF_V^{(k)} = v^{(k)}, \tag{8.2}$$

where $r^{(k)}$ and $v^{(k)}$ are the predictive mean and variance values for grid cell k, respectively, both computed by the Kernel DM+V/W algorithm (Sec. 7.1). The third objective that corresponds to exploration ("gathering information about the environment [104]") is implemented by the confidence map $\alpha^{(k)}$:

$$APF_C^{(k)} = -\alpha^{(k)}, \tag{8.3}$$

where $\alpha^{(k)}$ is the confidence value for grid cell k also determined by the Kernel DM+V/W algorithm. The APF contributions are additively combined with importance factors β_M, β_V, and β_C for each objective:

$$APF^{(k)} = \beta_M \cdot APF_M^{(k)} + \beta_V \cdot APF_V^{(k)} + \beta_C \cdot APF_C^{(k)}, \tag{8.4}$$

where

$$\beta_M + \beta_V + \beta_C = 1. \tag{8.5}$$

$APF_C^{(k)}$ creates a strong attraction if the confidence value in the respective cell k is low, while the other two APF contributions ($APF_M^{(k)}$ and $APF_V^{(k)}$) create a strong attraction if the respective quantity (mean and variance) is high.

Finally, n_{sp} locations are identified by selecting in each iteration $i \in [1, n_{sp}]$ the location at which the potential is maximum as a suggested measurement point and updating the APF by temporarily placing an additional measurement charge q at the selected location $x^{(i)}$:

$$APF_i^{(k)} = \underbrace{\beta_M \cdot APF_M^{(k)} + \beta_V \cdot APF_V^{(k)} + \beta_C \cdot APF_C^{(k)}}_{APF^{(k)}} + \beta_C \cdot APF_{Q_i}^{(k)}, \tag{8.6}$$

with

$$APF_{Q_i}^{(k)} = \sum\nolimits_{j=1}^{i} q \cdot \exp\left(\frac{|x^{(j)} - x^{(k)}|}{\sigma_d}\right), \tag{8.7}$$

where $x^{(j)}$ is the selected location in iteration j, $x^{(k)}$ is the location of cell center k, σ_d is a scaling parameter, which is set to $1m$. In the current implementation, same repulsive force is assigned to all temporarily selected locations and the virtual charge q is set to -1.

Theoretically, it may happen that the attractive forces towards an increased mean and an increased variance in the opposite direction cancel themselves out. In practice, it is unlikely that the attractive forces are completely balanced at the position of the sensor. Even if they were, the sensor would be directed towards one of the directions and in the next step the symmetry would be broken [Paper XII].

8.2.1 Locality Constraints for Adaptive Sensor Planning

The previously described sensor planning approach distributes its n_{sp} suggestions over the target area without any spatial order. Moving the mobile gas sensor directly to these locations (with highest APF values) tends to create a seesaw movement, which drains the batteries sooner, resulting in fewer measurements. Therefore, two different locality constraints are suggested to enhance the information gain within the battery lifetime of the micro-drone:

A: The *closest suggested* location is selected as the next measurement position (rather than the first suggestion) with

$$\min\left\{d_i \mid d_i = |p_m - p_i| \text{ with } i \in [1, n_{sp}]\right\}, \tag{8.8}$$

where p_m is the position of the micro-drone and p_i with $i \in [1, n_{sp}]$ corresponds to the suggested measurement locations.

B: The *most often suggested close-by* measurement location is selected from among n_{sp} suggestions from the basic sensor planning approach (rather than the first suggestion). This is implemented by a matrix S that has the same discretization as the gas distribution model. For each grid cell k, $S^{(k)}$ counts the number of the cell being suggested since it was actually visited the last time. The next measurement point is ultimately selected as the one with the highest ratio $S^{(k)}/d^{(k)}$ where $d^{(k)}$ is the distance between the sensor's current position and grid cell k. Thus, a location far away from the current position will only be selected if it was frequently suggested. In the current implementation, not only the counter for a suggested cell but also the counter of neighboring cells in the matrix S within a radius of $0.5m$ are increased by one. A radius of $0.5m$ corresponds to the drainage / turbulence area under the micro-drone (that has a diameter of $1m$) induced by the rotors.

The APF criterion – choosing from the remaining locations the one with the highest APF value – is applied if more than one possible next measurement location remains in the selection process.

8.3 Sensor and Path Planning Algorithm for the Micro-Drone

The initial measurement location is chosen randomly in the target area. Then, the sensor and path planning algorithm for the micro-drone (SPPAM) performs the following steps iteratively:

- collect gas sensor and wind measurements while keeping the micro-drone at a fixed position for a prolonged time (here: $20s$);
- average the sampling positions of the micro-drone and the gas concentration and wind measurements over the measurement time ($20s$); (A number of simulations showed that using every single sampling position leads to a relatively large, connected area of overlapping kernels which is disadvantageous for the performance of the algorithm.)

- compute the predictive gas distribution model using the Kernel DM+V/W algorithm (Sec. 7.1), the input to the algorithm is the averaged positions and the averaged gas concentration and wind measurements;
- derive an estimate of the source location from the predictive gas distribution map (detailed in Sec. 8.5);
- determine the n_{sp} suggested sampling locations with the APF-based sensor planning component (Sec. 8.2);
- select a sampling location based on one of the locality constraints described in Sec. 8.2.1;
- fly the micro-drone autonomously to the chosen sampling location and repeat using the first step. (Measurements between two sampling locations are not used to decrease the influence of a memory effect in the sensor response due to the slow sensor recovery.)

The algorithm terminates either if the battery becomes low or the confidence map $\alpha^{(k)}$ is above a defined threshold for each cell k. In the real-world experiments, the first criterion is used to terminate the algorithm, which resulted in approximately 24 to 35 sampling locations (Sec. 8.5). The whole adaptive sampling process is also visualized in Sec. 8.5.2, Fig. 8.11.

8.4 Simulation Experiments

Simulation experiments offer ground truth information which enables a quantitative comparison and performance evaluation of algorithms under repeatable conditions. The different sensor planning approaches (adaptive SP and SPPAM) are evaluated by comparing gas distribution models which were created using the measurements suggested by a particular sensor planning algorithm with the available ground truth model. The ground truth is built up using all available measurements of the simulation experiment, whereas the predictive models are built up after each iteration of the sensor planning approach by adding the measurements from the current sampling location to the model. Thus, each iteration represents a subset of the simulation data. As a measure of distribution similarity, the symmetric Kullback-Leibler (KL) distance (Appendix E) is used.

In order to evaluate the performance of SPPAM, the KL distance obtained with SPPAM is compared to the KL distance obtained with adaptive SP, pure random sampling, and sweeping (with step size set to $1m$). The Kernel DM+V/W algorithm is used to build the gas distribution model. For the predictive mean map, the *a priori* estimate $\bar{r}$ in the Kernel DM+V/W algorithm is set to the minimum concentration over all sensor readings to achieve a better comparability between the created maps and the ground truth [16]. Using the average concentration over all sensor readings to update the corresponding cells with low confidence is not a good *a priori* estimate compared to the large area in the ground truth map that contains low and zero concentration values because of the narrow plume. This is especially relevant if the first samples are taken randomly inside the plume.

Other performance parameters which were used to compare the different approaches with each other are the total traveled distance of the micro-drone, the average distance between two consecutive sampling locations, and the obtained coverage. The latter is approximated by a matrix that has the same size as the experiment area with a cell size of $0.01m$. The coverage is calculated as the ratio of the number of visited cells to the number of all matrix cells. To account for the radius of the micro-drone, neighboring cells within a radius of $0.5m$ are also assumed to be covered.

In each of the following simulation experiments, the parameters of the Kernel DM+V/W algorithm were set heuristically to $c = 0.10m$ (grid cell size), $\sigma = 0.40m$ (kernel width), $\sigma_\Omega = \mathcal{N}(0, \sigma = 0.4) \approx 1.0$, and $\gamma = 0.6s$. In comparison to the experiments performed in Sec. 8.5, γ is set to $0.6s$ to consider the low flow speed in the wind tunnel of $0.5ms^{-1}$. A total of up to 220 iterations ($\widehat{=}$ measuring positions) were performed for SPPAM, adaptive SP, pure random sampling, and sweeping. However, sweeping only needed 206 iterations to complete one full forward and one full backward sweep and was therefore stopped directly afterwards. Furthermore, the backward sweep was shifted to fill out the remaining gaps (Fig. 8.5(c)).

8.4.1 Theoretical Performance of SPPAM

8.4.1.1 Experiment Environment and Setup

To measure the idealistic performance of SPPAM under laminar flow conditions, simulations are carried out at a high abstraction level. For this purpose, the micro-drone is modeled as a dimensionless point with a perfect GPS positioning system and without influence of the rotors on the measurements. The wind and gas sensors are modeled as perfect sensors without noise and delay. The experiment area is a $12 \times 8m^2$ large section of a simulated wind tunnel environment with size $32 \times 8m^2$. The flow speed in the wind tunnel was set to $0.5ms^{-1}$. A circular gas source with a radius of $0.2m$ was placed in the experiment area approximately at position $(2,4)m$. The start position of the micro-drone was chosen randomly in each run within the experiment area.

First, to find a reasonably good parameter set for the adaptive SP algorithm, experiments with different importance factors are performed for each objective (high mean, high variance, and coverage). Next, the best parameter set is chosen to evaluate SPPAM with the locality constraints suggested in Sec. 8.2.1. The number of suggested measurement locations (n_{sp}) was set to 10. Each experiment was repeated 100 times with a total of up to 220 iterations.

8.4.1.2 Experiment Results

Fig. 8.1 shows a KL distance comparison of predictive mean maps to the ground truth map. The predictive mean maps are created using adaptive SP with different importance factors, sweeping, and random sampling. The ground truth is built up using all available measurements of the simulation experiment. The results demonstrate that random sampling is not a good reference strategy as its convergence to the final gas distribution model is slow. Sweeping, however, can provide a much better reference. It reaches a good model accuracy after already ≈ 100 sampling iterations (KL distance value of 0.21 ± 0.0) and a very good model accuracy after ≈ 200 sampling iterations (KL distance value of 0.05 ± 0.0). Furthermore, the micro-drone following a sweeping trajectory has to cover a much smaller distance than using random sampling. Sweeping needs $205.6m \pm 0.0m$, whereas random sampling needs $1082.5m \pm 40.7m$ (both determined after 206 iterations) to cover roughly the entire experiment area (coverage: $99.8\% \pm 0.0\%$ with sweeping and $79.5\% \pm 1.7\%$ with random sampling).

Adaptive SP with $(\beta_M, \beta_V, \beta_C)$ set to $(0.4, 0.4, 0.2)$ fails to build an accurate model of the gas distribution due to a too greedy parameter selection. The repulsive force cannot antagonize its opponents (predictive mean and variance) and the algorithm gets stuck in a local maximum. This can be seen in Fig. 8.1(a) in form of an in-

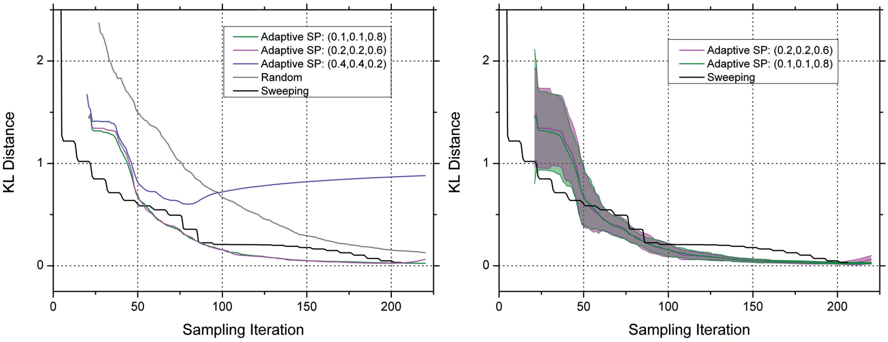

(a) (b)

Figure 8.1: *Results of the simulation experiments as functions of the number of iterations: KL distance comparison of predictive mean maps to the ground truth map (a) without and (b) with standard deviation. The predictive mean maps are created using adaptive SP with different importance factors, sweeping, and random sampling. The ground truth is built up using all available measurements of the simulation experiment.*

creasing KL distance value after 80 iterations and in Fig. 8.2, where a measurement taken at approximately $(4, 4)m$ stops any further exploration of the experiment area after iteration 82.

Fig. 8.1(b) shows a KL distance comparison of predictive mean maps to the ground truth map. The predictive mean maps are created using adaptive SP with $(\beta_M, \beta_V, \beta_C)$ set to $(0.1, 0.1, 0.8)$ and $(0.2, 0.2, 0.6)$, and sweeping. The ground truth is built up using all available measurements of the simulation experiment. A good parameter set for $(\beta_M, \beta_V, \beta_C)$ for adaptive SP has been found to be $(0.1, 0.1, 0.8)$. For both parameter configurations, the above described problem that exploitation dominates exploration (or: local maximum problem) only appears after the confidence map $\alpha^{(k)}$ reached a certain threshold for each cell k, which should serve as a stop criterion for the algorithm. This happens approximately after 200 iterations for the parameter configuration $(0.2, 0.2, 0.6)$ (Fig. 8.1(b)) and after about 240 iterations for the parameter configuration $(0.1, 0.1, 0.8)$. The latter was observed in an additional experiment with 20 runs with 400 iterations each (Fig. 8.3). In general, to avoid early stagnation of adaptive SP, the following inequality is suggested and must hold for each k (otherwise the locations with local maxima will be suggested in each iteration and the decision of the next sampling point will rely only on the

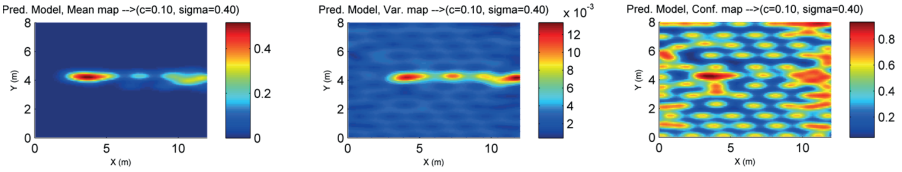

(a) Iteration = 82

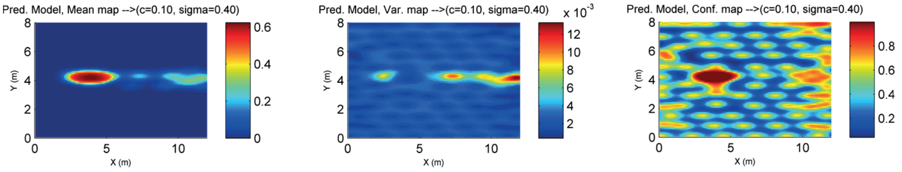

(b) Iteration = 86

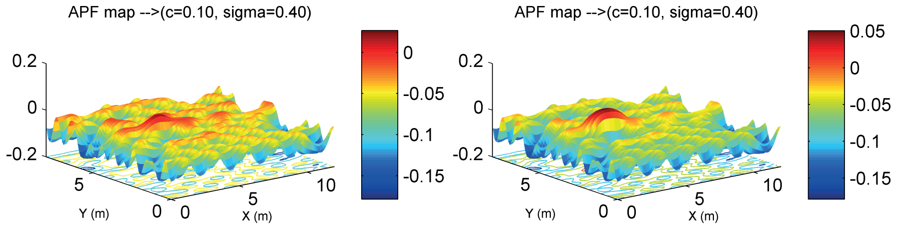

(c) Iteration = 82 (d) Iteration = 86

Figure 8.2: *Local maximum problem of adaptive SP with too greedy parameter selection: predictive mean (left), variance (middle), and confidence map (right) of the gas distribution with the corresponding APF maps after (a) and (c) 82 and (b) and (d) 86 iterations. Due to a local maximum approximately at position $(2, 4)m$ (corresponds to the position of the gas source), the algorithm gets stuck.*

locality constraint used):

$$\beta_M \cdot APF_M^{(k)} + \beta_V \cdot APF_V^{(k)} \leq \left|\beta_C \cdot APF_C^{(k)}\right| \tag{8.9}$$

Adaptive SP with $(\beta_M, \beta_V, \beta_C)$ set to $(0.1, 0.1, 0.8)$ outperforms sweeping after ≈ 50 iterations and converges after ≈ 150 iterations (KL distance value of 0.05 ± 0.02). To achieve this result, the micro-drone was sent along a $803.9m \pm 39.5m$ long trajectory and covered $79.1\% \pm 1.3\%$ of the experiment area. In comparison, the KL distance value of sweeping after ≈ 150 iterations is only 0.18 ± 0.0 (factor 3.6 worse than adaptive SP). Furthermore, sweeping covered a distance of $150.3m \pm 0.0m$ (approx. factor 5.4 times better than adaptive SP) and obtained a coverage ratio

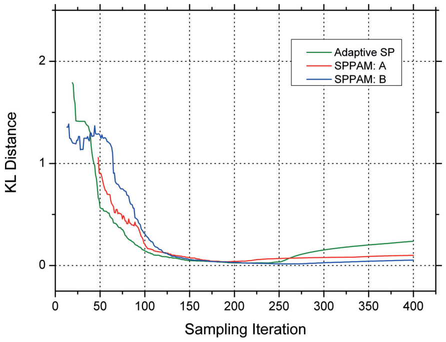

Figure 8.3: *Effect of the local maximum problem on the KL distance value of adaptive SP and SPPAM with locality constraint A and B (found out in an additional experiment with* 20 *runs with* 400 *iterations each) as a function of the number of iterations.*

of 86.2% ± 0.0%. Although sweeping has covered approximately 7% more of the experiment area, adaptive SP performs better as it prioritizes the exploitation of regions of high mean concentration and high concentration variance. A theoretical evaluation of the basic adaptive SP algorithm with a full parameter optimization can be found in [16].

A critical aspect due to the resource constraints of, e.g., a micro-drone (or a mobile robot) is the distance overhead of adaptive SP in comparison to sweeping. Moving around with a micro-drone is time and power consuming. Thus, additional locality constraints are needed to avoid sending the micro-drone in a seesaw movement over the experiment area (Fig. 8.5(b)), which drains the batteries quicker, resulting in fewer measurements.

Fig. 8.4 shows a KL distance comparison of predictive mean maps to the ground truth map. The predictive mean maps are created using SPPAM, adaptive SP, and sweeping. The ground truth is built up using all available measurements of the simulation experiment. Here, the importance factors $(\beta_M, \beta_V, \beta_C)$ were set to $(0.1, 0.1, 0.8)$ for SPPAM and adaptive SP. At first glance, SPPAM with locality constraints performs worse than adaptive SP. SPPAM with locality constraint A needs ≈ 16 iterations more (166 iterations) than adaptive SP to reach a KL distance value of 0.05 ± 0.02 and covers $80.8\% \pm 0.02\%$ of the experiment area (adaptive SP: 82.1% ± 0.01% and sweeping: 90.0% ± 0.0%). However, it reduces the traveled distance significantly to only $280.8m \pm 10.7m$. In comparison, adaptive SP needs $803.9m \pm 39.5m$ to reach a KL distance value of 0.05 ± 0.02. SPPAM with locality

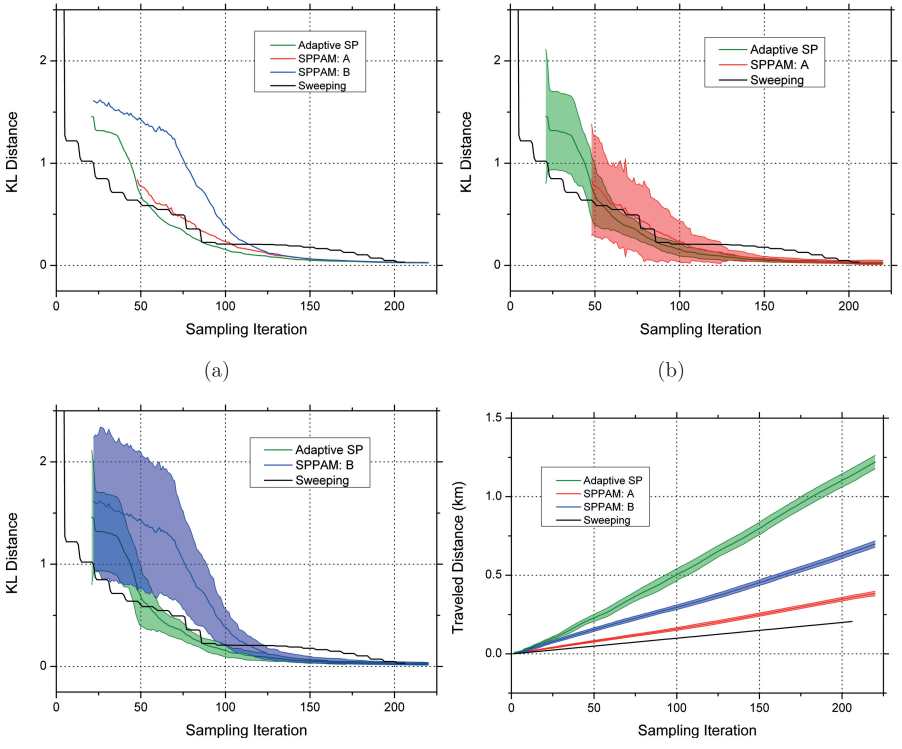

(a)

(b)

(c)

(d)

Figure 8.4: *KL distance comparison of predictive mean maps to the ground truth map (a) without and (b) and (c) with standard deviation as a function of the number of iterations. The predictive mean maps are created using SPPAM, adaptive SP, and sweeping. The ground truth is built up using all available measurements of the simulation experiment. (d) Traveled distance of the micro-drone over the number of sampling iterations using SPPAM, adaptive SP, and sweeping.*

constraint B needs $\approx$ 18 iterations more (168 iterations) than adaptive SP to reach a KL distance value of 0.05 ± 0.03 and covers $81.3\% \pm 0.01\%$ of the experiment area (adaptive SP: $82.5\% \pm 0.01\%$ and sweeping: $90.5\% \pm 0.0\%$). The traveled distance, however, could be reduced at least to $514.6m \pm 17.8m$. Sweeping on the other hand needs only $193.54m \pm 0.0m$ to reach a KL distance value of 0.05 ± 0.00, however this takes 194 iterations (i.e., 28 iterations more than SPPAM with locality constraint A). Table 8.1 shows a comparison of the performance of the algorithms to reach a

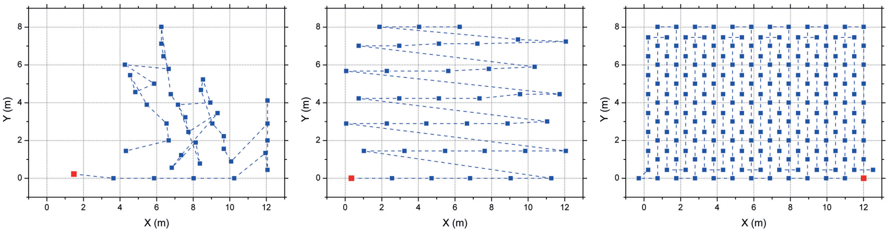

(a) Iteration = 39 (b) Iteration = 39 (c) Iteration = 206

Figure 8.5: *Sample trajectories of (a) SPPAM with locality constraint A, (b) adaptive SP, and (c) sweeping. The blue squares denote the measurement positions where the micro-drone stopped to take samples and the dashed blue line illustrates the trajectory of the micro-drone. The start position of the micro-drone is indicated by the red square.*

Table 8.1: *Comparison of the performance of the algorithms to reach a KL distance value of* 0.05.

Strategy	# Iterations	Traveled Distance (m)	Coverage (%)
Sweeping	194	193.54 ± 0.0	97.03 ± 0.0
Adaptive SP	150	803.9 ± 39.5	79.1 ± 0.01
SPPAM A	166	280.8 ± 10.7	80.8 ± 0.02
SPPAM B	168	514.6 ± 17.8	81.3 ± 0.01

KL distance value of 0.05. Fig. 8.4(d) shows a comparison of the traveled distance of the micro-drone using SPPAM, adaptive SP, and sweeping over time (sampling iterations) and Table 8.2 shows the experiment results after 206 iterations.

It can be seen from the experiment results that SPPAM with locality constraint A is a promising alternative to sweeping. Sweeping needs 194 iterations and sends the micro-drone along a $\approx 194m$ long trajectory to obtain a very good model accuracy ($\leq$ a KL distance value of 0.05). Adaptive SP can achieve this result in 150 iterations. However, the micro-drone needs to travel $\approx 804m$. SPPAM with locality constraint A obtains the same model accuracy after 166 iterations, but the mobile robot needs to travel only $\approx 281m$. SPPAM with locality constraint B avoids the local maximum problem, but 168 iterations with the micro-drone traveling $\approx 515m$ are needed to obtain the same result. Fig. 8.5 shows a sample trajectory for each of these three approaches. Although, SPPAM with locality constraint A is the preferable strategy, sweeping is a competitive alternative that needs to be considered.

Table 8.2: *Experiment results after 206 iterations.*

Strategy	Traveled Distance (m)	Coverage (%)	KL Distance Value
Sweeping	205.6 ± 0.0	99.8 ± 0.0	0.032 ± 0.000
Adaptive SP	1136.9 ± 43.8	88.8 ± 0.9	0.027 ± 0.009
SPPAM A	359.8 ± 12.4	86.5 ± 1.2	0.030 ± 0.020
SPPAM B	646.9 ± 18.8	87.6 ± 0.9	0.030 ± 0.015

8.4.2 Robotic Simulation

Simulations with a simulated micro-drone are used to study the impact of some real-world effects on the performance on adaptive SP and SPPAM.

8.4.2.1 Experiment Environment and Setup

The experiment setup is identical to the one described in Sec. 8.4.1.1 with the following exceptions: The minimum step size of the micro-drone was introduced and set to $1m$. The IR gas sensor model described in Sec. 4.3 was used to simulate the sensor response, and the gas concentration and wind measurements were taken for $20s$ with a sampling frequency of $1Hz$ at each measuring position. The wind sensor noise σ_θ^2 (Sec. 4.5) was set to 14.02. The simple disturbance model (Sec. 4.4) and the GPS model (Sec. 4.2) of the micro-drone were also used.

8.4.2.2 Experiment Results

Fig. 8.6 shows a KL distance comparison of predictive mean maps to the ground truth map. The predictive mean maps are created using adaptive SP and SPPAM, both with $(\beta_M, \beta_V, \beta_C)$ set to $(0.1, 0.1, 0.8)$, and sweeping. The ground truth is built up using all available measurements of the simulation experiment. It is evident that SPPAM with locality constraints performs inferior to sweeping. Only adaptive SP performs slightly better. However, especially in the beginning, the variance of adaptive SP is much smaller than that of sweeping (Fig. 8.6(b)). One reason for the high fluctuation of the KL distance values in the different runs of sweeping might be the GPS model of the micro-drone, which changes the measuring grid of the sweeping trajectory notably and results in irregular, large gaps between two consecutive measuring positions (Fig. 8.7). Adaptive SP is also affected by this GPS

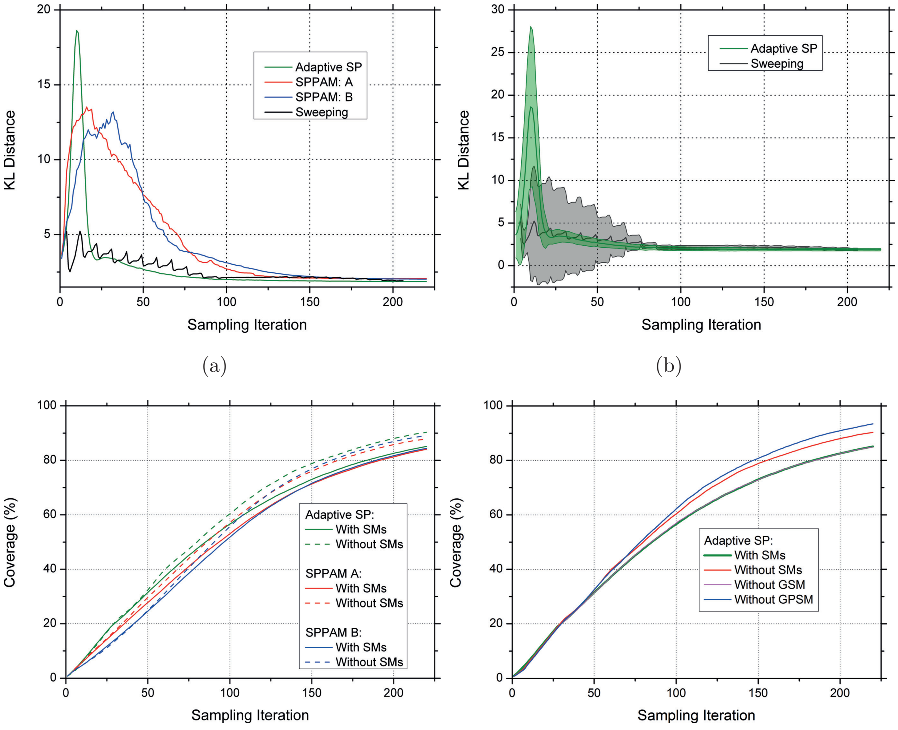

(a) (b)

(c) (d)

Figure 8.6: *Results of the robotic simulation experiments as functions of the number of iterations: KL distance comparison of predictive mean maps to the ground truth map (a) without and (b) with standard deviation. The predictive mean maps are created using SPPAM, adaptive SP, and sweeping. The ground truth is built up using all available measurements of the simulation experiment. (c) Coverage of adaptive SP and SPPAM with locality constraints obtained from theoretical and robotic simulations (SMs = sensor models). (d) Influence of the gas sensor and GPS model on the coverage of adaptive SP (GSM = gas sensor model and GPSM = GPS model).*

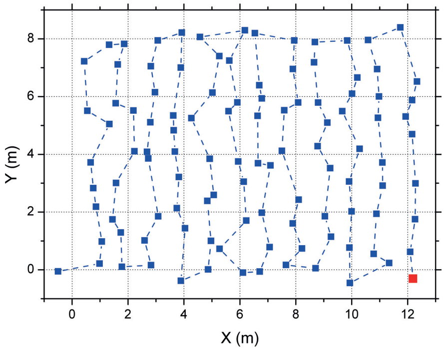

Figure 8.7: *Sample trajectory of sweeping of the first 109 iterations. The sampling locations of the micro-drone were averaged over the measuring time (the red dot indicates the micro-drone's start position).*

positioning system error, however, it seems that the corresponding KL distance values are affected slightly by this error. Furthermore, the traveled distance of the micro-drone (after 206 iterations) – in comparison to the theoretical simulation results – increased by almost $60m$ using adaptive SP (from $1136.9m \pm 43.8m$ to $1197.4m \pm 32.6m$), $88m$ using SPPAM with locality constraint A (from $359.8m \pm 12.4m$ to $447.7m \pm 11.8m$), and $64m$ using SPPAM with locality constraint B (from $646.9m \pm 18.8m$ to $711.2m \pm 18.9m$). The traveled distance for sweeping remains constant ($205.6m \pm 0.0m$). On the other hand, the covered experiment area is noticeably smaller in comparison to the results obtained in theoretical simulations (Fig. 8.6(c)).

The results from theoretical and robotic simulations are not consistent. In order to identify problems related to the simulated robotic platform (micro-drone), further experiments with 20 repetitions were performed *without* gas sensor model only and *without* GPS model, respectively (in this context, "without sensor model" refers to a perfect sensor that was used for the simulation instead of the modeled sensor presented in Ch. 4). The results of these experiments are given below.

Figs. 8.8(a) and 8.8(b) show the impact of the GPS positioning model on the simulation results (without gas sensor model). The results follow the same trend as those obtained from theoretical simulations. However, the KL distance value after 206 iterations for the different sampling approaches is unsatisfactory due to the introduced positioning error: 1.81 ± 0.13 for adaptive SP, 1.76 ± 0.13 for SPPAM with locality constraint A, 1.78 ± 0.19 for SPPAM with locality constraint B, and 1.81 ± 0.17 for sweeping (compare Figs. 8.9(a) and 8.9(b)). The traveled distance of the micro-drone (after 206 iterations) changed by almost $43m$ using adaptive SP (from $1136.9m \pm 43.8m$ to $1183.4m \pm 21.3m$), by $34m$ using SPPAM with locality constraint A (from $359.8m \pm 12.4m$ to $326.0m \pm 11.2m$), and by $11m$ using SPPAM with locality constraint B (from $646.9m \pm 18.8m$ to $658.1m \pm 21.2m$). The coverage is comparable to the above presented results where all sensor models were used (exemplarily shown in Fig. 8.6(d) for adaptive SP).

The comparison of the obtained coverage of the different SP strategies with and without certain sensor models (Fig. 8.6(c) and 8.6(d)) indicates that the GPS model of the micro-drone heavily affects the coverage area (and maybe the varying traveled distance as well). In general, in each iteration the location is chosen at which the potential takes its maximum. However, Fig. 8.7 already demonstrated that predefined measuring locations do not necessarily have to coincide with the real sampling locations of the micro-drone due to GPS inaccuracy. Correspondingly, the taken samples might be collected at locations with low potential (instead of taking samples at the location with maximum potential). As a result, the update of the APF might not affect the location with maximum potential. Thus, the location at which the potential is maximum will again be selected in the near future, reducing the efficiency of adaptive SP.

Figs. 8.8(c) and 8.8(d) show the impact of the gas sensor model on the simulation results (without GPS model). Ch. 7 already discussed the problem of the memory effect in the sensor response and what impact the slow sensor recovery has on the gas distribution maps created with sweeping. The gas sensor retains high measured concentrations for a rather long time due to the slow sensor recovery. The consequence being that the local measurement covers a much larger area while the concentration values keep decreasing when the micro-drone applies the sweeping movement (see Fig. 8.9(c)). As a result, the final gas distribution map will show a much wider plume than the ground truth map (compare Figs. 8.9(a) and 8.9(c)). This is even more problematic, when using adaptive SP or SPPAM. Due to the slow sensor recovery and the high chosen importance factor $\beta_C = 0.8$ that promotes exploration, alternate measurements inside and outside the plume will scatter the whole gas distribution map more heavily than using sweeping (that "only" results in a wider plume). Again, the traveled distances are comparable to

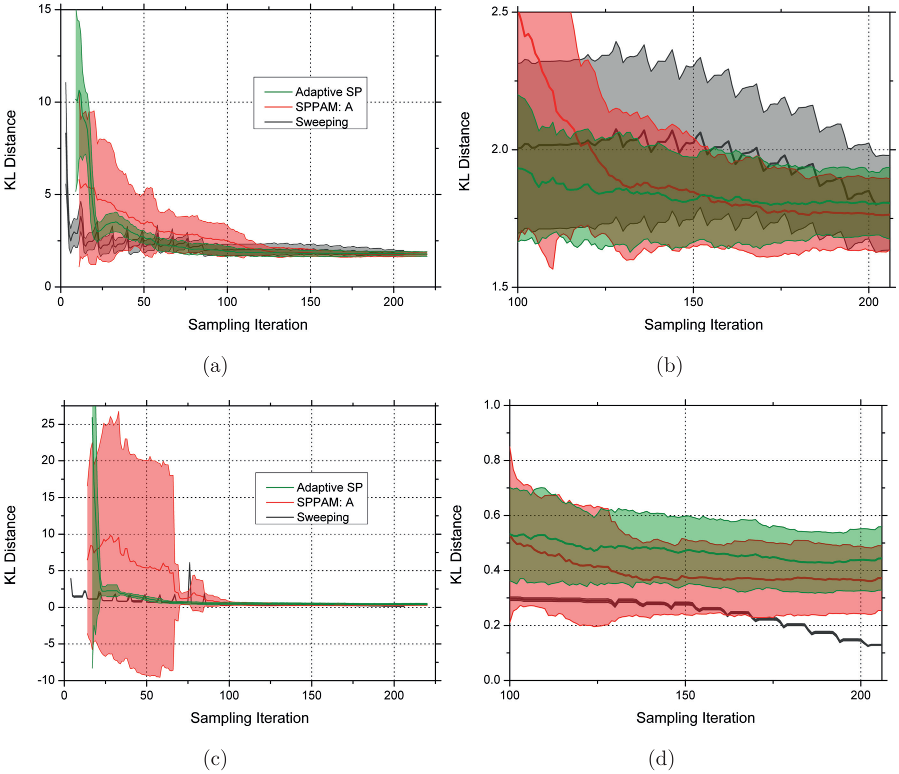

(a) (b)

(c) (d)

Figure 8.8: *Impact of the gas sensor and GPS model on the simulation results as a function of the number of iterations: KL distance comparison of predictive mean maps to the ground truth map (a) without gas sensor model and (c) without GPS model. The predictive mean maps are created using SPPAM with locality constraint A, adaptive SP, and sweeping. The ground truth is built up using all available measurements of the simulation experiment. (b) and (d) show a more detailed view of the results from iteration* 100 *to* 206*.*

the results obtained in theoretical simulations (Sec. 8.4.1.2). However, due to the above mentioned reasons the KL distance value after 206 iterations is much higher for adaptive SP and SPPAM than for sweeping (Fig. 8.8(b) and 8.8(d)): 0.44 ± 0.12 for adaptive SP, 0.37 ± 0.12 for SPPAM with locality constraint A, 0.53 ± 0.12 for SPPAM with locality constraint B, and 0.13 ± 0.001 for sweeping. The coverage, on the other hand, is more or less comparable to the results obtained in theoretical simulations where no sensor model is used (exemplarily shown in Fig. 8.6(d) for

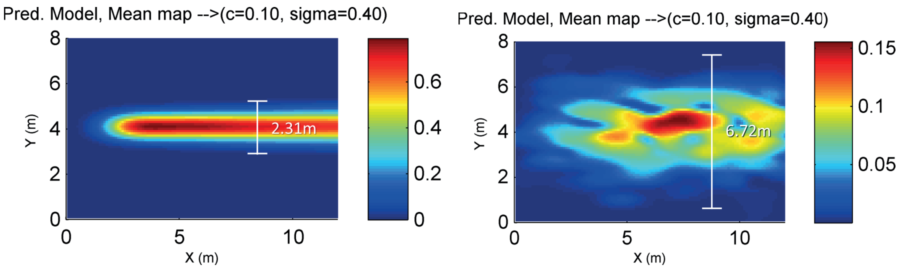

(a) Ground Truth

(b) Without Gas Sensor Model

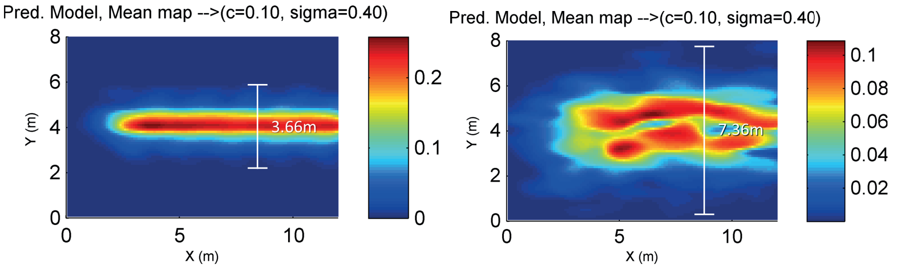

(c) Without GPS Model

(d) With Models

Figure 8.9: *Results of the robotic simulation experiments: Comparison of the (a) mean ground truth map with predictive mean maps created after* 206 *iterations using sweeping: (b) without gas sensor model, (c) without GPS model, and (d) with all sensor models.*

adaptive SP).

The results of the robotic simulations indicate that SPPAM with locality constraints and $(\beta_M, \beta_V, \beta_C)$ set to $(0.1, 0.1, 0.8)$ is not suitable for a micro-drone when accurate gas distribution maps are required. Although, other sensor planning strategies that are suitable for a micro-drone may exist. However, in this specific case, sweeping seems to be a much better strategy. In contrast, the results from theoretical simulations show the potential of adaptive SP and SPPAM when a perfect gas sensor and a perfect GPS positioning system are available. Future work should build on these results and introduce corresponding error models in the algorithm and improve the robotic platform itself.

8.5 Real-world Experiments

In addition to simulation experiments where ground truth is available, SPPAM was tested in several real-world experiments with a gas-sensitive micro-drone. However, the experiments took place at an early stage of the APF-based SP algorithm where the two APF contributions based on the predictive mean and variance maps were computed as:

$$APF_M^{(k)} = \sum\nolimits_{j \neq k} r^{(k)} \cdot \exp\left(-\frac{|x^{(j)} - x^{(k)}|}{\sigma_d}\right), \tag{8.10}$$

$$APF_V^{(k)} = \sum\nolimits_{j \neq k} v^{(k)} \cdot \exp\left(-\frac{|x^{(j)} - x^{(k)}|}{\sigma_d}\right), \tag{8.11}$$

where $x^{(j)}$ is the location of the recorded sample j, $x^{(k)}$ is the location of cell center k, and σ_d is a scaling parameter, which was set to 1. Instead of using the confidence map as repulsive potential, $APF_Q^{(k)}$ was calculated by placing charges at all $|D| = n$ previous measurement locations and q was set to -1:

$$APF_Q^{(k)} = \sum\nolimits_{j=1}^{|D|} q \cdot \exp\left(-\frac{|x^{(j)} - x^{(k)}|}{\sigma_d}\right). \tag{8.12}$$

Furthermore, only the wind measurements were averaged over the measurement time. Thus, each gas sensor measurement was included into the gas distribution model as if it was acquired together with a measurement of the average wind vector, i.e., the average wind vector was used for all individual gas sensor measurements acquired at the measurement position.

8.5.1 Experiment Environment and Setup

The first set of experiments was carried out in an $8 \times 12m^2$ outdoor area at Örebro University and on the BAM TTS with the Dräger X-am 5600 gas detector equipped with CO sensors (EC). The second set of experiments was performed in a $5 \times 5m^2$ area on the BAM TTS with the micro-drone equipped with the e-nose (MOX). The setup of the second set of experiments is the same as described in Sec. 7.3.2. A summary of the experiment setup is given below. Gas concentration and wind measurements were recorded with a frequency of $1Hz$. The measurement time at the measurement positions was set to $20s$.

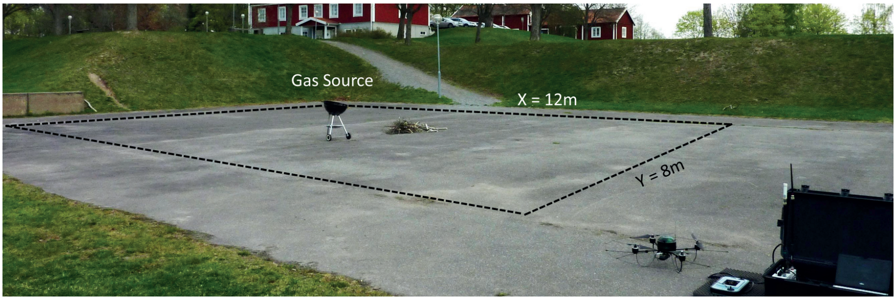

(a)

(b)

Figure 8.10: *(a) Experiment environment and setup at Örebro University. (b) A snapshot during a pollution monitoring mission in the experiment environment at BAM TTS of the first set of experiments.*

The parameters of the Kernel DM+V/W algorithm [85] were heuristically set to $c = 0.15m$ (grid cell size), $\sigma = 0.40m$ (kernel width), $\sigma_\Omega = \mathcal{N}(0, \sigma = 0.4) \approx 1.0$, $\gamma = 0.2s$, and equal importance factors for the APF contributions ($\beta_M = \beta_V = \beta_C$) were used. The "*most often suggested close-by*" locality constraint was used here. The flight speed of the micro-drone between the measurement positions was set to $1ms^{-1}$. Because of the low altitude of the micro-drone of 1 to $2m$, the altitude was kept constant manually during the experiments. Each trial in the first set of experiments took 14 to 19 minutes to complete depending on the battery consumption of the micro-drone. The second set of experiments took 8 to 13 minutes to complete. A barbecue filled with burning coal and fresh, damp wood was used as a pollution source in the first set of experiments (Fig. 8.10) and was placed approximately in the middle of the experiment area (at approx. $(6.3, 3.8)m$ from the bottom left corner).

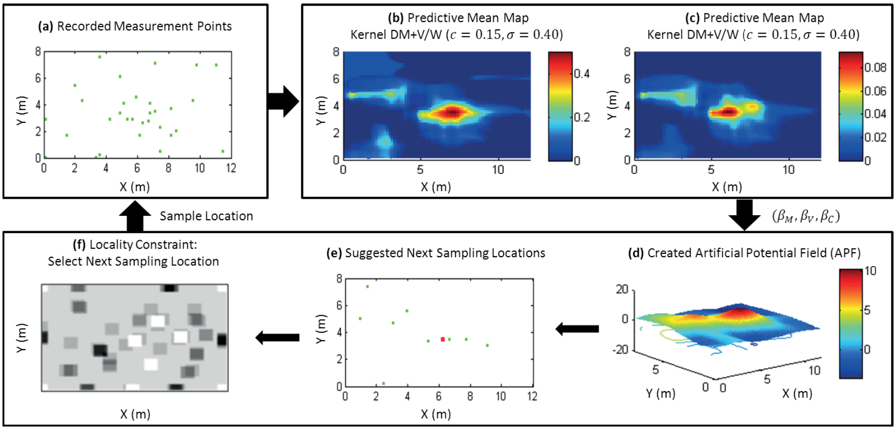

Figure 8.11: *Adaptive sampling process: (a) from the previously visited sampling locations, (b) predictive mean* $r^{(k)}$ *and (c) variance maps* $v^{(k)}$ *were created using the Kernel DM+V/W algorithm with* $\sigma = 0.4m$*,* $c = 0.15m$*, and* $\gamma = 0.2s$ *as meta-parameters. (d) Then, a set of next sampling points are selected from the APF. (e) These points and the estimated source location are denoted by green and red dots, respectively. (f) The next sampling location is chosen based on the locality constraint B, where the white cells are the previously selected cells and the darkest cells correspond to the most often suggested ones. All plots were created after the last time step of the SPPAM algorithm (trial #3, measurement 31).*

The gas source in the second set of experiments is a CH_4 gas cylinder positioned at approximately $(0.0, 3.0)m$ (Sec. 7.3.2) within the experiment area. The algorithm was activated directly after take-off, which started the experiment.

8.5.2 Experiment Results

8.5.2.1 First Experiment

The results presented in Figs. 8.11, 8.12(a), 8.12(b), and Table G.1 (see Appendix G) demonstrate the suitability of the proposed algorithm for GDM and its use for gas source localization. A total number of 16 trials were performed within these experiment sets. Fig. 8.12(b) and Table G.1 show for all 16 trials the distance between the true gas source location and six different estimates after the last measurement point. The first three estimates are derived by selecting grid cells in which the (A)

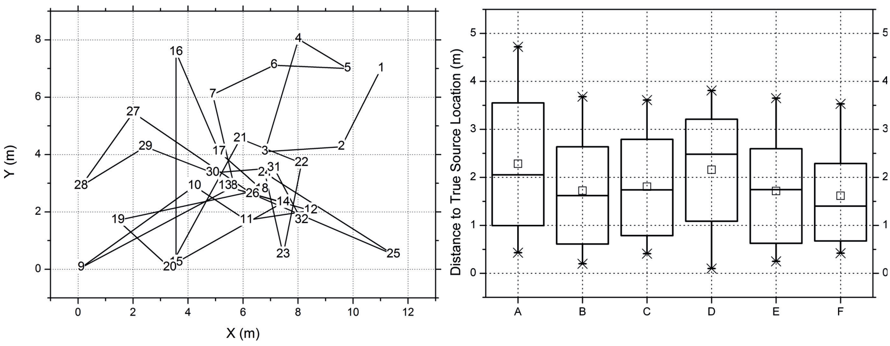

(a) (b)

Figure 8.12: *(a) Sample trajectory of SPPAM (trial #3) with starting position* $(x, y) = (11.02, 7.00)m$. *(b) Box-plot of the gas source location estimate (distance to true source location) of the 16 trials after 24 to 35 taken measurements: (A) peak mean, (B) peak variance, (C) peak mean·variance, (D) mean, (E) variance, and (F) mean·variance. The box shows the lower/upper quartile and the line denotes the median. The mean is denoted by the small* □. *The* × *symbol stands for outliers.*

predictive mean, (B) predictive variance, or (C) the product of mean and variance are maximum. The fourth estimate is derived by selecting grid cells in which (D) the predictive mean is greater than 90% of the maximum. The center of this area is taken as the source location estimate and the maximum extension in x- or y-direction is used to specify a confidence interval. In the same way, the last two estimates are computed using (E) the variance or (F) the product of mean and variance. The true source location was within the mean estimation area only in four trials and within the variance estimation area in six trials. This is in line with previous observations that the concentration variance often provides a better indication of the gas source location [1] than the mean.

Fig. 8.11 shows the final snapshot of trial #3 after 31 measurement points. The top row shows the previously visited sampling locations (left) and the corresponding mean distribution map $r^{(k)}$ (middle) and variance distribution map $v^{(k)}$ (right) produced by the Kernel DM+V/W algorithm with $\sigma = 0.4$, $c = 0.15m$ and $\gamma = 0.2s$ as meta-parameters. The bottom row shows a visualization of the APF with $\beta_M = \beta_V = \beta_C$ (right), the area with the next suggested sampling points and source location estimate, which are indicated by green and red dots, respectively

Table 8.3: *Wind conditions on the BAM TTS.*

Trial	Method	Sampling Points	Mean Wind Speed (ms^{-1})	σ (ms^{-1})	Mean Wind Direction (°)	Circular Variance
1	Sweeping	24	1.38	±0.71	247	0.32
2	Sweeping	24	1.65	±0.82	246	0.21
3	Sweeping	24	1.57	±0.82	259	0.26
4	SPPAM	22	1.60	±0.76	223	0.48
5	SPPAM	11	1.81	±0.82	23	0.33

(middle), and the matrix S, where the white cells are the previously selected cells and the darkest cells correspond to the most often suggested cells. Fig. 8.12(a) shows exemplarily the trajectory produced by the path planning algorithm in trial #3 with starting position $(x, y) = (11.02, 7.00)m$ (compare with Fig. 8.11). Initial results from these trials indicate the potential of adaptive sampling in providing a good estimate of gas source location with a relatively small number of samples. However, the source location estimate is a performance indicator that has not been evaluated in Sec. 8.4.

It proved difficult to keep the gas emission rate constant over time with the chosen gas source. A re-ignition of the almost extinguished source in trial #4 for example (after the 20th measurement) created an intense emission that caused very high concentrations also far away from the source. The 21st measurement taken at position $(x, y) = (8.85, 4.95)m$ was affected by this outburst, which caused a strong change in the gas source location estimate (see Appendix G – Table G.1). Another difficulty, which should be mentioned here, is the slow sensor decay. Flying from the current position to the next measurement position directly over the source can lead to an erroneous source location estimate (and inaccurate gas distribution map) when the sensor still responds to the high concentrations close to the source.

8.5.2.2 Second Experiment

A total number of only two trials were performed directly after the GDM experiment presented in Secs. 7.3.2 and 7.4.2 using the same experiment setup. The identical experiment setup and the barely changed wind and weather conditions (Table 8.3) permit an exemplary cross-comparison of the different sampling approaches. The availability of more trials would have been advantageous for a more detailed evaluation. However, a longer period of almost constant wind would be needed to be able to perform larger test sets. Unfortunately, such a day with the required wind conditions has not recurred on the BAM TTS.

Fig. 8.13(a) shows exemplarily the result of trial #1 of the GDM experiment. Here, the data was collected using a sweeping trajectory. Figs. 8.13(b) and 8.13(c) show trial #4 and #5 using SPPAM. In comparison to the sweeping trials, the stability of the wind conditions during the two trials using SPPAM decreased noticeably (Table 7.4): the average wind speed increased from approximately 1.4 to $1.7ms^{-1}$ and 1.6 to $1.8ms^{-1}$ and the average wind direction changed from 246° and 259° to 223° (#4) and 23° (#5), respectively. Here, the airflow produced by the fan can be neglected as the area of influence is only limited to the immediate proximity of the fan. The main wind direction of trial #4 correlates more or less with the three sweeping trials (compare exemplarily the airflow maps in Figs. 8.13(a) and 8.13(b)). However, the wind directions measured at the sampling locations 4 to 10 during trial #4 varied drastically from the main wind direction of 223°: 146° to 160° (at locations 4 to 8) and 344° to 35° (at locations 9 to 10). This fact is also reflected by the increased circular variance of 0.48. Trial #5 has to be considered separately as the main wind direction rotated by more than 120° although the circular variance of 0.33 is at least comparable to trial #1. Furthermore, only 11 sampling points could be taken within this trial due to a battery failure of the micro-drone.

Again, the altitude of the micro-drone had to be elevated manually in trial #4 and #5 to avoid a collision with the fan resulting in low concentration values close to the source and which moved the measured maximum concentrations further downwind (Sec. 7.4.2). Therefore, no accurate gas source location estimate could be obtained. However, reproducibility is only given for trial #1 and #4 as the qualitative and quantitative results remain similar in all created maps. Small variations in the plume propagation can be explained by the temporary change in the wind field during trial #4. The results from trial #5 differ more pronouncedly as the airflow map shows a significant change of the main wind direction.

Fig. 8.14 shows a comparison of the coverage of both strategies. The gray circles describe the coverage of the sweeping trajectory of trial #1 and the blue solid circles show the coverage of the trajectory of SPPAM in trial #4. The sequence of visits of trial #4 is specified in the blue circles. The size of the circles corre-

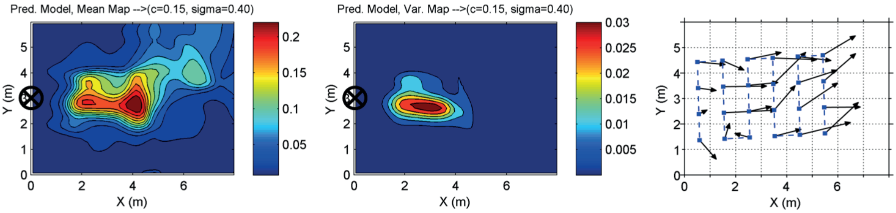

(a) GDM: Trial #1; CH_4

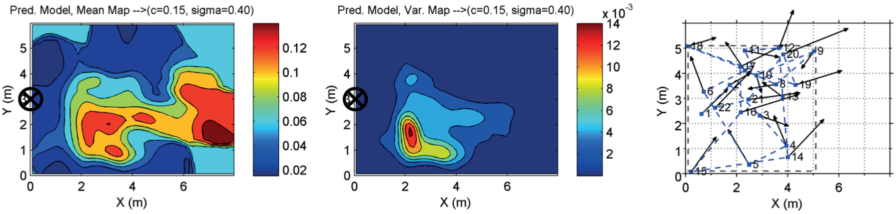

(b) SPPAM: Trial #4; CH_4

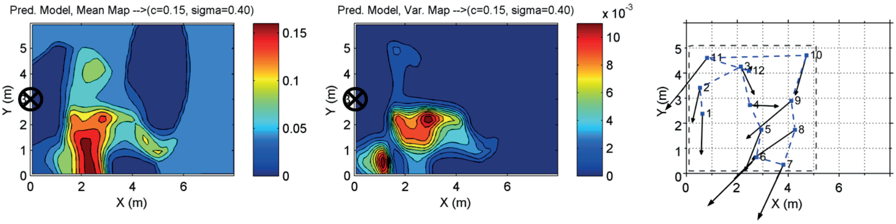

(c) SPPAM: Trial #5; CH_4

Figure 8.13: *BAM TTS: Predictive mean (left) and variance map (middle) of the gas distribution (a) using a sweeping trajectory (trial #1, see Sec. 7.4.2) and (b) to (c) using SPPAM (trial #4 and #5). The figures on the right show the corresponding mean airflow maps. The gas source was located approximately at position* $(0, 3)m$ *and is denoted by* $\otimes$. *The defined experiment area in (b) to (c) is indicated by the gray dotted line. The starting position of the micro-drone was located approximately at position (a)* $(5.5, 1.5)m$ *and (b) to (c) at* $(0.6, 2.4)m$. *The* CH_4 *concentration value is given in % by volume. All plots of (b) trial #4 and (c) trial #5 were created after the last time step of the SPPAM algorithm.*

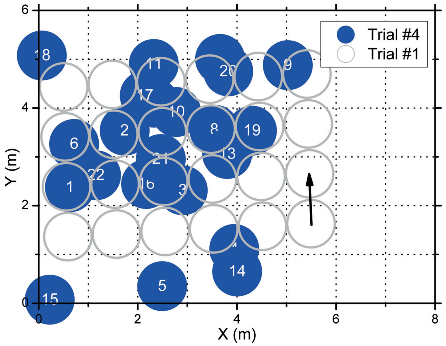

Figure 8.14: *Comparison of the coverage of GDM using a sweeping trajectory and SPPAM. The size of the circles corresponds to the diameter of the micro-drone of* $1m$*. The gray circles denote the sampling locations of the sweeping trajectory (trial #1), whereas the blue solid circles denote the sampling locations of SPPAM (trial #4). The sequence of visits of the sweeping trajectory is indicated by the arrow, whereas the blue circles are numbered to their sequence.*

sponds to the diameter of the micro-drone of $1m$. The sweeping strategy basically covers the whole search area. SPPAM, on the other hand, directs the micro-drone towards areas of high predictive mean and high predictive variance while maximizing the coverage area, which can be clearly seen in the distribution of the sampling points. In comparison to sweeping, SPPAM also took more measurements close to the plume centerline. The results demonstrate the suitability of the proposed algorithm for GDM and present an alternative to sweeping. However, more experiments are needed to verify this proposition.

8.6 Summary and Conclusions

In this chapter, a novel adaptive sampling strategy was applied for a gas-sensitive micro-drone. The adaptive SP approach uses the statistical gas distribution models obtained with the Kernel DM+V/W algorithm. Areas of high mean and variance are good candidates for further inspection and the corresponding locations are prioritized through strong contributions to an APF. These exploitation contributions are balanced by repulsive contributions at previous sampling locations that promote exploration. This adaptive SP approach was extended by introducing locality constraints that make the proposed trajectory more suitable for a mobile gas measurement system since it avoids large jumps between subsequent measurement locations. The results from theoretical simulations and real-world experiments with this extended adaptive SP algorithm (SPPAM) show the potential for gas distribution mapping. The robotic simulations highlight that future work should address the GPS positioning error of the micro-drone. In general, a more accurate and reliable positioning system of the micro-drone would be needed to obtain more accurate gas distribution maps. However, it was also observed that the produced maps (and particularly the variance prediction) are sufficient to provide good estimates of gas source location. The conclusion when comparing sampling along a predefined sweeping trajectory with the proposed adaptive SP approach is therefore that adaptive SP tends to arrive in fewer iterations at a meaningful map which allows inference of a reasonably accurate estimate of the gas source location. However, the theoretical simulations (Sec. 8.4.1) indicate a shorter path for sweeping than for adaptive SP. Furthermore, the robotic simulations (Sec. 8.4.2) suggest that adaptive SP with locality constraints is not suitable for a micro-drone when accurate gas distribution maps are required. In that specific case, sweeping seems to be a much better strategy. On the other hand, the results from theoretical simulations show the potential of adaptive SP when a perfect gas sensor and a perfect GPS positioning system are available. In general, if the sampling device is a gas-sensitive micro-drone then a strategy that avoids sampling at locations that provide little information is advantageous because of the resource constraints on the micro-drone. In addition, a smaller number of measurements also tends to interfere less with gas distribution. This effect is not taken into account in the current SP algorithm, however. Thus, suitable algorithms have to be developed that consider the resource constraints on the micro-drone and minimize the flight time of micro-drones so as to interfere less with gas distribution.

Future work should include a performance evaluation of the (extended) adaptive SP algorithm for different scenarios of gas release considering, e.g., turbulent flow, obstacles, different gas source locations, and varying size of the experiment area. In [16], Asadi will address some of these points in her Ph.D. thesis. Furthermore, to avoid the local maximum problem (i.e., exploitation dominates exploration) of adaptive SP and SPPAM, mechanisms have to be integrated that recognize when the robot is trapped in a region. To explore the rest of the experiment area (if necessary), the selection of next measuring locations could be driven by repulsiononly (by setting the importance factors for the mean and variance maps to zero). In a next step, ways will be investigated on how to introduce a criterion that allows minimizing the degradation of the observed gas distribution through the micro-drone itself. Moreover, the current implementation of the adaptive SP algorithm does not take into account the time when the measurements were made. Therefore, an extension of the approach that introduces time-dependency [16] will be studied. First, a time-dependent statistical gas distribution modeling algorithm will be used, for example the Time-Dependent (TD) Kernel DM+V algorithm introduced in [95]. Next, a study of an extension of the adaptive SP algorithm to the 3rd dimension is planned.

Autonomy and agent behavior are implemented in the adaptive SP strategy for gas distribution mapping. Since agent behavior in a swarm was not the focus of this Ph.D. thesis, this point was not elaborated on. However, strategies have to be integrated that coordinate the different agents of a swarm (micro-drones) collision-free within the inspection area.

Chapter 9

Conclusions and Future Work

Each chapter of this Ph.D. thesis contains a summary and conclusion section, where suggestions for future work are also presented. This chapter concludes the thesis as a whole and describes future work from a general perspective.

9.1 Conclusions

This Ph.D. thesis tackled gas source localization and gas distribution mapping of static gas sources in natural environments with the help of a gas-sensitive micro-drone. To the best of the author's knowledge, it is the first time that a gas-sensitive micro-drone was developed based on a quadrocopter which is able to perform in-situ measurements of gas concentrations and wind vectors without dedicated anemometer. This development is important as state-of-the-art measuring platforms are generally ground-based and cannot reach certain emission sources (due to, e.g., obstacles, rough terrain, and large gaps). At this stage, the prototype of a gas-sensitive micro-drone can be utilized to obtain an estimate of the risk potential in a variety of scenarios of gas emissions without endangering people in critical situations (Fig. 9.1). Targeted fields of operation are gas measurements in accident scenarios, emission control, monitoring of critical areas (including environmental monitoring tasks), and detection of gas leaks under difficult conditions. Extensive experiment results with the gas-sensitive micro-drone have demonstrated its suitability for these tasks.

It was demonstrated in several real-world environments that the gas-sensitive micro-drone is capable of tracking a gas plume along its entire length using three partly novel reactive bio-inspired plume tracking strategies. The application of these

Figure 9.1: *Micro-drone monitoring relevant parameters (gas concentrations, wind, temperature, and humidity), while the fire brigade extinguishes a bus on fire. Photo taken at BAM TTS during an artificial fire scenario.*

algorithms was enabled by the ability of the micro-drone to simultaneously perform gas concentration and wind measurements. The algorithms succeeded although the wind vector estimation approach introduced an angular inaccuracy of approximately ±14°. In combination with a novel particle filter-based gas source localization algorithm for declaring the location of a static gas source, a possible solution for the whole gas source localization task for a gas-sensitive micro-drone is suggested.

Furthermore, the problem of gas distribution mapping with the gas-sensitive micro-drone was studied. Two different sampling approaches were suggested to address this problem. First, predefined sweeping trajectories were used to explore the target area with the micro-drone in several real-world gas distribution mapping experiments. To more quickly arrive at a truthful gas distribution model, a second approach was evaluated that allows obtaining a reasonably accurate estimate of the gas source location. The adaptive sensor planning algorithm suggests next sampling points which are based on an Artificial Potential Field (APF). By introducing locality constraints, the results of the sensor planning component can be used to plan suitable paths for a micro-drone.

All algorithms presented in this work were evaluated in simulation and real-world experiments. However, the design of experiments that enable to study and develop robotic systems for airborne chemical monitoring is probably one of the most crucial aspects of research in mobile robot olfaction [PAPER II]. To carry out ground truth evaluated experiments in realistic environments by gas-sensitive mobile robots has always been a critical issue: The chaotic nature of gas dispersal with rapidly changing environmental conditions makes the plume evolution hard to predict and prevents the reproducibility of these experiments. Furthermore, the dispersion of chemicals in natural environments is difficult to observe since most of them produce an invisible plume. Thus, it is difficult to obtain ground truth that can be used to validate experiment results. Building a dense array of fixed installed gas sensors or measuring probes (used for, e.g., GC) [5] is not feasible over a large area not only for financial reasons, but also as gas distribution cannot be measured at the same height as with the micro-drone. This static sensor setup also influences the natural gas distribution. Using visible tracer gas is not practicable either as the tracer gas and the gas to be monitored should have the same distribution characteristics [5]. The usage of visible tracer gas is especially impracticable when performing monitoring experiments in geochemically active regions with gas sources emitting various gases at unknown and variable release rates. Furthermore, correlating the visible tracer gas to the measured concentration is also not straightforward. Experiments under controlled conditions indeed can provide ground truth to validate the experiment results, but it is hard to predict how the results obtained in such experiments can be applied to uncontrolled or rather realistic environments. It cannot be said that results obtained in an environment with, e.g., steady and controlled airflow automatically apply to more general and complex environments. It is very important that experiment setups, in which the claimed results are obtained, are described in detail.

Regarding real-world applications, the main limitations of this Ph.D. thesis can be summarized as follows:

- The micro-drone's rotor movement considerably disturbs the gas distribution and influences gas measurements. This limitation was expected and observed experimentally with an orange colored smoke bomb that was used to visualize these disturbances (see Ch. 3, Fig. 3.1(b)).

- The flight time of approximately $20min$ does not allow to perform monitoring or search tasks in large-area scenarios with a single micro-drone. For example, a fleet of micro-drones that conduct the exploration task consecutively or simultaneously may solve the problem of limited battery capacity.

- The long response times of current gas sensors are also problematic for generating truthful representations of the gas dispersion. Furthermore, shorter response times are also required in order to reduce the measurement time and to be able to cover larger areas. This conclusion is based on the experiments (see Ch. 7).
- The GPS positioning system of the micro-drone affects the accuracy of gas distribution maps and the localization performance of the algorithms presented. This limitation was observed during the evaluation of the experiments described in Ch. 7 and 8.
- The presented methods have been focused on the 2D case only because of the restrictions imposed by the micro-drone at ground level. This limitation was observed experimentally.

In view of the large number of real-world experiments performed in different natural environments under variable wind and weather conditions, this Ph.D. thesis constitutes an important contribution to the field of mobile robot olfaction. In comparison to experiments presented in previous work (Ch. 2), the real-world experiments were performed in uncontrolled outdoor environments or experiment setups were built where no artificial conditions were introduced to simplify the experiments. Furthermore, all suggested algorithms can be transferred to other robotic platforms regardless of the element the robot is specialized for (land, water, and air).

9.2 Future Work

The accuracy of the GPS positioning system of the micro-drone should be addressed in the future. A positioning system that only relies on jumpy GPS data is not desirable for a gas-sensitive micro-drone that perform gas distribution mapping. For instance, lightweight optical systems could be developed and integrated into the micro-drone that support more accurate position holding. The limitations of current gas sensors is another open issue. More research is needed to develop better gas sensors. New battery technologies, on the other hand, can support the extension of the flight time and miniaturization of such micro-drones and enable monitoring or search tasks in large-area scenarios. Smaller micro-drones also reduce disturbance to gas distribution.

Another limitation of the methods presented is that this Ph.D. thesis focused on the 2D case due to the restrictions imposed by the micro-drone. Thus, a general extension of this work may be to improve the micro-drone's flight capabilities and adapt the presented algorithms for the 3rd dimension, including a detailed statistical analysis of their performance and robustness in simulation and real-world experiments. The main focus should lie on the latter as almost all of the related work on gas-sensitive standard or micro UAVs has been validated in simulated experiments only. Furthermore, most gas source localization experiments have been performed with the help of ground-based mobile robots under simplified conditions such as a steady constant airflow and the presence of a single gas source emitting a known chemical compound at a constant release rate. It would be beneficial to find ways to perform meaningful ground truth evaluated real-world experiments.

Multi-robot collaboration was only touched on a rudimentary basis in this Ph.D. thesis. For example, Lochmatter already showed in [12] that some bio-inspired plume tracking algorithms cannot cope with disturbances and therefore are inherently suitable for single-robot systems only. This is especially relevant when using micro-drones for this task. For monitoring applications, however, a sophisticated multi-robot collaboration scheme may help to reduce the time needed to cover larger areas. But then, algorithms need to be developed able to cope with disturbances caused by multiple micro-drones (swarm). This will help obtain reliable gas distribution maps and identify the location of the gas source. Suggestions for possible approaches are presented in Ch. 7 and 8 of this thesis.

The integration of conventional SLAM techniques into the overall system may enable the micro-drone to build a map of the environment. This can then be combined with the presented gas source localization and gas distribution mapping algorithms to support rescue workers during mission.

Appendix A

Directional Statistics

The mean wind direction $\overline{\theta}$ is calculated using Eq. A.1 [146]:

$$\overline{\theta} = \arctan\left(\frac{\overline{s}}{\overline{c}}\right) + \begin{cases} 0^\circ & \overline{s} > 0,\, \overline{c} > 0 \\ 180^\circ & \overline{c} < 0 \\ 360^\circ & \overline{s} < 0,\, \overline{c} > 0 \end{cases} \tag{A.1}$$

with

$$\overline{s} = \frac{\sum_{i=1}^{n} \sin\theta_i}{n} \text{ and } \overline{c} = \frac{\sum_{i=1}^{n} \cos\theta_i}{n}, \tag{A.2}$$

where n is the total number of samples and θ_i is the angle of a single wind direction measurement.

The circular variance S_0 [146] is a dimensionless number and used here to describe the stability of the wind during the different real-world experiments. S_0 is calculated using a sample of n wind directions $\theta_i : i \in [0, n]$:

$$S_0 = 1 - \bar{R} \tag{A.3}$$

where

$$\bar{R} = \sqrt{\left(\frac{1}{n}\sum_{i=1}^{n}\cos(\theta_i)\right)^2 + \left(\frac{1}{n}\sum_{i=1}^{n}\sin(\theta_i)\right)^2}. \tag{A.4}$$

$\bar{R}$ is called the mean resultant length. It is used to characterize the dispersion of a sample. For example, a group of n vectors with identical direction results in $\bar{R} = 1$, whereas a group of perfectly opposing vectors results in $\bar{R} = 0$. This means, that a large value of $\bar{R}$ indicates a dense bundle of vectors with small spread and accordingly a small value of $\bar{R}$ indicates a more distributed set of vectors.

Appendix B

Coordinate Transformation

Fig. B.1 illustrates the simulation environment with micro-drone, gas source, plume, and area boundaries. Before a transformation between the global world geodetic system (WGS) and local coordinate system can be performed, the course between the positions $p_1 = (\theta_1, \phi_1)$ and $p_2 = (\theta_2, \phi_2)$ and the course between the positions $p_1 = (\theta_1, \phi_1)$ and $p_m = (\theta_m, \phi_m)$ (Fig. B.1) have to be calculated using Eq. B.1, where the positions $p_i = (\theta_i, \phi_i)$ with $i = [1, 4]$ and $p_m = (\theta_m, \phi_m)$ refer to the

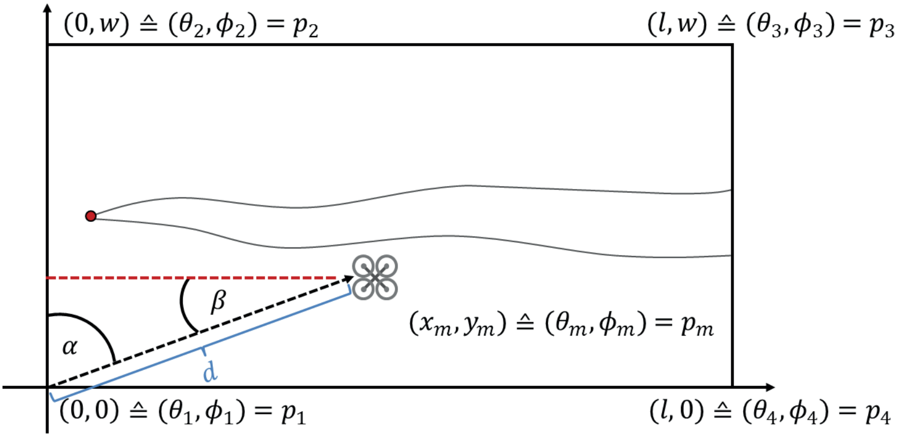

Figure B.1: *Simulation environment with micro-drone, gas source, and plume:* $(0,0)$*,* $(l,0)$*,* $(0,w)$*, and* (l,w) *are the local coordinates and* (θ_i, ϕ_i) *with* $i = [1,4]$ *are the corresponding global coordinates (*$\theta \widehat{=}$ *longitude and* $\phi \widehat{=}$ *latitude) of the area boundary. The position of the micro-drone is denoted by* $(x_m, y_m) \widehat{=} (\theta_m, \phi_m)$*.*

corners of the simulation environment borders and the position of the micro-drone, respectively. Eq. B.2 is further used to obtain the angle α (the angle β results from the equation of the interior angles):

$$\begin{aligned}\mathrm{course}(p_i, p_j) = \mathrm{atan2}(\, & \sin(\theta_j - \theta_i) \cdot \cos\phi_j, \\ & \cos\phi_i \cdot \sin\phi_j - \sin\phi_i \cdot \cos\phi_j \cdot \cos(\theta_j - \theta_i)),\end{aligned} \tag{B.1}$$

$$\alpha = (\mathrm{course}(p_1, p_m) - \mathrm{course}(p_1, p_2)) \bmod (2 \cdot \pi), \tag{B.2}$$

where $\theta_{i,j}$ is the longitude and $\phi_{i,j}$ is the latitude of the respective real-world coordinate $p_{i,j}$.

Furthermore, the distance d between positions $p_1 = (\theta_1, \phi_1)$ and $p_m = (\theta_m, \phi_m)$ has to be calculated:

$$d(p_i, p_j) = 2 \cdot \sin^{-1}\left(\sqrt{\left(\sin\frac{\phi_i - \phi_j}{2}\right)^2 + \cos\phi_j \cdot \left(\sin\frac{\theta_i - \theta_j}{2}\right)^2}\right) \cdot 6378137, \tag{B.3}$$

where the constant 6378137 is related to the World Geodetic System 1984 (WGS 84). Eqs. B.1 and B.3 are taken from [123].

Assuming that the micro-drone does not leave the first quadrant of the local coordinate system, the local position of the micro-drone can be calculated as:

$$x_m = \begin{cases} 0 & \text{, if } \alpha = 0 \\ d & \text{, if } \alpha = \frac{\pi}{2} \\ d \cdot \frac{\sin\alpha}{\sin\frac{\pi}{2}} & \text{, otherwise} \end{cases} \tag{B.4}$$

$$y_m = \begin{cases} d & \text{, if } \alpha = 0 \\ 0 & \text{, if } \alpha = \frac{\pi}{2} \\ d \cdot \frac{\sin\beta}{\sin\frac{\pi}{2}} & \text{, otherwise} \end{cases} \tag{B.5}$$

Appendix C

Distance Overhead

The distance overhead d_o is used as the performance metric to compare the plume tracking algorithms experiments with each other [12]. d_o is defined as:

$$d_o = \frac{d_t}{d_u}, \tag{C.1}$$

where d_t denotes the effectively traveled distance by the micro-drone and d_u the upwind distance to the gas source. The upwind distance d_u is calculated using the Euclidean distance between the position, where the micro-drone measures for the first time an average concentration above the threshold, and the source position (minus the distance at the end of the experiment). Therefore, it represents the shortest path a robot would take if the source location were known. The advantage of this performance metric is, that the distance overhead d_o is independent from different start positions of the micro-drone as long the plume structure (width, intermittency, and concentrations) remains the same over the whole length of the plume.

Appendix D

PF-based GSL Algorithm – Simulation Results

Tables D.1 and D.2 show the simulation results of the PF-based GSL algorithm for different meta-parameter combinations using the pseudo gradient plume tracking algorithm (Table D.1) and sweeping (Table D.2). Each cell of the tables contains the average error of successful localizations and its standard deviation as confidence interval and the success rate of the corresponding meta-parameter set.

Table D.1: *Experiment results of the PF-based algorithm for different parameter combinations using the pseudo gradient algorithm. A cell contains the average error of successful localizations $\pm\sigma$ given in m and the success rate given in %.*

β α	0.1	0.2	0.3	0.4	0.5	0.6	0.7	0.8	0.9	1.0
0.1	0.73	0.86	0.76	0.68	0.67	0.69	0.68	0.58	0.64	0.66
	±0.37	±0.34	±0.34	±0.35	±0.36	±0.33	±0.35	±0.33	±0.31	±0.37
	41%	64%	71%	78%	79%	80%	83%	79%	82%	76%
0.2	0.78	0.87	0.81	0.78	0.72	0.70	0.67	**0.62**	0.65	0.66
	±0.39	±0.36	±0.34	±0.41	±0.34	±0.38	±0.35	±0.37	±0.37	±0.38
	28%	53%	56%	64%	76%	81%	81%	**86%**	75%	77%
0.3	0.82	0.84	0.77	0.76	0.70	0.71	0.66	0.65	**0.64**	**0.65**
	±0.36	±0.37	±0.36	±0.37	±0.39	±0.37	±0.39	±0.34	±0.33	±0.37
	14%	42%	58%	63%	68%	80%	80%	79%	**89%**	**89%**
0.4	0.82	0.91	0.90	0.81	0.80	0.72	0.66	0.66	0.63	0.57
	±0.41	±0.37	±0.36	±0.38	±0.33	±0.37	±0.37	±0.34	±0.34	±0.34
	7%	31%	50%	54%	63%	79%	74%	84%	80%	80%
0.5	1.29	0.84	0.82	0.81	0.77	0.76	0.75	0.72	0.61	0.60
	±0.13	±0.44	±0.34	±0.31	±0.37	±0.39	±0.37	±0.37	±0.35	±0.35
	3%	16%	38%	47%	55%	69%	76%	77%	75%	74
0.6	0.82	0.87	0.98	0.79	0.83	0.66	0.71	0.67	0.62	0.60
	±0.24	±0.36	±0.36	±0.38	±0.30	±0.37	±0.37	±0.32	±0.36	±0.35
	4%	16%	31%	36%	57%	56%	67%	72%	80%	75%
0.7	-	0.69	1.04	0.79	0.93	0.72	0.77	0.66	0.71	0.56
	-	±0.39	±0.23	±0.37	±0.32	±0.38	±0.36	±0.31	±0.40	±0.31
	0%	8%	13%	33%	42%	53%	69%	82%	69%	80%
0.8	-	0.67	1.00	0.78	0.75	0.85	0.76	0.64	0.66	0.65
	-	±0.03	±0.28	±0.40	±0.32	±0.33	±0.40	±0.33	±0.37	±0.37
	0%	2%	9%	20%	33%	47%	59%	68%	74%	77%
0.9	-	1.34	0.62	0.87	0.92	0.80	0.79	0.79	0.68	0.70
	-	-	±0.25	±0.31	±0.34	±0.38	±0.38	±0.32	±0.36	±0.39
	0%	1%	3%	11%	26%	46%	%	59%	61%	76%
1.0	-	-	0.68	0.91	0.88	0.79	0.81	0.72	0.80	0.66
	-	-	±0.51	±0.35	±0.36	±0.37	±0.35	±0.33	±0.40	±0.35
	0%	0%	2%	12%	9%	35%	53%	57%	63%	71%

Table D.2: *Experiment results of the PF-based algorithm for different parameter combinations using sweeping. A cell contains the average error of successful localizations ±σ given in m and the success rate given in %.*

β α	0.1	0.2	0.3	0.4	0.5	0.6	0.7	0.8	0.9	1.0
0.1	- - 0%	0.69 ±0.31 15%	0.83 ±0.38 40%	0.71 ±0.30 68%	0.77 ±0.35 76%	0.70 ±0.34 80%	0.71 ±0.32 82%	0.68 ±0.33 85%	0.70 ±0.31 88%	0.73 ±0.32 82%
0.2	- - 0%	1.07 ±0.37 2%	0.77 ±0.34 28%	0.72 ±0.35 57%	0.77 ±0.39 68%	0.78 ±0.34 66%	0.73 ±0.34 83%	0.74 ±0.33 84%	0.66 ±0.36 89%	0.72 ±0.37 94%
0.3	- - 0%	- - 0%	1.28 ±0.08 3%	0.76 ±0.39 40%	0.79 ±0.36 44%	0.77 ±0.30 63%	0.75 ±0.36 76%	0.68 ±0.38 81%	0.69 ±0.38 86%	0.73 ±0.37 86%
0.4	- - 0%	- - 0%	0.78 ±0.46 3%	1.01 ±0.32 17%	0.76 ±0.38 41%	0.79 ±0.39 68%	0.72 ±0.36 83%	0.71 ±0.36 84%	**0.72** ±0.34 **95%**	0.73 ±0.34 89%
0.5	- - 0%	- - 0%	- - 0%	0.57 ±0.25 6%	0.88 ±0.36 33%	0.86 ±0.37 50%	0.74 ±0.39 75%	0.73 ±0.36 86%	0.78 ±0.36 81%	0.72 ±0.38 91%
0.6	- - 0%	- - 0%	- - 0%	- - 0%	0.84 ±0.39 15%	0.84 ±0.37 37%	0.82 ±0.37 61%	0.72 ±0.38 76%	0.67 ±0.35 83%	0.75 ±0.38 85%
0.7	- - 0%	- - 0%	- - 0%	0.79 - 1%	0.72 ±0.16 2%	0.81 ±0.37 29%	0.73 ±0.39 57%	0.72 ±0.36 71%	0.68 ±0.38 77%	0.67 ±0.36 84%
0.8	- - 0%	- - 0%	- - 0%	- - 0%	- - 0%	0.78 ±0.31 16%	0.82 ±0.39 38%	0.73 ±0.39 62%	0.73 ±0.37 73%	0.76 ±0.39 82%
0.9	- - 0%	- - 0%	- - 0%	- - 0%	- - 6%	0.96 ±0.42 34%	0.93 ±0.35 62%	0.81 ±0.35 71%	0.79 ±0.38 76%	0.69 ±0.38
1.0	- - 0%	- - 0%	- - 0%	- - 0%	- - 0%	1.40 - 1%	0.94 ±0.43 15%	0.77 ±0.39 49%	0.68 ±0.32 71%	0.70 ±0.35 74%

Appendix E

Kullback-Leibler Divergence

The Kullback-Leibler (KL) divergence or relative entropy for probability is a measure of distribution similarity (Sec. 8.4). The KL divergence is defined as:

$$KL(p|q) = -\int p(x) \ln \frac{q(x)}{p(x)} dx, \tag{E.1}$$

where $p(x)$ is the reference distribution (ground truth) and $q(x)$ is the modeled distribution. The KL divergence satisfies three properties:

$$KL(p|p) = 0 \tag{E.2}$$

$$KL(p|q) = 0 \leftrightarrow p(x) = q(x) \tag{E.3}$$

$$\forall p, q : KL(p|q) \geq 0 \tag{E.4}$$

Here, the symmetric version of the KL distance measure is used as $KL(p|q) \not\equiv KL(q|p)$. It is defined as:

$$KL(p, q) = \frac{1}{2} KL(p|q) + \frac{1}{2} KL(q|p). \tag{E.5}$$

Since gas distribution maps are not probability distributions, a normalization is applied such that the sum over all values equals one [94].

Appendix F

Particle Filter – Linear Time Resampling

Carpenter et al. proposed in [138] a *resampling* algorithm, which runs in linear time in the number of particles. They obtain a sorted random number sequence in linear time using the cumulative sum of the negative logarithm of N random numbers uniformly distributed in $[0, 1]$. The number of sorted random numbers that appear in each interval of the cumulative sum represents the number of copies of a particle to be propagated [134].

Algorithm F.1 represents a formal description of the algorithm. The input of the algorithm is an array of importance weights and the output is an array of indices describing which particles are going to propagate forward. Note that the arrays start at 1.

Line 1 calculates the cumulative sum of the importance weights as:

$$Q_j = \sum_{l=1}^{j} \omega_t^{[l]}.$$

Lines 2 – 4 determine a sorted random number sequence in linear time ($\mathcal{O}(N)$) by calculating the cumulative sum of the negative logarithm of N random numbers uniformly distributed in $[0, 1]$.

Lines 6 – 13 determine the number of copies of a particle to be propagated. A particle with small importance weight has only a small chance to be propagated as the corresponding cumulative sum interval is also small. Thus, there is only

Algorithm F.1 Linear time resampling algorithm (from [134]).

```
Require: $\Omega_t$
Ensure: $\sum_{i=1}^{N} \omega_t^{[i]} = 1$
Q = GetCumSum($\Omega_t$)
t = GetNegLogRandomArray($N + 1$)
T = GetCumSum(t)                                ▷ $T_j = \sum_{l=1}^{j} t_l$
T = T / T[$N + 1$]
$i = j = 1$
while $i \leq N$ do
    if T[$i$] < Q[$j$] then
        idx[$i$] = $j$
        $i = i + 1$
    else
        $j = j + 1$
    end if
end while
return idx
```

a small chance that any of the random numbers appear in this interval. On the other hand, the corresponding cumulative sum interval of a particle with large importance weight is large and many random numbers can be found in it. Therefore, many duplicates of particles with large importance weight are going to survive.

Appendix G

SPPAM – Real-World Experiment Results

Table G.1 shows the distance between the true gas source location and six different estimates after the last measurement point for all 16 trials performed. The first three estimates are derived by selecting grid cells in which the predictive mean, predictive variance, or the product of mean and variance are maximum. The fourth estimate is derived by selecting grid cells in which the predictive mean is greater than 90% of the maximum. The center of this area is taken as the source location estimate and the maximum extension in x- or y-direction is used to specify a confidence interval. In the same way the last two estimates are computed using the variance (fifth result) or the product of mean and variance (sixth result). The true source location was within the mean estimation area only in four trials and within the variance estimation area in six trials. This is in line with previous observations that the concentration variance often provides a better indication of the gas source location [1] than the mean.

A re-ignition of the almost extinguished source in trial #4 (after the 20th measurement) created an intense emission that caused very high concentrations also far away from the source. The 21st measurement taken at position $(x, y) = (8.85, 4.95)m$ was affected by this outburst, which caused a strong change in the gas source location estimate. The results of trial #4 for the 20 measurement points before this event are indicated in bold face in Table G.1. The results of the entire trial are shown one line below.

Table G.1: *Results of the real-world experiments using SPPAM.*

Run	Measurement Points	Time (*min*)	Distance to True Source Location Peak Mean (*m*)	Peak Variance (*m*)	Peak Mean·Variance (*m*)	Mean (*m*)	Variance (*m*)	Mean·Variance (*m*)
1	27	17	1.60	1.46	1.60	1.66±0.75	1.52±0.71	1.57±0.49
2	24	14	2.64	2.82	2.82	2.64±0.65	2.84±0.68	2.75±0.46
3	31	17	0.66	0.20	0.43	0.68±0.77	0.25±0.80	0.46±0.57
4	**20**	**10**	**1.94**	**1.88**	**1.88**	**3.01±2.43**	**2.05±0.89**	**1.98±0.65**
	34	19	2.10	2.50	2.30	1.84±1.32	2.51±0.50	2.35±0.42
5	32	17	1.85	0.70	1.25	1.72±0.80	0.74±0.86	1.18±0.70
6	32	18	3.49	1.78	3.49	3.35±5.28	0.46±4.13	1.18±3.27
7	35	19	3.83	1.18	1.05	3.81±0.78	1.13±0.62	0.89±0.64
8	30	18	2.17	1.99	1.99	2.32±1.07	1.97±0.98	2.06±0.68
9	27	14	0.56	0.42	0.41	0.59±0.65	0.84±1.27	0.46±0.50
10	29	17	3.46	3.59	3.61	3.40±0.73	3.65±0.57	3.53±0.42
11	31	17	4.72	3.36	3.17	3.07±5.50	3.40±1.22	3.15±0.73
12	30	18	1.33	1.13	1.22	1.49±1.08	2.28±2.74	1.23±0.61
13	29	17	0.43	0.41	0.43	0.37±1.30	0.46±1.08	0.43±0.85
14	30	18	3.61	3.68	2.76	2.75±5.10	2.99±3.65	2.40±2.88
15	26	14	3.80	2.45	2.24	3.62±0.93	2.35±0.57	2.18±0.62
16	30	19	0.48	0.52	0.52	0.10±1.73	0.51±1.13	0.42±0.96
∅			2.30 ± 1.40	1.76 ± 1.19	1.83 ± 1.13	2.09 ± 1.22	1.74 ± 1.15	1.64 ± 1.02

Bibliography

[1] A. J. Lilienthal, T. Duckett, F. Werner, and H. Ishida, "Indicators of Gas Source Proximity using Metal Oxide Sensors in a Turbulent Environment," in *Proceedings of the IEEE / RAS-EMBS International Conference on Biomedical Robotics and Biomechatronics (Biorob)*, February 20 – 22 2006.

[2] T. Lochmatter and A. Martinoli, "Tracking Odor Plumes in a Laminar Wind Field with Bio-Inspired Algorithms," in *11th International Symposium on Experimental Robotics 2008 (ISER 2008)*, vol. 54, pp. 473–482, Springer, 2009.

[3] H. Ishida, K. Suetsugu, T. Nakamoto, and T. Moriizumi, "Study of autonomous mobile sensing system for localization of odor source using gas sensors and anemometric sensors," *Sensors and Actuators A*, vol. 45, pp. 153–157, 1994.

[4] Susan Phillips, "Earthquake Could Cause Gas Leaks," August 2011.

[5] A. Lilienthal, *Gas Distribution Mapping and Gas Source Localisation with a Mobile Robot.* Ph.D. Thesis, Wilhelm-Schickard Institute, University of Tübingen, 2004.

[6] "Berliner Feuerwehr: GW Messtechnik (2008, January 24). Available: `http://www.berliner-feuerwehr.de`."

[7] "Rheinmetall Defence: ABC-Spürsystem Fuchs (November 2010). Available: `http://www.rheinmetall-defence.com`."

[8] "Bundesamt für Bevölkerungsschutz und Katastrophenhilfe: ABC Schutz (Februrary 2011). Available: `http://www.bbk.bund.de`."

[9] W. Smyth and J. Moum, "Three-dimensional turbulence.," *Encyclopedia of Ocean Sciences*, vol. 6, pp. 2947–2955, 2001.

[10] P. W. Roberts and D. R. Webster, "Turbulent Diffusion," *Environmental Fluid Mechanics - Theories and Application*, 2002.

[11] L. Marques, N. Almeida, and A. de Almeida, "Olfactory sensory system for odour-plume tracking and localization.," in *Proceedings of IEEESensors*, vol. 1, pp. 418–423, 2003.

[12] T. Lochmatter, *Bio-Inspired and Probabilistic Algorithms for Distributed Odor Source Localization using Mobile Robots.* Ph.D. Thesis, EPFL, Lausanne, Switzerland, February 2010.

[13] A. Hayes, A. Martinoli, and R. Goodman, "Distributed Odor Source Localization," *IEEE Sensors Journal*, vol. 2, pp. 260–271, 2002.

[14] A. J. Lilienthal, M. Reggente, M. Trincavelli, J. L. Blanco, and J. Gonzalez, "A Statistical Approach to Gas Distribution Modelling with Mobile Robots - The Kernel DM+V Algorithm.," in *Proceedings of the IEEE/RSJ International Conference on Intelligent Robots and Systems (IROS)*, pp. 570–576, October 11 – October 15 2009.

[15] S. Pashami, S. Asadi, and A. J. Lilienthal, "Integration of OpenFOAM Flow Simulation and Filament-Based Gas Propagation Models for Gas Dispersion Simulation.," in *Proceedings of the Open Source CFD International Conference*, (Munich, Germany), 2010.

[16] S. Asadi, *Gas Distribution Modelling and Sensor Planning Strategies.* Ph.D. Thesis, Örebro University, 2013 (to be submitted).

[17] D. Link, S. Stampka, and J. Spillman, "Green House Gas Strategies - What do we do?," tech. rep., Gas Machinery Research Council, 2011.

[18] J. Janata, *Principles of Chemical Sensors.* Springer Publishing Company, Incorporated, 2nd ed.2nd printing. ed., 2009.

[19] R. A. Russell, "Survey of Robotic Applications for Odor-Sensing Technology," *The International Journal of Robotics Research*, vol. 20, no. 2, pp. 144–162, 2001.

[20] P. Moseley, A. Stoneham, and D. Williams, *Techniques and mechanisms in gas sensing.* Bristol, U.K.: Adam Hilger, 1991.

[21] U. Ostermann, ed., *Dräger-Sensorhandbuch: Boden-, Wasser- und Luftuntersuchungen sowie technische Gasanalyse.* Dräger Safety AG & Co. KGaA Lübeck, 2009.

[22] J. Chou, *Hazardous Gas Monitors: A Practical Guide to Selection, Operation, and Applications.* McGraw-Hill Book Company, New York, 2000.

[23] M. Trincavelli, *Gas Discrimination for Mobile Robots.* Ph.D. Thesis, Örebro University, 2010.

[24] J. Watson, "The tin oxide gas sensor and its applications," *Sensors and Actuators*, vol. 5, no. 1, pp. 29 – 42, 1984.

[25] A. J. Lilienthal, A. Loutfi, and T. Duckett, "Airborne Chemical Sensing with Mobile Robots," *Sensors*, vol. 6, pp. 1616–1678, October 2006.

[26] H. Bai and G. Shi, "Gas Sensors Based on Conducting Polymers," *Sensors*, vol. 7, no. 3, pp. 267–307, 2007.

[27] J. W. Gardner and P. N. Bartlett, "A brief history of electronic noses," *Sensors and Actuators B: Chemical*, vol. 18, no. 1–3, pp. 210–211, 1994.

[28] G. Kowadlo and R. A. Russell, "Robot Odor Localization: A Taxonomy and Survey," *Int. J. Rob. Res.*, vol. 27, no. 8, pp. 869–894, 2008.

[29] A. T. Hayes, A. Martinoli, and R. M. Goodman, "Swarm robotic odor localization: Off-line optimization and validation with real robots," *Robotica*, vol. 21, no. 4, pp. 427–441, 2003.

[30] L. Marques, U. Nunes, and A. T. Almeida, "Particle swarm-based olfactory guided search," *Auton. Robots*, vol. 20, pp. 277–287, June 2006.

[31] W. Jatmiko, K. Sekiyama, and T. Fukuda, "A Mobile Robots PSO-based for Odor Source Localization in Dynamic Advection-Diffusion Environment," in *Intelligent Robots and Systems 2006 IEEERSJ International Conference on*, pp. 4527–4532, 2006.

[32] W. Jatmiko, K. Sekiyama, and T. Fukuda, "A PSO-based Mobile Sensor Network for Odor Source Localization in Dynamic Environment: Theory, Simula-

tion and Measurement," in *Proceedings of the IEEE Congress on Evolutionary Computation (CEC)* (K. Sekiyama, ed.), pp. 1036–1043, 2006.

[33] W. Jatmiko, K. Sekiyama, and T. Fukuda, "A PSO-based mobile robot for odor source localization in dynamic advection-diffusion with obstacles environment: theory, simulation and measurement," *Computational Intelligence Magazine, IEEE*, vol. 2, no. 2, pp. 37–51, 2007.

[34] J.-B. Masson, M. B. Bechet, and M. Vergassola, "Chasing information to search in random environments," *Journal of Physics A: Mathematical and Theoretical*, vol. 42, no. 43, p. 434009, 2009.

[35] R. Cardé and M. Willis, "Navigational Strategies Used by Insects to Find Distant, Wind-Borne Sources of Odor," *Journal of Chemical Ecology*, vol. 34, pp. 854–866, 2008. 10.1007/s10886-008-9484-5.

[36] Y. Kuwana, I. Shimoyama, and H. Miura, "Steering control of a mobile robot using insect antennae," in *Proceedings. 1995 IEEE/RSJ International Conference on Intelligent Robots and Systems 95. "Human Robot Interaction and Cooperative Robots" Volume 2*, vol. 2, (Pittsburgh, PA, USA), pp. 530–535, IEEE Computer Society, 1995.

[37] Y. Kuwana, I. Shimoyama, Y. Sayama, and H. Miura, "Synthesis of pheromone-oriented emergent behavior of a silkworm moth.," in *Proceedings of the 1996 IEEE/RSJ International Conference on Intelligent Robots and Systems. IROS 96. Robotic Intelligence Interacting with Dynamic Worlds*, vol. 3, pp. 1722–1729, 1996.

[38] Y. Kuwana and I. Shimoyana, "Pheromone-guided mobile robot that behaves like a silkworm moth with living antennae as pheromone sensors.," *International Journal of Robotics Research*, vol. 17, no. 9, pp. 924–933, 1998.

[39] Y. Kuwana, S. Nagasawa, I. Shimoyama, and R. Kanzaki, "Synthesis of the pheromone-oriented behaviour of silkworm moths by a mobile robot with moth antennae as pheromone sensors.," *Biosensors and Bioelectronics*, vol. 14, no. 2, pp. 195–202, 1999.

[40] H. Ishida, T. Nakamoto, T. Moriizumi, T. Kikas, and J. Janata, "Plume-tracking robots: a new application of chemical sensors.," *Biological Bulletin*, vol. 200, no. 2, pp. 222–226, 2001.

[41] P. Pyk, S. Bermúdez I Badia, U. Bernardet, P. Knüsel, M. Carlsson, J. Gu, E. Chanie, B. S. Hansson, T. C. Pearce, and P. F. J. Verschure, "An artificial moth: Chemical source localization using a robot based neuronal model of moth optomotor anemotactic search," *Auton. Robots*, vol. 20, no. 3, pp. 197–213, 2006.

[42] F. Grasso, J. Dale, T. Consi, D. Moutain, and J. Atema, "Purely chemotactic robot lobster reveals different odor dispersal patterns in the jet region and the patch field of a turbulent plume.," *Biological Bulletin*, vol. 191, pp. 312–313, 1996.

[43] F. W. Grasso, T. R. Consi, D. C. Mountain, and J. Atema, "Biomimetic robot lobster performs chemo-orientation in turbulence using a pair of spatially separated sensors: Progress and challenges," *Robotics and Autonomous Systems*, vol. 30, pp. 115–131, January 2000.

[44] R. Russell, A. Bab-Hadiashar, R. Shepherd, and G. Wallace, "A comparison of reactive chemotaxis algorithms.," in *Robotics and Autonomous Systems*, vol. 45, pp. 83–97, 2003.

[45] R. Kanzaki, N. Sugi, and T. Shibuya, "Self-generated zigzag turning of Bombyx mori males during pheromone-mediated upwind walking.," *Zoological Science*, vol. 9, no. 3, pp. 515–527, 1992.

[46] E. A. Arbas, M. A. Willis, and R. Kanzaki, "Organization of goal-oriented locomotion: pheromone-modulated flight behavior of moths," in *Proceedings of the workshop on "Locomotion Control in Legged Invertebrates" on Biological neural networks in invertebrate neuroethology and robotics*, (San Diego, CA, USA), pp. 159–198, Academic Press Professional, Inc., 1993.

[47] A. Mafra-Neto and R. Cardé, "Fine-scale structure of pheromone plumes modulates upwind orientation of flying moths.," *Nature*, vol. 369, pp. 142–144, 1994.

[48] R. Cardé and A. Minks, *Insect Pheromone Research: New Directions.* London, Chapman & Hall, 1997.

[49] R. Kanzaki, “Coordination of wing motion and walking suggests common control of zigzag motor program in a male silkworm moth.,” *Journal of Comparative Physiology A: Sensory, Neural, and Behavioral Physiology*, vol. 182, no. 3, pp. 267–276, 1998.

[50] M. Willis and E. Arbas, “Variability in odor-modulated flight by moths.,” *Journal of Comparative Physiology A: Sensory, Neural, and Behavioral Physiology*, vol. 182, no. 2, pp. 191–202, 1998.

[51] J. Belanger and E. Arbas, “Behavioral strategies underlying pheromone-modulated flight in moths: lessons from simulation studies.,” *Journal of Comparative Physiology A: Sensory, Neural, and Behavioral Physiology*, vol. 183, no. 3, pp. 345–360, 1998.

[52] R. T. Cardé and B. G. J. Knols, “Effects of light levels and plume structure on the orientation manoeuvres of male gypsy moths flying along pheromone plumes,” *Physiological Entomology*, vol. 25, no. 2, pp. 141–150, 2000.

[53] K. A. Justus and R. T. Cardé, “Flight behaviour of males of two moths, Cadra cautella and Pectinophora gossypiella, in homogeneous clouds of pheromone,” *Physiological Entomology*, vol. 27, no. 1, pp. 67–75, 2002.

[54] K. A. Justus, S. W. Schofield, J. Murlis, and R. T. Cardé, “Flight behaviour of Cadra cautella males in rapidly pulsed pheromone plumes,” *Physiological Entomology*, vol. 27, no. 1, pp. 58–66, 2002.

[55] B. Webb, R. Harrison, and M. Willis, “Sensorimotor control of navigation in arthropod and artificial systems.,” *Arthropod Structure and Development*, vol. 33, no. 3, pp. 301–329, 2004.

[56] L. P. S. Kuenen and H. C. Rowe, “Cowpea weevil flights to a point source of female sex pheromone: analyses of flight tracks at three wind speeds,” *Physiological Entomology*, vol. 31, pp. 103–109, June 2006.

[57] J. Belanger and M. Willis, “Biologically-inspired search algorithms for locating unseen odor sources,” in *Proceedings of the IEEE ISIC/CIRA/ISAS Joint Conference Galthersburg, MD, USA*, pp. 265–270, 1998.

[58] W. Li, J. A. Farrell, and R. T. Cardé, “Tracking of fluid-advected odor plumes: strategies inspired by insect orientation to pheromone,” *Adapt. Behav.*, vol. 9, no. 3-4, pp. 143–170, 2001.

[59] E. Balkovsky and B. I. Shraiman, “Olfactory search at high Reynolds number.,” *Proceedings of the National Academy of Sciences of the United States of America*, vol. 99, no. 20, pp. 12589–12593, 2002.

[60] J. Farrell, “Chemical plume tracing via an autonomous underwater vehicle.,” *IEEE Journal of Oceanic Engineering*, vol. 30, no. 1, pp. 428–442, 2005.

[61] G. Ferri, E. Caselli, V. Mattoli, A. Mondini, B. Mazzolai, and P. Dario, “SPIRAL: A novel biologically-inspired algorithm for gas/odor source localization in an indoor environment with no strong airflow,” *Robotics and Autonomous Systems*, vol. 57, no. 4, pp. 393–402, 2009.

[62] A. Lilienthal and T. Duckett, “Approaches to gas source tracing and declaration by pure chemotropotaxis.,” in *Proceedings of AMS 2003, 18. Fachgespräch, Karlsruhe, 4./5. Dezember 2003*, pp. 161–171, 2003.

[63] A. Lilienthal, D. Reiman, and A. Zell, “Gas Source Tracing With a Mobile Robot Using an Adapted Moth Strategy,” in *Autonome Mobile Systeme (AMS), 18. Fachgespräch*, pp. 150–160, GDI, December 4 – 5 2003.

[64] R. Russell, “Chemical Source Location and the RoboMole Project,” in *Proceedings of the Australasian Conference on Robotics and Automation.*, 2003.

[65] A. Lilienthal and T. Duckett, “Experimental Analysis of Gas-Sensitive Braitenberg Vehicles,” *Advanced Robotics*, vol. 18, pp. 817–834, 2004.

[66] A. Dhariwal, G. S. Sukhatme, and A. A. G. Requicha, “Bacterium-inspired Robots for Environmental Monitoring,” in *IEEE International Conference on Robotics and Automation (ICRA)*, pp. 1436–1443, 2004.

[67] C. Lytridis, G. S. Virk, and E. E. Kadar, “A systematic approach to the problem of odour source localization.,” *Auton. Robot*, vol. 20, pp. 261–276, 2006.

[68] D. Martinez, O. Rochel, and E. Hugues, “A biomimetic robot for tracking specific odors in turbulent plumes,” *Auton. Robots*, vol. 20, pp. 185–195, June 2006.

[69] A. J. Rutkowski, M. A. Willis, and R. D. Quinn, “Simulated Odor Tracking in a Plane Normal to the Wind Direction,” in *Proceedings of the 2006 IEEE International Conference on Robotics and Automation, ICRA 2006, May 15-19, 2006, Orlando, Florida, USA*, pp. 2047–2052, 2006.

[70] A. J. Rutkowski, R. D. Quinn, and M. A. Willis, “A Sensor Fusion Approach to Odor Source Localization Inspired by the Pheromone Tracking Behavior of Moths,” in *2007 IEEE International Conference on Robotics and Automation,ICRA 2007, 10-14 April 2007, Roma, Italy*, pp. 4873–4878, 2007.

[71] H. Ishida, K. Yoshikawa, and T. Moriizumi, “Three-dimensional gas-plume tracking using gas sensors and ultrasonic anemometer.,” in *Proceedings of IEEESensors*, vol. 3, pp. 1175–1178, 2004.

[72] H. Ishida, M. Zhu, K. Johansson, and T. Moriizumi, “Three-dimensional gas/odor plume tracking with blimp.,” in *Proceedings of the Asia-Pacific Conference of Transducers and Micro-Nano Technology, Sapporo, Japan*, 2004.

[73] B. I. Shraiman and E. D. Siggia, “Scalar Turbulence,” *Nature*, vol. 405, pp. 639–646, 2000.

[74] M. Vergassola, E. Villermaux, and B. I. Shraiman, “’Infotaxis’ as a strategy for searching without gradients,” *Nature*, vol. 445, pp. 406–409, January 2007.

[75] M. Vergassola, E. Villermaux, and B. I. Shraiman, “Supplementary Materials for ”Infotaxis: searching without gradients”,” 2007.

[76] E. Martin Moraud and D. Martinez, “Effectiveness and robustness of robot infotaxis for searching in dilute conditions,” *Frontiers in Neurorobotics*, vol. 4, no. 0, 2010.

[77] J.-G. Li, Q.-H. Meng, F. Li, M. Zeng, and D. Popescu, “Mobile robot based odor source localization via particle filter,” in *Proceedings of the 48th IEEE Conference on Decision and Control, CDC 2009, combined with the 28th Chinese Control Conference, December 16-18, 2009, Shanghai, China*, pp. 2984–2989, 2009.

[78] J.-G. Li, Q.-H. Meng, Y. Wang, and M. Zeng, “Odor source localization using a mobile robot in outdoor airflow environments with a particle filter algorithm,” *Auton. Robots*, vol. 30, pp. 281–292, Apr. 2011.

[79] W. Li, J. A. Farrell, S. Pang, and R. M. Arrieta, “Moth-inspired chemical plume tracing on an autonomous underwater vehicle,” *IEEE Trans. on Robotics and Automation*, vol. 22, no. 2, pp. 292–307, 2006.

[80] S. Pang and J. Farrell, “Chemical plume source localization.,” *IEEE Transactions on Systems, Man, and Cybernetics-Part B: Cybernetics*, vol. 36, no. 5, pp. 1068–1080, 2006.

[81] A. Lilienthal and T. Duckett, “Gas Source Localisation by Constructing Concentration Gridmaps with a Mobile Robot,” in *Proceedings of the European Conference on Mobile Robots (ECMR)*, pp. 159–164, September 4–6 2003.

[82] J. Farrell, S. Pang, and Li, “Plume mapping via Hidden Markov Methods.,” *IEEE Transactions on Systems, Man, and Cybernetics-B*, vol. 33, no. 6, pp. 850–863, 2003.

[83] C. Stachniss, C. Plagemann, A. Lilienthal, and W. Burgard, “Gas Distribution Modeling using Sparse Gaussian Process Mixture Models,” *Autonomous Robots*, vol. 26, no. 2-3, pp. 187–202, 2009.

[84] A. J. Lilienthal and T. Duckett, “Building Gas Concentration Gridmaps with a Mobile Robot,” *Robotics and Autonomous Systems*, vol. 48, pp. 3–16, August 31 2004.

[85] M. Reggente and A. J. Lilienthal, “Using Local Wind Information for Gas Distribution Mapping in Outdoor Environments with a Mobile Robot,” in *Proceedings of IEEE Sensors*, pp. 1715–1720, 2009.

[86] A. Lilienthal and T. Duckett, “Experimental Analysis of Smelling Braitenberg Vehicles,” in *Proceedings of the IEEE International Conference on Advanced Robotics (ICAR 2003)*, pp. 375–380, 2003.

[87] G. Kowadlo, D. Rawlinson, R. A. Russell, and R. A. Jarvis, “Bi-modal Search using Complementary Sensing (Olfaction/Vision) for Odour Source Localisation,” in *Proceedings of the 2006 IEEE International Conference on Robotics and Automation, ICRA 2006, May 15-19, 2006, Orlando, Florida, USA*, pp. 2041–2046, 2006.

[88] G. Cabrita, P. Sousa, and L. Marques, “Odor guided exploration and plume tracking - Particle Plume Explorer,” in *Proceedings of the 5th European Conference on Mobile Robots ECMR 2011, September 7-9, 2011, Örebro, Sweden*, 2011.

[89] S. Asadi, M. Reggente, C. Stachniss, C. Plagemann, and A. J. Lilienthal, *Statistical Gas Distribution Modelling Using Kernel Methods. Intelligent Systems for Machine Olfaction: Tools and Methodologies*, ch. 6, pp. 153–179. IGI Global, 2011.

[90] H. Ishida, T. Nakamoto, and T. Moriizumi, “Remote sensing and localization of gas/odor source and distribution using mobile sensing system,” in *Proceedings of the International Conference on Solid State Sensors and Actuators*, vol. 1, pp. 559–562, 1997.

[91] A. H. Purnamadjaja and R. A. Russell, “Pheromone communication in a robot swarm: necrophoric bee behaviour and its replication,” *Robotica*, vol. 23, no. 6, pp. 731–742, 2005.

[92] H. Ishida, M. Tsuruno, K. Yoshikawa, and T. Moriizumi, “Spherical Gas-Sensor Array for Three-Dimensional Plume Tracking.,” in *IEEE International Conference on Advanced Robotics (ICAR 2003)*, pp. 369–374, 2003.

[93] M. Reggente and A. J. Lilienthal, “Three-Dimensional Statistical Gas Distribution Mapping in an Uncontrolled Indoor Environment,” in *AIP Conference Proceedings Volume 1137: Olfaction and Electronic Nose - Proceedings of the 13th International Symposium on Olfaction and Electronic Nose (ISOEN)*, pp. 109–112, 2009.

[94] M. Reggente and A. J. Lilienthal, “The 3D-Kernel DM+V/W Algorithm: Using Wind Information in Three Dimensional Gas Distribution Modelling with a Mobile Robot.,” in *Proceedings of IEEE Sensors*, 2010.

[95] S. Asadi, S. Pashami, A. Loutfi, and A. J. Lilienthal, “TD Kernel DM+V: Time-Dependent Statistical Gas Distribution Modelling on Simulated Measurements,” in *Olfaction and Electronic Nose - Proceedings of the 14th International Symposium on Olfaction and Electronic Nose (ISOEN)*, 2011.

[96] A. Muttreja, A. Raghunathan, S. Ravi, and N. K. Jha, “Active Learning Driven Data Acquisition for Sensor Networks,” in *Proceedings of the 11th IEEE Symposium on Computers and Communications*, pp. 929–934, 2006.

[97] A. Singh, A. Krause, C. Guestrin, W. J. Kaiser, and M. A. Batalin, “Efficient planning of informative paths for multiple robots,” in *Proc. International Joint Conference on Artificial Intelligence (IJCAI)*, pp. 2204–2211, 2007.

[98] A. Krause, A. Singh, and C. Guestrin, “Near-Optimal Sensor Placements in Gaussian Processes: Theory, Efficient Algorithms and Empirical Studies,” *Journal of Machine Learning Research (JMLR)*, vol. 9, pp. 235–284, February 2008.

[99] Y. Yang and R. S. Blum, “Sensor Placement in Gaussian Random Field Via Discrete Simulation Optimization,” *IEEE Signal Processing Letters*, vol. 15, pp. 729–732, November 2008.

[100] A. Meliou, A. Krause, C. Guestrin, and J. Hellerstein, “Nonmyopic informative path planning in spatio-temporal models,” in *AAAI*, pp. 602–607, 2007.

[101] G. Hollinger and S. Singh, “Proofs and experiments in scalable, near-optimal search by multiple robots,” in *RSS*, 2008.

[102] C. Stachniss, G. Grisetti, and W. Burgard, “Information gainbased exploration using rao-blackwellized particle filters,” in *RSS*, 2005.

[103] N. Roy, G. Gordon, and S. Thrun, “Finding approximate pomdp solutions through belief compression,” in *JAIR*, vol. 23, pp. 1–40, 2005.

[104] A. Singh, “Nonmyopic Adaptive Informative Path Planning for Multiple Robots.,” tech. rep., UC Los Angeles: Center for Embedded Network Sensing., 2009.

[105] A. Howard, M. J. Mataric, and G. S. Sukhatme, “Mobile Sensor Network Deployment using Potential Fields: A Distributed, Scalable Solution to the Area Coverage Problem,” in *6th International Symposium on Distributed Autonomous Robotic Systems (DARS)*, pp. 299–308, 2002.

[106] M. Schwager, D. Rus, and J.-J. Slotine, “Unifying geometric, probabilistic, and potential field approaches to multi-robot deployment,” *The International Journal of Robotics Research*, vol. 30, pp. 371–383, March 2011.

[107] M. A. Kovacina, D. Palmer, G. Yang, and R. Vaidyanathan, “Multi-agent control algorithms for chemical cloud detection and mapping using unmanned air vehicles,” in *IEEE/RSJ International Conference on Intelligent Robots and System*, vol. 3, pp. 2782–2788, 2002.

[108] S. B. i Badia, U. Bernardet, A. Guanella, P. Pyk, and P. Verschure, “A Biologically Based chemo-sensing UAV for Humanitarian Demining,” *Int. Journal of Advanced Robotic Systems*, vol. 4, no. 2, pp. 187–198, 2007.

[109] R. J. Bamberger, D. P. Watson, D. H. Scheidt, , and K. L. Moore, “Flight Demonstrations of Unmanned Aerial Vehicle Swarming Concepts,” *Johns Hopkins APL Technical Digest*, vol. 27, no. 1, 2006.

[110] Y. Kuroki, G. S. Young, and S. E. Haupt, “UAV navigation by an expert system for contaminant mapping with a genetic algorithm,” *Expert Syst. Appl.*, vol. 70, no. 5, pp. 4687–4697, 2010.

[111] A. Bürkle, F. Segor, and M. Kollmann, “Towards Autonomous Micro UAV Swarms,” *J. Intell. Robotics Syst.*, vol. 61, pp. 339–353, January 2011.

[112] K. Daniel, S. Rohde, N. Goddemeier, and C. Wietfeld, “Cognitive Agent Mobility for Aerial Sensor Networks,” *IEEE Sensors Journal*, vol. 11, pp. 2671–2682, Nov. 2011.

[113] D. Molnar, A.; Stojcsics, "New approach of the navigation control of small size UAVs," in *IEEE 19th International Workshop on Robotics in Alpe-Adria-Danube Region (RAAD)*, pp. 125–129, 2010.

[114] A. V. den Kroonenberg, T. Martin, M. Buschmann, J. Bange, and P. Vörsmann, "Measuring the Wind Vector Using the Autonomous Mini Aerial Vehicle M2AV," *Journal of Atmospheric and Oceanic Technology*, vol. 25, no. 11, pp. 1969–1982, 2008.

[115] G. Gremillion and J. S. Humbert, "System Identification of a Quadrotor Micro Air Vehicle," in *AIAA Conference on Atmospheric Flight Mechanics, AIAA-2010-7644, Toronto, Canada*, 2010.

[116] R. Büchi, *Faszination Quadrokopter: Technik, Elektronik, Flugpraxis.* Vth, 2010.

[117] M. Grewal, L. Weill, L. Weill, and A. Andrews, *Global positioning systems, inertial navigation, and integration.* Wiley-Interscience, 2007.

[118] P. R. Warburton, M. P. Pagano, R. Hoover, M. Logman, K. Crytzer, and Y. J. Warburton, "Amperometric Gas Sensor Response Times.," *Analytical Chemistry*, vol. 70, no. 5, pp. 998–1006, 1998.

[119] "ANSI/IEC 60529-2004: Degrees of Protection Provided by Enclosures (IP Code)," 2004.

[120] D. Turner, *Workbook of atmospheric dispersion estimates: an introduction to dispersion modeling.* Lewis Publishers, 1994.

[121] M. Beychok, *Fundamentals of stack gas dispersion.* M.R. Beychok, 2005.

[122] W. Nitsche and A. Brunn, *Strömungsmesstechnik.* VDI-Buch, Springer, 2006.

[123] E. Williams, "Aviation Formulary V1.46." `http://williams.best.vwh.net/`, 04 2011.

[124] B. Siciliano and O. Khatib, eds., *Springer Handbook of Robotics.* Springer, 2008.

[125] J. Farrell, J. Murlis, X. Long, W. Li, and R. Cardé, “Filament-based atmospheric dispersion model to achieve short time-scale structure of odor plumes.,” *Environmental Fluid Mechanics*, vol. 2, no. 1–2, pp. 143–169, 2002.

[126] A. Lilienthal and T. Duckett, “A Stereo Electronic Nose for a Mobile Inspection Robot,” in *Proceedings of the IEEE International Workshop on Robotic Sensing (ROSE)*, (Örebro, Sweden), IEEE, 2003.

[127] K. Levenberg, “A Method for the Solution of Certain Non-Linear Problems in Least Squares.,” in *The Quarterly of Applied Mathematics 2*, pp. 164–168, 1944.

[128] V. Braitenberg, *Vehicles: Experiments in Synthetic Psychology.* Cambridge, MA, USA: The MIT Press, February 1986.

[129] T. Duckett, M. Axelsson, and A. Saffiotti, “Learning to Locate an Odour Source with a Mobile Robot,” in *Proceedings of the IEEE International Conference on Robotics and Automation (ICRA 2001), Seoul, South Korea*, pp. 21–26, 2001.

[130] A. Lilienthal and T. Duckett, “Creating gas concentration gridmaps with a mobile robot.,” in *Proceedings of the IEEE/RSJ Int. Conf. on Intelligent Robots and Systems Las Vegas, NV*, vol. 1, pp. 118–123, 2003.

[131] A. Lilienthal, H. Ulmer, H. Fröhlich, A. Stützle, F. Werner, and A. Zell, “Gas Source Declaration with a Mobile Robot,” in *Proceedings of the IEEE International Conference on Robotics and Automation (ICRA 2004)*, pp. 1430–1435, 2004.

[132] W. Li, “Moth plume-tracing derived algorithm for identifying chemical source in near-shore ocean environments,” in *2007 IEEE/RSJ International Conference on Intelligent Robots and Systems, October 29 - November 2, 2007, Sheraton Hotel and Marina, San Diego, California, USA*, pp. 2162–2167, 2007.

[133] S. Thrun, W. Burgard, and D. Fox, *Probabilistic Robotics (Intelligent Robotics and Autonomous Agents series).* Intelligent robotics and autonomous agents, The MIT Press, 2005.

[134] I. M. Rekleitis, “A Particle Filter Tutorial for Mobile Robot Localization,” Tech. Rep. TR-CIM-04-02, Centre for Intelligent Machines, McGill University, 3480 University St., Montreal, Québec, CANADA H3A 2A7, 2004.

[135] B. Limketkai, D. Fox, and L. Liao, “CRF-Filters: Discriminative Particle Filters for Sequential State Estimation,” in *2007 IEEE International Conference on Robotics and Automation*, pp. 3142–3147, 2007.

[136] E. W. Weisstein, “"Line-Line Intersection."” From MathWorld–A Wolfram Web Resource. `http://mathworld.wolfram.com/Line-LineIntersection.html`.

[137] W. R. Franklin, “PNPOLY - Point Inclusion in Polygon Test,” 2009.

[138] J. Carpenter, P. Clifford, and P. Fearnhead, “An Improved Particle Filter for Non-linear Problems,” in *IEE Proceedings - Radar, Sonar and Navigation*, vol. 146, pp. 2–7, 1999.

[139] R. Douc, O. Cappé, and E. Moulines, “Comparison of Resampling Schemes for Particle Filtering,” *ISPA 2005.PROCEEDINGS OF THE 4TH INTERNATIONAL SYMPOSIUM ON*, vol. 2005, p. 64, 2005.

[140] J. S. Liu, *Monte Carlo strategies in scientific computing.* Springer, 2001.

[141] J. Liu, R. Chen, and T. Logvinenko, *A Theoretical Framework for Sequential Importance Sampling and Resampling*, pp. 225 – 242. Sequential Monte Carlo Methods in Practice, New York: Springer Verlag, 2001.

[142] K. R. Beevers, “Sampling Strategies for Particle Filtering SLAM,” in *IEEE INTERNATIONAL CONFERENCE ON ROBOTICS AND AUTOMATION (ICRA 2007)*, 2007.

[143] A. Loutfi, S. Coradeschi, A. J. Lilienthal, and J. Gonzalez, “Gas distribution mapping of multiple odour sources using a mobile robot,” *Robotica*, vol. 27, no. 2, pp. 311–319, 2008.

[144] M. Reggente, *Monitor Pollution in Uncontrolled Micro Environment Using Autonomous Mobile Sensors and Statistical Gas Distribution Mapping.* Ph.D. Thesis, Örebro University, 2012, to appear.

[145] J. Gonzalez-Jimenez, J. Monroy, and J. Blanco, “The Multi-Chamber Electronic Nose - An Improved Olfaction Sensor for Mobile Robotics,” *Sensors*, vol. 11, no. 6, pp. 6145–6164, 2011.

[146] G. L. Gaile and J. E. Burt, *Directional Statistics. Concepts and Techniques in Modern Geography*, vol. 25 of *Geo Books.* Norwich, England: Institute of British Geographers, 1980.

List of Publications

The work presented in this thesis has also been presented in a number of journals, conference proceedings, and workshops. Where appropriate, results which correspond to specific chapters in this Ph.D. thesis are referenced in the text using the labels indicated in the following list:

Journals

PAPER I M. Bartholmai and P. Neumann, "Adaptive ortsaufgelöste Gaskonzentrationsmessung mit einer Mikrodrohne," *tm – Technisches Messen, Oldenbourg Wissenschaftsverlag GmbH*, vol. 78, pp. 470–478, 2011.

PAPER II V. Hernandez Bennetts, A. J. Lilienthal, P. P. Neumann, and M. Trincavelli, "Mobile Robots for Localizing Gas Emission Sources on Landfill Sites: Is Bio-Inspiration the Way to Go?," *Frontiers in Neuroengineering*, vol. 4, no. 20, 2012.

PAPER III P. P. Neumann, S. Asadi, J. H. Schiller, A. J. Lilienthal, and M. Bartholmai, "Micro-Drone for Wind Vector Estimation and Gas Distribution Mapping," *IEEE Robotics and Automation Magazine (RAM)*, vol. 19, no. 4, pp. 50–61, 2012.

PAPER IV P. P. Neumann, V. Hernandez Bennetts, A. J. Lilienthal, M. Bartholmai, and J. H. Schiller, "Gas Source Localization with a Micro-Drone using Bio-Inspired and Particle Filter-based Algorithms," *Advanced Robotics (AR)*, Special Issue on Aerial Robots, vol. 27, no. 9, 2013, to appear.

Conference Proceedings

Paper V P. Neumann, M. Bartholmai und B. Wiggerich, "Mikrodrohne zur Charakterisierung und selbstoptimierenden Suche von gasförmigen Gefahrstoffquellen," in *Sensoren und Messsysteme 2010*, Vorträge der 15. ITG / GMA-Fachtagung vom 18. bis 19. Mai in Nürnberg, VDE VERLAG GMBH, pp. 753–757, 2010.

Paper VI P. Neumann, B. Wiggerich, and M. Bartholmai, "Micro-Drone for the Characterization and Self-Optimizing Search of Hazardous Gaseous Substance Sources," in *International Micro Air Vehicle Conference and Flight Competition IMAV 2010*, Braunschweig, Germany 06 - 09 July 2010, German Institute of Navigation / Deutsche Gesellschaft für Ortung und Navigation e.V. (DGON), 2010.

Paper VII M. Bartholmai and P. Neumann, "Micro-Drone for Gas Measurement in Hazardous Scenarios via Remote Sensing," in *The 6th WSEAS International conference on remote sensing (REMOTE '10) - Selected topics in power systems and remote sensing (2010)*, WSEAS Press, Iwate Prefectural University, Japan, pp. 149–152, 2010.

Paper VIII M. Bartholmai, E. Köppe, and P. Neumann, "Sensor Technologies and Electronic Systems," in *Proceedings of KCESS 2011, Kuwait Conference on e-Services and e-Systems*, Kuwait, 2011.

Paper IX P. P. Neumann, V. Hernandez Bennetts, and M. Bartholmai, "Adaptive Gas Source Localization Strategies and Gas Distribution Mapping using a Gas-sensitive Micro-Drone," in *Sensoren und Messsysteme 2012*, Vorträge der 16. ITG / GMA-Fachtagung vom 22. bis 23. Mai in Nürnberg, VDE VERLAG GMBH, 2012.

Paper X P. P. Neumann, S. Asadi, V. Hernandez Bennetts, A. J. Lilienthal, and M. Bartholmai, "Monitoring of CCS Areas using MUAVs," in *Energy Procedia 2012*, to appear.

Workshops

Paper XI P. Neumann, M. Bartholmai, J. H. Schiller, M. Manolov, and B. Wiggerich, “Self Optimizing Search and Characterization of Gaseous Hazardous Substance Sources using a Micro-Drone: A new Approach to determine Wind Speed and Direction,” in *IEEE International Workshop on Robotic and Sensors Environments (ROSE)*, Phoenix, AZ, USA, 2010.

Paper XII P. P. Neumann, S. Asadi, J. H. Schiller, A. J. Lilienthal, and M. Bartholmai, “An Artificial Potential Field based Sampling Strategy for Gas-Sensitive Micro-Drone,” in *Proceedings of Workshop on Robotics for Environmental Monitoring (WREM2011) on IEEE/RSJ International Conference on Intelligent Robots and Systems (IROS 2011)*, San Francisco, CA, USA, 2011.

List of Figures

List of Tables

List of Algorithms

Nomenclature

KL	Kullback-Leibler
pdf	probability density function
ppm	parts per million
Pt	Platinum
rpm	revolutions per minute
AirShield	Airborne Remote Sensing for Hazard Inspection by Network Enabled Lightweight Drones
APF	Artificial Potential Field
AUV	Autonomous Underwater Vehicles
AW	Acoustic Wave
BAM	Bundesanstalt für Materialforschung und -prüfung (Federal Institute for Materials Research and Testing)
BAM TTS	BAM Testgelände Technische Sicherheit (BAM Test Site 'Technical Safety')
BAW	Bulk Acoustic Wave
bio-inspired	biologically inspired
BMWi	Bundesministerium für Wirtschaft und Technologie (Federal Ministry of Economics and Technology)
Cat	Catalytic
CBRNE	Chemical, Biological, Radiological, Nuclear, and Explosive
CCS	Carbon Capture & Storage
CFD	Computational Fluid Dynamics
CP	Conductive Polymer
CRW	Cooperative-repelling Random Walk
DFU	Data Fusion Unit

DWD	Deutscher Wetterdienst (German Weather Service)
e-nose	electronic nose
EC	Electrochemical
EMA	exponential moving average
Ex	Explosion-proof
GasBot	Monitoring of Landfill Sites with a Gas-Sensitive Mobile Robot
GC	Gas Chromatography
GDM	Gas Distribution Mapping
GIS	Geographic Information System
GP	Gaussian Process
GPM	Gaussian Process Mixture
GPS	Global Positioning System
GPSM	GPS Model
GSL	Gas Source Localization
GSM	Gas Sensor Model
GUI	Graphical User Interface
IMU	Inertial Measurement Unit
IR	Infrared
Kernel DM	Kernel extrapolation Distribution Mapping
MCE-nose	Multi-Chamber Electronic Nose
MI	Mutual Information
MNE	Maximum Neighbors Estimate
MOX	Metal Oxide
MS	Mass Spectrometry
MSE	Mean Squared Error
MUAV	Micro Unmanned Aerial Vehicle
OpenFOAM	Open Field Operation and Manipulation
OV	Organic Vapors
OV-A	Organic Vapors Class A
PF	Particle Filter
POMDP	Partially Observable Markov Decision Process
PPE	Patch Path Envelope
PSO	Particle Swarm Optimization

QCM	Quartz Crystal Microbalance
RMSE	Root Mean Squared Error
SAW	Surface Acoustic Wave
SLAM	Simultaneous Localization And Mapping
SM	Sensor Model
SMC	Sequential Monte Carlo Method
SP	Sensor Planning
SPF	Stigmergic Potential Field
SPPAM	Sensor and Path Planning Algorithm for the Micro-Drone
SRW	Self-repelling Random Walk
UAV	Unmanned Aerial Vehicle
VTOL	Vertical Take-Off and Landing
WGS 84	World Geodetic System 1984
WP	Waypoint